

# REPORT DOCUMENTATION PAGE

Form Approved  
OMB No. 0704-0188

Public reporting burden for this collection of information is estimated to average 1 hour per response, including the time for reviewing instructions, searching data sources, gathering and maintaining the data needed, and completing and reviewing the collection of information. Send comments regarding this burden estimate or any other aspect of this collection of information, including suggestions for reducing this burden to Washington Headquarters Service, Directorate for Information Operations and Reports, 1215 Jefferson Davis Highway, Suite 1204, Arlington, VA 22202-4302, and to the Office of Management and Budget, Paperwork Reduction Project (0704-0188) Washington, DC 20503.

PLEASE DO NOT RETURN YOUR FORM TO THE ABOVE ADDRESS.

1. REPORT DATE (DD-MM-YYYY) 15-02-2002			2. REPORT DATE Final Technical Report		3. DATES COVERED (From - To) 1996-1999	
4. TITLE AND SUBTITLE Brittle to Ductile Transition in Cleavage Fracture of Alpha-Iron: Experiments and Modeling of Mechanisms					5a. CONTRACT NUMBER N00014-96-1-0629	
					5b. GRANT NUMBER N00014-96-1-0629	
					5c. PROGRAM ELEMENT NUMBER	
					5d. PROJECT NUMBER	
6. AUTHOR(S) Ali S. Argon Professor of Mechanical Engineering					5e. TASK NUMBER	
					5f. WORK UNIT NUMBER	
7. PERFORMING ORGANIZATION NAME(S) AND ADDRESS(ES) Massachusetts Institute of Technology 77 Massachusetts Avenue Cambridge, MA 02139						
9. SPONSORING/MONITORING AGENCY NAME(S) AND ADDRESS(ES) Office of Naval Research, Materials Science Prg ONR Code 331 800 N. Quincy Street, Balston Tower 9 Arlington VA 22217-5000					10. SPONSOR/MONITOR'S ACRONYM(S) ONR	
					11. SPONSORING/MONITORING AGENCY REPORT NUMBER 99R00006-01	
12. DISTRIBUTION AVAILABILITY STATEMENT ONR Program Officer Dr. George Yoder; Administrative Grants Office; Director NRL; DTIC Othrewise Unlimited						
13. SUPPLEMENTARY NOTES						
14. ABSTRACT In this research the mechanisms of the brittle to ductile transition of fracture initiated primarily by crack tip processes under both quasi-static as well as dynamic conditions was studied experimentally, and mechanistically modeled. Additional experiments and modeling included the role of grain boundaries in resisting cleavage cracking among grains in Fe-3%Si alloy, also associated with modeling.						
15. SUBJECT TERMS Brittle to Ductile Fracture Transitions; Modeling Crack-tip Plastic Response; Crack Arrest by Grain Boundaries						
16. SECURITY CLASSIFICATION OF:			17. LIMITATION OF ABSTRACT	18. NUMBER OF PAGES	19a. NAME OF RESPONSIBLE PERSON	
a. REPORT	b. ABSTRACT	c. THIS PAGE			19b. TELEPHONE NUMBER (Include area code)	
U	U	U	U		Ali S. Argon, Princip. Invest (617) 253-2217	

20020322 145

OFFICE OF NAVAL RESEARCH

FINAL TECHNICAL REPORT

for

GRANT N00014-96-1-0629

PR Number 99R00006-01

BRITTLE TO DUCTILE TRANSITION IN CLEAVAGE FRACTURE OF ALPHA-  
IRON: EXPERIMENTS AND MODELING OF MECHANISMS

Ali S. Argon  
Professor of Mechanical Engineering  
Massachusetts Institute of Technology  
77 Massachusetts Avenue, Cambridge, MA 02139

February 15, 2002

Reproduction in whole, or in part, is permitted for any purpose of the  
United States Government.

This document has been approved for public release and sale, its distribution is unlimited.

# **BRITTLE TO DUCTILE TRANSITION IN CLEAVAGE FRACTURE OF ALPHA-IRON: EXPERIMENTS AND MODELING OF MECHANISMS**

## **I. Summary of Research Carried out under the Program**

The research results reported here in this final technical report are a continuation of an earlier program supported by the ONR Mechanics Division under Contract #N00014-92-J-4022 where the emphasis was on an experimental study of the brittle-to-ductile transition of fracture in silicon single crystals by thermal crack arrest and on modeling of dislocation emission from crack tips. Similarly, the research initiated under the ONR Program reported here, supported by the Materials Science Division and studying the role of grain boundaries in the crack growth resistance is now being continued under NSF support.

The principal thrust in the completed research program under ONR support was on two experimental studies. One thrust was the completion of earlier research on the study of brittle to ductile fracture transition in silicon single crystals as stated above, while the second thrust was on a study of the role of grain boundaries in the enhancement of cleavage crack-growth-resistance in Fe – 3 % Si alloy.

The principal results are summarized in the three sections below:

## **II. Research Report**

### *1.0 Plastic Zones of Thermal Crack Arrest in Silicon.*

A limiting form of a Brittle-to-Ductile (BD) transition in intrinsically brittle covalent solids is by crack tip shielding resulting from the development of a plastic zone initiated from a crack tip in an initially dislocation free crystal. Where the BD transition temperature is governed by the kinetics of slip-induced-shielding. To account for this effect in dislocation-free silicon crystals the well known crack tip stress relaxation model of Riedel and Rice (1980) for creep deformation was adopted successfully through the use of fundamental crystal plasticity data on silicon to account for the shift of the BD transition temperature on loading rate in Si and to predict the dislocation content of the crack tip arrest zone. This represents the first realistic modeling of the mechanism of crack arrest in Si, and explains the experimental observations very well.

### *2.0 Experimental Study of the Crack Arrest Zones in Silicon.*

The main experimental study was on crack arrest in Si single crystals for cracks propagating up a temperature gradient. These verified the rate dependence of the arrest phenomenon and permitted the determination of the activation energy of crystallographic

slip processes from the crack velocity-dependence of the BD transition temperature. Detailed observations of the types and distributions of the dislocations in the plastic zones by combined etch pitting and Berg-Barrett type x-ray topographic imaging of dislocations verified the criteria for the selection of particular slip systems on the basis of ease of nucleation of dislocation embryos at the crack tip from cleavage ledges.

### *3.0 Role of Grain Boundaries in Cleavage Cracking-Resistance in Fe-3% Si bi-crystals.*

In this experimental investigation and associated modeling the role of grain boundaries in impeding cleavage crack propagation was studied in a statistically relevant sampling of the behavior of large bi-crystals of Fe-3% Si harvested from a large ingot donated by the Allegheny Ludlum Steel Co. In the experiments the temperature and lattice-misorientation-dependence of  $\Delta K$  that is required to propagate a cleavage crack across a substantial set of specific large angle grain boundaries were measured to identify the factors that govern the crack propagation resistance of individual grain boundaries.

The measured levels of resistances  $\Delta K$  resulted partly from additional cleavage plane area produced in the neighboring grain and partly from the plastic-tearing-work bridging these separated cleavage strips. An associated model demonstrated that these resistances are far more importantly affected by the twist misorientation across the boundary plane rather than the tilt misorientation. These results were used to guide a more global study of cleavage cracking-resistance of a field of randomly misoriented grains in a polycrystal. All models quite successfully related to the experimental measurements. Much of this investigation that had been started under ONR support has been carried out under NSF support.

### **III. Publications Resulting from the ONR Program**

1. A. S. Argon, "Mechanics and Physics of Brittle to Ductile Transitions in Fracture", **J. Engng. Mater. & Technology**, **123**, 1, 2001.
2. A. S. Argon and B. J. Gally, "Selection of Crack-Tip-Slip Systems in the Thermal Arrest of Cleavage Cracks in Dislocation-Free Silicon Single Crystals", **Scripta Mater.**, **45**, 1287, 2001.
3. A. S. Argon and Y. Qiao, "Cleavage Cracking-Resistance of High Angle Grain Boundaries in Fe-3% Si Alloy", **Phil. Mag.**, in the press.
4. B. Gally and A. S. Argon, "Brittle-to-Ductile Transition in the Fracture of Silicon Single Crystals by Dynamic Crack Arrest", **Phil. Mag.**, **81**, 699, 2001.
5. Y. Qiao and A. S. Argon, "Cleavage Cracking-Resistance of High Angle Grain Boundaries in Fe-3% Si Alloy", **Mechanics of Materials**, in the press.
6. G. Xu, A. S. Argon and M. Ortiz, "Critical Configurations for Dislocation Nucleation from Crack Tips", **Phil. Mag.**, **75**, 341, 1997.



#### **IV. Personnel Associated with the ONR Program.**

1. A. S. Argon, principal investigator, Quentin Berg Professor of Mechanical Engineering. Massachusetts Institute of Technology, Cambridge, MA
2. B. J. Gally, Research Assistant, Materials Science and Engineering Department, M.I.T., recipient of Ph.D. Degree in 1999.
3. R. Kappaser, Research Assistant, Mechanical Engineering Department, M.I.T. withdrew after one year in 1997.
4. Y. Qiao, Research Assistant, Mechanical Engineering Department, candidate for Ph.D. degree 2002.

#### **Honors Received**

1. ASME Nadai Medal, 1998.
2. ETH-Zürich, Switzerland, Standinger Dürer Medal, 1999.

#### **V. Appendices**

**REPRINTS OF PUBLISHED PAPERS AND PRE-PUBLICATION**

**COPIES OF PAPERS PRESENTLY IN THE PRESS**

**Under Grant N00014-96-1-0629**

# Mechanics and Physics of Brittle to Ductile Transitions in Fracture<sup>1</sup>

**A. S. Argon**

Department of Mechanical Engineering,  
Massachusetts Institute of Technology,  
Cambridge, MA 02139

*The mechanisms of brittle-to-ductile transition of fracture in intrinsically brittle crystalline solids such as structural steel have been of great technological interest for a long time. While much useful phenomenology on this important bifurcation behavior has evolved through material testing and alloy development throughout the period following the large scale fractures in Liberty ships during and after World War II, fundamental mechanistic understanding has been lacking until recent times. Over the past decade or so, a renewed level of interest has resulted in a number of fundamental studies of both experimental nature and modeling of crack-tip response which demonstrated a remarkable connection of atomic level processes at tips of cleavage cracks and the macroscopic fracture transitions. These mechanistic connections have not only gone a long way in providing basic rationale for some of the successful empirical practices in alloy design and microstructure control, but clear the way for further advances based on basic atomic level processes governing crystal plasticity. Here we give an overview of some recent developments in this area emanating from our own researches.*

[DOI: 10.1115/1.1325408]

**Keywords:** Brittle-to-Ductile Fracture Transitions, Cleavage Fracture, Crack Tip Modeling

## 1 Introduction

Ductile to brittle (D-B) transitions of fracture in steel structures are familiar to most mechanical engineers. Many celebrated cases starting with the famous molasses tank fracture in Boston in the winter of 1919 with its bizarre tales of people and horses drowned in molasses; the rash of welded Liberty ships breaking apart on the high seas in World War II and after; the ever continuing discussions on the fate of the Titanic being perhaps due to the brittleness of its steel; the collapse in earthquakes of elevated highway superstructures that were thought to be ductile, all keep the problem current and scary.

Through the surge of research and development after World War II in the U.S. and Britain on the D-B transitions, considerable attention was given to the operational aspects of the problem which resulted in much useful alloy development and material testing procedures. This phenomenological perspective, often inspired by some mechanistic insight, has continued up to the present, introducing, more recently, probabilistic aspects of the D-B transition based on the triggering processes that initiate brittle response in structures undergoing ductile behavior. While these developments have resulted in unquestionable improvements in practical applications, they have shed little light on the fundamental governing processes that have wide ranging applications to all intrinsically brittle solids including e.g., ice. Here we will take a brief excursion into some of these fundamental developments with particular emphasis on our own research.

## 2 Intrinsically Ductile and Intrinsically Brittle Solids

An important insight into the bifurcation phenomenon of fracture came with Kelly et al. [1], and more specifically with Rice and Thomson [2] who conceived of a fundamental behavior pattern for a theoretical criterion establishing which materials are intrinsically ductile and not subject to a D-B transition, and those

that are intrinsically brittle that can exhibit brittle behavior at low temperatures and high strain rates. In the Rice and Thomson scenario if an atomically sharp mode-I crack in a solid, containing no other imperfections, can emit dislocations from its tip that can then freely multiply before the crack can propagate by cleavage, the solid is identified to be intrinsically ductile under all conditions. Crystalline materials capable of such response are few and are restricted primarily to the metals Ag, Al, Au, Cu, Ni, Nb, Pb, Pt, and Ta, and to some types of amorphous metals. According to this classification all other metals, semiconductors and compounds, including inorganic glasses and possibly all polymers are intrinsically brittle. The latter possess important energy barriers to dislocation emission from crack tips or to initiation of other forms of plasticity in the case of amorphous solids. Nevertheless, they can exhibit ductile behavior above a certain temperature, for a given rate of loading, where these energy barriers can be overcome.

It is the mechanisms of fracture transitions in such intrinsically brittle solids ranging from metals to semiconductors to polymers that we have investigated over the years that will be the subject of this paper. Here we will concentrate only on the processes in crystalline solids that are the best understood, and particularly in iron and silicon which represent two special limiting forms of this type of behavior.

## 3 Ductile to Brittle or Brittle to Ductile Transitions

While the principal familiarity in engineering practice in structural applications is with the D-B transitions, the fundamental aspects are best pursued by considering the reverse process that permits an intrinsically brittle solid to behave in a ductile manner. In one of the more searching early studies on polycrystalline steel, Hahn et al. [3] noted that in smooth bar experiments with a low carbon steel in the D-B transition range of low temperatures the eventual brittle behavior was ushered in by the appearance of grain sized microcracks. These were produced mostly by intersections of deformation twins inside grains; or by cracked carbides. The steel was noted to continue to be ductile when these microcracks were arrested by grain boundaries and rendered ineffective

<sup>1</sup>The 1998 ASME Nadai Medal Award Lecture.

Contributed by the Materials Division for publication in the JOURNAL OF ENGINEERING MATERIALS AND TECHNOLOGY. Manuscript received by the Materials Division June 19, 2000. Associate Technical Editor: D. L. McDowell.

by blunting. A transition to brittle behavior was observed at lower temperatures and higher flow stresses when such cleavage microcracks broke through grain boundaries. This specific role of grain boundaries that has not been studied further in any detail is now under investigation by us [4] in special bi-crystal specimens where cleavage cracks are probing grain boundaries of different inclination separating grains having different angles of twist and tilt relative to each other. These experiments are indicating that while additional work of fracture is required for cleavage cracks to break through grain boundaries in a variety of ways involving different kinematical forms, the principal role of the boundary is to stop the cleavage crack for a certain length of time. This permits thermal processes to initiate plastic behavior at the crack tip that can eventually render it ineffective by shielding or blunting. This indicates that the basic mode of the fracture transition is one from brittle-to-ductile (B-D) behavior that involves a crack-tip-initiated thermally-assisted process of emission of dislocations followed by their rapid multiplication in the overstressed crack tip environment. While it might be expected that plastic response in the background, away from the crack tip, can also produce beneficial shielding of the crack tip, this is usually far less effective for several reasons. First, aging often immobilizes the background dislocations making them difficult to displace. Second, stresses drop sharply away from the crack making such displacements less likely. Thus, in what follows we concentrate on the B-D transition under two different but complementary histories based on crack-tip-initiated plasticity.

First, we consider stationary mode-I cleavage cracks undergoing a transition from a brittle cleavage response to a tough one with increasing temperature dependent on loading rate. Second, we consider brittle cleavage cracks propagating up a temperature gradient at different constant velocities until they are arrested at a temperature dependent on crack velocity. In both cases the remarkable fact is that, while the transition is in all aspects a macroscopic phenomenon, the key element that governs it involves atomic level processes at the cores of dislocations that control their mobility in different classes of materials. In all cases the eventual tough response of the material involves massive generation and motion of dislocations resulting in large plastic strains at crack tips. Nevertheless, two quite different rate controlling processes can be identified for two separate classes of intrinsically brittle solids based on their dislocation core properties. In the first category are all the BCC transition metals which in pure form exhibit a strong stress dependence of dislocation velocity [5], which has been related to a single energy barrier to the motion of a dislocation line from one lattice potential valley into the next, requiring the nucleation of only a double kink with no further barrier present to impede the motion of these kinks along the dislocation lines, as depicted in Fig. 1(a). Metals in this category should include Fe, Cr, Mo, W. In these metals the process that triggers the plastic response is thought to be primarily the formation of embryos of fresh dislocations from the crack tip, which can then freely undergo a profuse form of multiplication in the highly stressed crack tip environment to produce the required densities of dislocation line for the development of large plastic strains without further impediment. In the second category are most of the rest of the intrinsically brittle solids in which the motion of the dislocation line from one lattice potential valley into the next, requires not only the nucleation of a double kink but also the motion of the kinks along the dislocation line which is subject to further substantial secondary energy barriers, leading to very sluggish dislocation motion that is only weakly stress dependent. In these materials, among which Si has been widely studied, the final transition to ductile behavior is controlled by the mobility of the groups of dislocations away from the crack tip as depicted in Fig. 1(b). Nevertheless, even in these materials, experiments indicate that the dislocations that produce the large plastic strains are those that have the lowest energy barrier to their formation at the crack tip. This rather startling behavior that such a major macroscopic

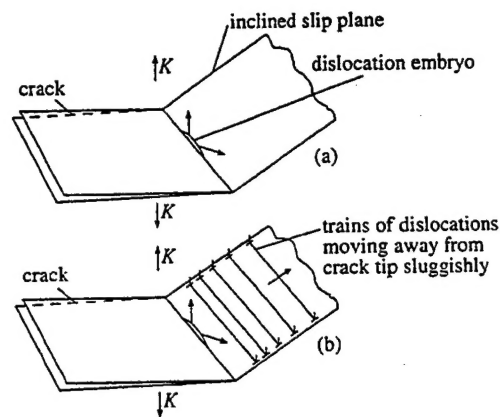


**Fig. 1 Configurations of crack tip processes leading from brittle to ductile behavior: (a) formation of a dislocation embryo which can expand freely to result subsequently in unimpeded intense dislocation multiplication as is approximately the case in BCC transition metals; (b) emission of a train of dislocations, sluggishly moving away from the crack tip in materials with high lattice resistance to kink motion along dislocations such as in Si and compounds**

transition from a brittle to ductile form, that is known to be affected by microstructure can, nevertheless, ultimately be controlled by atomic level processes at the cores of dislocations is the major finding of the recent fundamental studies. In what follows we take some brief excursions into these recent developments in modeling and review some key experimental results.

#### 4 Modes of Dislocation Nucleation From Crack Tips

Based on expectations, three basic modes of dislocation emission from tips of cleavage cracks were considered in the modeling studies [6,7]. These are illustrated in Figs. 2(a)–2(c) and consist of nucleation of dislocation embryos on inclined slip planes, going through the crack front, on oblique planes intersecting the crack front, and finally on microscopic cleavage ledges produced frequently by small perturbations of the local mode-I loading axis away from the normal to the cleavage planes.

The method of analysis that had the required flexibility to deal with the expected three-dimensional forms of the critical dislocation embryos was the variational boundary integral (VBI) technique developed earlier by Xu and Ortiz [8] for dealing with arbitrary convolutions of crack fronts involved in crack trapping, arising from tough local heterogeneities forcing brittle cracks to overcome them by bowing around them. In the VBI method the approach is based on the use of continuously distributed densities of curved segments of dislocations of infinitesimal strength, to rigorously construct any required shape of crack front. In its present application the VBI method is used to model the emergence at the crack tip of incipient local nonlinear displacements involved in the production of dislocations as the crack tip stresses approach the ideal shear strength of a perfect crystal. The methodology is precise and has been discussed fully in previous publications [6–9]. In the next section we outline briefly the key aspects of the VBI approach that is pertinent to the determination of the special activation configurations related to the modes of dislocation nucleation illustrated in Figs. 2(a)–2(c).

We consider a semi-infinite cleavage crack and an inclined slip plane intersecting the crack front, as depicted in Fig. 3, as a generic possibility. The crack/slip plane system is loaded remotely by a  $K$ -field. The crystallographic slip plane is chosen to be the most advantageous one for slip. As the driving force increases, an embryonic dislocation forms progressively until it reaches an unstable equilibrium configuration. The energy release rate  $G_I$  corresponding to this unstable configuration is defined as the critical

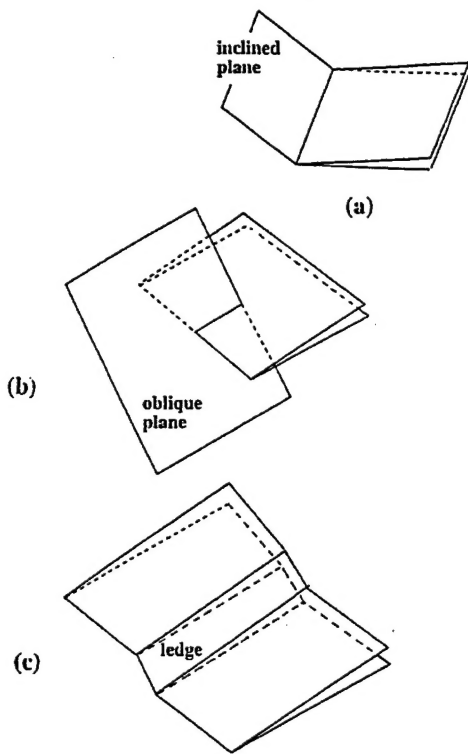


Fig. 2 Three modes of dislocation emission from the tip of a cleavage crack: (a) on an inclined plane going through the crack front; (b) on an oblique plane intersecting the crack front; (c) on a small cleavage surface ledge at the crack front

“driving force” for dislocation nucleation. The embryonic dislocation profile is characterized as a distribution of interplanar inelastic displacements, defined by Rice [10] as

$$\delta = \Delta - \Delta^e \quad (1)$$

where  $\Delta$  and  $\Delta^e$  denote the total and the elastic interplanar displacements, respectively. The opening displacements  $u$  of the crack surface, including the inelastic displacements along the slip plane, can be written as

$$u = \bar{u} + \delta \quad (2)$$

where  $\bar{u}$  is the displacement of a standard  $K$ -field for a reference semi-infinite crack. The term  $\bar{u}$  matches the behavior of the opening displacements of the crack far away from the crack tip and serves as a boundary condition of the system. Consequently, the additional term  $\delta$ , modifying the former, and which is the primary

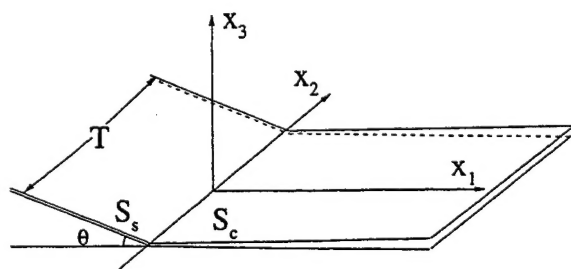


Fig. 3 A generic semi-infinite crack with an inclined plane going through the crack front defining the parameters of the variational boundary integral method of analysis

Table 1 Material properties for  $\alpha$ -Fe [7]

slip system	$T$ (°K)	$\mu$ (10 <sup>5</sup> MPa)	$c$	$\gamma_{us}^{(u)}$ (Jm <sup>-2</sup> )	$2\gamma_s$
(1/2)[111](110)	4.2	0.756	3.125	0.517	3.33
(1/2)[111](112)	4.2	0.756	3.125	0.581	3.80

where

$\mu$  shear modulus  
 $c$  uniaxial strain elastic modulus  
 $\gamma_{us}^{(u)}$  unrelaxed unstable stacking energy<sup>2</sup>  
 $\gamma_s$  surface energy

unknown in the analysis, is expected to decay rapidly to zero with distance away from the crack tip in either direction. In this manner,  $\delta$  can be considered in a finite domain around the crack front on the crack surface and on the slip plane connected to the crack.

Following the procedure introduced by Xu et al. [6,7] the potential energy of the whole system can be written in the form

$$\Pi[\bar{u} + \delta] = W[\bar{u} + \delta] + V[\delta] = W_1[\bar{u}] + W_1[\delta] + W_2[\bar{u}, \delta] + V[\delta] \quad (3)$$

where we identify  $W_1[\bar{u}]$  as the elastic strain energy of the system, free of inelastic modifications,  $W_1[\delta] + V[\delta]$  as the self energy of the system of inelastic modifications consisting of the distributed dislocations and the interplanar interaction energy on the slip plane, and  $W_2[\bar{u}, \delta]$  as the interaction energy of the initial unmodified system with the second system of modifications. Of these energies the ones of relevance in the variational approach are those that depend on the unknown inelastic modification  $\delta$ . Their specific forms have been given elsewhere [6,7].

The potential energy  $V[\delta]$  of the interplanar inelastic deformation on the slip plane is a key ingredient of the method and is given as

$$V[\delta] = \int_{\hat{S}_s} \Phi[\delta] dS, \quad (4)$$

where  $\Phi[\delta]$  is the interplanar tension/shear potential, defined per unit area of the slip plane  $\hat{S}_s$ . It adopts the constrained displacement hypothesis of Rice [10] and Sun et al. [11], in which the interplanar shear displacement  $\Delta_s$  is constrained along the Burgers vector direction. The shear and tension separation resistances,  $\tau$  and  $\sigma$ , respectively, follow as functions of the inelastic shear displacements  $\delta_s$  and tensile separation displacement  $\delta_\theta$  on the slip plane. The associated traction-displacement relation has been modeled by Rice et al. [12] and was modified somewhat by Xu et al. [6] to incorporate an element of skewness and a surface production resistance. The resulting forms have been presented in detail elsewhere [6].

The unknown displacements are obtained by rendering the potential energy  $\Pi[\bar{u} + \delta]$  stationary. This is achieved by discretizing the integral equation with six noded elements distributed on the crack surface. The nonlinear equations are solved by a Newton-Raphson iteration. The saddle point configurations are activated by introducing a small perturbation into the system at the bifurcation point, based on the solution of a first-order eigenvalue problem if necessary. Solutions are obtained by recourse to interplanar displacement control achieved through the introduction of Lagrange multipliers [6,7].

The material constants for  $\alpha$ -Fe used in the present calculations are given in Table 1.

<sup>2</sup>The unstable stacking energy relates to an interplanar shear configuration where two atomic layers are displaced parallel to each other by half a periodicity displacement, that for symmetrical forward and backward shear responses takes the system to a free energy maximum. The excess energy of this half-step sheared configuration is the unstable stacking energy.

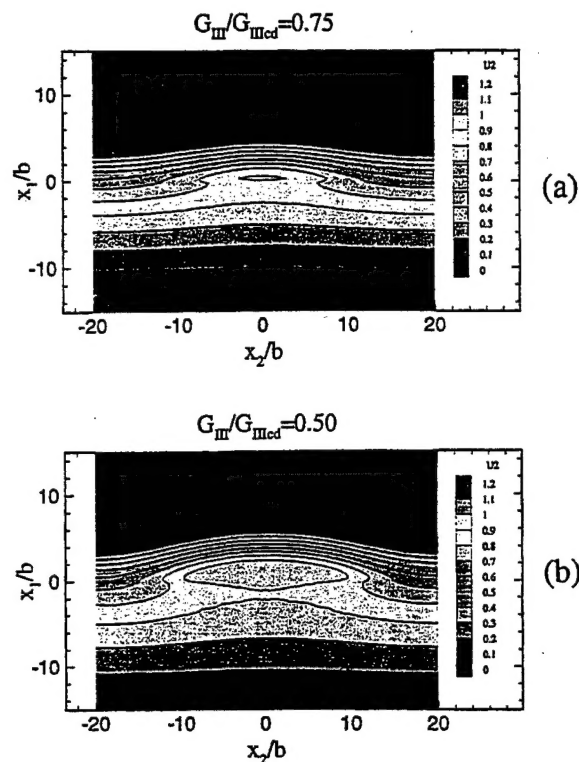


Fig. 4 Two activation (saddle-point) configurations of nucleated embryos at a cleavage ledge along a crack front: (a) at a high energy release rate level  $G_{III}/G_{IIIcd}=0.75$ ; (b) at a lower energy release rate level of  $G_{III}/G_{IIIcd}=0.5$  (after reference [7], courtesy of Taylor and Francis Ltd.)

Figures 4(a) and 4(b) show two critical activation configurations of dislocation embryos forming at a cleavage ledge as depicted in Fig. 2(c). The dislocation, which is in the process of being formed, is of a pure screw nature which has the lowest energy barrier by virtue of having the smallest line energy and involving no significant free surface production during its formation. The line of  $x_1=0$  is the initial edge of the cleavage ledge and the level contours indicate the local nonlinear relative interplanar displacement  $\delta_x=u_2$  of material toward the formation of a fully formed dislocation. All distances and displacements are normalized by the magnitude  $b$  of the Burgers vector of a fully formed dislocation. Figures 4(a) and 4(b) are for two levels of "driving force"  $G_{III}$  in units of the energy release rate  $G_{IIIcd}$  for the spontaneous release of the dislocation from the ledge. As expected, the activation configuration for the higher energy release rate is smaller and has a lower energy barrier. It is interesting to note that the saddle-point displacement  $u_2$  at the edge of the ledge is less than a full Burgers displacement, and that the saddle-point configuration consists entirely of dislocation core material.

Figure 5 shows the result of such activation analysis with the VBI approach for all three of the modes depicted in Figs. 2(a)–2(c) in terms of the activation free energies  $\Delta U_{act}$ , all in units of the dislocation line energy factor  $\mu b^3$  per atom length of line, given as a function of the normalized "driving force"  $G_{Icd}/G_{IC}$ , where  $G_{IC}$  is the critical energy release rate for the extension of the cleavage crack. The "cut-off" levels of  $G_{Icd}/G_{IC}$  for all cases are larger than unity, as expected, indicating that iron ( $\alpha$ -Fe); the material considered, is intrinsically brittle, and that triggering ductile behavior is overwhelmingly influenced by cleavage surface imperfections in the form of small cleavage ledges. Other possibilities such as the two cases indicated in Figs. 2(a) and 2(b), that appear at first sight more likely, are subject to much higher energy barriers and are far less likely to govern.

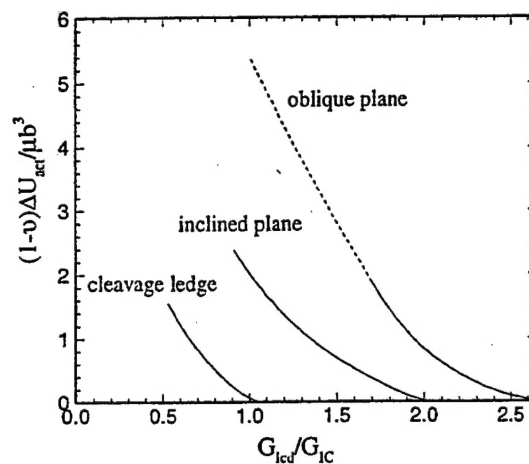


Fig. 5 Dependence of activation energies on levels of crack tip driving "forces" for dislocation embryo formation for the three modes of emission given in Fig. 2, for alpha iron (after reference [7], courtesy of Taylor and Francis Ltd.)

## 5 Brittle-to-Ductile Transitions in Intrinsically Brittle Solids With High Dislocation Mobility

The results of the previous section on emission of dislocations from crack tips as a critical phenomenon triggering ductile behavior should be applicable to explain the B-D transition in solids in which high dislocation mobility assumes intense dislocation multiplication and development of plastic zones, such as in BCC metals. In order to examine this possibility the results of the previous section can be translated into B-D transition temperatures, for which a reasonable model would be a crack arrest scenario [13]. In this a cleavage crack is considered traveling up a temperature gradient with a given velocity  $v$  until it is arrested at a temperature (the  $T_{BD}$ ) where the average waiting time for a successful crack tip dislocation emission process becomes of the order of the residence time of the crack tip at a material element having the dimensions of the crack tips dislocation embryo. This transition temperature is

$$T_{BD} = \left( \frac{\ln(c/v)}{\alpha} + \eta \frac{T_o}{T_m} \right)^{-1} T_o \quad (5)$$

where, for  $\alpha$ -Fe,  $T_o = \mu b^3/k(1-\nu) \approx 1.2 \times 10^5$  K,  $T_m = 1809$  K, and  $\alpha = ((1-\nu)\Delta U_{act}/\mu b^3)$  is the normalized activation energy given in Fig. 5, while  $c$  is the speed of sound and  $\eta=0.5$  relates to the temperature dependence of the shear modulus. Then, the  $T_{BD}$  of Eq. (5) can be broadly evaluated for the three modes of dislocation emission of Figs. 2(a)–2(c) for a given crack velocity (say  $v=1$  cm/s for purposes of visualization). Figure 6 shows the result for some appropriate ranges of the parameter  $\alpha$  for each of these modes of dislocation emission of Figs. 2(a)–2(c) and indicates that of these modes only the one based on emission from cleavage surface ledges result in B-D transition temperatures in a reasonable range of 280 K, or close to room temperature and roughly what the  $T_{BD}$  is considered to be for low carbon steels. Considering that similar conditions should hold for other BCC transition metals such as Cr, Mo, and W, Eq. (5) can provide estimates for these as well, as 1.26, 1.95, and 2.51 multiples, respectively, of the  $T_{BD}$  of steel, using appropriate elastic constants and physical properties.<sup>3</sup>

Clearly, an effective transition from brittle cleavage to tough ductile behavior must be accompanied by massive dislocation ac-

<sup>3</sup>The published literature on the actual levels of the  $T_{BD}$  of BCC metals, particularly when different small concentrations of other elements are present varies widely and depends on testing procedure. For a documentation of this on steels see Parker [16].



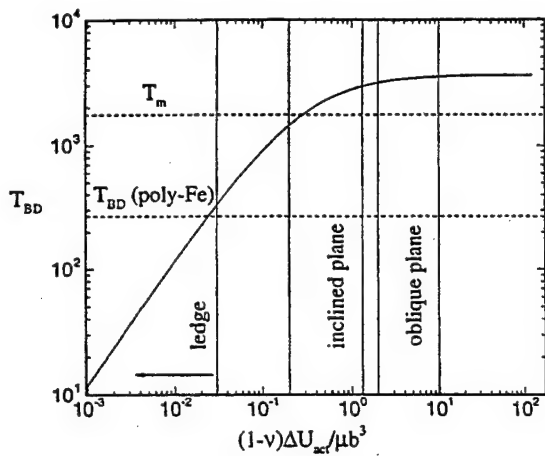


Fig. 6 Estimates of the B-D transition temperature for alpha iron for the three modes of dislocation emission from the crack tip in a scenario of arrest of a brittle cleavage crack travelling up a temperature gradient (after reference [7] courtesy of Taylor and Francis Ltd.)

tivity at the crack tip to arrest its propagation by cleavage, and that emission of an embryonic dislocation triggering the process must be at best only a necessary condition. Experimental evidence suggests that in intrinsically brittle solids having good dislocation mobility (i.e., negligible energy barriers to kink motion along dislocation lines) such as in the BCC transition metals of Fe, Cr, Mo, and W the conditions come close to this relatively simple "triggering" process. Nevertheless, there is considerable evidence for both Mo [14] and W [15] that the level of the  $T_{BD}$  can be markedly influenced by overall mobility of the crack-tip-initiated dislocations away from the crack tip. In this, both interactions of the released dislocations with solute atoms and with existing dislocation networks appear to play important roles. These additional interactions, which have their own energy barriers to the motion of the released dislocations, can affect the actual transition temperatures.

In distinction to these cases of the BCC transition metals, most other intrinsically brittle crystalline solids with sluggish dislocation mobility (due to substantial energy barriers to kink motion along dislocation lines) the emission of dislocations from the crack tip is only a necessary condition for a successful transition to ductile behavior where the sufficiency arises from the sluggishness of dislocation multiplication and motion away from the crack tip. A good example for such behavior is the case of Si which we will discuss in the following sections. Even in these cases, however, we will note that the crack arrest process is still unmistakably governed by the character of the initial dislocation emission process.

## 6 Brittle-to-Ductile Transition in Intrinsically Brittle Solids With Sluggish Dislocation Mobility

**6.1 Fracture Toughness Experiments at Different Temperatures and Different Loading Rates.** The B-D fracture transition has been studied widely in silicon single crystals because Si is obtainable commercially in single crystalline form at closely controlled purities, free of dislocations and in large sizes at relatively low cost. In addition, specimen preparation procedures have been extensively developed by the device industry. These experiments carried out over the years by St. John [17], Brede and Haasen [18], Hirsch et al. [19], George and Michot [20], and others, have demonstrated quite clearly the nature of the fracture transition process as a competition between cleavage fracture and processes of sluggish plasticity that oppose it by crack tip stress relaxation. In particular, the meticulous and elegant experi-

ments of George and Michot [20] have demonstrated that development of crack tip shielding by emitted dislocations leading to an eventual fracture transition is associated with a complex set of dislocations moving away from the crack tip. When the loading rate  $\dot{K}$  in static fracture toughness experiments results in a more rapid rate of crack tip stress increase than the rate of stress relaxation resulting from the sluggish dislocation activity in the crack tip plastic zones brittle behavior will follow. The opposite holds when the crack tip stresses never reach levels required for decohesion in the plane of the crack.

The above competition is readily modeled based on fundamental information on the kinetics of crystal plasticity in silicon studied by Alexander and Haasen [21] and the stress relaxation model of Riedel and Rice [22] around mode-I cracks in creeping solids.

Alexander and Haasen showed that in Si single crystals under appropriate conditions of tensile loading the tensile (equivalent) strain rate  $\dot{\epsilon}$ , at steady-state flow, is a power function of the tensile (equivalent) stress  $\sigma$  given by an expression

$$\dot{\epsilon} = \alpha (\sigma/\sigma_o)^3 \exp\left(-\frac{U}{kT}\right) \quad (6)$$

where  $\alpha/\sigma_o^3 = 1.34 \times 10^3 \text{ MPa}^{-3} \text{ s}^{-1}$  and  $U = 2.2 - 2.4 \text{ eV/atom}$  is the activation energy for dislocation glide (by the continued production and motion of kinks along the dislocation lines), when at steady state a mobile dislocation density of  $4.9 \times 10^{11} \text{ m}^{-2}$  is established.

Using this constitutive law the crack tip stress relaxation can be modeled through the Riedel-Rice solution developed for alloys responding to a power-law steady-state creep constitutive relation. Such a consideration gives the crack tip tensile stress  $\sigma_{\theta\theta}$  across the plane of the crack at  $r = r_c \approx b$  where, for a cleavage mode of crack extension, this stress must reach the ideal cohesive strength  $\sigma_{ic}$  when  $K_I = K_{IC}$ , as [23],

$$\sigma_{\theta\theta}(r) = \sigma_{ic} \bar{\sigma}_{\theta\theta}(0.3) \times \left[ \left( \frac{K_I}{K_{IC}} \right)^2 \frac{(1-\nu^2)}{\sigma_{ic}^2 E I_3} \left( \frac{\pi}{2} \right) \left( \frac{\sigma_o^3}{\alpha} \right) \frac{1}{t \exp(-U/kT)} \right]^{1/4} \quad (7)$$

Here, for  $(K_I/K_{IC} < 1.0)$ ,  $n=3$  was taken for the stress exponent in keeping with Eq. (6),  $I_3 = 5.39$  as the well-known definite integral constant of the Hutchinson-Rice and Rosengren (HRR) model for  $n=3$  [24] and  $\bar{\sigma}_{\theta\theta}(0.3) = 1.9$  as the angle-dependent scaling constant for  $\theta=0$  and  $n=3$ . The crack tip stress at  $r_c = b$  has been given in units of  $\sigma_{ic}$ , the ideal cohesive strength of Si, determined from the Universal Binding Energy relation of Rose et al. [25], which for  $K_{IC} = 0.9 \text{ MPa}\sqrt{\text{m}}$  as determined from experiments at low temperatures [14, 17-20] is  $\sigma_{ic} = 17.7 \text{ GPa}$ .

The expression for crack tip stress relaxation now permits development of a model to account for the B-D transition temperature and its dependence on loading rate in the fracture toughness experiments carried out on Si by the earlier experimenters [17-20]. As was developed in the more stylized model of Brede [26], we view the B-D transition as a competition between the rise of crack tip stress through increases in  $K_I$  and the stress relaxation due to the sluggish crack tip dislocation activity. Then, the increase in crack tip tensile stress at  $r = r_c$  is

$$d\sigma_{\theta\theta} = \left( \frac{\partial \sigma_{\theta\theta}}{\partial K_I} \right)_t dK_I + \left( \frac{\partial \sigma_{\theta\theta}}{\partial t} \right)_{K_I} dt \quad (8)$$

where

$$\left( \frac{\partial \sigma_{\theta\theta}}{\partial K_I} \right)_t = \frac{1}{\sqrt{2\pi r_c}} = \frac{\sigma_{ic}}{K_{IC}} \quad (9a)$$

and



$$\left(\frac{\partial \sigma_{\theta\theta}}{\partial t}\right)_{K_I} = -\frac{\sigma_{ic} A}{4} \left(\frac{K_I}{K_{IC}}\right)^{1/2} \left(\frac{1}{t^3 \exp(-U/kT)}\right)^{1/4} \quad (9b)$$

obtainable directly from Eq. (7) where

$$A = \bar{\sigma}_{\theta\theta}(0,3) \left[ \frac{(1-\nu)^2}{\sigma_{ic}^2 E I_3} \left( \frac{\pi}{2} \right) \left( \frac{\sigma_o^3}{\alpha} \right) \right]^{1/4} = 1.28 \times 10^{-3} (s)^{1/4} \quad (9c)$$

for the appropriate quantities of Si given above.

At the B-D transition,

$$\sigma_{\theta\theta}(r=r_c) = \sigma_{ic}, \quad \text{while} \quad \frac{d\sigma_{\theta\theta}(r=r_c)}{dt} = 0. \quad (10)$$

These conditions, with  $t = K_I / \dot{K}_I$  and Eqs. (8)–(9c), give a simple dependence of the B-D transition temperature  $T_{BD}$  on loading rate  $\dot{K}_I$  as

$$T_{BD} = T_o / \ln(\dot{K}_o / \dot{K}_I) \quad (11)$$

where

$$T_o = \frac{U}{k} = 2.78 \times 10^4 \text{ K} \quad (12a)$$

and

$$\dot{K}_o = \frac{4K_{IC}}{A^4} = 1.42 \times 10^{12} \text{ MPa}\sqrt{\text{m/s}} \quad (12b)$$

Moreover, the actual level of fracture toughness  $K'_{IC}$  at the verge of the fracture transition, in units of the intrinsic fracture toughness,  $K_{IC}$  becomes

$$\frac{K'_{IC}}{K_{IC}} = \frac{1}{4} \frac{\dot{K}_o}{\dot{K}} \exp(-U/kT). \quad (13)$$

The experimental support for the dependence of the  $T_{BD}$  on loading rate is excellent, as given by Eq. (11) as

$$\frac{d \ln \dot{K}_I}{d(1/T_{BD})} = -T_o = -2.78 \times 10^4 \text{ K} \quad (14)$$

while the values of this dependence reported by Brede and Haasen [18] range from  $2.08 \times 10^4$  K(G) [17], to  $2.32 \times 10^4$  K(E) and  $2.67 \times 10^4$  K(F) [27] and  $2.10 \times 10^4$  (A) [18], all for intrinsic Si [18].

Figure 7 shows the expression of Eq. (11) plotted as line (1)

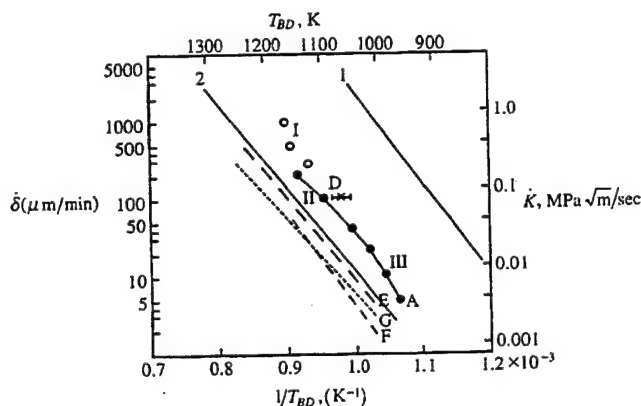


Fig. 7 Dependence of  $T_{BD}$  on loading rate  $\dot{K}_I$  for a cleavage crack on a (111) plane parallel to a [112] direction. Data from [18]. Line (1) result from Eqs. (11) and (14) using direct data from [21]. Line (2) with adjustment for  $\alpha/\sigma_o^3$ , more appropriate for actual experimental conditions (after reference [18], courtesy of Pergamon Press).

together with all the data of the experimental investigations. While the line parallels the slope of the average behavior of all experiments, its predicted magnitude is lower by about 250 K. A better fit shown as line (2) would require an adjustment in  $\alpha/\sigma_o^3$  to  $1.63 \times 10^{-4} \text{ MPa}^{-3} \text{ s}^{-1}$  or almost a factor of  $10^7$  lower than the steady-state deformation value given by Alexander and Haasen [21]. While this adjustment would appear bizarre, it actually reflects the fact that unlike the Alexander and Haasen constitutive relation of Eq. (6), in the fracture experiments the starting material is dislocation-free and it evolves toward a steady state in the plastic zone, but under the conditions of the fracture transition the actual average dislocation density in the plastic zone is still far removed from a steady state. The results of the dynamic crack arrest experiments presented in Section 6.2 will verify this state of affairs. Meanwhile, with the adjustment of  $\alpha/\sigma_o^3$  downward by the appropriate amount, the stress relaxation model based on the Riedel-Rice development furnishes an appropriate model for the fracture transition in the fracture toughness experiments, and as we will demonstrate in Section 6.3, most other details of the crack tip arrest plastic zone.

**6.2 Crack Arrest Experiments in a Temperature Gradient Field.** Another manifestation of a B-D transition is through the arrest of cleavage cracks propagating up a temperature gradient. Such experimental studies in steel plates have been conducted widely in the early post World War II studies and extensive analyses of them have been given by Kanninen and Popelar [28]. The experimental framework is particularly attractive for Si where in an initially dislocation-free material, the material elements at different temperatures are subjected to a crack-tip stress field traveling at a given velocity requiring the fracture transition to develop within a given residence time of the high stress field. Such a set of experiments have been initiated by Brede et al. [29] and more extensively developed by Gally and Argon [30] on double cantilever beam (DCB) specimens in which cleavage cracks on (110) type planes are made to propagate up a temperature gradient, in the [110] direction as depicted in Fig. 8, where the crack front is approximately parallel to the [001] direction. The figure shows a so-called Thompson tetrahedron superposed on the crystallography of the cleavage plane. Its faces represent the potential {111} slip planes and the edges the possible (110) slip directions in these planes (or directions of principal Burgers vectors) in the Si, diamond-cubic lattice [31]. In this particular geometry of crack advance two sets of two equivalent slip systems could potentially take part in the plasticity of crack arrest. These are: (a) the oblique set of ABC and ABD (referred to in the Thompson tetrahedron notation as the  $\delta$  and  $\gamma$  planes) which have a peak resolved shear stress Schmid factor of 0.551 in the crack tip stress field and (b) the vertical set BCD and ACD ( $\alpha$  and  $\beta$ , respectively, in the Thompson notation) having a lower peak resolved shear stress Schmid factor of 0.482.

Because of the increasing specimen compliance with growing crack length in the DCB Specimen the pin load  $P$  should mono-

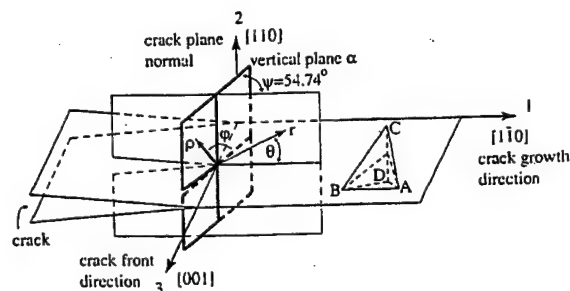


Fig. 8 Sketch showing the geometrical arrangement of the set of two "vertical" slip planes  $\alpha$  and  $\beta$  on which dislocation emission has been observed in Si DCB specimens

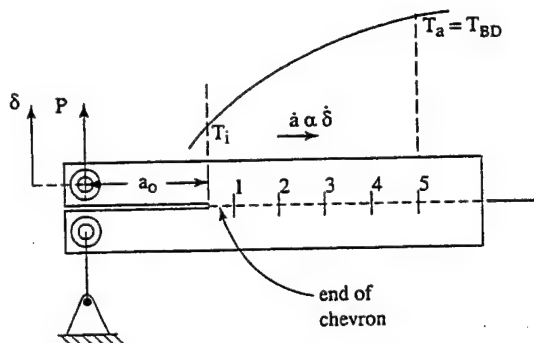
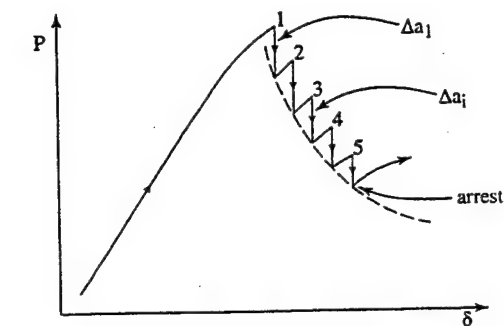


Fig. 9 Depiction of a relatively idealized jerky crack advance scenario in which the step-wise advancing crack is systematically put into new environments at progressively increasing temperatures until it is eventually arrested

tonically decrease with increasing pin displacements  $\delta$ , as shown by the dotted curve in Fig. 9(a), once the starter cleavage crack goes through a chevron shaped region shown by the rising curved region of the  $P$ - $\delta$  curve. In reality, due to a variety of perturbations, both resulting from specimen shape inaccuracies as well as from those inherent in the loading equipment, the actual advance of the crack will be jerky, advancing the crack-tip up the temperature gradient in discrete jumps as depicted in Fig. 9(a). This puts the crack front systematically into environments at increasing temperatures where the residence time decreases with increasing pin displacement rates. If in a given location "i" of the specimen length the residence time increment  $\Delta t_i$  is inadequate to initiate an

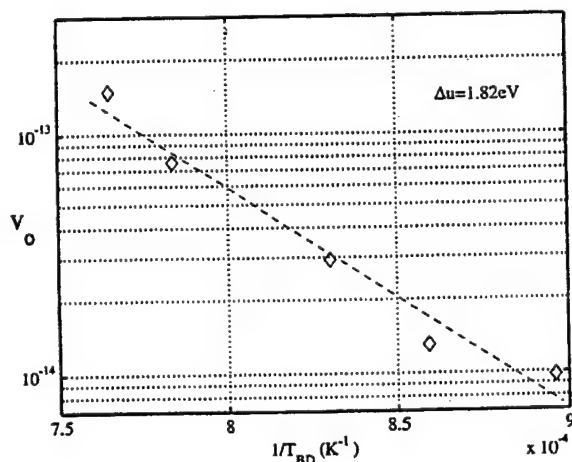


Fig. 10 Dependence of the  $T_{BD}$  on the average crack velocity  $v_0$  as defined by Eq. (15). The measured dependence reflects an activation energy of 1.82 eV in Si DCB specimen.

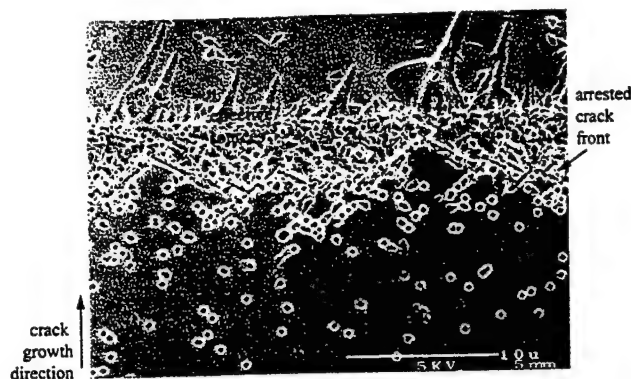


Fig. 11 Etched fracture surface of a crack tip region in a sample with an arrested crack front. The etch pits outline the intersection of the dislocations emitted from the crack front with the crack plane. The trails emanating from the sources (s) indicate that the dislocations are placed alternatively on the  $\alpha$  and  $\beta$  "vertical" slip planes in the Si DCB specimen.

arrest process, the crack will jump further during continued pin displacements, until at some final point (5) in Fig. 9(b) a fully developed arrest process occurs to stop the crack. Clearly, with increasing pin displacement rates, amounting to increasing averaged crack velocity, the arrest temperature should increase. Figure 10 shows the dependence of  $T_{BD}$  on the averaged normalized velocity  $v_0$  in five reasonably successful arrest experiments, where this average velocity is defined as

$$v_0 = \frac{\Delta a_f \dot{\delta}}{c \Lambda} \approx \exp\left(-\frac{\Delta U}{k T_{BD}}\right) \quad (15)$$

where now  $\Delta a_f$  is the final crack jump length,  $\dot{\delta}$  the imposed pin displacement rate,  $c$  the shear wave velocity and  $\Lambda = \sqrt{3 E h^3 / 16 G_{IC}}$  is a characteristic length scale of the DCB specimen with height  $2h$ , Young's modulus  $E$  and intrinsic critical cleavage energy release rate of  $G_{IC}$ . From the slope of the line in Fig. 10 an activation energy  $\Delta U = 1.82$  eV per atom can be determined which approaches the activation energy of 2.2 eV per atom,

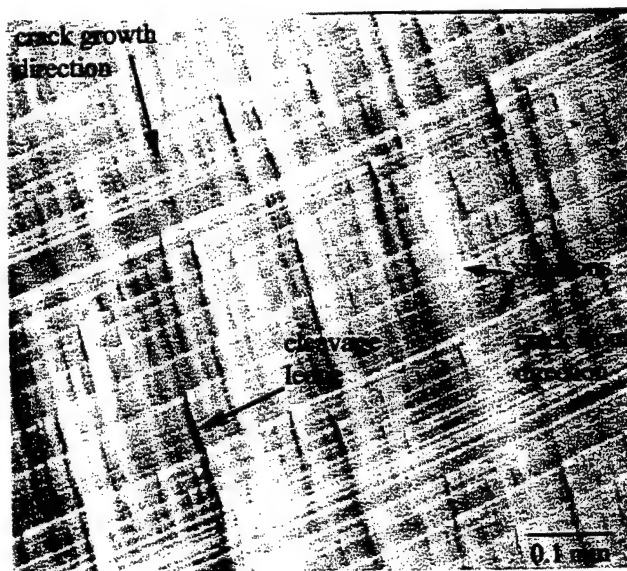


Fig. 12 Nomarski interference contrast micrograph of the (110) cleavage fracture surface of a typical specimen showing both straight striations parallel to the crack front and cleavage ledges roughly parallel to the crack growth direction

characteristic of dislocation mobility in intrinsic Si. The discrepancy is attributed to the sparse nature of the number of successful arrest experiments.

A more interesting aspect of the arrest experiments was the information they provided on the actual arrest process. Figure 11 shows the etched portion of the fracture surface at the arrested crack front. The etch pits relating to the points of exit of dislocations emitted from the crack tip at the time of arrest indicate that they emanate from well-defined sources "s" having an average spacing of  $5\text{ }\mu\text{m}$  along the crack front. The emitted dislocations, by and large, are parallel to certain lines making an angle of about  $55\text{ deg}$  with the crack growth direction, outlining the slip planes on which the dislocation activity has occurred. As Fig. 8 shows, these correspond to the lines of intersection with the cleavage plane of the two vertical sets of slip planes  $\alpha$  and  $\beta$ . The cloud of isolated etch pits in the back of the crack front indicate that some dislocation emission has occurred on these planes before the final arrest in regions of somewhat lower temperature where, however,

the mobility was inadequate to accomplish a full crack arrest. As we discussed in Sections 4 and 5, the most effective sites along the crack front from which dislocations can be emitted are cleavage surface ledges resulting from small variations in the angle between the normal to the cleavage plane and the principal mode-I loading axis. Figure 12 shows a light-optical micrograph in Nomarski interference contrast of the cleavage fracture surface well before the crack arrest. It shows two prominent sets of lines. The first referred to as striations are long and straight and roughly parallel to the cleavage crack front. They are all of one type, i.e., all ascending (or descending) and are attributed to a slight misalignment between the  $\{110\}$  cleavage plane and the geometrical central plane at the DCB specimen. The second set, clearly emanating from the striations, are crack plane cleavage ledges of a height of approximately several tens of nm. A rough count gives the spacing of those that can be resolved in the micrograph as  $15\text{ }\mu\text{m}$ , or in the range of the spacing of sources seen in Fig. 11.

While the etch pit information referred to above is interesting, it

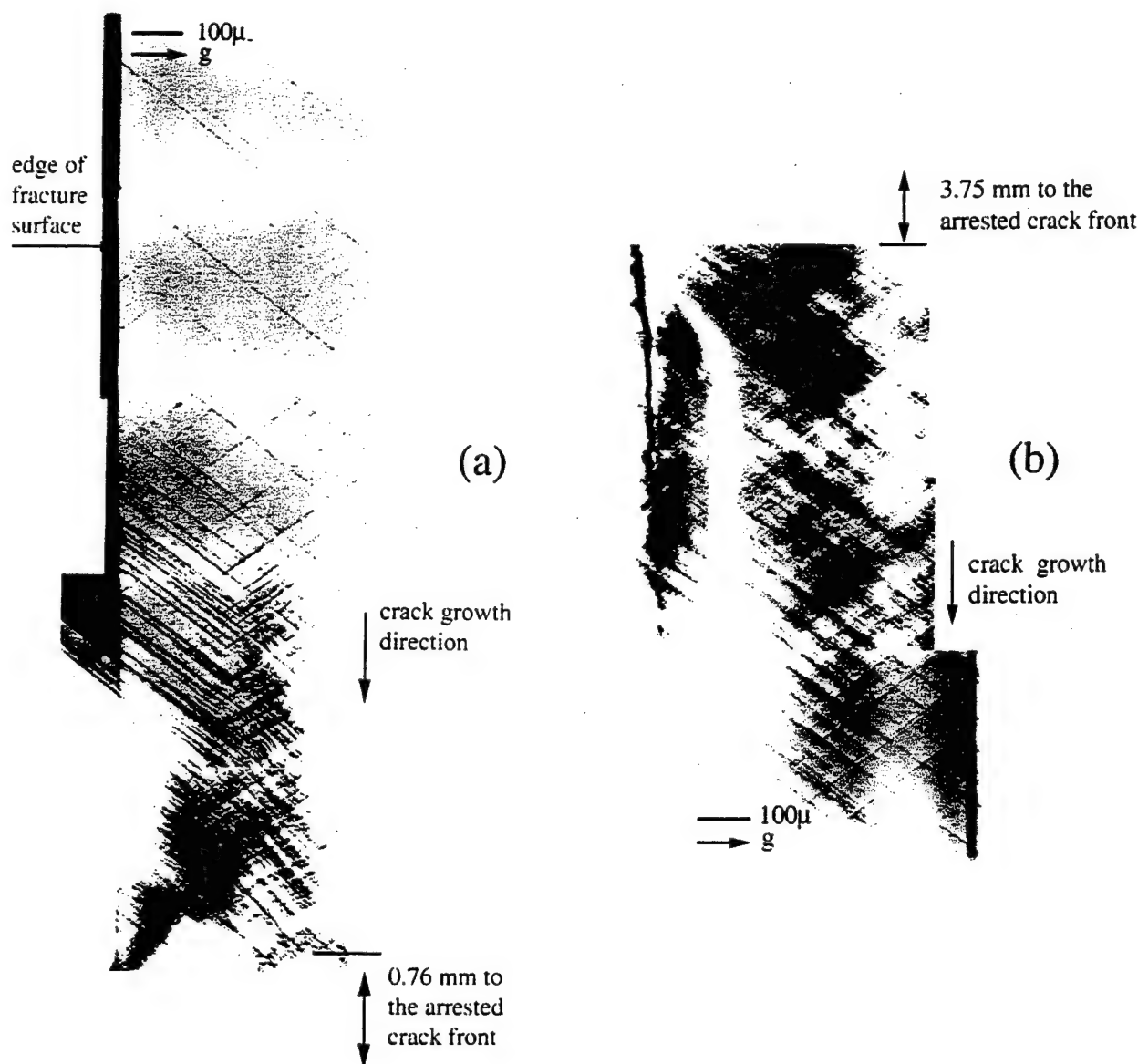


Fig. 13 Two complementary Berg-Barrett X-ray imaging topographs produced from  $(333)$  Bragg reflections from a  $1\text{ }\mu\text{m}$  thick zone parallel to the cleavage fracture plane: (a) region behind the crack front; (b) region ahead of the crack front. These images indicate that the entire set of plastic zone dislocations are a result of multiplications of screw dislocation embryos emitted from crack tip cleavage ledges.

reveals only the exit sites of dislocations through the cleavage plane but lends no information on their distribution in depth. This lacking information is best obtained by an X-ray topographic imaging technique referred to as the Berg-Barrett (B-B) technique, which has the capability of gathering information from a penetration depth of about  $1\text{ }\mu\text{m}$  over very large areas. In this technique a well-collimated very narrow fan of monochromatic X-rays is systematically scanned over the surface of interest, "illuminating" the crystal to obtain Bragg reflections from certain crystallographic planes, with the diffracted X-rays leaving the surface nearly perpendicularly. The diffracted X-ray fan is printed on high resolution nuclear track plates on which it registers the enhanced scattering emanating from dislocations and dislocation groupings as dark lines. The plates are then developed and photographically enlarged and printed. While the obtainable magnification is only of the order of the photographic enlargement, i.e.,  $20\times$  or so, the scanned areas are very wide indeed. In Figs. 13(a) and 13(b), B-B topographs are shown collected from the flank regions of the cleavage crack in the back and in the front (after fracturing the specimen at room temperature), respectively, of the arrested crack. The topographs show quite clearly that dislocations that have taken part in the arrest process of the crack are all on the vertical sets of the  $\alpha$  and  $\beta$  planes, fully supporting the etch-pit observations. These observations demonstrate that the dislocations producing the arrest are on the  $\alpha$  and  $\beta$  planes, which, while having a lower Schmid factor of peak resolved shear stress, are the ones particularly favored for emitting dislocations from crack tip cleavage ledges as the analyses of Sections 4 and 5 have indicated. There is no detectable slip activity on the oblique  $\gamma$  and  $\delta$  planes, even though the peak resolved shear stress Schmid factor on these planes is 14 percent higher than on the vertical  $\alpha$  and  $\beta$  planes. These planes have a clear disadvantage with a very large energy barrier to dislocation emission.

**6.3 Dislocation Content of Plastic Zones of Arrested Cracks.** The Riedel-Rice development for stress relaxation around sharp cracks in creeping solids that was used in Section 6.1 to determine B-D transition temperatures of fracture toughness experiments also lends itself very well to analyze the dislocation content of plastic zones of arrested cracks.

The R-R solution gives a convenient form for the distribution of equivalent creep strains  $\epsilon_c^e$  inside the creep zone, which in our context we interpret as the equivalent plastic strain inside the plastic zone of the arrested crack. It is

$$\epsilon_c^e = \left[ \left( \frac{K_I \sigma_{ic}}{K_{IC} E} \right)^2 \frac{2\pi(1-\nu^2)}{I_3} \frac{r_c}{r} \right]^{3/4} \times \left[ 4\alpha t \left( \frac{E}{\sigma_0} \right)^3 \exp\left(-\frac{U}{kT}\right) \right]^{1/4} \bar{G}(\theta, 3), \quad (16)$$

using the same symbolism introduced in Sec. 6.1 where however, now,

$$\bar{G}(\theta, 3) = \frac{2\bar{\epsilon}_{r\theta}^e}{\sqrt{3}} \sqrt{1 + \left( \frac{\bar{\epsilon}_{\theta\theta}^e}{\bar{\epsilon}_{r\theta}^e} \right)^2} \quad (17)$$

where  $\bar{\epsilon}_{r\theta}^e$  and  $\bar{\epsilon}_{\theta\theta}^e$  are the angle-dependent HRR factors. The shape and the principal plane of extension of the creep zone is obtained by equating the equivalent strains  $\epsilon_c^e$  of the surrounding elastic  $K$  field to the creep strains  $\epsilon_c^e$  gives the bounding contour of the plastic zone as [30]

$$\frac{r(\theta)}{r_c} = \left( \frac{3}{1+\nu} \right)^4 \left( \frac{2\pi(1-\nu^2)}{I_3} \right)^3 \left( \frac{K_I \sigma_{ic}}{K_{IC} E} \right)^2 \times \left[ 4\alpha t \left( \frac{E}{\sigma_0} \right)^3 \exp\left(-\frac{U}{kT}\right) \right] \left( \frac{\bar{G}(\theta, 3)}{\bar{H}(\theta)} \right)^4 \quad (18)$$

where  $\bar{H}(\theta)$  is a collection of the angle-dependent factors of the elastic mode-I stress distribution [30]. Analysis of the plane of symmetry of this plastic zone contour  $r(\theta)$  gives the principal plane to be located at an angle of  $\theta=109$  deg, while the experimental observations of the shape of plastic zones given in Fig. 14 show it to be crystallographically confined to an angle of nearly  $\pi/2$ .

Integration of the relative shear displacements between the two opposing sides of the narrow plastic zone along the contour of the plastic zone gives a measure of the relative effective opening displacement  $u_r$  of the plastic zone. This, when divided by the magnitude of the Burgers vector  $b$ , gives the total number of dislocations  $N(r)$  at a distance  $r$  from the crack tip, sent into the interior of the plastic zone given as

$$N(r) = \frac{u_r(r)}{b} = \frac{MR_c}{6} \sqrt{\frac{r}{R_c} \left( 1 - \frac{r}{R_c} \right)} \left[ \left( \frac{R_c}{r} \right)^{3/4} - 1 \right] \quad (19)$$

where  $R_c$  is the furthest extent of the plastic zone obtainable from Eq. (18) by finding the maximum in  $r(\theta)$  with  $\theta$ . In Eq. (19),

$$M = 2 \left( \frac{1+\nu}{3} \right) \left( \frac{K_I \sigma_{ic}}{K_{IC} E} \right) \left( \frac{r_c}{R_c} \right)^{1/2} \frac{\bar{H}(\theta)}{\bar{G}(\theta, 3)} \bar{\epsilon}_{r\theta}^e(\theta_c, 3) \quad (20)$$

where, of course  $\theta_c \cong \pi/2$  is now taken as the inclination of the principal plane of symmetry of the narrow plastic zone. Proceeding a bit further, the linear (along the spine of the plastic zone) density of the dislocations can be readily determined by differentiation and is

$$-\frac{d}{dr} N(r) = \frac{M}{4b} \left[ \frac{(R_c/r)^{3/4} + (r/R_c)^{1/4} + 2 - (r/R_c)}{\sqrt{(r/R_c)(1-(r/R_c))}} \right] \quad (21)$$

where the  $(-)$  sign arises from the fact that the dislocation count is made from the outside in, i.e., from  $R_c$  to the crack tip.

The experimental means of probing the dislocation content of crack tip arrest plastic zones consisted of sectioning several of the DCB specimens by electrical discharge machining (EDM) along the median plane parallel to the front and back surfaces of the

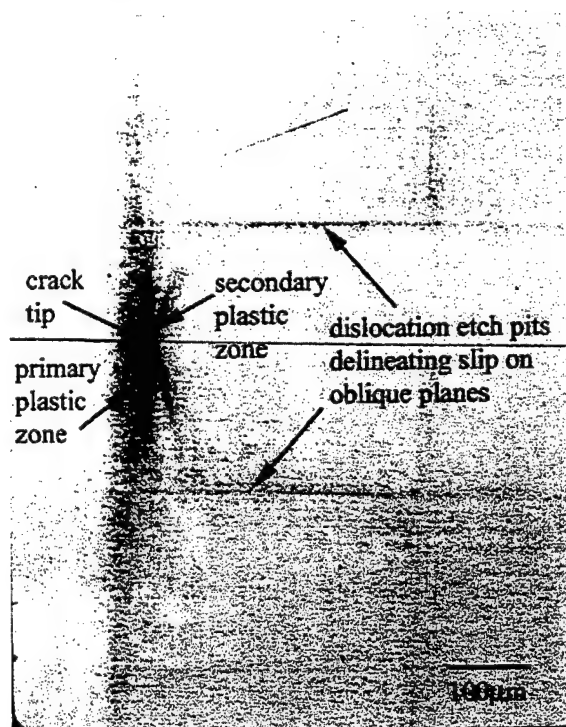


Fig. 14 Crack-tip stress relaxation zone of an arrested crack tip viewed on an etched median plane of a DCB sample of Si

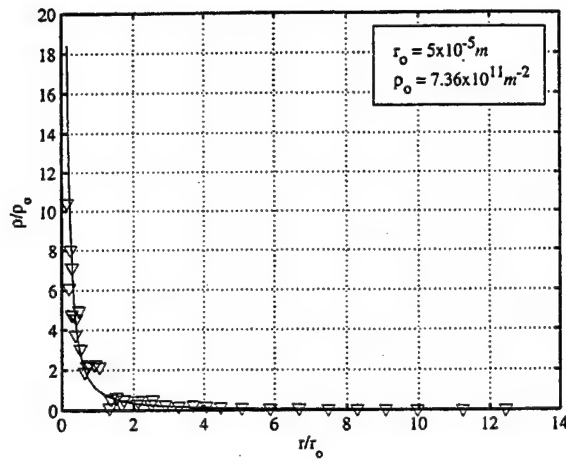


Fig. 15 Etch pit density distribution along the spine at  $\theta = \theta_c = \pi/2$  of the plastic arrest zone

DCB specimen, after the arrest experiment at high temperature. Upon extensive mechanical polishing to remove the EDM-damaged surface layers, the exposed median plane surfaces were etched outlining the plastic zone and revealing its dislocation content as shown in Fig. 14. Figure 15 shows the measured dislocation density distribution along the spine of the plastic zone, while Fig. 16 shows the integrated dislocation density of the model (integrated from the outer limits of the plastic zone toward the crack tip) by the smooth broken curve and the actual integrated etch pit density given by the solid curve [30]. The comparison shows the actual experimental dislocation density to be larger by a factor of about 2 in most of the intermediate regions of the plastic zone, apparently due to the various cross slip events which distribute the crack tip emitted dislocations into the width of the plastic zone. The overall integration of dislocation populations gives a crack tip opening displacement based on the Riedel-Rice model of  $8.1 \times 10^{-7}$  m and  $5.5 \times 10^{-6}$  m based on the measured etch pit counts. Since the Riedel-Rice creep zone model was introduced only for the purpose of providing a rational stress relaxation scheme, and there are a number of approximations that have been introduced in the constitutive model with regard to mobile dislocation densities as discussed above, the agreement, in form, between the model and the experiments on the dislocation content of the plastic zones is considered satisfactory.

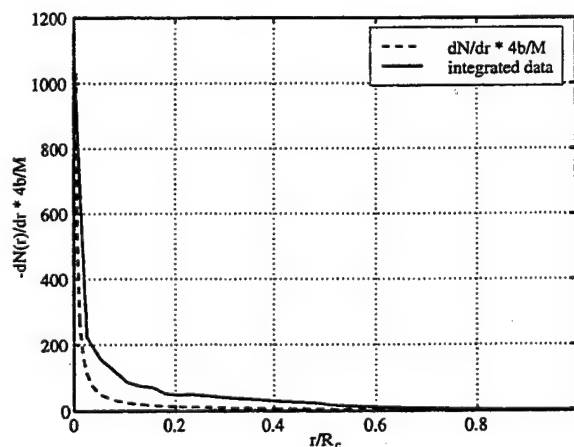


Fig. 16 Linear dislocation etch pit density, comparing measured quantities with densities assessed from the Riedel-Rice crack tip stress relaxation model

## 7 Discussion

The mechanistic model developments and the findings of the crack arrest experiments on Si single crystals have provided a very useful insight into the B-D transitions in fracture where other microstructural complexities such as grain boundaries, carbide particles, and the like, are absent. Apart from the generally pleasing agreements between the models and experiments a fundamental finding of great surprise is the rather definite mechanistic connection of the quite macroscopic fracture transition phenomenon to very local processes at the crack tip involving embryonic forms of nucleated dislocations that initiate the plastic response. A particularly clear demonstration of this in the crack arrest experiments in Si single crystals has been the fact that the entire arrest process is accomplished by the multiplication and spatial spreading of only one type of dislocation producing crystallographic glide strains, not on the most highly stressed slip planes, but on the considerably less highly stressed planes which, however, have the overwhelming advantage of being preferred because of a particularly low energy barrier to dislocation nucleation from crack face cleavage ledges. This effect is even more surprising since the kinetics of the crack arrest in the case of Si is not governed by the kinetics of dislocation nucleation, as it apparently is in the case for BCC metals as discussed in Sec. 5, but instead is governed by the mobility of the nucleated dislocations. Without this mechanistic explanation where nucleation is a precondition for plastic response the overall response could not be explained [20].

Clearly, in polycrystalline steel with many more microstructural complexities such as grain boundaries, carbides and other related internal inhomogeneities, such as globules of silica left from welding processes, the explanation of the B-D transition is more complex. Even in these cases, however, when the microstructure is cleaned up to leave only grain boundaries as the prominent crack obstacles, the fracture transition scenario becomes again more readily explainable [4].

## Acknowledgments

The research described in this communication has been supported by the Office of Naval Research, first by the Applied Mechanics Division (through Grant No. N00014-92-J-4022) and more recently by the Materials Science Division (through Grant No. N00014-96-1-0629). For this support I am grateful to Drs. Roshdy Barsoum and George Yoder, respectively. I also acknowledge the donation of large boules of highly pedigreed Si single crystals from MEMC Electronic Materials Inc. for which I am grateful to Dr. Harold Korb. Moreover, I acknowledge gratefully the key aid by Drs. Gabrielle Long and David Black of NIST in the X-ray topographic imaging experiments of sub-surface dislocations at the Brookhaven National Laboratory on the NIST beam line. Finally, I acknowledge receipt of a special grant from the ARO (through Grant No. P-33768-MA-RIP) for computer purchases. My able collaborators in this research were, in alphabetical order, Brian Gally, now at Exponent in Natick, MA; Prof. Michael Ortiz of CALTECH and Dr. Guanshui Xu, now at U. Cal at Riverside. Their dedicated collaboration was crucial.

## References

- [1] Kelly, A., Tyson, W. R., and Cottrell, A. H., 1967, *Philos. Mag.*, **15**, pp. 567-586.
- [2] Rice, J. R., and Thomson, R., 1974, *Philos. Mag.*, **29**, pp. 73-97.
- [3] Hahn, G. T., Averbach, B. L., Owen, W. S., and Cohen, M., 1959, *Fracture*, Averbach, B. L., et al. eds., MIT Press, Cambridge, MA, pp. 91-116.
- [4] Qiao, Y., and Argon, A. S., to be published.
- [5] Stein, D. F., 1966, *Acta Metall.*, **14**, pp. 99-104; Turner, A. P. L., and Vreeland, T., 1970, *Acta Metall.*, **18**, pp. 1225-1235.
- [6] Xu, G., Argon, A. S., and Ortiz, M., 1995, *Philos. Mag.*, **72**, pp. 415-451.
- [7] Xu, G., Argon, A. S., and Ortiz, M., 1997, *Philos. Mag.*, **75**, pp. 341-367.
- [8] Xu, G., and Ortiz, M., 1993, *Int. J. Numer. Methods Eng.*, **36**, pp. 3675-3701.
- [9] Xu, G., Argon, A. S., Ortiz, M., and Bower, A., 1995, *Computational Mechanics 95*, Atluri, S. N., et al., eds., Springer, Berlin, Vol. 2, pp. 2874-2889.



- [10] Rice, J. R., 1992, *J. Mech. Phys. Solids*, **40**, pp. 235-271.
- [11] Sun, Y., Beltz, G. E., and Rice, J. R., 1993, *Mater. Sci. Eng.*, **A170**, pp. 67-85.
- [12] Rice, J. R., Beltz, G. E., and Sun, Y., 1992, *Topics in Fracture and Fatigue*, Argon, A. S., ed., Springer, Berlin, pp. 1-58.
- [13] Argon, A. S., 1987, *Acta Metall.*, **35**, pp. 185-196.
- [14] Hirsch, P. B., and Roberts, S. G., 1996, *Cleavage Fracture: George R. Irwin Symposium*, Chan, K. S., ed., TMS, Warrendale, PA., pp. 137-145.
- [15] Gumbsch, P., Riedle, J., Hartheimer, A., and Fishmeister, H., 1998, *Science*, **282**, pp. 1293-1295.
- [16] Parker, E. R., 1957, *Brittle Behavior of Engineering Structures*, Wiley, New York.
- [17] St. John, C., 1975, *Philos. Mag.*, **32**, pp. 1193-1212.
- [18] Brede, M., and Haasen, P., 1988, *Acta Metall.*, **36**, pp. 2003-2018.
- [19] Hirsch, P. B., Roberts, S. G., Samuels, J., and Warren, P. D., 1989, *Advances in Fracture Research*, Salama, K., et al., eds., Pergamon Press, Oxford, Vol. 1, pp. 139-158.
- [20] George, A., and Michot, G., 1993, *Mater. Sci. Eng.*, **A164**, pp. 118-134.
- [21] Alexander, H., and Haasen, P., 1968, *Solid State Physics*, Seitz, F., and Turnbull, D., eds., Academic Press, New York, Vol. 22, pp. 28-158.
- [22] Riedel, H., and Rice, J. R., 1980, *Fracture Mechanics: Twelfth Conference*, Paris, P. C., ed., ASTM STP-700, ASTM, Philadelphia, pp. 112-130.
- [23] Argon, A. S., Xu, G., and Ortiz, M., 1997, *Cleavage Fracture: G. R. Irwin Symposium*, Chan, K. S., ed., TMS, Warrendale, PA, pp. 125-135.
- [24] Hutchinson, J. W., 1979, "Nonlinear Fracture Mechanics," Technical University of Denmark, Copenhagen.
- [25] Rose, J. H., Ferrante, J., and Smith, J. R., 1981, *Phys. Rev. Lett.*, **47**, pp. 675-678.
- [26] Brede, M., 1993, *Acta Metall. Mater.*, **41**, pp. 211-228.
- [27] Michot, G., and George, A., 1985, *Strength of Metals and Alloys*, McQueen, H. J., et al., eds., Pergamon Press, Oxford, Vol. 2, pp. 1187-1192.
- [28] Kanninen, M. F., and Popelar, C. H., 1985, *Advanced Fracture Mechanics*, Clarendon Press, Oxford.
- [29] Brede, M., Hsia, K. J., and Argon, A. S., 1991, *J. Appl. Phys.*, **70**, pp. 758-771.
- [30] Gally, B., and Argon, A. S., *Philos. Mag.*, in press.
- [31] Hirth, J. P., and Lothe, J., 1982, *Theory of Dislocations, Second Edition*, Wiley, New York.



PERGAMON

Scripta Materialia 45 (2001) 1287–1294



[www.elsevier.com/locate/scriptamat](http://www.elsevier.com/locate/scriptamat)

# Selection of crack-tip slip systems in the thermal arrest of cleavage cracks in dislocation-free silicon single crystals

A.S. Argon\* and B.J. Gally<sup>1</sup>

*Department of Mechanical Engineering, Massachusetts Institute of Technology, Room 1-306, MIT,  
77 Massachusetts Avenue, Cambridge, MA 02139-4307, USA*

Received 10 April 2001; received in revised form 3 September 2001

## Abstract

New B–D fracture transition experiments in dislocation-free Si single crystals are described based on arrest of cleavage cracks propagating up a temperature gradient. Combined etch pitting and Berg–Barrett imaging shows that the fracture transitions are accomplished exclusively on planes with the most advantageous conditions for dislocation nucleation from crack-tip cleavage ledges. © 2001 Acta Materialia Inc. Published by Elsevier Science Ltd. All rights reserved.

**Keywords:** Fracture transitions; Silicon; Dislocation emission

## Introduction

From its earliest stages of development in 1934, crystal plasticity, based on dislocations as the fundamental “carriers” of plasticity was faced with the need to explain the kinetics of processes required to maintain active dislocation fluxes that produce the plastic strain. Most often the assumption is made that dislocations enjoy numerous topological possibilities that assure the maintenance of adequate densities of mobile line length and that it is sufficient to be concerned only with the factors that control their mobility. However, there are many plastic relaxation problems, in which the rate is vitally influenced by dislocation generation since with no dislocations present there can be no flux, regardless of what controls the latter. These problems include plastic relaxation around misfitting nano-scale particles [1], in epitaxial thin films in computer devices [2], in creep resistance of super-alloy single crystals [3], inception of plastic

\* Corresponding author. Tel.: +1-617-253-2217; fax: +1-617-258-8742.

E-mail address: [argon@mit.edu](mailto:argon@mit.edu) (A.S. Argon).

<sup>1</sup> Present address: Iridigm Corp., San Francisco, CA 94107, USA.



response in nearly perfect metal whiskers [4], and many instances of fracture transitions between brittle-to-ductile (B–D) in initially dislocation-free material [5–7]. The surprising element in some of these macro-scale mechanical phenomena is that the fundamental processes are governed at the level of the dislocation core and by the energetics of very local saddlepoint activation configurations. These considerations and the forms of their kinetics have initiated considerable controversy between governing phenomena of dislocation production, whether these are entirely driven by rare events requiring imperfections as had been understood for many decades or should new possibilities be favored based on cooperative instabilities [8–10].

Since a very decisive test bed for these considerations is the (B–D) transition phenomenon in initially perfect intrinsically brittle solids such as silicon, we will consider a set of new B–D transition experiments performed on dislocation-free silicon single crystals in this light. Earlier experimental studies of B–D transitions in dislocation free Si have been summarized recently by Argon [11].

Previous experiments have been performed nearly all under static conditions in which mode I cracks on mostly the  $\{111\}$  cleavage plane, but occasionally also on the  $\{110\}$  cleavage plane were, subjected to monotonically increasing driving force by an applied  $\dot{K}$ , at different temperatures, until conditions were reached at a well defined temperature where a purely brittle cleavage response was replaced by a tough response of no cleavage cracking. In this scenario two fundamental processes, of initiation of cleavage cracking and stress relaxation compete in the same material elements in a complex manner. In the new experiments a more difficult but more rewarding scenario is created in which cleavage cracks in dislocation-free Si single crystals are propagated along the  $\{110\}$  cleavage planes in the  $\langle 110 \rangle$  direction, up a temperature gradient, with different externally controlled velocities. Under these conditions cleavage crack arrest occurs at increasing temperatures with increasing average crack velocity. The chosen geometry and the conditions described above result in mechanistically well defined scenarios of B–D transitions with a richer information content than what had been available from the previous experiments. These Si experiments have been described in full detail elsewhere [12]. Here we will discuss only the major findings and their significance related to the points of consideration presented above.

### Description of material and experimental conditions

The silicon single crystals used in the present experiments were Czochralski-grown, doped with boron to a resistivity of  $0.017 \Omega \text{ cm}$  and had oxygen and carbon contents of 11.7 and 0.5 ppm respectively. The boules of 6–8" diameter were dislocation free. The experiments were performed on double cantilever beam (DCB) samples of this material, having dimensions of roughly 115 mm length, 25 mm total height, and 5 mm thickness, arranged to propagate cleavage cracks on the  $\{110\}$  planes in the  $\langle 110 \rangle$  direction. Side grooves of 0.5 mm depth were added on both sides to prevent the cleavage crack from drifting away from the median plane of the DCB specimens. Specimens were cut from the boules by EDM, and underwent meticulous polishing of all surfaces to eliminate any

and all processing damage. Chevrons were introduced at the tip of the initial cut crack to assure a relatively smooth start of the cleavage process. The far end of the DCB samples penetrated into a small Mo-wire-wound furnace capable of reaching temperatures in the range of 1000–1200 °C. The required temperature gradient along the sample from the far end down to the crack end was achieved naturally by effective radiation cooling from the long specimen surfaces to the cold walls of the vacuum chamber. The resulting temperature profiles were somewhat non-linear but were determined exactly for each sample by a series of thermocouples attached to the backside of the DCB samples. All experiments were carried out in a vacuum of  $6 \times 10^{-6}$  Torr. Other details of specimen preparation and conduct of the experiments are described elsewhere [12,13].

Because of less than adequate stiffness difference between the load train and the DCB samples, crack advance in the specimens up the temperature gradient was always jerky under different imposed velocities of pin motion of the DCB arms. These jerky extensions, however, provided a coarse means of monitoring crack advancement through changes in sample compliance. In several instances, however, each advance was monitored directly by viewing the crack through a large quartz window in the vacuum chamber by a special technique of laser illumination of the specimen and recording the advance of the illuminated borders of the crack by either a position-sensitive detector or by a high speed digital camera, as described in detail elsewhere [14]. Actual final determination of crack advance could be achieved after the test by examining the markings on the fracture surfaces, with the aid of Nomarski interference contrast microscopy. Such observations also revealed two sets of markings on the fracture surfaces prior to crack arrest. One set consisting of straight striations parallel to the fracture front was interpreted to result from a slight misalignment between the preferred  $\{110\}$  cleavage plane and the median plane of the DCB sample. These were not considered of much importance. Nearly normal to the striations was another set of fainter markings of shorter persistence. These were interpreted to be cleavage ledges formed by slight random departures between the DCB pull axes and the normal to the  $\{110\}$  cleavage plane. These cleavage ledges, which proved to be quite significant in governing the arrest phenomenon, had an average spacing of 10–15  $\mu\text{m}$  [12].

Fig. 1 shows the geometrical arrangement of the two sets of available slip planes on which massive dislocation activity could achieve the arrest of the propagating cleavage

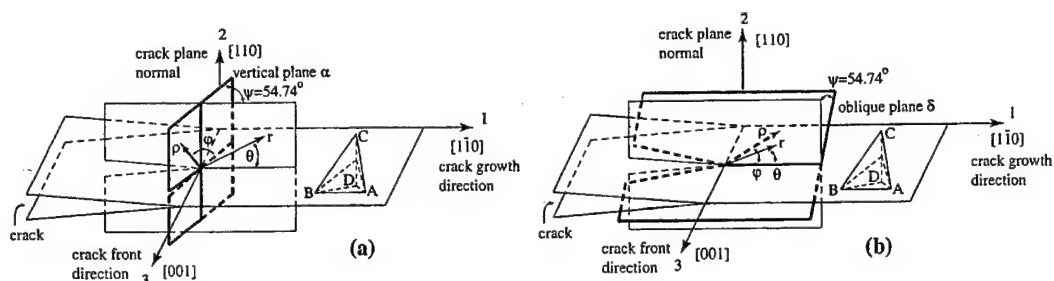


Fig. 1. Sketches showing the geometrical arrangement of the two sets of potential slip systems: (a) the vertical  $\alpha$  and  $\beta$  system; (b) the oblique  $\gamma$  and  $\delta$  system in relation to the crack plane and the crack front.

cracks in the chosen configuration. The set of two symmetrically arranged planes  $\alpha$  and  $\beta$  (in the Thompson tetrahedral notation) shown in Fig. 1a, contained a slip set with a peak Schmid factor of 0.482, while the second set of two symmetrically arranged  $\gamma$  and  $\delta$  planes, oblique to the cleavage plane and the crack front contained a slip set with a larger Schmid factor at a level of 0.551, is depicted in Fig. 1b.<sup>2</sup>

## Experimental results

### *Kinetics of crack arrest*

The crack arrest experiments indicated a clear dependence of the B–D transition temperature,  $T_{B-D}$ , on average crack velocity, through which an activation energy of crack arrest of 1.82 eV was obtained. This energy is on the low end of the possibilities and was attributed to the scarcity of the experimental information.

Upon the arrest of cracks at the various  $T_{B-D}$  the samples were cooled down to room temperature and fractured. The  $K_{IC}$  values of the samples with the shielded cracks due to the plastic dissipations at the crack tip at high temperature considerably exceeded the  $K_{IC}$  of virgin samples of  $0.89 \text{ MPa(m)}^{1/2}$  and were, on the average, in the range of  $1.50 \text{ MPa(m)}^{1/2}$ .

### *Nature of dislocation activity associated with crack arrests*

Of primary interest in these experiments was the morphology of slip activity making up the stress relaxation processes associated with the crack arrest. These were studied by two complementary methods: etch pitting the fracture surfaces exposed in the room temperature fracture of the DCB specimens following the high temperature crack arrest and X-ray topographic imaging of the fracture surface by the Berg–Barrett method to reveal the nature of crack tip plastic accommodation in depth.

Fig. 2 shows a typical pattern of etch pits in the flank region of the arrested crack front, revealed through the use of the so called Secco etch. A number of “V” shaped origins of slip activity are clearly visible emanating from the arrested crack front, in addition to a decreasing density of individual pits left behind the front in regions of lower temperature. While the latter are indicative of sporadic dislocation emissions just prior to full arrest, the “V” shaped origins represent the early phases of the final arrest process. The pattern shown in Fig. 2 is for an arrest process in which further slip development was curtailed by quick unloading of the specimen. There are no etch pits observable ahead of the arrested crack front for reasons explained elsewhere [12]. We note that the “V” shaped sources give the outlines of the  $\alpha$  and  $\beta$  slip planes, with no evidence of corresponding trails due to the  $\gamma$  and  $\delta$  planes which, if present, would have appeared normal to the arrested crack front.

<sup>2</sup> The Schmid factor on the appropriate slip plane at the crack tip is defined as  $\bar{\sigma}_{\mu\nu}/\bar{\sigma}_{\phi\phi}(\phi=0)$  where  $\bar{\sigma}_{\mu\nu}$  is the crack tip singular stress field coefficient on the slip plane ( $\mu$ ) in the Burgers vector direction ( $\nu$ ), normalized with the peak crack tip tensile coefficient  $\sigma_{\phi\phi}(\phi=0) = 1.0$ .

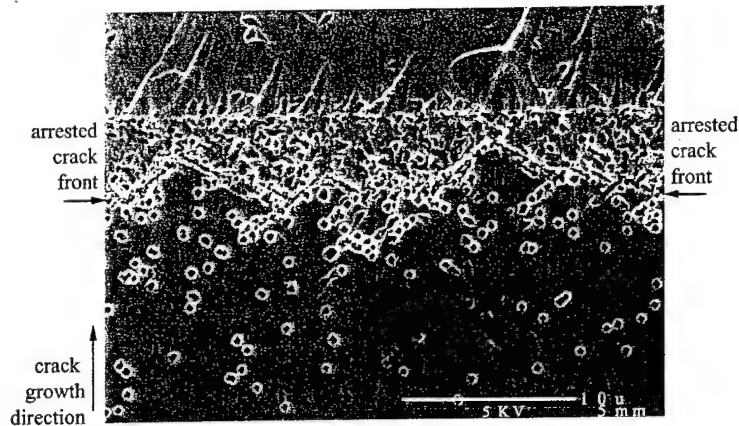


Fig. 2. Etch pit patterns of dislocations emitted on the  $\alpha$  and  $\beta$  planes from crack-tip sources roughly a distance of  $5 \mu\text{m}$  apart. The sources are envisioned to be associated with cleavage ledges, ideally suited to emitting CD-type screw dislocations. (from Ref. [12], courtesy of Taylor and Francis).

While the etch pitting reflects well, the points of exit of the dislocations created by the arrested crack, it gives no information on the distribution of the dislocations in depth. This was explored by Berg-Barrett X-ray topographic imaging from the (3 3 3) symmetrical reflections, obtained by examining a number of fracture surfaces at the Brookhaven National Laboratory Synchrotron Light Source, utilizing the NIST beam line (for these topographic imaging studies we gratefully acknowledge the help of Drs. G. Long and D. Black of NIST). The pairs of topographic images on Fig. 3a and b show a typical crack tip field of the sub-surface dislocation patterns in the flank region and

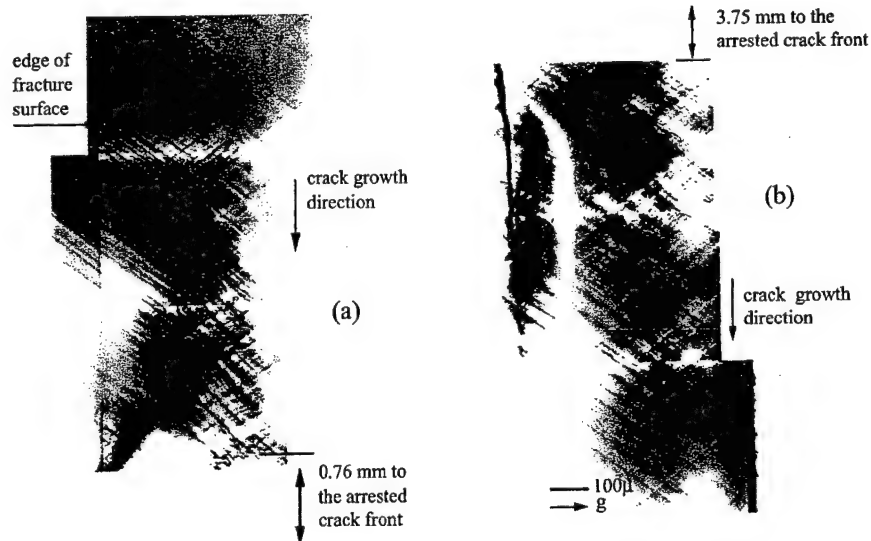


Fig. 3. Two complementary BB topographs produced from (3 3 3) plane reflections showing sub-surface arrangements of the emitted dislocations on the  $\alpha$  and  $\beta$  planes: (a) dislocation arrangements in the flank region; (b) in the region ahead of the arrested crack (from Ref. [12], courtesy of Taylor and Francis).

in the region ahead of the arrested crack, respectively. The outlined X-ray diffraction contrast is indicative of only activity on the  $\alpha$  and  $\beta$  planes down to a penetration depth of 1  $\mu\text{m}$ . While no unique Burgers vector determination could be made through extinction of dislocation patterns, the dislocations present are consistent with those having their Burgers vector perpendicular to the  $\{110\}$  cleavage surface i.e. of CD type as depicted in Fig. 1. These, and X-ray reflections from other crystallographic planes showed no evidence of activity on the  $\gamma$  and  $\delta$  set of planes in the interior regions. A very limited set of activity related to those planes was found near the two free side surfaces where the absence of a plane-strain stress favors emission of dislocations from the side grooves on the oblique planes [15].

Thus, in summary, the crystallographic slip processes that resulted in the arrest of the cleavage cracks were entirely a consequence of activity on the symmetrical  $\alpha$  and  $\beta$  slip set, and involved only a single Burgers vector CD perpendicular to the  $\{110\}$  cleavage plane. We recall that the maximum Schmid factor on these planes was fully 13% less than that on the outwardly more favored  $\gamma$  and  $\delta$  plane set. Such apparently anomalous activity had been reported earlier by George and Michot [7] in their B–D transition experiments.

## Discussion

### *Analysis of the crack arrest process*

A number of models have been developed in the past to analyze the B–D transition in Si for the static relaxation processes by using a variety of simplified reverse dislocation pile-ups [16–18] to account for the crack tip shielding that suppresses the eventual brittle cleavage. While all these models are quite stylized the one of Brede [17] has many interesting elements but still comes short of representing the collective action of the large density of dislocations in the crack tip zone spreading out on many parallel planes. To neutralize such objections a homogenized model was developed making use of the stress relaxation solutions of Riedel and Rice [19] for sharp creep cracks. Using this solution to represent the competition between crack tip stress rise under an imposed loading rate  $\dot{K}$  and concurrent stress relaxation based on the known kinetics of glide in Si, Argon et al. [20] have developed a successful model for the dependence of  $T_{\text{B-D}}$  on  $\dot{K}$  reported by all previous investigators [11,21], that also lend itself very well to model the dislocation distributions in the plastic zones of the arrested cracks. This analysis and its good agreement with experiments has been discussed fully elsewhere [11,12].

### *Character of the crack arrest*

While the good agreement between the measured dislocation density gradient and the gradient of equivalent creep strain in the crack tip plastic zone model described above was pleasing, the more important finding derived from the experiment was the observed choice of the active slip systems leading to crack arrest. In their detailed experimental study George and Michot [7] had noted that the B–D transition was often governed by activity on slip systems having Schmid factors less than on other available systems on

which, however, no activity was observed. They noted, moreover, that crack tip dislocation emission occurs preferentially from cleavage ledges at the crack front. These observations acquired a firm basis from detailed models of saddle-point configurations of dislocation embryos formed at crack tips that were carried out by Xu et al. [15] who determined that the overwhelmingly most favored mode of emission is from cleavage ledges on the crack front, while emission from oblique planes or from inclined planes going through the crack front should be energetically very unfavorable. This has been the case found in the present crack arrest studies. Our present observations have demonstrated that while the overall B–D fracture transition by crack arrest is indeed governed by the mobility of a very large group of dislocations moving away from the crack tip, these dislocations are entirely of one type and bear the signature of the pre-mordial process of their emission from crack front cleavage ledges. The overall correlation of this fundamental process is excellent. The spacing of the “V” shaped etch patterns of Fig. 2, identified as the basic dislocation sources, have a characteristic mean spacing of roughly 5  $\mu\text{m}$  while the spacing between the cleavage ledges observed by Nomarski interference contrast were 10–15  $\mu\text{m}$  [12].

Arguing that the very sharp B–D fracture transitions reported by Brede and Haasen [6] and Hirsch, et al. [16] cannot be explained by the usual Arrhenian chemical kinetics formalisms, Khantha, et al. [8–10] have proposed that these transitions are in the nature of a defect mediated melting process, and have attributed them to cooperative dislocation nucleation processes under stress and not necessarily connected to the crack front. These models, if correct, would predict dislocation activity on all slip systems near an arrested crack front, with levels of activity ordered according to the prevailing Schmid factors on the available slip systems. Our observations are in complete variance with these predictions. They show no evidence for such collective nucleation, but rather that all activity is associated with slip systems that have the lowest energy barrier to dislocation emission *from the crack front cleavage ledges* and showing a distinct character of heterogeneous nucleation. Thus, the very sharp fracture transitions are not a result of massive cooperative nucleation but rather involve relatively rare heterogeneous nucleation events followed by massive dislocation multiplication by topological “mushrooming” processes [22], that had been elucidated by the elegant pioneering studies of Johnston and Gilman in LiF [23].

Finally, our observations make a very pleasing connection to the earliest considerations of dislocation theory [24] which recognized that while dislocations were “carriers” of plasticity their origin also mattered.

### Acknowledgements

This research was supported by the Office of Naval Research, first through the Applied Mechanics Division under contract N00014-92-3-4022 and more recently through the Materials Science Division under grant N00014-96-1-0629. For this support and for their continued interest we are grateful to Drs. R. Barsoum and G. Yoder respectively.

## References

- [1] Ashby, M. F., & Johnson, L. (1969). *Philos Mag* 20, 1009.
- [2] Gao, H., Ozkan, C. S., Nix, W. D., Zimmerman, J. A., & Freund, L. B. (1999). *Philos Mag* 79, 349.
- [3] Pollock, T. M., & Argon, A. S. (1992). *Acta Metall Mater* 40, 1.
- [4] Brenner, S. S. (1958). In: *Growth and Perfection of Crystals* (p. 157). New York: Wiley.
- [5] StJohn, C. (1975). *Philos Mag* 32, 1193.
- [6] Brede, M., & Haasen, P. (1988). *Acta Metall* 36, 2003.
- [7] George, A., & Michot, G. (1993). *Mater Sci Eng A* 164, 118.
- [8] Khantha, M., Pope, D. P., & Vitek, V. (1994). *Phys Rev Lett* 73, 684.
- [9] Khantha, M., Pope, D. P., & Vitek, V. (1994). *Scripta Met* 31, 1349.
- [10] Khantha, M., & Vitek, V. (1997). *Acta Mater* 45, 4675.
- [11] Argon, A. S. (2001). *J Eng Mater Techn* 123, 1.
- [12] Gally, B. J., & Argon, A. S. (2001). *Philos Mag* 81, 699.
- [13] B. J. Gally, Ph.D. Thesis, MIT, Cambridge, MA, 1999.
- [14] Brede, M., Hsia, K. J., & Argon, A. S. (1991). *J Appl Phys* 70, 758.
- [15] Xu, G., Argon, A. S., & Ortiz, M. (1997). *Philos Mag B* 75, 341.
- [16] Hirsch, P. B., Roberts, S. G., & Samuels, J. (1989). *Proc Roy Soc A* 421, 25.
- [17] Brede, M. (1993). *Acta Metall Mater* 41, 211.
- [18] Hirsch, P. B., & Roberts, S. G. (1996). In K. S. Chan (Ed.). *Cleavage Fracture: George R. Irwin Symposium* (p. 137). Warrendale, PA: TMS.
- [19] Riedel, H., & Rice, J. R. (1980). *Proceedings of the 12th Nat'l Symp Fract Mech, ASTM-STP 700* (p. 112). Philadelphia, PA: ASTM.
- [20] Alexander, H., & Haasen, P. (1968). *Solid State Physics* (Vol. 22, p. 27). New York: Academic Press.
- [21] Argon, A. S., Xu, G., & Ortiz, M. (1996). In K. S. Chan (Ed.). *Cleavage Fracture: George R. Irwin Symposium* (p. 125). Warrendale, PA: TMS.
- [22] Argon, A. S., & Orowan, E. (1964). *Philos Mag* 9, 102.
- [23] Johnston, W. G., & Gilman, J. J. (1959). *J Appl Phys* 30, 129.
- [24] Orowan, E. (1934). *Z Physik* 89, 605, 634.



# CLEAVAGE CRACKING RESISTANCE OF HIGH ANGLE GRAIN BOUNDARIES IN *Fe-3%Si* ALLOY

A. S. Argon\* and Y. Qiao

Massachusetts Institute of Technology

Cambridge, MA 02139

## ABSTRACT

High angle grain boundaries in steel offer an important resistance to the propagation of cleavage cracks that affects the fracture toughness and can modulate the ductile to brittle transition temperature of fracture downward. This behavior has been studied now in bicrystals of *Fe-3%Si* alloy in detail. It was noted that the twist misorientation across a high angle boundary has a more profound effect on cleavage fracture resistance than the tilt misorientation. Specific measurements of such resistance at  $-20^{\circ}\text{C}$  over a random selection of high angle grain boundaries in bicrystals and associated fractographic studies have led to quantitative models of this resistance. The study has also revealed a transition from pure cleavage to mixed cleavage around  $0^{\circ}\text{C}$  for this alloy above which the observed increment of fracture work could be associated with the sigmoidal plastic bending and rupture of ligaments left between separate primary cleavage strips in the adjoining grain.

**Keywords:** high angle grain boundaries; cleavage resistance of boundaries; *Fe-3%Si* alloy.

---

\* Author for correspondence; e-mail: [argon@mit.edu](mailto:argon@mit.edu); Fax: (617)253-2217

## 1.0 INTRODUCTION

The subject of high angle grain boundaries and their role in affecting the plastic resistance and fracture behavior of polycrystals has been of continued interest. In an early fundamental experimental study of the processes that lead to transitions of fracture from ductile to brittle forms in polycrystalline steel, Hahn, et al. (1959) noted that with decreasing temperature and rapidly increasing plastic resistance, prior to the onset of full brittleness, slip induced dormant, grain-sized, microcracks appear. This indicated that grain boundaries offer an important resistance to the propagation of cleavage cracks in the nature of acting as "fire breaks". It is this particular role of high angle grain boundaries in affecting cleavage cracking resistance that is of primary interest here. While this behavior has been well appreciated, definitive studies of it are rare. The few existing studies have been limited to the assessment of such resistance by individual grain boundaries with known lattice misorientation in hydrogen charged *Fe-3%Si* alloy by Gell and Smith (1967), and to some models considering such resistance by Anderson, et al (1994), by Crocker, et al. (1996) and by McClintock (1997).

In the present study we have explored in considerable detail the particular forms of break-through of cleavage cracks across specific grain boundaries with known tilt and twist misorientation. The full details of the study are being reported elsewhere (Qiao and Argon, 2002a). Here we provide only a summary of the essential findings.

## 2.0 EXPERIMENTAL DETAILS

### 2.1 Material

The present study using pedigreed bicrystals became possible through the donation of a large ingot of  $Fe-3\%Si$  alloy by the Allegheny Ludlum Steel Co. In the slowly cooled ingot of about 12cm thickness the size of grains ranged from roughly 5mm diameter on the outside to about 50-80mm in the interior. The chemical composition of the material by weight percent consisted of 0.63C, 3.4Si with P and S being less than 0.1 and the balance being Fe. Metallographic examination of the as-received ingot revealed a large concentration of very substantial size elongated carbides and a high concentration of ubiquitous narrow deformation twins, in most of the possible variant directions. The carbides were removed by a special two-step schedule of decarburization that is described in detail elsewhere (Qiao and Argon, 2002a). After decarburization the carbon content decreased to 0.06% and was entirely in solution.

## **2.2 Material Preparation**

### *2.2.1 Extraction of bicrystals from the ingot*

The entire set of bicrystals used in this investigation were extracted from a 6mm thick slice taken from the  $Fe-3\%Si$  alloy ingot. The slice was surface ground to a fine finish and etched for approximately 10 hours in a 3% *nital* etch to reveal the low energy (100) cleavage facets in the large collection of grains contained in the slice. Using a special optical scanning procedure of the reflections of light from the (100) etching facets it was possible to determine quite effectively those large grains that had (100) planes parallel to the ground surface, and thus contained a pair of mutually perpendicular cleavage planes normal to the ground surface. X-ray Laue back reflection analysis confirmed the accuracy of the crystal orientation. These large grains, identified as *A*, with their adjoining family of attached grains became candidates for extraction as bicrystals by electrical discharge

machining (Qiao and Argon, 2002a). The orientation of the surrounding *B* grains to be used in separate bicrystals were all obtained by X-ray Laue back reflection analysis.

### *2.2.2 Characterization of lattice misorientations of surrounding grains*

As will become clear from our experimental results to be presented in Section 3, the form of interaction of a cleavage crack plane with a grain boundary is governed primarily by the tilt and twist orientations of the adjoining grain across the grain boundary. The angles of tilt  $\psi$ , and twist  $\phi$  of grain *B* across the grain boundary plane, relative to grain *A* can be given as (Qiao and Argon, 2002a)

$$\psi = \frac{\pi}{2} - \cos^{-1} \alpha_{32} \quad (1a)$$

$$\phi = \frac{\pi}{2} - \cos^{-1} \alpha_{31} \quad (1b)$$

where  $\alpha_{31}$  and  $\alpha_{32}$  are the direction cosines locating the unit normal vector of the principal cleavage plane of grain *B* relative to the principal axes of grain *A*, parallel to its [100] and [010] directions respectively. Through the form of preparation described below, 17 different bicrystal pairs with relatively random distribution of tilt and twist angles  $\psi$  and  $\phi$  became available. The characteristics of these bicrystals are given in Table I.

### *2.2.3 Welding of bicrystals into double cantilever beam "carrier" samples*

The average size of the extracted and decarburized bicrystal slabs was 40×10×4mm. These were electron-beam welded into fine grain 1020 steel carriers according to a special welding procedure to minimize residual stresses in the production of the double cantilever beam (DCB) specimens. After welding, the DCB specimens were stress-

relieved at 400°C for 3 hours, and subsequently surface ground to a final thickness of somewhat under 4.0mm, and were provided with shallow side grooves of 60° angle with a 45° chevron at the tip of the initial crack. Figure 1 depicts the DCB samples used in the experiments to probe the grain boundary.

### **2.3 Single Crystal Tension Tests**

Single crystal tension specimens were cut out from a single large grain to carry out stress-strain experiments to determine the temperature dependence of the plastic resistance and fracture behavior of the material of interest. The Schmid factor of the principal {110}<111> type slip system was 0.44 while that for the alternative {112}<111> type system was 0.37. Because of the low temperature in the test and the higher Schmid factor, the {110}<111> system was taken to be the active one in the evaluation of the plastic glide resistance.

### **2.4 The Wedge-loading Test Configuration**

To achieve the best conditions of propagating the cleavage cracks to probe the grain boundary in bicrystals in the most stable manner, a stiff wedge-loading arrangement having a minimal compliance  $C_m$  was devised. The measured overall compliance  $C_m$  of the loading system was  $9.0 \times 10^{-8}$  m/N, which was roughly 1% of the opening compliance of a typical DCB specimen. A simple environment chamber was constructed to control the test temperature through flow of cold nitrogen gas fed into the chamber. Temperature uniformity in the specimen was reached typically within 15 minutes.

## **3.0 EXPERIMENTAL RESULTS**

### 3.1 Single Crystal Experiments

The temperature dependence of the tensile yield stress, the fracture stress and the critical resolved shear stress (CRSS) on the primary  $\{110\}\langle 111 \rangle$  system and the alternative  $\{112\}\langle 111 \rangle$  system is given in Fig.2. The rise of the CRSS below  $50^{\circ}\text{C}$  is attributed to a combination of lattice resistance and solid solution resistance arising from  $\text{Si}$ . The scatter in the yield stress in the low-temperature region arises from profusion of twinning where the dotted line can be considered as a twinning-related yield stress.

### 3.2 Bicrystal Fracture Experiments at $-20^{\circ}\text{C}$

Figure 3 shows a result of a typical experiment of the dependence of the DCB opening force  $P$  on the associated crack opening displacement  $\delta$  at the contact point of the wedge. Because the crack tip was usually imperfect as produced, the crack propagation was not of a quasi-static nature. In the figure the solid contour represents the recorded experimental data while the dashed curve represents an ideal quasi-static reference response. During the load rise from 0-1 the macrocrack with length  $a_0$  ( $=a_1$ ), as depicted in Fig.1, is flexed, exerting an increasing stress intensity at the tip of the crack across the median cleavage plane of grain  $A$ . Because of crack tip imperfections the crack becomes overstressed to reach a  $K_I$  level exceeding somewhat the  $K_{IC}$  for quasi-static growth. At point 1,  $K_I$  for initiation of crack growth is reached, the somewhat overstressed crack jumps in an unrestrained manner across grain  $A$  to come to rest at the grain boundary, and begins to penetrate partially into grain  $B$ , but a full penetration requires an increase in the crack driving force  $K_I$  along a new loading line with smaller slope due to the increased compliance. When point 3 is reached, under the increment  $\Delta K_I$ , the crack breaks through the grain boundary and penetrates into grain  $B$  by a further unstable jump, to come to rest

on the opposite border of grain *B* with the polycrystalline background, i.e. at point 4. The subsequent serrated loading behavior past point 4 conveys little relevant information. The curve of Fig.3 shows that some frictional effects are present between the wedge and the contacting faces in the DCB specimen even after the application of lubricant, demonstrated by the fact that the loading does not start from zero but from a finite resistance. This artifact is formally rectified by shifting the origin of the loading curves to zero.

From basic beam theory the stress intensity probing the crack tip in grain *A* can be stated as

$$K_I = \Gamma P a_1 \quad (2)$$

where

$$\Gamma = \sqrt{\frac{12}{(1-\nu^2)bb_n h^3}} \quad (2a)$$

in which *P* is the applied DCB opening load with an initial crack length of *a*<sub>1</sub>, *b* is the specimen thickness, *b*<sub>n</sub> the thickness across the root of the side grooves and *h* is the arm height of the DCB sample with *ν* being the Poisson's ratio. Thus, the initial crack growth resistance *K*<sub>ICA</sub> for grain *A* is

$$K_{ICA} = \Gamma P_1 a_1 \quad (3)$$

where *a*<sub>1</sub> is the initial crack length and *P*<sub>1</sub> the critical load to initiate its extension at point 1 in Fig.3. Finally, the stress intensity *K*<sub>I3</sub> to break through the grain boundary can be taken similarly as

$$K_{I3} = \Gamma P_3 a_2 \quad (4)$$



where  $a_2$  is the total length of the crack abutting on the grain boundary. Then, the incremental fracture toughness  $\Delta K_{\text{ICGB}}$  attributable to the grain boundary fracture resistance is

$$\Delta K_{\text{ICGB}} = \Gamma a_2 (P_3 - P_2). \quad (5)$$

In this manner altogether 17 bicrystal samples with different lattice misorientation between grain *B* and grain *A* were probed. The resulting measurements of the  $\Delta K_{\text{ICGB}}$  for these 17 bicrystal experiments are given in Table I normalized with  $K_{\text{ICA}}$  and as a function of the individual tilt and twist angles  $\psi$  and  $\phi$ . The measured fracture toughnesses of grains *A* are quite reproducible at an overall level of  $K_{\text{ICA}} = 14.1 \pm 0.6 \text{ MPa}\sqrt{\text{m}}$ . This relatively high fracture toughness needs some explanation that we will furnish below.

### 3.3 Fracture Transition Experiments in Bicrystals

To explore how the grain boundary modulates the cleavage cracking across it with changing temperature two sets of additional bicrystal samples were prepared for use in wedge cracking experiments in a temperature range between  $-20^\circ\text{C}$  to  $22^\circ\text{C}$ . In the first set labeled as "C" (Sample 6 in Table I) six other available bicrystal samples identified as sample 6 in Table I, with tilt and twist angles of  $\psi=7^\circ$ ;  $\phi=42^\circ$  were used. For the second set labeled as "D" nine bicrystals of a rather different misorientation consisting of  $\psi=8^\circ$   $\phi=12^\circ$  was extracted from the remaining large slice of the same ingot. The measured  $\Delta K_{\text{ICGB}}$  values normalized with  $K_{\text{ICA}}$  for these two specimen sets are shown in Fig.4. over the temperature range. The figure shows that there is a readily recognizable transition in the grain boundary cracking resistance between  $-2^\circ\text{C}$  and  $0^\circ\text{C}$  in these two sets, with values for set "C" being distinctly higher. Since the fracture appearance in the entire

temperature range remained to be substantially of a cleavage nature, the transition has been labeled as a *cleavage-to-mixed-cleavage transition*. The source of the additional fracture work above the transition temperature is clarified below in Section 3.4.3.

### 3.4 Fractographic Observations

#### 3.4.1 Fracture surfaces in grain A

Figure 5 shows portions of the cleavage fracture surfaces of grain A (in a sample that was not decarburized) at  $-20^{\circ}\text{C}$ . A significant interaction of the cleavage crack with the deformation twins is discernable. There are many examples of repeated arrest of the cleavage crack by the narrow twins followed by points of break-through marked by river markings emanating from these points. Stereoscopic SEM observations of the encounters of the crack with twins indicated that the repeated arrest and reinitiation events of the cleavage crack by the twins, fragments the crack plane into separated strips advancing at different levels. Since the fracture toughness in cleavage-like fracture processes correlates well with the fracture surface roughness, this roughness was measured with a Zygo Interferometer\* on several fracture surfaces of grain A in the low temperature range and was found to be of a rms roughness amplitude of  $2.7\mu\text{m}$ .

#### 3.4.2 Fracture across grain boundaries at $-20^{\circ}\text{C}$

Fractographic examination of the penetration of the cleavage crack from grain A across the boundary into grain B exhibited two limiting modes, with most of the penetrations being of a mixed nature. Figure 6a is a micrograph of a "regular mode" of entry of the cleavage crack from grain A to grain B in bicrystal 14 with similar twist and tilt

---

\* An instrument that uses scanning white light interferometry to image and measure the micro structure and topography of surfaces in three dimensions (New View System 5000 produced by Zygo Corp. of Middlefield, Connecticut).

misorientation ( $\psi=26^\circ$ ,  $\phi=21^\circ$ ). After initial arrest, and within the characteristic increment of crack tip driving force, as depicted in Fig.3, the arrested cleavage crack front penetrates into grain *B* at a number of relatively evenly spaced points an average distance  $w$  apart, in the form of a series of "stair-case-like" tiers with flat surfaces of the twist inclination of the planes relative to the cleavage crack plane in grain *A*. In a transition region the individual cleavage facets bow into the designated strips as depicted in the sketch of Fig.6b, forming the tiered cleavage facets of grain *B*. The primary cleavage facets in grain *B* that undercut each other to some extent are bridged by secondary cleavage cracking to complete the stair-case type propagation of cleavage into grain *B*.

Since the distances  $w$  between the break-through points along a grain boundary were judged to be an important dimension in assessing the penetration resistance of a grain boundary, the number distribution of  $w$  was measured for several grain boundaries. An example of this distribution in bicrystal 14 is shown in Fig.7. All such measured distributions of  $w$  showed similar shapes that fitted reasonably well to a lognormal distribution function, with a most probable value in the range of roughly 2.5-3.0 $\mu\text{m}$  and quite independent of the twist misorientation. While the origin of this characteristic dimension is unclear, it is likely to be governed by some grain boundary structure and the dynamic nature of the probing. In some other cases, the form of penetration of the cleavage crack across the grain boundary was more irregular than that shown in Fig.6.

#### *3.4.3 Fractures across grain boundaries above the cleavage to mixed-cleavage transition*

Fractographic observations of cleavage transition from grain *A* to grain *B* above the 0°C transition temperature indicated very similar features with, however, a significant

difference in the appearance of the cleavage fracture surface of grain *B*. The cleavage facets in grain *B* are apparently produced in a very similar manner as depicted in the sketch of Fig.6b. However, instead of the easy formation of secondary cleavage processes bridging the primary facets, the ligaments between facets have undergone considerable sigmoidal plastic bending, shown in Fig.8a and as depicted in the sketch of Fig.8b. This suggests that a significant portion of the additional fracture work in the mixed cleavage plateau occurs not in the initial penetration of the grain boundary but immediately *subsequent* to it, affecting the fracture work of grain *B* all along its length, but requiring a substantial initial increase in the rate of production of fracture work.

## 4.0 MODELS

### 4.1 Work of Cleavage in a Grain

As indicated in Table I, the measured fracture toughness  $K_{ICA}$  of  $14.1 \text{ MPa}\sqrt{\text{m}}$  of individual grains *A* of the bicrystal pairs at  $-20^\circ\text{C}$  converts to a very substantial work of fracture of  $G_{ICA}$  of  $850 \text{ J/m}^2$ . This very high fracture energy requires explanation. Examination of the fracture surfaces shown in Fig.5 shows only characteristic cleavage markings, but also much evidence of strong interactions of cleavage cracks with deformation twin bands as already noted above, producing fragmentation of the plane of the cleavage crack into separate strips, at somewhat different levels. The net effect of these crack plane shunting processes has been a tiered fracture surface with an rms roughness of  $2.7\mu\text{m}$  as reported above. We view this fragmentation of the crack plane as the source of the crack opening displacement  $\delta_c$  associated with the crack advance. These fracture surface features are not satisfactorily explained by conventional interpretations of

excess fracture work where this work is considered expanded before crack advance. We view the events of crack advance in a different order.

We start by noting that the *Fe-3%Si* alloy is an intrinsically brittle solid, embrittled further by the large concentration of *Si* which is a potent solid solution strengthening agent in *Fe*. When a “steady state” form of crack advance is established, with all of its jerky features, as evidenced from the fracture surface markings of Fig.5 as already noted, the average crack plane becomes fragmented into a set of cleavage strips of average width  $w_c$ , and dispersed randomly in height by roughly  $2.7\mu\text{m}$ . This form of the crack topography sets the scale of the work of fracture.

In our view, illustrated in Fig.9a, the cleavage strips of average width  $w_c$  penetrate into undeformed material at the tip of a process zone (PZT), of extent  $\Delta_c$ , without any accompanying plastic dissipation at their tips. This is in conformity with expectations from an intrinsically brittle solid, well below its transition temperature (at  $250^\circ\text{C}$  as determined by us, Qiao and Argon, 2002b). As the cleavage strips of the process zone tip advance on planes randomly separated in height over a range of  $\delta_c$ , the edges of the strips that are left behind undergo secondary cleavage, plastic rubbering and some fragmentation. The major element of dissipative work is then done in the process zone of extent  $\Delta_c$ , until the two rough crack flanks are separated by the distance  $\delta_c$  and all contact is terminated at point, CT, of the crack tip. Such a process in which the inelastic dissipation is *subsequent* to the advancement of the cracking front resembles those cases frequently encountered in brittle composites reinforced with discrete fibers of a given length ( $\delta_c$ ) (Argon, 2000). The mechanism of the advance of such a process zone in

which a characteristic traction-separation process, illustrated in Fig.9b, “processes” unbroken solid into fully separated crack flanks has been considered in detail by Andersson and Bergkvist (1970). We adopt the findings of their model to our phenomenon. In the Anderson and Bergkvist model which approximates the descending portion of the traction-separation process relation by a straight line over the separation distance  $CCOD = \delta_c$ , the critical zone size  $\Delta_c$  is given by:

$$\Delta_c = \beta_c \frac{E}{\sigma_B} (CCOD) \quad (6)$$

where the constant  $\beta_c = 0.43$  is obtained from a numerical simulation, and  $\sigma_B$  is the average cohesive strength that needs to be overcome to advance the cleavage front forward, and  $CCOD$  is taken as the rms roughness range  $\delta_c = 2.7 \times 10^{-6} \text{m}$  as reported above. With the prevailing parameters given above and  $\sigma_B$  taken as 1.0 GPa, the process zone size is estimated to be  $2.5 \times 10^{-4} \text{m}$ . Moreover, the Anderson and Bergkvist development gives the essential work of fracture consisting of the inelastic dissipation process in the process zone as

$$G_{ICA} = \frac{\sigma_B \cdot CCOD}{2} \quad (7)$$

For the above chosen parameters  $G_{ICA}$  is  $1,350 \text{J/m}^2$ , and somewhat larger than the measured value of  $850 \text{J/m}^2$ , with the discrepancy being readily accountable by the drooping shape of the actual traction-separation relation, differing from that given in Fig.9b.

## 4.2 Cleavage Resistance of Grain Boundaries



We refer to Fig.6a, representing the regular mode of penetration of the crack across the grain boundary, and to the sketch of Fig.6b. By a quasi-regular sampling process, the nature of which is not fully clear, the cleavage crack from grain *A* penetrates into grain *B* at points, on the average, a distance  $w$  apart on the cleavage surface of grain *A* along the outline of the boundary and spreads out on the cleavage terraces in grain *B*, separated by distances  $w\sin\phi$ , much like in a crack trapping model of a brittle crack going through tough heterogeneities (Bower and Ortiz, 1991; Mower and Argon, 1995) where the, as yet to be sheared, triangular grain boundary segments are acting momentarily as the heterogeneities. Upon the penetration of the fragmented cleavage terraces into grain *B* by increasing distances  $\Delta x$  (as projected to the extension of the cleavage plane of grain *A*), at a critical  $\Delta x_c$  the opening displacements of the cleavage terraces force apart the remaining triangular grain boundary islands by a combination of cleavage and grain boundary shear over a relative displacement  $\delta_B = \beta\Delta x/\cos\psi$ . The remaining triangular grain boundary islands finally give-way suddenly when  $\delta_B \rightarrow \delta_{Bc}$  and  $\Delta x$  reaches a critical level  $\Delta x_c$ , where the maximum grain boundary resistance is reached.

The increase in the expanded energy  $\Delta U$  required to overcome the boundary resistance is then, made up of two contributions: an increase in exposed cleavage surface  $\Delta A$  along the terraces of width  $w\cos\phi$ , with associated bridging secondary cleavage processes connecting the terraces of height  $w\sin\phi$ , and the grain boundary shear work  $\Delta W_p$ , expanded over the relative grain boundary displacement  $\delta_{Bc}$ . This gives

$$\Delta U = G_{ICA}\Delta A + \Delta W_p \quad (8)$$

where

$$\Delta A = \Delta x \frac{w}{\cos^2\psi} [\sin\phi + \cos\phi] \quad (9)$$

is the increase of cleavage surface with each penetration distance  $\Delta x$  of the crack into grain  $B$  (both as projected back on the extension of the cleavage plane of grain  $A$ ), and the tilt angle  $\psi$  and twist angle  $\phi$  accounting for the geometrical projection effects of the actual cleavage areas onto the mean crack advance plane coincident with the extension of the cleavage plane of grain  $A$ . In Eqn(8) we have assumed that the actual specific work of separation across cleavage areas has remained to be  $G_{ICA}$ , the specific fracture work across grain  $A$ . The work of separation of grain boundary islands, forced apart by the crack penetrating into grain  $B$ , can be given as

$$\Delta W_p = \frac{\beta w^2 \Delta x}{4} k \frac{\sin \phi \cos \phi}{\cos \psi} \quad (10)$$

where  $k$  is the grain boundary plastic shear resistance. At the point of maximum resistance of the boundary, when  $\Delta x$  reaches  $\Delta x_c$  and  $\delta_B$  reaches  $\delta_{Bc} = \beta \Delta x_c$ , the increment of expanded energy will reach its peak value as:

$$\Delta U = G_{ICA} w \Delta x_c \frac{1}{\cos^2 \psi} (\sin \phi + \cos \phi) + \beta \frac{k w^2 \Delta x_c}{4} \frac{\sin \phi \cos \phi}{\cos \psi}, \quad (11)$$

and the overall specific peak grain boundary break-through resistance becomes

$$G_{ICGB} = \frac{\Delta U}{w \Delta x_c} = G_{ICA} \frac{1}{\cos^2 \psi} (\sin \phi + \cos \phi) + \frac{\beta k w}{4} \frac{\sin \phi \cos \phi}{\cos \psi}, \quad (12)$$

giving the peak stress intensity to break-through the grain boundary as:

$$K_{ICGB} = \sqrt{\frac{E G_{ICGB}}{1 - \nu^2}}. \quad (13)$$

Beyond the peak resistance the second term in Eqn(12) is no longer present and  $G_{ICB}$  the resistance of the grain  $B$  consists of only the first term on the RHS of Eqn(12). Finally, the differential cracking resistance of a grain boundary, normalized with  $K_{ICA}$ , becomes simply,

$$\frac{\Delta K_{ICGB}}{K_{ICA}} = \sqrt{\frac{1}{\cos^2 \psi} (\sin \varphi + \cos \varphi) + C \frac{\sin \varphi \cos \varphi}{\cos \psi}} - 1 \quad (14)$$

where the constant  $C = \frac{\beta k w}{4 G_{ICA}}$  (15)

is a material constant combining together both well known and ill-defined factors. The remainder of Eqn(15) is of a purely geometrical nature. We note that for  $\psi$  and  $\varphi$  going to zero the grain boundary resistance as given by Eqn(15) vanishes as it should. We consider the parameter  $C$  as adjustable. To obtain the best fit between the model and the experimental measurements for the 17 different bicrystal experiments, we use experiment 13 with a contribution of substantial tilt and twist to fix  $C$  as 0.25. With this single fitting constant we have calculated the predictions of Eqn(14) for all 17 cases and compared the model prediction with the experimental measurements. The results represented as a ratio  $(\Delta K_{ICGB})_E/(\Delta K_{ICGB})_C$  of the experimental measurements to the computed values are given in Table I. While there is some scatter with the largest departure being about 13%, the overall average ratio was found to be:

$$(\Delta K_{ICGB})_E/(\Delta K_{ICGB})_C = 1.00 \pm 0.05 \quad (16)$$

which we consider this to be quite good.

Pursuing the model further we consider Eqn(14) also as a framework to calculate the boundary penetration resistance above the cleavage to mixed-cleavage transition where considerable additional dissipative work is being done in the sigmoidal plastic bending of the ligaments connecting the individual cleavage strips in grain  $B$ . We consider this additional work formally associated with the grain boundary shear work  $\Delta W_p$  of Eqn(10). This is possible by a reinterpretation of the nondimensional constant  $C$  in Eqns(14) and

(15). A new choice of  $C$  at a level of 1.70 then also successfully accounts for the considerably larger break-through toughness in the two orientations “C” and “D” shown in Fig.4.

Clearly, these fitting exercises demonstrate only a proper framework for considering relative ordering of the measured parameters and does not constitute a fully accurate model.

## 5.0 DISCUSSION

In the present bicrystal experiments we have demonstrated that the transit of cleavage cracks across grain boundaries is a topologically relatively simple process in the range well below the usual ductile-to-brittle fracture transition in  $Fe-3\%Si$  alloy. The latter transition in polycrystalline samples of this material occurs at a temperature around  $250^{\circ}C$  (Qiao and Argon, 2002a). Thus, at  $-20^{\circ}C$ , where most of the bicrystal experiments were performed the alloy under consideration is very brittle and the specific role of grain boundaries becomes relatively easily understandable. In our experiments we have found that the work of fracture (critical energy release rate)  $G_{ICA}$  of the well aligned grain  $A$  was in the range of  $850J/m^2$  which is quite substantial. This high level was accounted for by a model that attributes the high plastic dissipation to the plastic “rubbing” of rough crack flanks as they are being separated. A relatively simple geometrical model guided by relevant SEM fractographs has resulted in a successful framework to account for the break-through resistance of grain boundaries. How these considerations apply to the accounting of the cleavage fracture resistance in polycrystals in the lower-shelf region is the subject for a separate communication (Qiao and Argon, 2002b).

#### ACKNOWLEDGEMENT

This research has been supported at its inception by the Material Science Division of the ONR under Grant N00014-96-1-0629 for which we are grateful to Dr. George Yoder. The research has been supported more recently by the NSF under Grant DMR-9906613. We also gratefully acknowledge receipt of two large blocks of Fe-3%Si ingots from Allegheny Ludlum Steel Co., which made the bicrystal research possible. For this we are particularly grateful to Dr. James A. Salsgiver of the AL Technical Center.

## References

- Anderson, T. L., Stienstra, D., Dodds Jr., R. H., (1994), in "*Fracture Mechanics: Twenty-Fourth Volume*", edited by Landes, J. D., McCake, D. E. and Boulet, J. A. M., ASTM STP-1207, ASTM: Philadelphia, PA, p.186
- Andersson, H. and Bergkvist, H., (1970), *J. Mech. Phys Solids*, **18**, 1.
- Argon, A. S., (2000), in "*Comprehensive Composite Materials*", edited by Kelly, A. and Zweben, C., vol. 1 (edited by Chou, T.-W.), Pergamon/Elsevier: Amsterdam, p.763.
- Bower, A. F. and Ortiz, M., (1991), *J. Mech. Phys. Solids*, **39**, 815.
- Crocker, A., Smith, G., Flewitt, P. and Moskovic, R., (1996), in "Proceedings of the 11<sup>th</sup> European Conference on Fracture (ECF11)", Eng. Mater. Advis. Serv., Warley, UK, vol.1, pp233-6.
- Gell, M. and Smith, E., (1967), *Acta Metall.*, **15**, 253.
- Hahn, G. T., Averbach, B. L., Owen, W. S., and Cohen, M., (1959), in "*Fracture*", edited by Averbach, B. L., Felbeck, D. K., Hahn, G. T. and Thomas, D. A., MIT Press: Cambridge, MA, p.91.
- McClintock, F. A., (1997), in "*Cleavage Fracture: George R. Irwin Symposium Proceedings*", edited by Chan, K. S., TMS: Warrendale, PA, p.81.
- Mower, T. M. and Argon, A. S., (1995), *Mech. Mater.*, **19**, 343.
- Qiao, Y. and Argon, A. S., (2002a), *Mech. Mater.*, submitted for publication.
- Qiao, Y. and Argon, A. S., (2002b), to be published.

## Figure Captions

- Fig.1 Sketch of double cantilever beam specimen showing the electron-beam welded bicrystal insert (grains *A* and *B*) and means of wedge loading by  $T_0$  to producing opening loads  $P$ .
- Fig.2 The temperature dependence of the tensile yield stress, fracture stress and critical resolved shear stresses on the possible  $\{110\}\langle 111 \rangle$  and  $\{112\}\langle 111 \rangle$  slip systems of single crystal experiments.
- Fig.3 A typical example of the dependence of opening load  $P$  on opening displacement  $\delta$  in a wedge loading experiment (Sample 6).
- Fig. 4 Transition in the normalized fracture resistance from cleavage to mixed-cleavage.
- Fig.5 A SEM micrograph of the fracture surface in grain *A* showing repeated arrest and reinitiation of the cleavage crack by deformation twins.
- Fig.6 (a) A SEM micrograph showing a regular mode of break-through of the grain boundary from grain *A* to grain *B* with entry of the cleavage crack across the grain boundary at points a distance  $w$  apart and spreading out in grain *B* on a tiered staircase-like mode (in bicrystal 10); (b) A sketch depicting the process of the cleavage crack penetrating from grain *A* into grain *B* in a regular mode, as shown in Fig.6a.
- Fig. 7 The measured frequency distribution of distance  $w$  at a grain boundary with intermediate misorientation angles  $\psi = 11^\circ$  and  $\varphi = 26^\circ$  (in bicrystal 14). Other distributions for grain boundaries with smaller and larger misorientations give similar results.

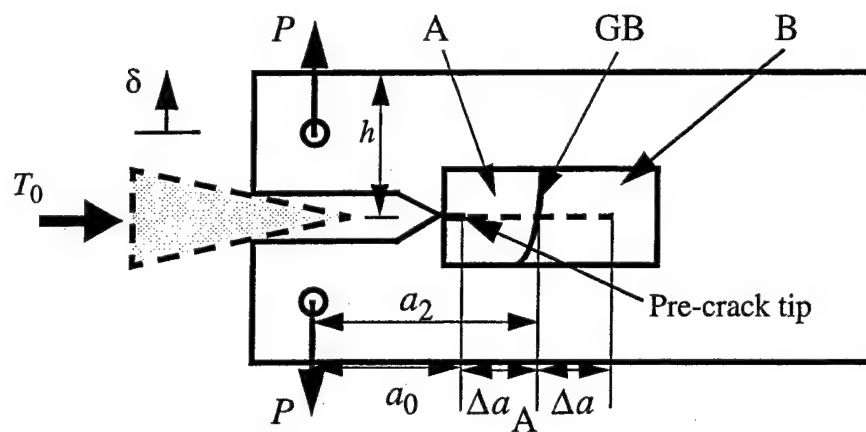


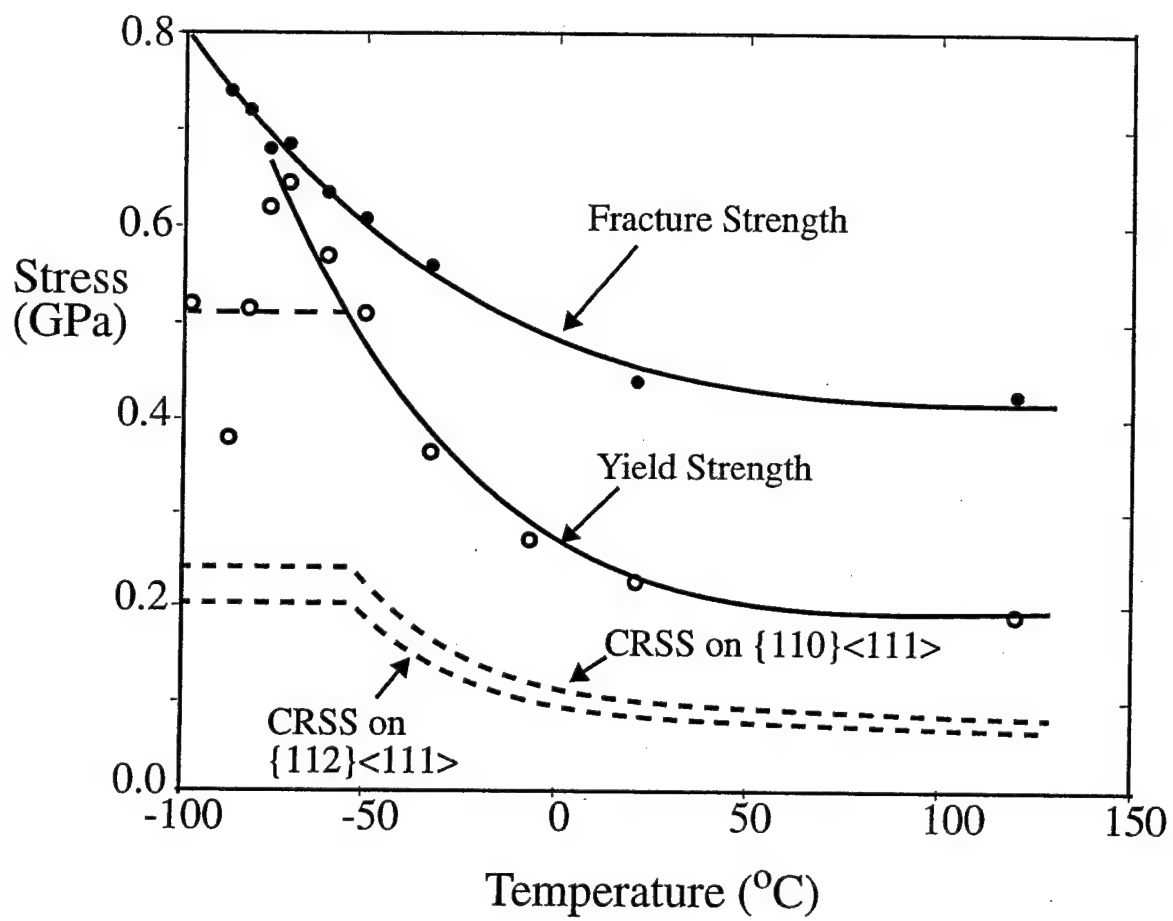
Fig. 8 (a) A SEM micrograph showing break-through across a grain boundary above the cleavage to mixed-cleavage transition; (b) cartoon depicting the nature of additional plastic dissipation by sigmoidal plastic bending and rupture of ligaments.

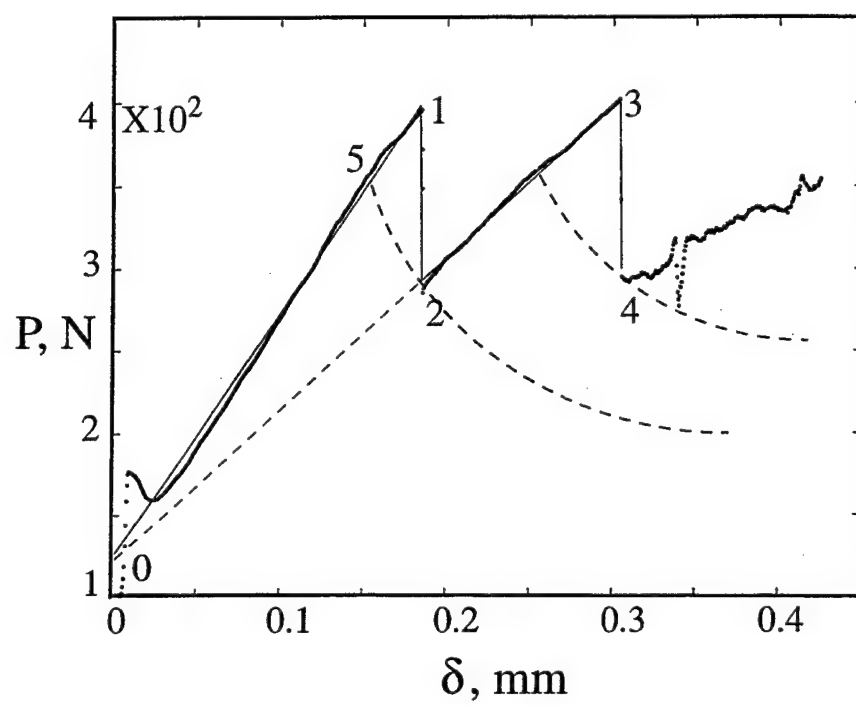
Fig. 9 (a) Propagation of a fragmented cleavage crack in grain *A* showing the nature of the plastic dissipation by plastic shear work in the bridging of cleavage strips; (b) The assumed tension/separation profile acting in a process zone of extent  $\Delta_c$ .

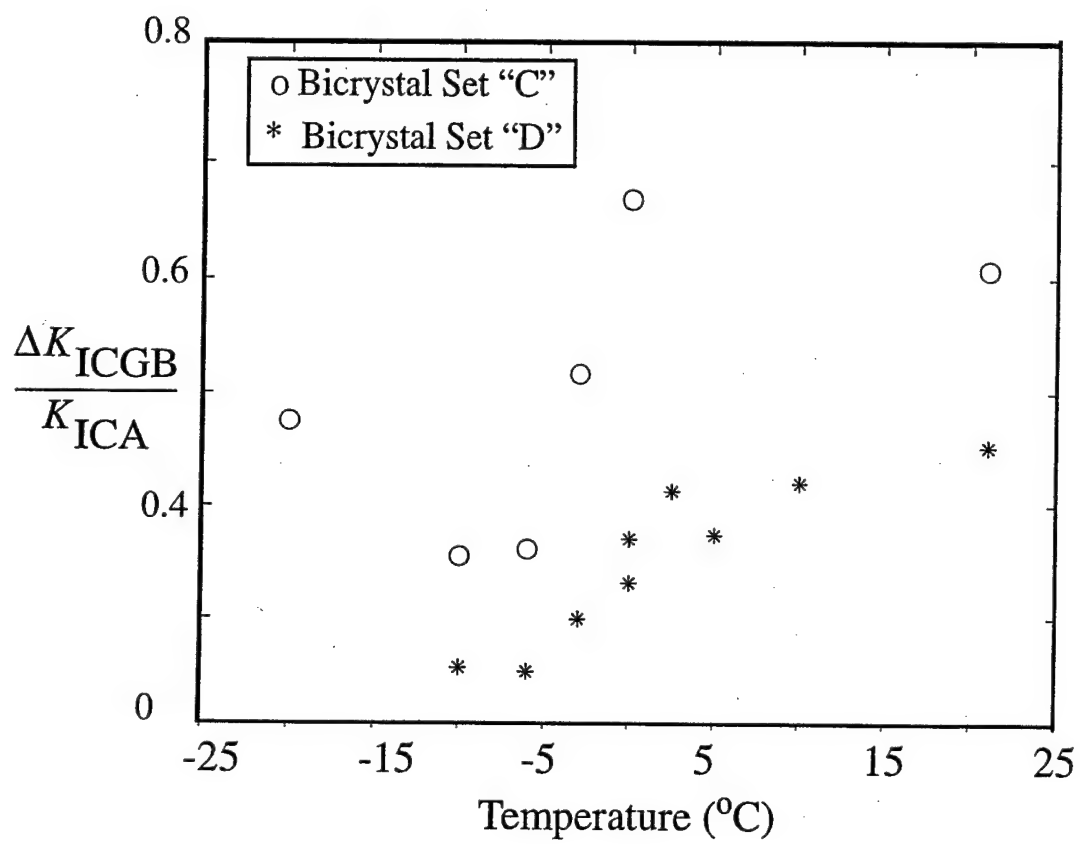
**Table I Characteristics of the 17 bicrystal samples: measured values of  $K_{ICGB}/K_{ICA}$  and normalized experimental and computed toughness compared**

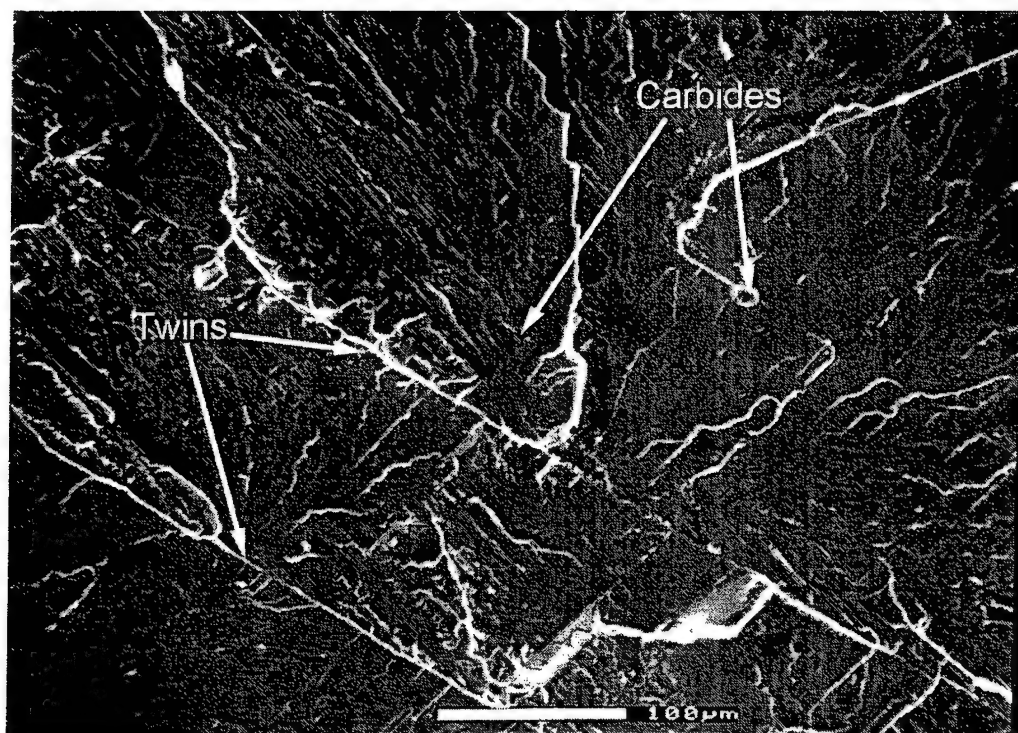
Sample	1	2	3	4	5	6	7	8
$\psi$	0.175	0.210	0.331	0.157	0.140	0.122	0.140	0.594
$\phi$	0.559	0.052	0.245	0.367	0.332	0.734	0.069	0.210
$K_{ICGB}/K_{ICA}$	1.461	1.049	1.168	1.226	1.192	1.575	1.042	1.233
$(\Delta K_{ICGB})_E/(\Delta K_{ICGB})_C$	1.132	0.942	0.977	0.967	1.046	1.096	0.964	0.984
Sample	9	10	11	12	13	14	15	16
$\psi$	0.229	0.402	0.052	0.385	0.210	0.367	0.490	0.524
$\phi$	0.455	0.699	0.052	0.297	0.227	0.455	0.245	0.069
$K_{ICGB}/K_{ICA}$	1.283	1.602	1.036	1.225	1.141	1.404	1.204	1.121
$(\Delta K_{ICGB})_E/(\Delta K_{ICGB})_C$	1.030	0.923	1.002	0.995	1.000	1.078	0.969	0.921
Sample	17							
$\psi$	0.280							
$\phi$	0.542							
$K_{ICGB}/K_{ICA}$	1.425							
$(\Delta K_{ICGB})_E/(\Delta K_{ICGB})_C$	1.073							



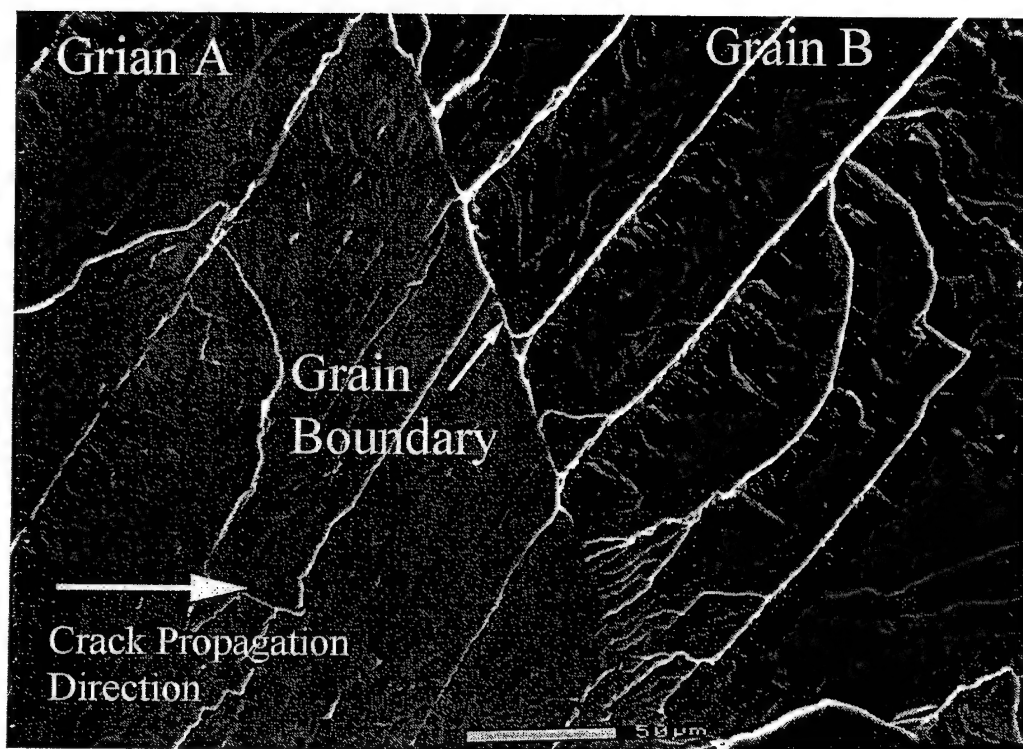


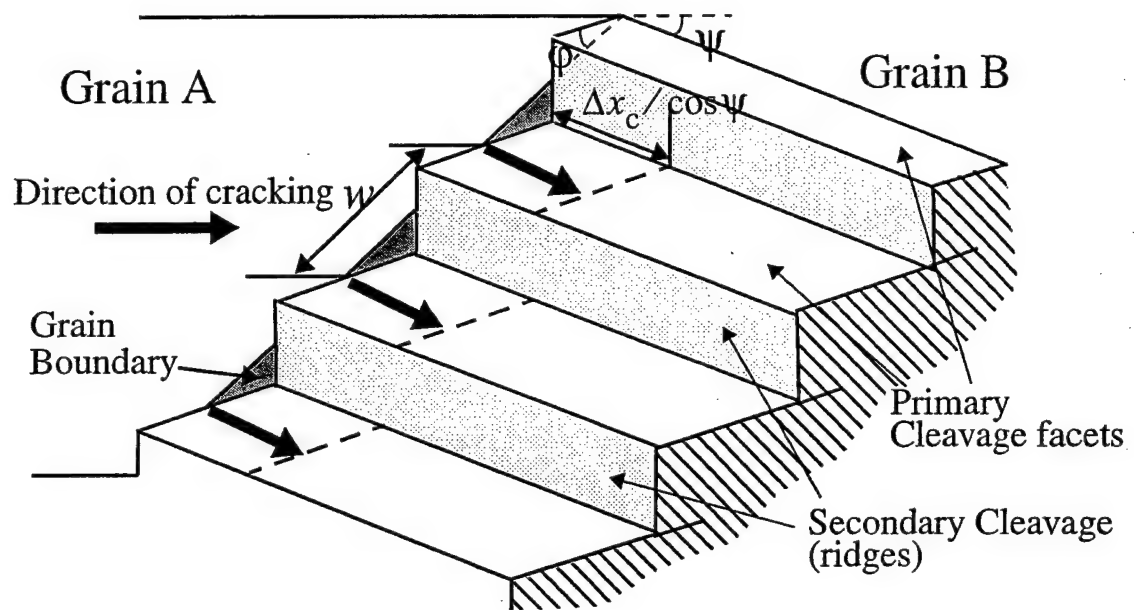




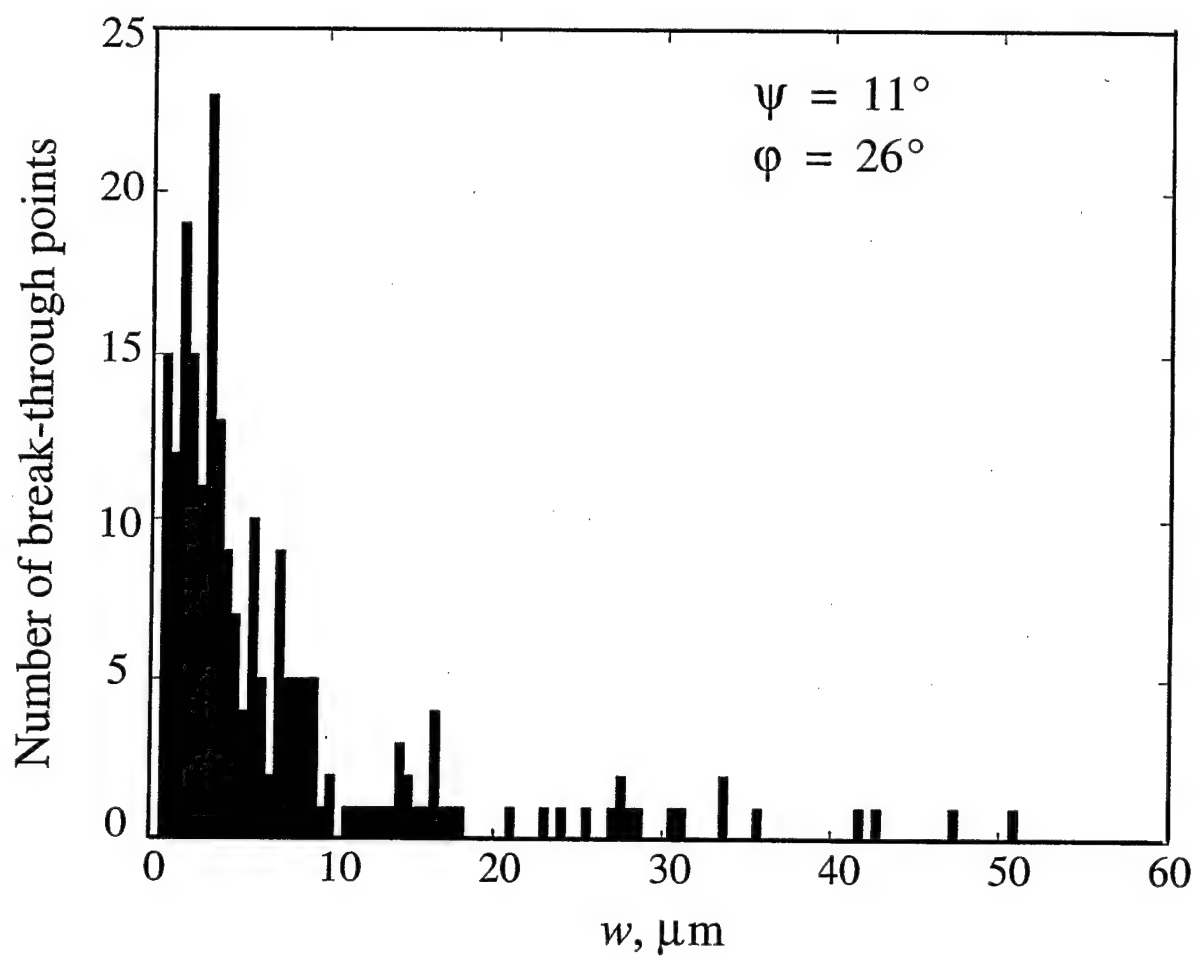


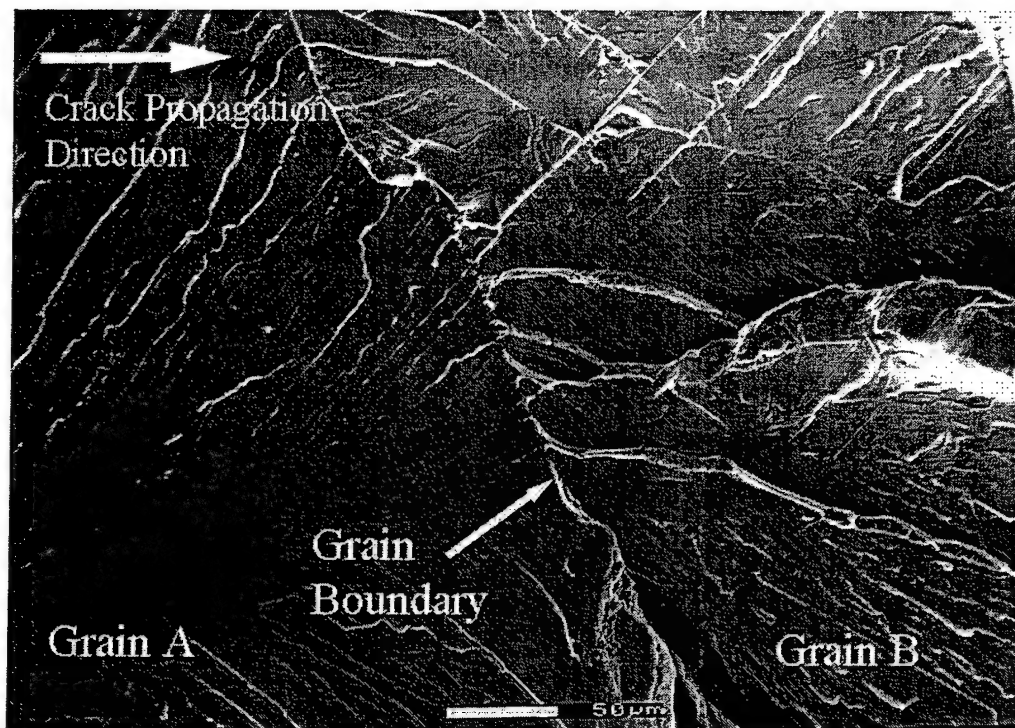




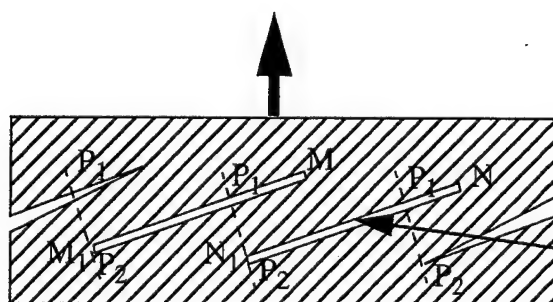


(b)

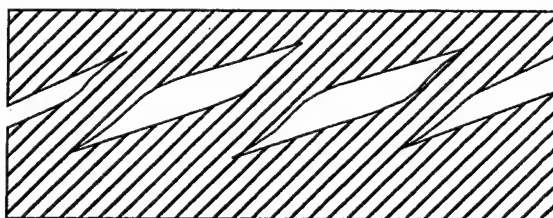




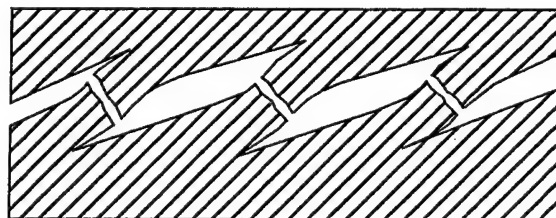
$T < T(C-MC)$



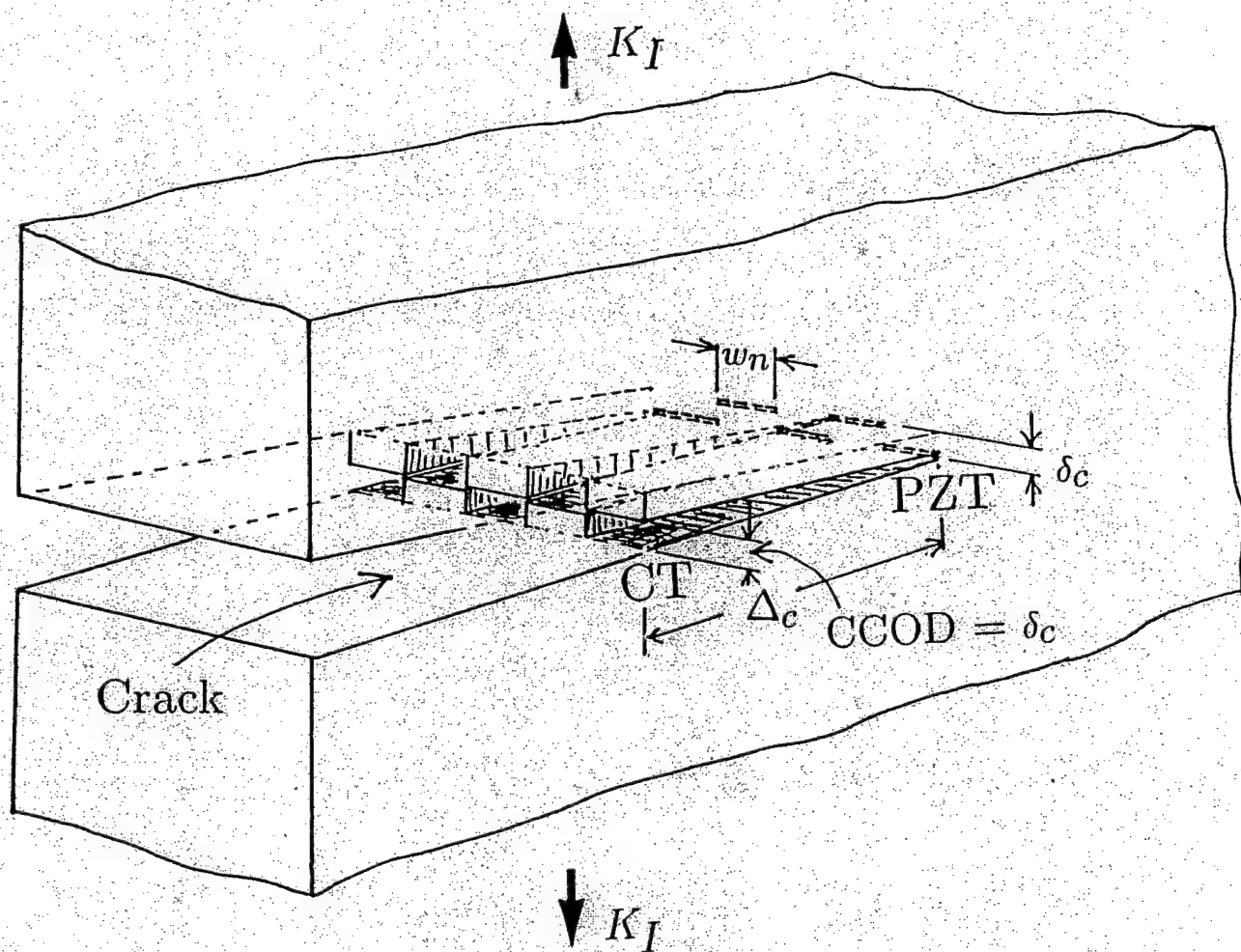
Cleavage terraces  
in Grain B

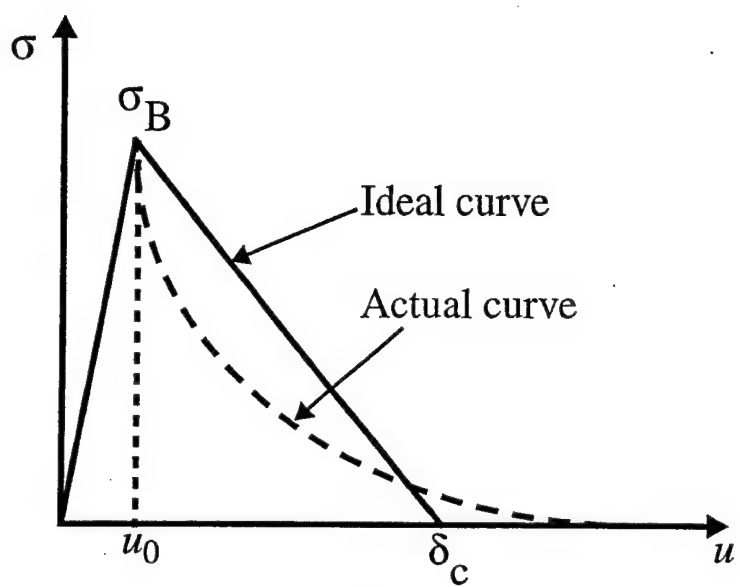


$T > T(C-MC)$



(b)





(b)





## Brittle-to-ductile transitions in the fracture of silicon single crystals by dynamic crack arrest†

B. J. GALLY‡ and A. S. ARGON§

Massachusetts Institute of Technology, Cambridge, Massachusetts 02139, USA

[Received 16 February 2000 and accepted in revised form 8 June 2000]

### ABSTRACT

Experiments have been conducted on the brittle-to-ductile transition of fracture in silicon single crystals through the arrest of cleavage cracks made to propagate on the (110) cleavage planes up a temperature gradient. An activation energy of 1.82 eV has been determined for the transition process based on the dependence of the  $T_{BD}$  on an averaged crack velocity, inferred from a jerky mode of crack advance. The dislocation patterns in the arrest zones have been studied in detail by a combination of etch pitting and Berg–Barrett X-ray topographic imaging after the arrest. These observations indicated that the plasticity of the entire arrest process is accomplished by slip activity on a set of two symmetrically placed vertical slip planes in which only one type of dislocation was involved. These planes do not have the highest resolved shear stresses but have the advantage of a very low energy barrier to the nucleation of dislocations from crack tip cleavage ledges. A close correspondence was noted between the spacing of dislocation sources along the crack tip and the density of cleavage ledges observable by Nomarski interference contrast on the cleavage surface prior to arrest. A homogenized model of crack tip plasticity is presented that is based on the Riedel–Rice model of stress relaxation at tips of cracks in creeping solids which serves to characterize well all nonlinear aspects of the arrest process. The results have also been contrasted with the predictions of a brittle-to-ductile fracture transition model based on defect mediated melting and were found to be uniformly inconsistent with that model.

### §1. INTRODUCTION

The abrupt transition in fracture from an anticipated ductile form to a brittle form remains a key phenomenon of concern in the structural use of steels at low temperatures. The worst-case scenario is considered to be the triggering of a brittle cleavage mode of crack propagation in a structure undergoing local large-strain plastic flow. Nevertheless, the complementary point of view of the arrest of brittle cleavage cracks by reduction of crack tip driving forces or by means of local micro-structural toughening has been recognized as being of equal fundamental importance in understanding the processes involved in fracture transitions. The early experimental study of Hahn *et al.* (1959) on coarse-grained E-Steel demonstrated that in

† This paper is dedicated to the memory of Professor Peter Haasen, the former director of the Institut für Metalphysik at the University of Göttingen, who was a pioneer in the recent studies of the brittle-to-ductile transitions in silicon.

‡ Present address: Exponent, Natick, Massachusetts, USA.

§ Author for all correspondence. Email: argon@mit.edu

smooth bar experiments, in the fracture transition range of low temperatures, continued tough behaviour results when deformation-induced grain-sized cleavage microcracks could be arrested at grain boundaries. These and more recent experiments (Qiao and Argon 2001) on Fe-3% Si indicate that the principal role of grain boundaries in fracture transitions appears to be to stop the crack for a certain length of time during which thermal processes can result in local plastic relaxations either to shield or to blunt the crack tip. Thus, purely thermally initiated processes of plasticity at crack tips must be considered as playing a key role in the brittle-to-ductile transitions of fracture in all cases.

In the present paper we report an experimental investigation of the processes governing the arrest of cleavage cracks in single crystals of silicon. All previous fracture transition experiments in silicon (St John 1975, Brede and Haasen 1988, Hirsch, *et al.* 1989, George and Michot 1993) have investigated the brittle-to-ductile transition on static cracks subjected to different rates  $\dot{K}$  of loading at a series of increasing temperatures where the stationary crack either starts to propagate in an unstable manner at lower temperatures or becomes completely shielded by crack-tip-initiated plasticity at or above a certain critical transition temperature and cannot be propagated under the given rate of loading. These experiments have clarified the kinetics of the crack tip shielding process for stationary cracks and probed the specific crystallographic slip processes involved in the shielding (George and Michot, 1993). However, they have not clarified the bifurcation conditions for a crack tip either to propagate by continued cleavage or to be stopped by a progressive evolution of crack tip shielding. Such competing processes involved in the shielding of cracks were observed in LiF by Gilman *et al.* (1958) and by Burns and Webb (1970a,b). The latter, in particular, observed the formation of plumes of shielding dislocations emanating from propagating cleavage cracks. Similar experiments involving arrest of propagating cracks in silicon single crystals by Brede *et al.* (1991) and Hsia and Argon (1994) were inconclusive.

## §2. CRYSTAL PLASTICITY AT CRACK TIPS IN SILICON

For fundamental experiments exploring the purely thermal processes involved in brittle-to-ductile transitions, silicon is an ideal intrinsically brittle model material of choice. It can be obtained in large sizes in dislocation-free form with precise levels of doping, because of its widespread use in electronic devices which require highly characterized material. Moreover, its crystal plasticity has been extensively studied (Alexander and Haasen 1968, Alexander 1986). The diamond-cubic crystal structure of silicon has the same slip systems as fcc metals but has rather more complex dislocation core structures owing to its strong tetrahedral bonding. The core structures of partial dislocations in silicon and their role in the mobility of extended dislocations have been modelled in detail (Bulatov *et al.* 1995, Cai *et al.* 2000), in very good agreement with numerous experimental studies of the kinetics of dislocation mobility. Silicon cleaves on both the {111} and the {110} planes with slightly lower surface energies for the latter planes than the former ( $K_{Ic} = 0.89 \text{ MPa m}^{1/2}$  for {110} and  $0.93 \text{ MPa m}^{1/2}$  for {111} planes (Michot 1988)). This provides alternative choices for either threefold or twofold symmetry for the possible modes of crystal plasticity at the crack tips. In the experimental studies of St John (1975) and those of Brede and Haasen (1988) the {111} plane was chosen for cleavage with the crack propagating in a  $\langle 110 \rangle$  direction, resulting in a complex form of crystal plasticity in the crack tip region lacking symmetry with respect to the cleavage plane and making

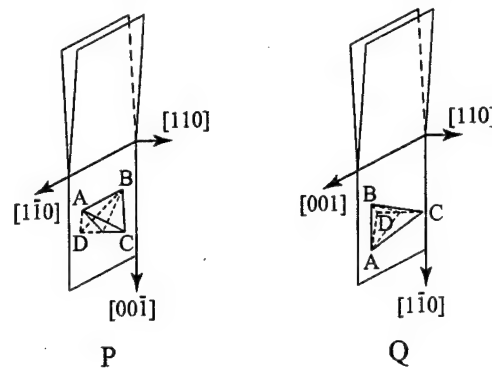


Figure 1. Two crack tip configurations having (110) as the cleavage plane. These represent two of the five configurations introduced by George and Michot (1993) which they referred to as  $\epsilon$  and  $\gamma$  respectively. In the present study, only the Q configuration with the highest degree of symmetry was considered.

mechanistic analysis difficult. In comparison, George and Michot (1993) considered and explored five different crystallographic configurations of the crack fronts involving both the {111} and the {110} cleavage planes of which both the P and the Q configurations, reproduced in figure 1, utilize cleavage on the more symmetric {110} planes. Of these the P configuration offers a symmetrical set of inclined planes  $\gamma$  and  $\delta$ , in the Thompson notation, that would appear to be well suited to crack tip blunting and a symmetrical set of vertical planes  $\alpha$  and  $\beta$ , in the Thompson notation, as apparently less well suited alternatives for crack tip blunting. The Q configuration in comparison offers a symmetrical set of vertical planes ( $\alpha$  and  $\beta$ ) with a better potential for crack tip blunting than the corresponding set of vertical planes of the P configuration and a second symmetrical set of oblique planes ( $\gamma$  and  $\delta$ ) that possess similar possibilities for crack tip shielding by dislocation plumes as observed in LiF by Burns and Webb (1970a). Since the  $\gamma$  and  $\delta$  planes, in the P configuration, also have a high potential for cleavage, they make this configuration less attractive for a study of crack arrest. Therefore, the Q configuration was chosen as the only configuration for the present crack arrest studies.

### §3. EXPERIMENTAL CONDITIONS

#### 3.1. The crack arrest experiment

##### 3.1.1. Specimen geometry and characteristics

An initial attempt to use specially contoured elongated constant stress intensity samples possessing the geometrical advantage for propagation of cleavage cracks at constant velocity by maintaining constant pin displacement rates (Brede *et al.* 1991, Hsia and Argon 1994) was abandoned owing to its extreme sensitivity to minor perturbations. Instead, a double cantilever-beam (DCB) geometry was adopted, which is intrinsically stable since the crack tip stress intensity decreases with increasing crack length.

Figure 2 shows the basic test configuration of the DCB specimen subjected to a temperature gradient in the crack growth direction, ranging from  $T_1$  at the crack tip, being too low to initiate any slip activity, to  $T_2$  representing a potential temperature

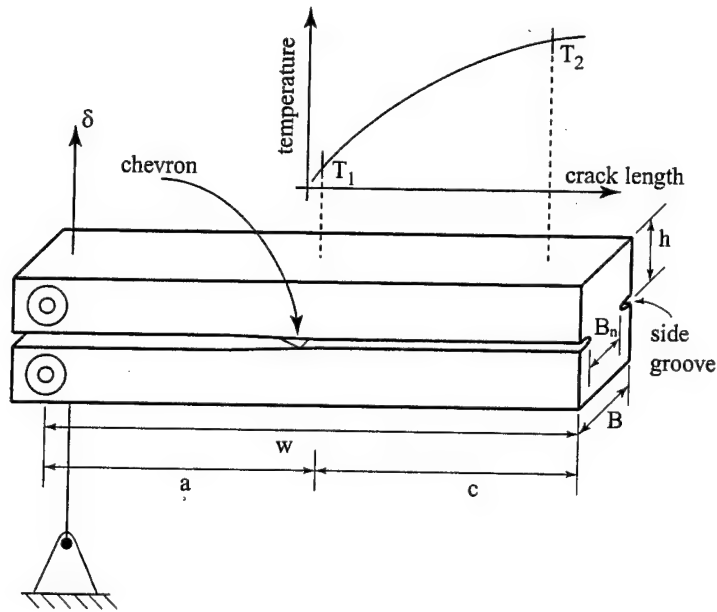


Figure 2. Sketch showing the DCB specimen used in the crack arrest experiments labelling dimensions and showing the associated imposed temperature gradient.

where crack arrest can be accomplished for cracks traveling with given velocity. Figures 3(a) and (b) show the specific geometrical arrangement of the two separate sets of potential slip planes: the symmetrically placed oblique  $\gamma$  and  $\delta$  planes as well as the symmetrically placed vertical  $\alpha$  and  $\beta$  planes in the Q configuration depicted in figure 1.

The crack tip stress intensity factor for the DCB specimen configuration is,

$$K_I = \frac{3^{1/2} E h^{3/2} \lambda^2 \delta}{1 - \nu^2} f(a, w, \lambda), \quad (1)$$

where  $E$ ,  $\nu$ ,  $\delta$  and  $h$  are Young's modulus, Poisson's ratio, the relative displacement of the loading pins and the height of the arms of the DCB specimen, with  $\lambda = 6^{1/4}/h$  being a convenient normalization length. The factor  $f(a, w, \lambda)$  determined by Kanninen (1973) is given in appendix A, § A.1, and is plotted in figure 4. It represents the dependence of the stress intensity on the crack length  $a$ , of the DCB specimen of total length  $w$ .

### 3.1.2. Stability of crack advance in the double-cantilever-beam

Stable crack propagation at controlled rates of pin displacement requires a very stiff external agency that imposes the pin displacement, assuring that the elastic energy released by crack extension in the DCB specimen comes overwhelmingly from the specimen. This requires that

$$C_m \leq \frac{2(dC_s/da)^2}{d^2 C_s/da^2} - C_s, \quad (2)$$

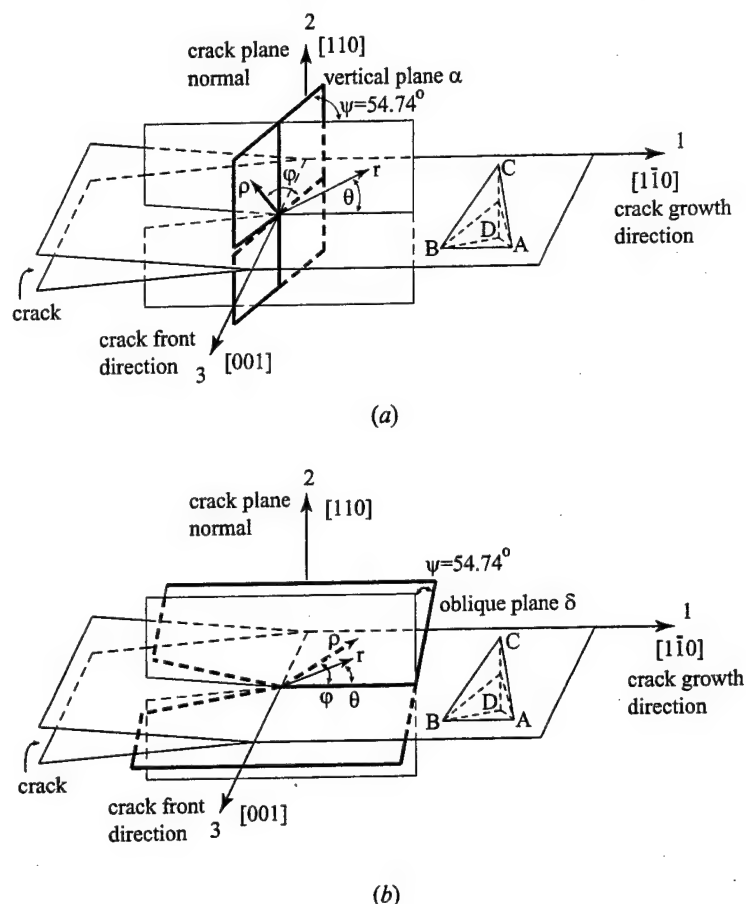


Figure 3. Sketches showing the geometrical arrangement of the two sets of potential slip systems of the Q configuration: (a) the vertical  $\alpha$  and  $\beta$  system; (b) the oblique  $\gamma$  and  $\delta$  systems in relation to the crack plane and the crack front.

where  $C_m$  is the machine frame compliance and  $C_s$  is the total DCB specimen compliance (Kanninen and Popelar 1985). In the present study this condition was satisfied comfortably for  $a/w > 0.5$  at room temperature as shown in figure 5. However, in some of the high-temperature experimental conditions, significant temperature rises in the specimen pull rods resulted in adverse stiffness reductions in  $C_m$ , affecting overall stability conditions. Even after rectification of the problem by proper insulation the level of stability was less than fully desirable, resulting in relatively larger crack jumps (Gally 1999). As we discuss in § 4.1, this resulted in few (often only one) jumps of the crack between initiation and final arrest. A separate destabilizing influence in this behaviour is a frequently occurring initial excess in the crack growth resistance  $K_{Icinit}$  due to geometrical irregularities at the crack tip. This is counteracted to some extent by a chevron-shaped taper at the initial crack tip.

Under ideal conditions in the DCB specimen for cracks advancing stably, the crack velocity  $\dot{a}$  should be related to the pin displacement rate  $\dot{\delta}$  by (Burns and Webb 1970a)

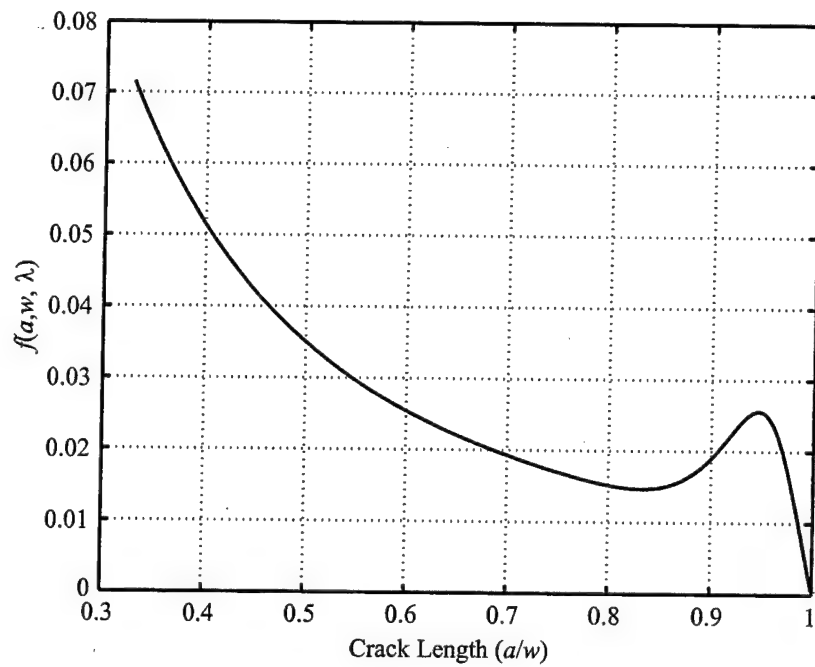


Figure 4. The changes with crack length in the finite-field correction factor for the DCB specimen, calculated on the basis of equation (A 1).

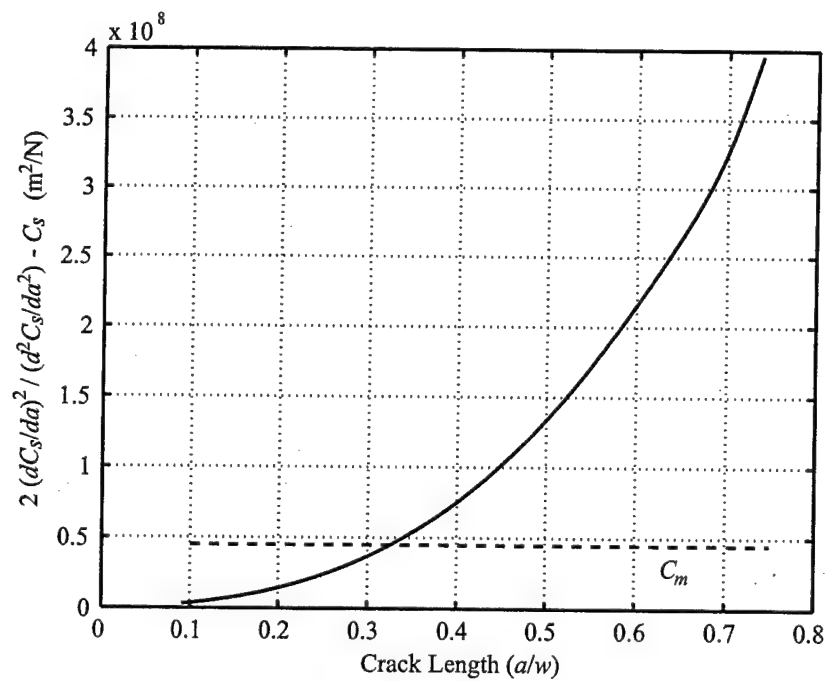


Figure 5. The dependence on the crack length of the stability criterion for cleavage crack growth, computed on the basis of equation (2) using appropriate stiffnesses of the DCB specimen and that of the external machine system, as experimentally determined.

$$\dot{a} = \frac{\dot{\delta}}{2a} \left( \frac{9EI}{4BG_{1c}(1 + 3\rho\dot{\delta}^2 h/14G_{1c})} \right)^{1/2}, \quad (3)$$

where  $I = Bh^3/12$  is the moment of inertia of the DCB specimen arm of height  $h$ ,  $G_{1c} = 2\chi_s(B_n/B)$  is the critical energy release rate for cleavage,  $B$  the beam thickness and  $B_n$  the net ligament thickness (equal to  $B - 2d$ ) at the root of the side grooves of depth  $d$ .  $\chi_s$  is the specific free surface energy of the cleavage plane and  $\rho$  the material density. Under quasistatic conditions of crack advance the pin displacement rates used in the experiments were in the range of  $(1-10) \times 10^{-7} \text{ ms}^{-1}$  for which the second term in parentheses in the denominator in equation (3) considering inertial effects becomes negligible.

Under conditions of quasistatic loading behaviour of the DCB specimen with a crack length  $a$  the characteristic pin load  $P/B$  (per unit thickness) and pin displacement  $\delta$  are related by simple beam theory:

$$\frac{P}{B} = \frac{Eh^3}{8a^3} \delta. \quad (4)$$

Once the crack begins to grow in a brittle manner against a constant energy release rate  $G_{1c}(=2\chi_s(B_n/B))$ , a characteristic decline in pin load with pin displacement should result which can be given as

$$\frac{P}{B} = \left( \frac{2G_{1c}}{3} \right) \left( \frac{\Lambda}{\delta} \right)^{1/2}, \quad (5)$$

where  $\Lambda = (3Eh^3/16G_{1c})^{1/2}$  is a characteristic length scale for cracking of the DCB specimen. For a beam with a finite foundation stiffness, equation (4) needs to be modified by a factor of  $1/\psi(a, c, \lambda)$  given in appendix A, § A.2, to incorporate such foundation properties (Kanninen 1973) where  $c$  is the remaining uncracked length of the DCB geometry. Equation (5) needs no such modification.

Because of many perturbations in the specimen geometry and loading system the actual decrease in the pin load versus pin displacement relation was usually made up by a series of jerky extensions of the crack, as already stated above.

### 3.2. Crack length measurements

During a typical experiment, in a coarse measure, the crack length  $a$  in a specimen was routinely inferred from the specimen stiffness  $d(P/B)/d\delta$  after every jerky extension of the crack:

$$a = \frac{h}{2} \left( \frac{E}{\psi d(P/B)/d\delta} \right)^{1/3}. \quad (6)$$

The initial coarse estimates of crack growth increments were finally corrected using actual measurements of the final arrested crack length. In many cases the actual crack length was also measured directly by a method of laser light scattering from the edges of the elongating crack, which was described in detail earlier by Brede *et al.* (1991), using either a position sensitive detector to record the current crack length or a high-speed (Kodak Ektapro) video camera. In such instances the side from which the crack length was measured was free of a side groove. Figure 6 shows an example of jerky crack extension at room temperature through the chevron region of a specimen where the effective ligament thickness at the fracture plane between side grooves



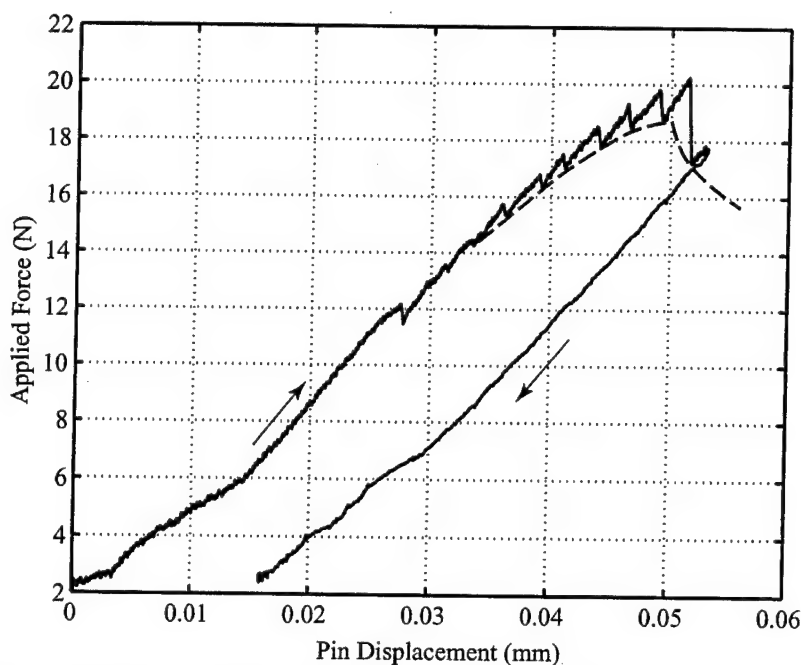


Figure 6. A typical force-pin displacement plot resulting from the room-temperature crack extension into and through the crack tip chevron. This was the first step of a crack arrest experiment which placed an atomically sharp cleavage crack in a position to propagate up the temperature gradient.

increases linearly to the final thickness  $B_n (= B - 2d)$ . The broken contour represents the expected smooth extension behaviour of the crack in the absence of perturbations. In the last major load drop the crack has begun to extend through the final full thickness of the ligament. Such preparatory extension of the crack through the chevron region at room temperature was used regularly as an initial step of the actual high-temperature crack arrest experiments to reduce destabilizing perturbations in the initial phases of crack growth.

### 3.3. Temperature gradients in specimens

In the crack arrest experiments the end of the DCB specimen was immersed through a series of radiation shields into a small specially constructed molybdenum wire-wound heating chamber which readily achieved temperatures of 1000°C or higher at the specimen ends. The temperature distribution in the sample was a result of heat conduction along the specimen toward the pinned end and radiant cooling from the side surfaces of the specimen to the water-cooled walls of the vacuum chamber in which the experiments were carried out (Brede *et al.* 1991, Gally, 1999). Temperature distributions obtained by a series of up to ten thermocouples attached to the back face of the specimen gave excellent agreement with the results of a numerical solution of the heat transfer problem. In spite of such good agreement the actual temperature distribution in every crack arrest experiment was measured directly by such an array of thermocouples attached to the specimen by a ceramic glue. Figure 7 shows a typical temperature distribution in a DCB crack arrest experiment sample determined from individual temperature measurements, a cubic fit to

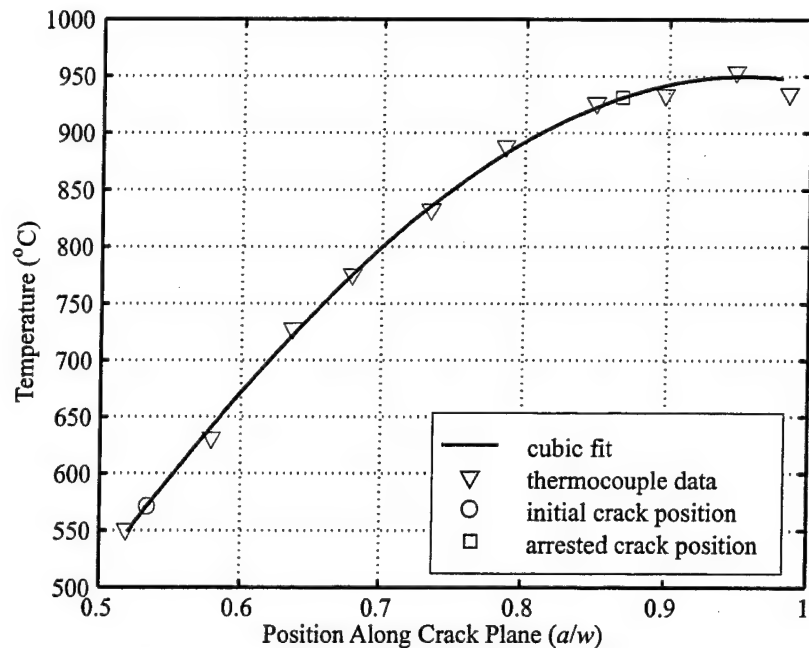


Figure 7. A typical temperature distribution in the DCB specimen showing the experimentally measured temperatures ( $\nabla$ ) and the two points of the initial crack length ( $\circ$ ) as well as the point ( $\square$ ) at which the crack was arrested.

the distribution, as well as both the initial and the final crack length where arrest actually occurred in a successful experiment.

#### 3.4. Conduct of a typical crack arrest experiment

The DCB sample of the correct orientation with polished surfaces, containing polished side grooves with a chevron tapering down to a point at the tip of the crack, prepared in the manner described below, was first pre-loaded at room temperature to permit the cleavage crack to initiate and propagate through the chevron as described above. Once this condition was attained, the specimen was partially unloaded prior to establishment of the required temperature gradient while maintaining a slight positive pin load to prevent misalignment. The sample was then subjected to the desired pin displacement rate and the resulting load-pin displacement history was recorded.

In the desired scenario the crack grows through the region of increasing temperature in a number of jerky steps as depicted in figure 8. With each increment of crack advance the crack tip is repositioned in a higher temperature region and is maintained there over the next period of pin displacement, positioning the crack tip in a still higher-temperature region. During each increment the crack tip has the opportunity to initiate an arrest process involving the generation of dislocations from the crack tip, followed by their multiplication and expansion away from the crack tip to achieve a combination of blunting and shielding that prevents further crack growth. Such a sequence of processes are associated with a characteristic response time, decreasing exponentially with increasing temperature, governed by the collective mobility of the nucleated dislocations away from the crack tip. When

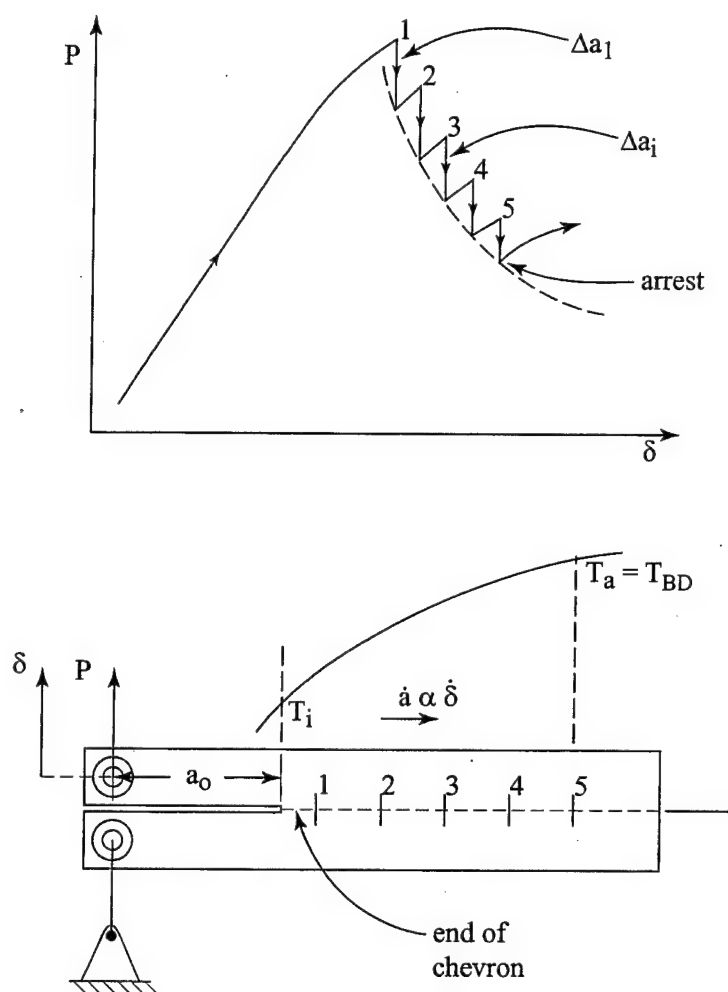


Figure 8. Depiction of a relatively idealized jerky crack advance scenario in which the step-wise advancing crack is systematically put into new environments at progressively increasing temperature until it eventually is arrested.

this response time becomes of the order of the residence time of the crack tip at a certain temperature the arrest processes can develop. Under the less ideal conditions of inadequate excess machine stiffness of the present experiments, the crack reached the final arrest position after only one or at most two jumps, leading to considerable uncertainty for the actual time period during which the full sequence of arrest processes were accomplished.

In most cases the specimen was unloaded after a major load drop, that had positioned the crack tip in a region of high temperature where a bona fide arrest was expected. While in most cases a substantially completed arrest phenomenon had indeed occurred, in a few cases no dislocation activity could be detected in the subsequent examination of the crack tip region at room temperature, indicating insufficient elapsed time at a high temperature for the arrest processes to develop. In most cases the samples with the arrested cracks were then reloaded to fracture at

room temperature to reveal the crack front for detailed examination by methods discussed in the following sections. In a few cases the cracked and unloaded specimens were not reloaded to full fracture at room temperature but were sectioned along the median plane, followed by polishing and etching to outline the plastic arrest zone and its dislocation content for analysis as discussed in §§ 5.3 and 5.4 below.

### 3.5. Material and sample preparation

The DCB samples were cut from a single crystal boule of 6 inch diameter and 8 inch length with a [001] axis orientation, donated by MEMC Electronic Materials Inc. The crystal was grown by the Czochralski method and was heavily doped with boron to a resistivity of  $0.017 \Omega \text{cm}$ . The oxygen content was 11.7 at. ppm with carbon content below 0.5 at. ppm. The heavy boron doping permitted ready cutting by electrical discharge machining (EDM). The relatively high oxygen content resulted in some expected oxide precipitation in the hot zones of the DCB samples and some associated dislocation loop punching as is explained in § 4.4, with, however, negligible consequences for the arrest experiments.

The cutting of the specimens to required orientations (always within  $\pm 2^\circ$ ), their polishing, the introduction of side grooves with a  $14^\circ$  included angle chevron at the crack tip, and the drilling of the pin holes have been discussed in detail elsewhere (Gally 1999). Of these procedures, two proved to be of greater importance than others. After being made somewhat oversize by EDM drilling, the pinholes were filled with cylindrical lava-stone inserts, were glued in place with ceramic adhesive and were subsequently drilled and reamed out by conventional machining to give accurately positioned holes for seating the ground tungsten loading pins. After premature dislocation emission from the inadequately finished surfaces of the side grooves in early experiments had resulted in considerable scatter, a detailed and meticulous process of polishing the surfaces of these side grooves was instituted. The finishing steps in this preparation involved chemical polishing with a 22% KOH bath which exposed selectively the {111} surfaces of the side grooves and sharpened them to a 'V' shape. This was followed by further exposure to HF,  $\text{HNO}_3$  and  $\text{CH}_3\text{COOH}$ , eliminating entirely any spurious dislocation emission from the side grooves by eliminating all EDM-damaged material. Since the polishing of the side groove surfaces rounded the tip of the chevron, a cleavage crack was initiated at the tip by a sharp razor blade.

The properly prepared samples used in the successful crack arrest experiments were essentially dislocation free. The main crack, sharpened by the previously described pre-loading scheme, was the only potential source for dislocations in the crack arrest process. Nevertheless, while the side groove surfaces were smooth and free of residual EDM damage, small gentle variations remained in the ligament of thickness  $B_n$  with a certain density of etching facets resulting from the KOH polishing step. These still contributed to the ubiquitous perturbations, producing jerky crack extension, together with the unavoidable residual 'noise' in the motion of the hydraulic actuator producing the pin displacements.

### 3.6. Means of examination of fracture surfaces and crack tip crystal plasticity

Cleavage fracture surfaces were viewed routinely with Nomarski interference contrast microscopy and to a lesser extent examined by atomic force microscopy (AFM). These examinations showed a high density of quite straight but shallow

surface steps (striations) parallel to the average crack front direction clearly visible in figure 9. AFM showed these to be arranged as a staircase in the same direction. While their origin was not satisfactorily explainable, they were attributed to a possible slight systematic misalignment of the actual  $\{110\}$  cleavage plane with the geometrical median plane of the DCB specimen best suited to crack propagation. In addition to these striations a series of less straight steps of apparently random polarity and nearly perpendicular to the crack front were also observed. These were identified to be cleavage ledges. As is clear from figure 9, they were related in their formation to the striations parallel to the crack front and had a high incidence of having been generated at the time when the striations were formed. The spacing of these cleavage ledges along the striations appeared to be a characteristic of these experiments, with their average spacing remaining close to  $5\text{ }\mu\text{m}$ . They persisted only for short distances and were smoothed out, only for new cleavage ledges to appear and take their place. From the resolution limits of Nomarski contrast microscopy and AFM measurements the heights of either the striations or the cleavage ledges were estimated to be in the range of  $10\text{ nm}$ . While striations parallel to the crack front were considered to be of little consequence, the cleavage ledges perpendicular to them were of considerable consequence in efficient emission of dislocations at crack tips as discussed by Zhou and Thomson (1991) and more specifically by Xu *et al.* (1997). Those cleavage ledges were attributed to small local variations between the normal to the cleavage crack plane and the mode I axis.

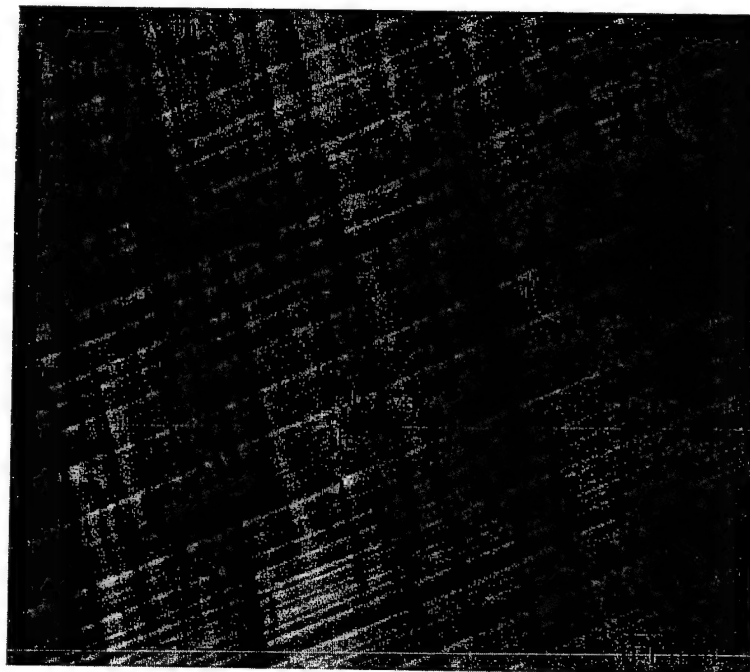


Figure 9. Nomarski interference contrast micrograph of the  $\{110\}$  cleavage fracture surface of a typical specimen showing straight striations parallel to the crack front and cleavage ledges parallel to the crack growth direction which are spawned from the striations and eventually smooth out but are continually replaced with new cleavage ledges.

The nature of the crack tip crystal plasticity at the arrest zone was investigated by two methods that have the overwhelming advantage of both surveying large areas or volumes and providing a considerable level of resolution. They consisted of etch pitting the (110) cleavage fracture surface and the (001) median plane parallel to the external specimen surfaces, which served to map out the nature, extent and dislocation content of the crack tip plastic zones. For these studies the etch employed by Secco d'Aragona (1972) was found to be most reliable to reveal dislocations threading through these two crystallographic planes. While the etch results in a uniform background roughness on a fine scale over the entire surface, the dislocation pits always stand out well and also exhibit a certain conical shape with often eccentrically placed tips suggesting a non-normal emergence angle of the dislocation line relative to the surface. The description of such rich detail which is not of primary interest here can again be found elsewhere (Gally 1999).

The in-depth distribution of the crack tip arrest dislocations was visualized by Berg-Barrett (BB) X-ray topographic imaging of the fracture surface after room-temperature separation. Topographs of fracture surfaces were taken from several suitable diffracting planes which included symmetric (220) and asymmetric (333), (331) and ( $\bar{6}20$ ) reflections with information gathered down to a penetration depth limit of nearly 1.0  $\mu\text{m}$ . Of these the (333) reflections were of the highest quality and were the most informative. Images were recorded on Ilford L-4 plates with emulsions 10  $\mu\text{m}$  thick and silver halide grain size of 0.25  $\mu\text{m}$ . On the original plates, referred to as negatives, dislocation lines appear as dark lines. All original plates were photographically enlarged by about 20 $\times$  and were printed as negatives, preserving the original contrast form. The dislocation line widths varied from 3.6  $\mu\text{m}$  for mixed dislocations to roughly 6.7  $\mu\text{m}$  for screw dislocations with Burgers vectors parallel to the [110] direction.

The BB X-ray topographic imaging method is well developed and has been discussed in great detail in the literature. More detail on its specific use in the present experiments can again be found elsewhere (Gally 1999).

#### §4. EXPERIMENTAL RESULTS

##### 4.1. Kinetics of crack arrest

The details of all the experiments, considered as successful in crack arrest, are listed in table 1 as A. In these, cracks started from the cold end of the specimens and were finally arrested, as expected, in the hot zone near the heating chamber. In a second set of three experiments identified as B the temperature at the hot end of the specimens was not sufficiently high to arrest the propagating cracks, and complete brittle fracture resulted. In two experiments identified as C, cracks jumped into the hot zone where bona fide arrests were expected. However, upon unloading and fracturing the specimens at room temperature, examination of the arrest zone showed no trace of plasticity, indicating that the residence time of the crack in the hot zone was insufficiently long or the temperature in the crack tip region was not high enough for the given pin displacement rate to initiate and develop a shielding process. Finally, in some of the earlier experiments where the anticipated arrest temperatures for higher pin displacement rates required higher temperatures at the hot end, the temperatures at the low end at the initial crack length became too high. This prevented initiation of brittle crack advance. Subsequent examination of the

Table 1. Crack arrest experiments.

Test	Experimental (DCB specimen number)†	Pin displacement rate ( $\mu\text{m s}^{-1}$ )	Initial crack temperature ( $^{\circ}\text{C}$ )	Crack arrest temperature ( $^{\circ}\text{C}$ )	Final crack jump length (mm)	Arrest crack length (mm)	Post arrest room temperature $K_{Ic}$ ( $\text{MPa m}^{1/2}$ )	$v_0 = \frac{1}{c} \frac{\Delta a_f}{\dot{a}}^\ddagger$
1	A (40)	1.0	645	1034	37.2	92.6	1.76	$1.49 \times 10^{-13}$
2	A (49)	0.5	645	1003	37.9	97.3	1.35	$7.58 \times 10^{-14}$
3	A (58)	0.2	571	931	36.6	95.4	1.49	$2.93 \times 10^{-14}$
4	A (41)	0.1	600	891	32.7	92.8	1.69	$1.31 \times 10^{-14}$
5	A (46)	0.1	526	843	24.3	83.0	1.59	$9.72 \times 10^{-15}$
6	C (43)	0.08	504	544	3.5	61.2	1.66, but no dislocation activity	
7	C (45)	0.08	481	570	9.5	70.6	detected§ 1.39, but no dislocation activity	
8	B	0.8	657	no cleavage crack arrest			detected§	
9	B	0.12	660	no cleavage crack arrest			detected§	
10	B	0.08	586	no cleavage crack arrest			detected§	

† Successful crack arrest experiments are denoted A. Those experiments where cleavage initiated at the cold end, but where no subsequent crack arrest occurred are denoted B. These samples cleaved into two halves. The third set of experiments, denoted C, were those where the cracks jumped into the hot region of the sample, but in which no subsequent evidence of crack tip plasticity was found.

‡  $\dot{A} = (3Eh^3/16G_{Ic})^{1/2} = 60.7 \text{ m}$ .

§ These  $K_{Ic}$  values were anomalously high and inconsistent with the absence of emission of dislocations and may have been a consequence of considerable unaccountable crack healing.

crack tip indicated that dislocation activity had initiated in these instances at temperatures greater than 650°C.

Figure 10 shows the dependence of the crack arrest temperatures on a normalized 'averaged' crack velocity  $v_0$  defined on the basis of the jerky form of crack extension, depicted in figure 8, giving

$$v_0 = \left( \frac{\Delta a}{\Delta t} \right)_f \frac{1}{c} = \frac{\Delta a_f \delta}{cA} \approx \exp \left( - \frac{\Delta U}{kT_{BD}} \right), \quad (7)$$

where  $\Delta a_f$  is the final crack jump length and where  $c$ , the shear wave velocity and  $A$ , the characteristic DCB dimension defined in connection with equation (5), were used as normalization parameters. Owing to the jerky nature of the crack advance this 'averaged' velocity understates the actual crack velocity of arrest. The values of calculated  $v_0$  are listed in table 1 for the five bona fide crack arrest experiments. The plot in figure 10 shows an expected Arrhenian behaviour with an activation energy of 1.82 eV. This is considerably lower than most of the reported activation energies of 2.2 eV for the glide of dislocations in the present silicon with boron doping (Imai and Sumino 1983). The discrepancy is attributed to the jerky form of crack advance where the correct magnitude of the final period  $\Delta t_f$ , during which the crack resides in the temperature range where the full arrest develops, is not accurately determinable.

The critical fracture toughness values  $K_{Ic}$  for subsequent room temperature fracture of the samples possessing the arrest plastic zones are listed also in table 1 and show considerable increases in fracture toughness compared with that of the virgin material of  $K_{Ic0} = 0.89 \text{ MPa m}^{1/2}$  on the (110) cleavage plane.

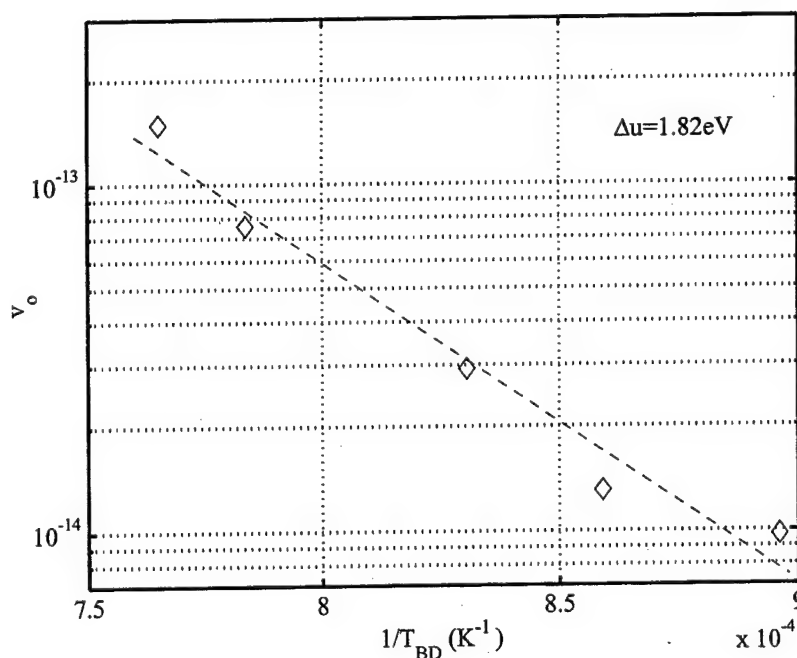


Figure 10. Dependence of  $T_{BD}$  on the average non-dimensional crack velocity  $v_0$  as defined by equation (7). The measured dependence reflects an activation energy of 1.8 eV.



#### 4.2. Stress relaxation experiments

The few experiments where premature crack tip stress relaxation precluded the proper initiation of cleavage crack growth were continued and converted into stationary crack tip stress relaxation experiments. A fracture transition, for the applied displacement rate, was considered to have occurred if the applied force exceeded by 50% the level of the typical required fracture loads in the DCB samples. Owing to the jerky nature of crack extension, the crack tip positions and hence the crack tip temperatures as well as the applied stress intensities were not readily determinable during the high temperature relaxation experiments but were determined after the experiment. The relevant characteristics of three such experiments are given in table 2.

These stress relaxation experiments were used to probe the evolution of the plastic zones and their dislocation contents. After the stress relaxation periods listed in table 2 were complete, the specimens were cooled under stress and subsequently sectioned along their median (001) planes followed by polishing these surfaces to remove all sectioning damage. A final step of etching revealed the outlines of the plastic zones and their dislocation content. These results will be described below in § 5.3 and analysed in connection with a crack tip model.

#### 4.3. Etch pit observations on fracture surfaces

Following a crack arrest experiment at a high temperature the regions behind and in front of the crack tips were examined by dislocation etch pitting the fracture surfaces.

The arrested crack fronts were smoothly curved with the crack front lagging slightly behind in the interior of the specimen, apparently because of the additional stress intensification present owing to the side grooves which served to pull the propagating crack ahead near the free surfaces.

The most important portion of the arrested crack front was the region in the interior of the sample, away from the side grooves, where plane-strain conditions prevailed. In this region the dislocation etch pits were characteristically arranged as V-shaped rows emanating from well defined sites along the front of the decelerating crack at roughly 5  $\mu\text{m}$  spacing as shown in figure 11. The rows of pits make an angle of  $110^\circ$  with each other and are symmetrically arranged with respect to the crack growth direction of  $[1\bar{1}0]$ . The origins of these rows, labelled *s*, are interpreted to be potent dislocation sources at the crack tip that finally produced sufficient dislocation line length to shield the crack tip fully. These rows outline the intersections with the cleavage fracture surface of the pairs of vertical  $\alpha$  and  $\beta$  planes which were expected to be the preferred pair since nucleation of pure screw dislocations on these planes, from cleavage ledges, is the energetically most favourable possibility as was estab-

Table 2. Characteristics of stress relaxation experiments.

Test	Pin displacement rate ( $\mu\text{m s}^{-1}$ )	Crack tip temperature ( $^\circ\text{C}$ )	Crack length (mm)	$K_I$ applied ( $\text{MPa m}^{1/2}$ )	Relaxation time (min)
11	2.0	919	73.2	2.39	12
12	0.4	750	68.2	3.07	30
13	0.3	661	63.8	2.52	60

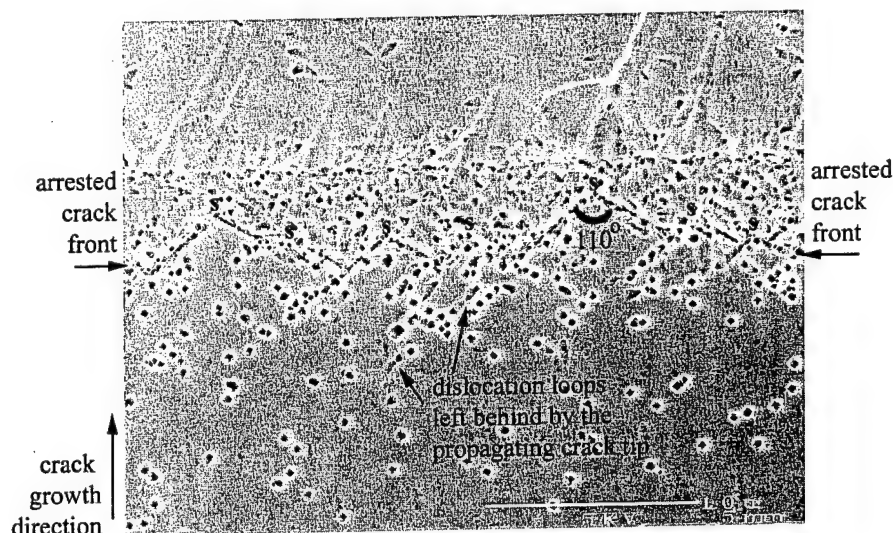


Figure 11. Etched fracture surface of sample 4 showing the flank portions of the arrested crack front. The pits outline the intersection of the dislocations emitted from the crack front that have produced the crack arrest. Seven clearly identified dislocation sources are visible. The trails emanating from sources *s* indicate that the dislocations are placed alternately on  $\alpha$  and  $\beta$  planes of the vertical system. The sources are envisaged to be cleavage ledges ideally suited to emitting CD-type screw dislocations.

lished by Xu *et al.* (1997). While the V-shaped trails of pits were the most dramatic feature, other individual pit rows parallel to one or the other direction of the V, indicating activity on only one or the other of the  $\alpha$  or  $\beta$  planes, were also found to be common in the center section of the arrested crack front. In this crack front region there was no evidence of activity on the oblique set of the  $\gamma$  and  $\delta$  planes, which would have left trails of pits parallel to the crack growth direction. More complete confirmation of this important conclusion is presented in § 4.6 below, giving results of the BB X-ray topographic imaging experiments that outline the arrangement of the dislocation patterns in the interior of the samples.

Examination of the pattern of etch pits in the arrested crack front region shown in figure 11 suggests a relatively intricate series of processes involved in the final arrest of the crack. Ahead of the well delineated zone of sources is a region of high density of etch pits, terminated sharply at a straight border roughly  $5\text{ }\mu\text{m}$  away from the zone of sources. We offer the following explanation for this pattern. In the initial stages of arrest the crack front has a slightly cuspy shape owing to the attached cleavage ledges that act as a series of retarding forces. The nucleated dislocation embryo along the cleavage ledge, and being almost entirely of CD screw nature must by necessity be emitted on the  $\alpha$  and  $\beta$  planes towards the forward direction of the crack, as depicted in figure 10 of the paper by Xu *et al.* (1997). As we discuss in § 5.2 in some detail, the nature of the resolved shear stresses on the  $\alpha$  and  $\beta$  planes are such that the emitted dislocation should expand only slightly into the region ahead of the crack but should expand much more readily toward the flank regions of the crack where they apparently form the well delineated V-shaped trails of pits and result in effective inelastic crack opening displacements. The portions of the loops expanding ahead of the crack progress only a short distance away from the jagged crack front where they reach the straight border. The portions of the loop initially expanding

backwards towards the flanks must in short order expand further toward both the front and the back of the crack and by a series of multiple cross-slip steps populate the crack tip plastic zone with a high density of dislocation lines.

In addition to the rows of pits associated directly with the arrested crack front a decreasing density of pits were also found on the flank regions behind the arrested crack front, to a distance as far back as 40  $\mu\text{m}$ , where the temperature was 16 K lower than at the arrested crack front. Based on their alignment and on the skewed conical shapes of these pits that indicated the line directions of these intercepted dislocations in their slip planes, it could be ascertained that they were also exclusively on either the  $\alpha$ - or the  $\beta$ -type vertical planes. These pits that were not connected to the arrested crack tip indicated that emission of dislocations from the crack tip had started before the final arrest but that their mobility had been insufficient to keep up with the advancing crack to shield it and to accomplish the arrest at these lower temperatures.

In the central regions of the specimen where plane-strain conditions prevailed there was a near complete absence of etch pits in front of the arrested crack. The explanation for this resides directly with the shapes of the plastic zones of the arrested cracks which will be presented later in §§ 5.1–5.3 below.

Near the free surfaces of the specimens, adjacent to the side grooves where conditions are more akin to plane stress, and the stresses on the oblique planes are considerably higher, a larger density of etch pits was found, which spread both in front and behind the arrested crack. Here, there was also clear evidence of some slip activity on the  $\gamma$  and  $\delta$  oblique planes, in keeping with the favourable energetics of dislocation emission on these planes from the crack tip where it borders on the free surfaces as was expected from the analysis by Xu *et al.* (1997).

The principal observation of these etch pit studies is that in the plane-strain region of the crack tip the arrest is accomplished exclusively by activity on the pairs of  $\alpha$  and  $\beta$  vertical planes on which the kinetically preferred types of dislocation would be of screw nature with the Burgers vector perpendicular to the cleavage surface. As enumerated below in § 5.1, these dislocations have the lowest energy barrier to their nucleation from cleavage ledges and, therefore, appear to dominate the crack arrest process. Thus, the continued emission of these dislocations on to the  $\alpha$  and  $\beta$  planes followed by their multiplication results in effective crack tip blunting. The observed average source spacing of 5  $\mu\text{m}$  is attributed entirely to the characteristic spacing of the larger cleavage surface ledges occurring naturally on the cleavage plane. The spacing of sources corresponded closely to the spacing of these cleavage ledges shown in figure 9. The sawtooth nature of the blunting is observable directly from the shape of the unetched crack front showing the characteristic cusps as illustrated in figure 12 and depicted in the sketch in figure 13.

#### 4.4. Oxide precipitation

While the as-grown silicon boules, received from MEMC, appeared to be completely homogeneous with the trace second constituents of boron and oxygen being in solid solution, considerable oxide precipitation was encountered in the hot zones of the DCB specimens that were routinely subjected to temperatures in the range 800–1000°C at their hot ends for periods of the order of a few hours. Such precipitation in Czochralski-grown silicon crystals has been well documented (Bender and Vanhellemont, 1994). These, quartz-type precipitates of various rod-like and plate-like forms result in considerable levels of misfit stress in their surroundings which are often relieved, at least partially, by one or more misfit dislocation loops surrounding

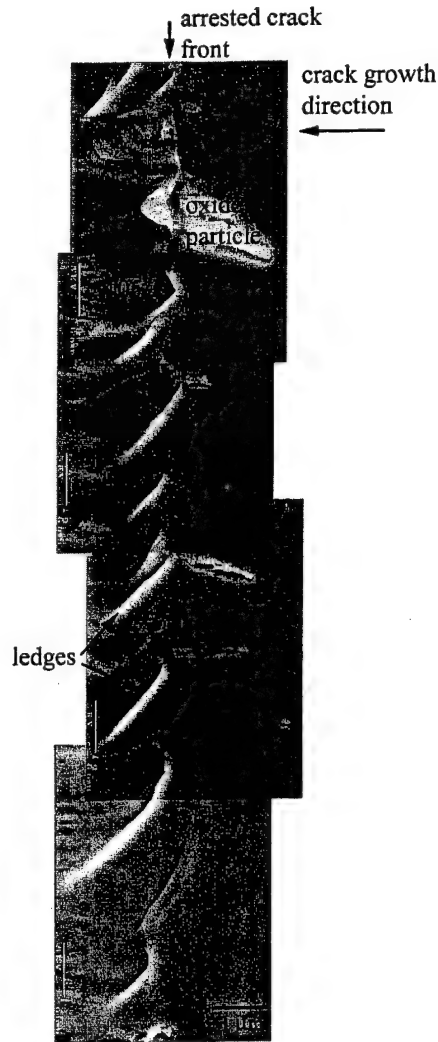


Figure 12. Unetched fracture surface at the crack front in sample 5 showing the sawtooth nature of the crack tip blunting ledges formed by the emitted dislocations. The actual geometry is expected to be altered during the final cleavage fracture at room-temperature separation of the blunted crack front.

them (Tan and Tice, 1976, Tempelhoff *et al.* 1977). A significant concentration of such quartz precipitation was also encountered in the present experiments and the consequences of misfit loop production was studied to some extent to assess any possible role in crack arrest. Even in isolated cases when a quartz precipitate was found on or near the arrested crack front the etch pitting showed no evidence of any important 'catalytic' interaction (Gally 1999). Therefore, these precipitates were ignored in assessing the findings of this study.

#### 4.5. Plastic zones in crack arrest and stress relaxation experiments

As discussed in § 3.6, the shapes of the crack tip plastic zones were revealed in three of the specimens (samples 11, 12 and 13 in table 2) that had undergone stress

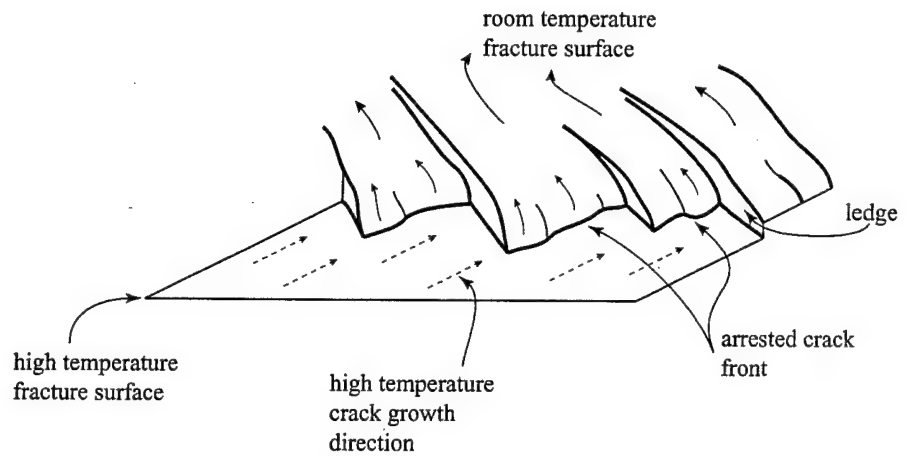


Figure 13. Sketch depicting the nature of the cleavage ledges produced during the final room-temperature separation of the blunted crack front.

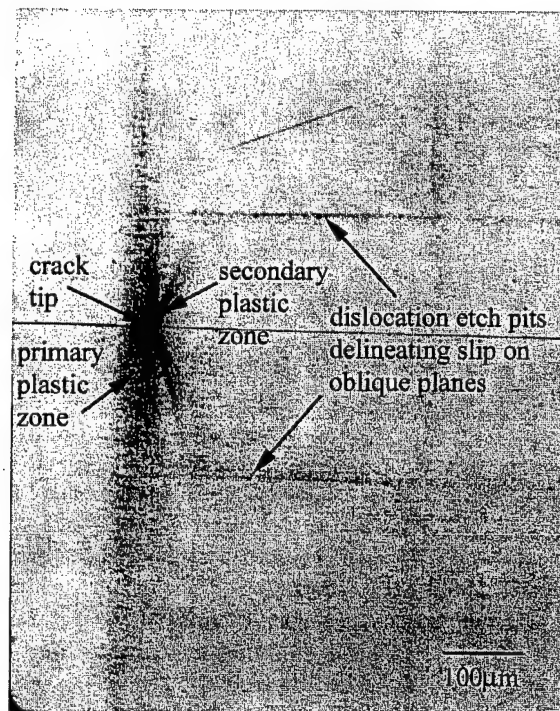


Figure 14. Crack tip stress relaxation zone of sample 12 viewed on a median (001) sectioning plane. The main plastic zone and two small offshoots that had spread vertically away from the cleavage plane are outlined clearly by the etching. The two trails parallel to the crack plane are due to oblique slip plane activity issuing from the side grooves. The dislocation density gradients are analysed in connection with a model in § 5.3. Crack growth was from left to right in the figure.

relaxation. Such samples were cooled to room temperature after the test and sectioned by EDM along a median plane as depicted in figure 3. Upon extensive mechanical polishing to remove the EDM-related damage, the exposed median plane surfaces were etched, outlining the plastic arrest zone as shown in figure 14 for sample 12. The shapes of these arrest zones and their dislocation contents are discussed in detail in § 5.3 and are related to a crack tip zone model presented in § 5.4.

#### 4.6. *Berg-Barrett X-ray topographic imaging of dislocations in the arrest fronts*

While the BB X-ray topographic imaging technique does not have the resolution even of the relatively coarse etch pit technique for observing dislocation structures, in the present situation it proved to be the ideal complement to the etch pitting technique in revealing patterns of dislocation arrangements in depth, below the fracture surface, within a penetration depth of X-rays to nearly 1  $\mu\text{m}$ . The BB technique which has not been favoured in recent experimental research had been investigated extensively in the past (Newkirk 1959, Lang 1973) from both the kinematical and the dynamical diffraction points of view. The present experiments were carried out at the Brookhaven National Laboratory on the National Synchrotron Light Source, utilizing the National Institute of Standards and Technology (NIST) beam line. The most satisfactory BB topographs were obtained from the (333) asymmetric reflections, viewing the cleavage surfaces in the regions of the arrested crack fronts. At the final photographic magnifications of about 20 $\times$ , it was possible in some regions to obtain images of individual dislocations and their characteristic contrast effects, indicating the planes on which they were positioned and their directions into the interior. These observations, however, were of less value than the larger groupings to which we will limit our attention here.

Figure 15(a) shows two (333) topographs of sample 4 (table 1) in an associated but slightly displaced form of both the flank region behind and the region ahead of the arrested crack front, with its gentle curvature of the lagging interior portion.

The outlines of the  $\alpha$  and  $\beta$  planes in the flank region emanating from the crack tip are revealed clearly. In the region ahead of the arrested crack front the arrangement of subsurface curved dislocations appear less regular but some outlines of the vertical  $\alpha$  and  $\beta$  planes are still discernible, albeit obscured by the shapes of the dislocation loops. A region of the crack front of roughly 50  $\mu\text{m}$  thickness appears denuded. This is attributed to a particularly high density of dislocation lines, producing substantial random local lattice rotations which remove this material from the Bragg condition of diffraction from the (333) planes. A more detailed image of the emitted dislocations on a set of the vertical planes at the crack tip of sample 4 is shown in figure 15(b).

A more informative pair of (333) topographs obtained from sample 1 are shown in figures 16(a) and (b). In this sample, after crack arrest, the plastic zone was allowed to enlarge further under constant pin loading conditions in a stress relaxation mode. The arrangement of the subsurface dislocations within the penetration depth of 1  $\mu\text{m}$  in both the forward and the reverse directions, to distances of the order of 2.5–4.0 mm are clearly outlined. The very orderly pattern is made up exclusively of dislocations on the  $\alpha$  and  $\beta$  vertical planes. This demonstrates clearly the rather unique nature of crystal plasticity in the crack arrest plastic zones of these initially dislocation-free single crystals of silicon. The entire pattern of the stored dislocations is made up of a single family with one Burgers vector, reflecting the

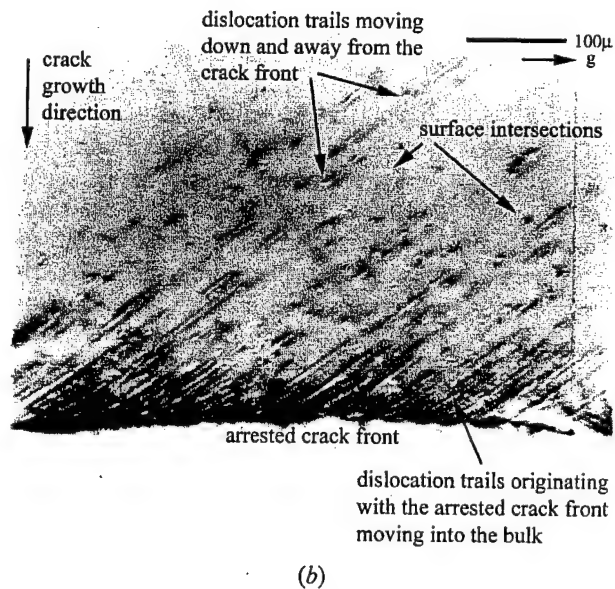
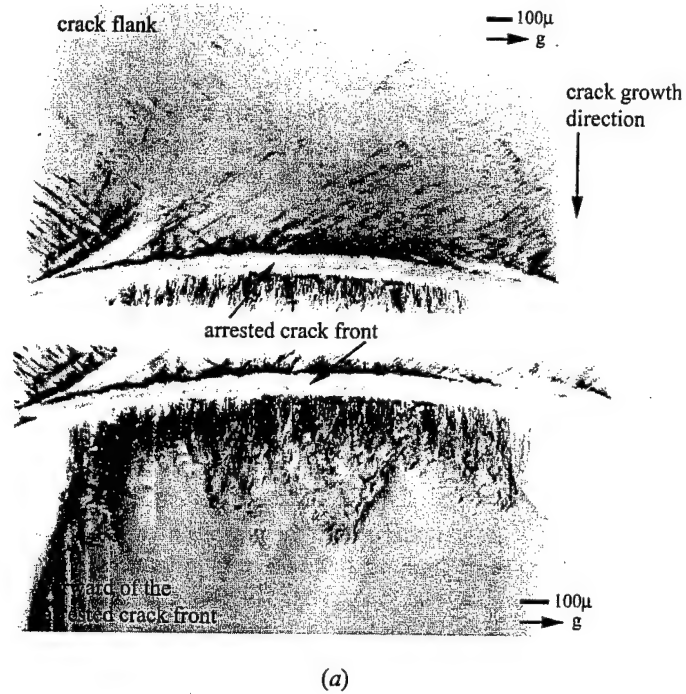


Figure 15. (a) Two BB X-ray topographs of the crack arrest front region of sample 4 formed from (333) diffracting planes. The upper topograph shows the flank region with the  $\alpha$  and  $\beta$  trails of dislocations well delineated. The lower topograph shows the curved subsurface dislocation lines of the  $\alpha$  and  $\beta$  systems ahead of the front of the arrested crack. (b) A different portion of the flank region of the arrested crack in sample 4 showing activity on only one of the sets of  $\alpha$  and  $\beta$  planes.



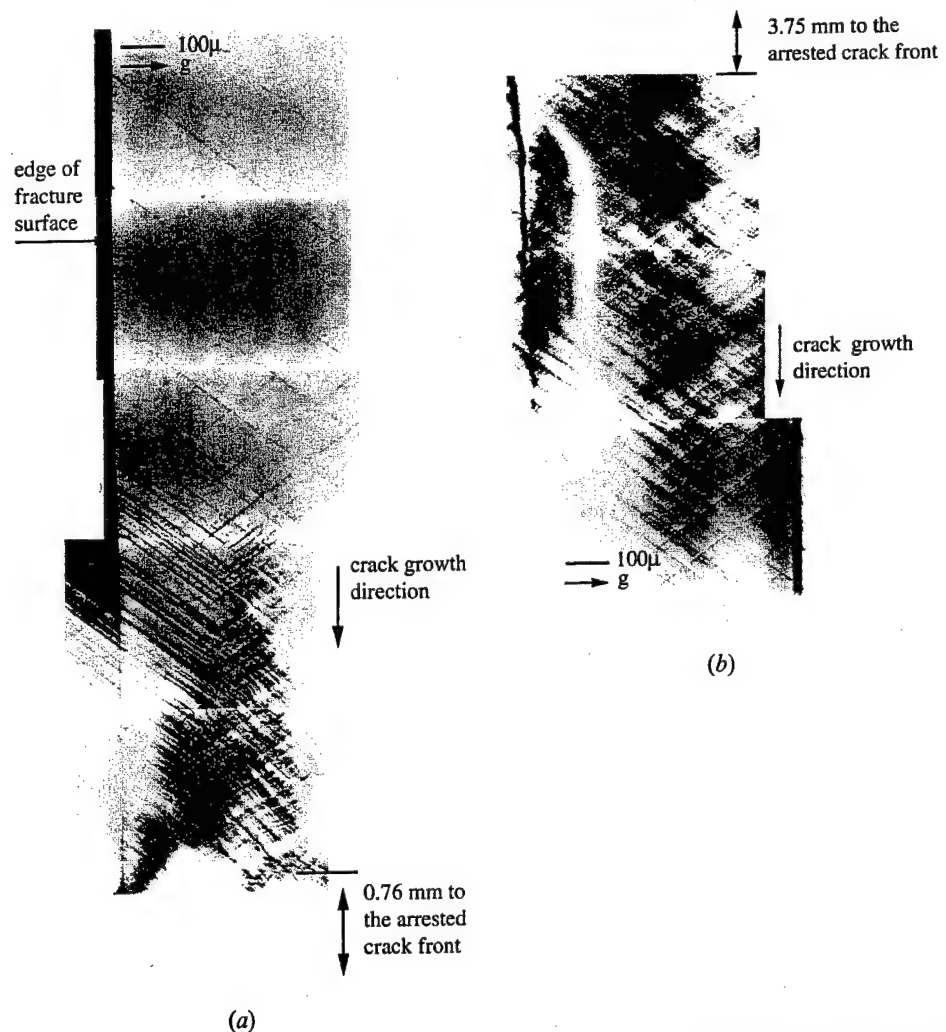


Figure 16. Two complementary BB topographs produced from (333) reflections showing subsurface dislocation patterns in sample 1 that had undergone prolonged stress relaxation after a crack arrest: (a) the dislocation arrangements in the flank regions well behind the crack front; (b) the dislocation arrangements in front of the arrested crack and also well ahead of the crack front. The dislocation density around the crack front was too high to produce resolvable images.

energetically favoured conditions of their emission from the crack tip in a primordial state in the arrest process. These crack tip-emitted dislocations have expanded away from the crack tip and, through numerous steps of multiple cross-slip, have populated the entire plastic zone. No other set of dislocations with other Burgers vectors on other planes were observable.

## § 5. ANALYSIS OF RESULTS

### 5.1. Stresses on active slip systems

Clearly, both the etch pit studies and BB X-ray topographic imaging results indicated that primary slip activity occurred on the vertical  $\alpha$  and  $\beta$  planes of the



Q crack tip slip system configuration (figure 1). There were two alternative slip systems sharing the vertical slip planes in the Q configuration. First was the possibility that slip resulted from screw dislocations with Burgers vectors parallel to the  $[110]$  direction (**CD**, in the Thompson tetrahedron notation) perpendicular to the crack plane and was capable of activating both the  $\alpha$  and the  $\beta$  plane systems. Alternatively, slip could have resulted from  $60^\circ$  mixed dislocations with Burgers vectors parallel to either  $[01\bar{1}]$  or  $[\bar{1}0\bar{1}]$  on the  $(1\bar{1}\bar{1})$  slip planes, or either  $[0\bar{1}\bar{1}]$  or  $[10\bar{1}]$  on  $(\bar{1}\bar{1}\bar{1})$  slip planes. In the Thompson tetrahedron notation these  $60^\circ$  dislocations are designated **AC** and **AD** on ( $\beta$ ) or similarly **BC** and **BD** on ( $\alpha$ ). Recognizing that plastic deformation could only have been accomplished with dislocations nucleated at the crack tip, the former **CD** screw dislocations should have been preferred for three reasons. First, these dislocations would have been nucleated as pure screw dislocations, with significantly lower line energy than the remaining  $60^\circ$  dislocations, which have substantial edge character. Second, the **CD** screw dislocations were likely to have nucleated at crack tip ledges which are potent nucleation sites (Zhou and Thomson, 1991, Xu *et al.* 1997). This would have been less favourable for the  $60^\circ$  dislocations (see § 4.4 of the paper by Xu *et al.* (1997)). Furthermore, nucleation of the latter would have required the creation of a concomitant surface ledge, with a substantial energy cost (Xu *et al.* 1997), making such nucleation unlikely. The **CD** screw dislocations would not have involved such surface production were they nucleated at such cleavage surface ledges. Third, the peak resolved shear stress on the vertical slip planes acting parallel to the  $[110]$  direction is 27% greater than that acting on the  $60^\circ$  mixed dislocations. This is evident from inspection of the levels of resolved shear stresses activating the available slip systems in the Q configuration of the crack tip as we discuss below.

Following the anisotropic elastic crack tip model of Hoenig (1982), the crack tip stress fields of the Q configuration were evaluated utilizing the anisotropic elastic compliances of silicon. The crack tip stress components are given in the 1–3 coordinate system (1 parallel to  $[1\bar{1}0]$ , 2 parallel to  $[110]$  and 3 parallel to  $[001]$ ) as shown in figures 3(a) and (b) in the form:

$$\sigma_{ij} = \frac{K_1}{(2\pi r)^{1/2}} \operatorname{Re} [f_{ij}(\theta, \mu_1, \mu_2)], \quad (8)$$

where  $r$  and  $\theta$  have their usual meanings, and  $\mu_1$  and  $\mu_2$  are complex roots of a characteristic quadratic function of the elastic compliances. How this permits the determination of the specific distributions of shear stress on the potential slip planes is outlined in appendix A, § A.3.

The full plane-strain stress field can be resolved on to the possible  $\alpha$ ,  $\beta$ ,  $\gamma$  and  $\delta$  slip systems yielding equations of the form

$$\sigma_{nm} = \frac{K_1}{(2\pi\rho)^{1/2}} \operatorname{Re} [g_{nm}(\varphi, \psi, \mu_1, \mu_2)], \quad (9)$$

where  $n$  is the slip plane normal,  $m$  is the slip direction parallel to the appropriate Burgers vector,  $g_{nm}$  are the new angle-dependent terms of the resolved shear stress on the slip plane where  $\rho$  and  $\varphi$  are in the slip planes and are analogues to  $r$  and  $\theta$  and, finally,  $\psi$  is the angle between the slip plane and the plane normal to the crack front as seen in figures 3(a) and (b). The factors  $\operatorname{Re}(g_{nm})$  for the resolved shear stresses  $\sigma_{nm}$  were computed with the elastic compliances appropriate for

silicon, that is,  $s_{11} = 0.7685 \times 10^{-11} \text{ Pa}^{-1}$ ,  $s_{12} = -0.2139 \times 10^{-11} \text{ Pa}^{-1}$  and  $s_{44} = 1.2563 \times 10^{-11} \text{ Pa}^{-1}$  (Simons and Wang 1971). The results for the vertical  $\alpha$  and  $\beta$  slip planes are plotted in figures 17(a) and (b), and those on the oblique  $\delta$  and  $\gamma$  planes in figures 18(a) and (b).

While the nucleation of CD-type screw dislocations with Burgers vectors parallel to  $[110]$  should have been preferred, the BB X-ray topography results were unable to differentiate between these screw dislocations and the  $60^\circ$  mixed dislocations of AC or AD type through a standard extinction contrast analysis. Both families of dislocations exhibited extinction contrast on all the surface diffractions taken. In spite of the favourable conditions for the nucleation of CD-type screw dislocations, George and Michot (1993) have reported observing only the  $60^\circ$  mixed dislocations on the vertical  $\alpha$  and  $\beta$  slip planes in the plastic zones of cracks in the Q crack tip configuration. Their experiments were performed, however, on samples of only 0.6 mm thickness as opposed to the 3 mm samples used here. When their Burgers vector analysis could be performed, sufficient plasticity must have developed for the crack tip plane strain stress to relax substantially. This is expected to change significantly the resolved shear stresses activating slip on the various slip systems and may be the explanation for their observations.

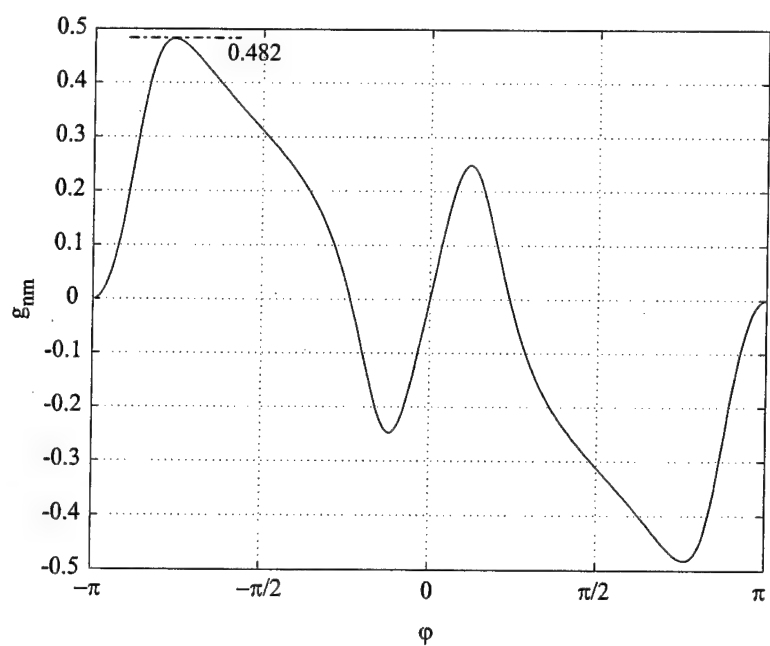
### 5.2. Shapes of emitted dislocation loops

The resolved shear stresses calculated in § 5.1 can also yield information on the initial shapes of expanding dislocation loops which are of particular interest for the CD screw dislocations on the  $\alpha$  and  $\beta$  planes. To a first approximation, dislocations should expand, at least initially, on their slip planes to a shape along which the force acting to expand them is constant. This shape can be obtained by contours of resolved shear stress acting on the slip plane, parallel to the Burgers vector of the dislocation. Such contours can be determined by solving equation (9) for  $\rho(\varphi)$ , resulting in curves for loop shapes given by

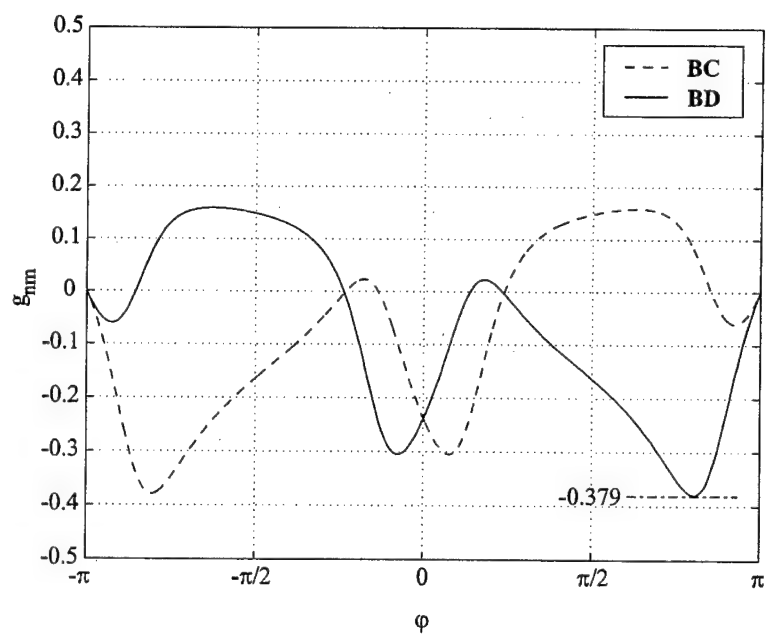
$$\rho_{nm}(\varphi) = \frac{K_1^2}{2\pi\sigma_{nm}^2} \{\text{Re}[g_{nm}(\varphi, \psi, \mu_1, \mu_2)]\}^2. \quad (10)$$

For constant  $K_1$  and  $\sigma_{nm}$  the contours along which the resolved shear stress is constant are given by the square of the angle-dependent term of equation (9),  $\{\text{Re}[g_{nm}(\varphi, \psi, \mu_1, \mu_2)]\}^2$ . The contour for the CD dislocation on the  $\alpha$  or  $\beta$  plane is plotted in figure 19, which is of particular interest to elucidate the etching pattern in figure 11. Subject to the crack tip shear stresses, dislocation lines emitted from the cleavage ledges should begin to expand outward from the crack tip maintaining an approximation to the suggested shapes. Hence, the crack-tip-nucleated CD screw-type dislocations on the vertical slip planes should expand primarily out along the crack flank, as was observed both in the etch pit patterns of figure 11 and in the BB topographic images of figure 15 rather than in front of the arrested crack tip. Furthermore, the dislocation lines should expand into the bulk away from the arrested crack front as was observed in the topographic image of sample 4 in figure 15(b).

Of further interest was the skew symmetry with respect to the crack plane of the resolved shear stress acting on the CD-type screw dislocations on the vertical slip planes. Since dislocation loops with a given Burgers vector could expand only within an angular region where the resolved shear stress was of one sign, loops of this type

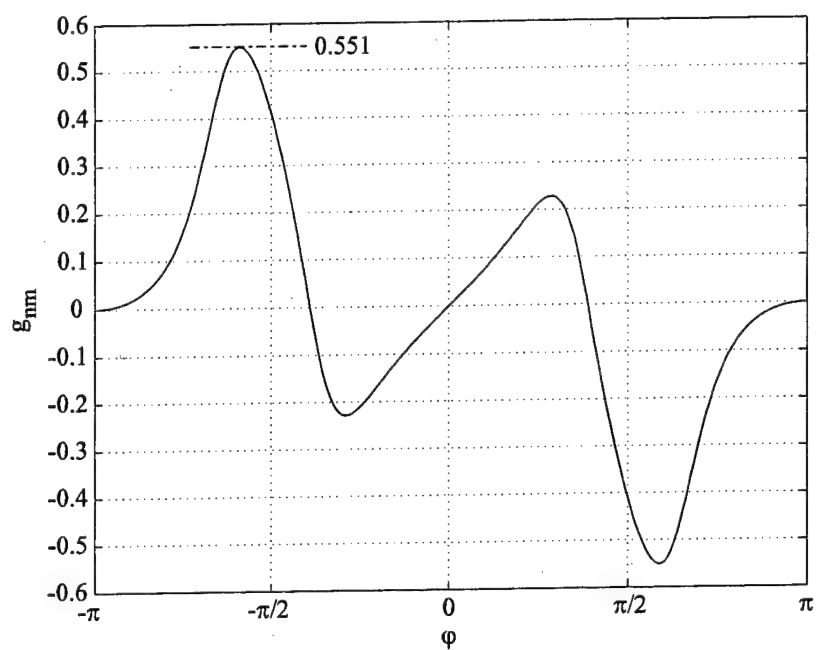


(a)

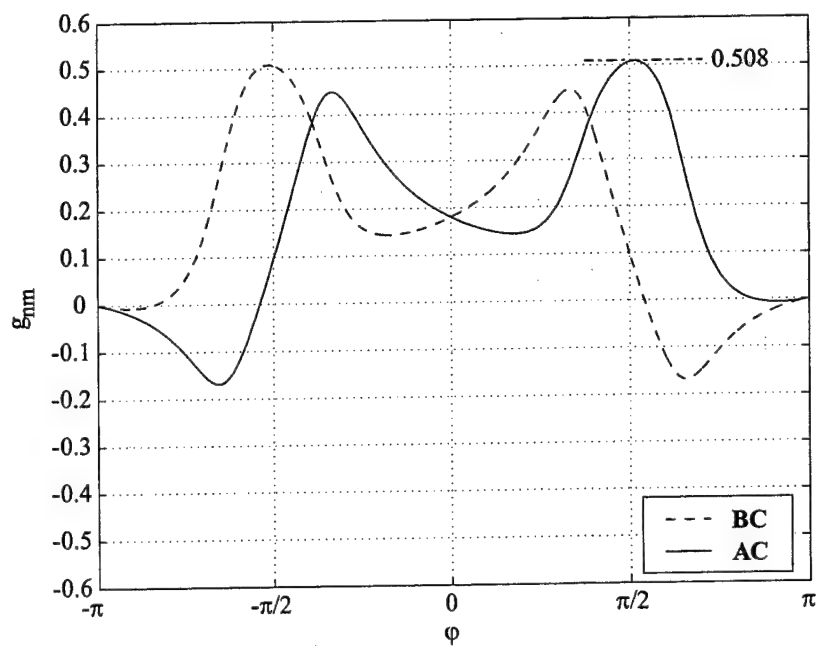


(b)

Figure 17. The angle-dependent stress distribution functions  $g_{nm}(\varphi, \psi, \mu_1, \mu_2)$  of the resolved shear stresses on the vertical  $\alpha$  and  $\beta$  slip planes: (a) for the system with the **CD** dislocation on the  $\alpha$  plane; (b) for the systems with the **BC** or **BD**  $60^\circ$  mixed dislocations on the  $\alpha$  plane. The  $\beta$ -plane distributions will be identical.



(a)



(b)

Figure 18. The angle-dependent stress distribution functions  $g_{nm}(\phi, \psi, \mu_1, \mu_2)$  of the resolved shear stresses on the oblique  $\gamma$  and  $\delta$  slip planes: (a) for the system with the BA dislocations on the  $\delta$  and  $\gamma$  slip planes; (b) for systems with the BC or AC dislocations on the  $\delta$  plane. The  $\gamma$ -plane distributions will be identical.

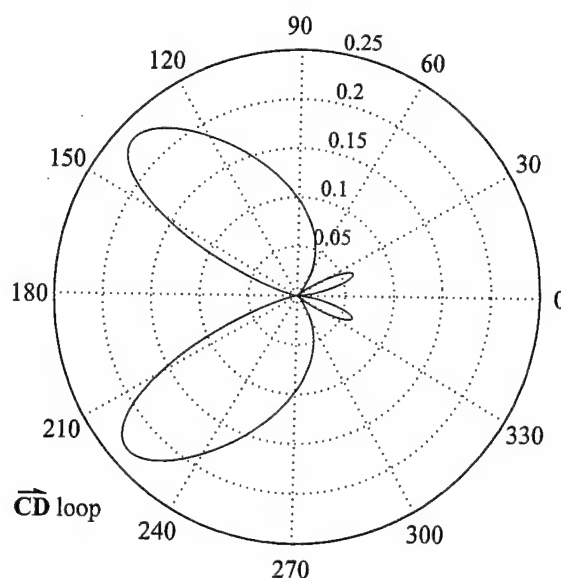


Figure 19. Possible initial shape of a crack-tip-emitted dislocation loop  $\overline{CD}$  calculated on the basis of equation (10). The plane of the figure is that of  $\alpha$  or  $\beta$  plane. The crack extends from the  $180^\circ$  direction towards  $0^\circ$ , with the tip in the centre of the figure.

could not cross the crack plane in front of the crack tip. Therefore, dislocation loops of this type nucleate and expand exclusively on one side of the crack tip, independent of loops on the opposite side of the crack plane. Thus, etch pits of dislocations of this type should not necessarily match across the fracture surface. This was indeed observed. We note that the  $60^\circ$  mixed dislocations, if active, could have bowed out in front of the crack tips and could have formed loop shapes that were continuous across the crack plane. This, however, was not observed.

### 5.3. Dislocation content of crack tip plastic zones in crack arrest and crack tip stress relaxation experiments

As indicated in § 4.5, the shapes of the plastic zones of some of the arrested cracks and three of the experiments that had undergone more or less extensive stress relaxation were probed by sectioning the DCB specimens along their median planes followed by etching. As figure 14 for sample 12 showed, the overwhelming slip activity in the primary plastic zone and its small secondary offshoot were attributable to be on the  $\alpha$  and  $\beta$  vertical planes. Two additional well defined trails of pits parallel to the crack growth direction and at a distance of about  $175\text{ }\mu\text{m}$  away from the trace of the crack plane in figure 14 were attributed to concentrated slip activity on the oblique planes initiated from the root of the side grooves or close to them, where the absence of the plane-strain stress  $\sigma_{33}$  strongly favours such activity as discussed by Xu *et al.* (1997). In two other instances (samples 11 and 13) where the dislocation content of the crack tip plastic zones were sparse, a few other and very lightly populated trails of pits parallel to the crack growth direction were also observable. These represented the only isolated cases where additional sporadic activity on the oblique planes were present. These could all be related to sources within a distance of

about 100  $\mu\text{m}$  of the side grooves where the crack tip stress state departed closer to plane stress than to plane strain.

We note that the plane of symmetry of the crack tip plastic zone outlined by the etch pits is nearly perpendicular to the crack plane but is leaning slightly towards the flank regions of the crack. We take the plane of symmetry of the plastic zone for our analysis to be perpendicular to the crack plane, that is with  $\theta = \pi/2$ . Recalling that the slip activity in these plastic zones is entirely on the  $\alpha$  and  $\beta$  planes and belongs overwhelmingly to the multiplication of the crack-tip-generated CD-type screw dislocations, we conclude that with the multiplicity of repeated double-cross slip events which must have promoted the extension of the plastic zone away from the crack plane, representation of this plasticity requires a more homogenized model rather than the stylized models developed by previous investigators (Brede 1993, Hirsch and Roberts, 1996a). We introduce such a model in § 5.4 below and compare its predictions with the gradients of pit densities in figure 21 also below.

#### 5.4. A model for the crack tip zones for arrested cracks and cracks undergoing stress relaxation

While the unique form of plasticity in these experiments with initially dislocation-free crystals would appear to require a special approach as taken by previous investigators (for example Brede (1993) and Hirsch and Roberts (1996a)) the form of dislocation multiplication that has been noted in the plastic zones would justify a more homogenized deformation approach. As pointed out by Argon *et al.* (1996) in connection with a model of brittle-to-ductile transition experiments of St John (1975), Brede and Haasen (1998) and Hirsch *et al.* (1989), involving stationary cracks, such a homogenized model already exists, developed by Riedel and Rice (RR) (1980) for cracks in creeping solids. In the RR model a singular field solution is provided for stress relaxation around a mode I crack in an elastic solid undergoing power-law creep obeying a constitutive relation of the form

$$\dot{\epsilon}_e^c = \dot{\epsilon}_0(T) \left( \frac{\sigma_e}{\sigma_0} \right)^n, \quad (11)$$

where  $\dot{\epsilon}_e^c$  is the effective steady-state creep rate of the solid subjected to an effective stress  $\sigma_e$  with  $\dot{\epsilon}_0(T)$  and  $\sigma_0$  being normalizing factors that can be fitted to actual material response. In the present case this relation has a direct validation through the comprehensive study of Alexander and Haasen (1968) on silicon and germanium, giving

$$\dot{\epsilon}^c = \alpha \left( \frac{\sigma}{\sigma_0} \right)^3 \exp \left( -\frac{U}{kT} \right), \quad (12)$$

where  $\dot{\epsilon}^c$  is the uniaxial tensile plastic strain rate at steady state flow under an applied tensile stress  $\sigma$  with  $\alpha$  and  $\sigma_0$  being convenient normalization constants and having dimensions of  $\alpha/\sigma_0^3 = 1.34 \times 10^3 \text{ MPa}^{-3} \text{ s}^{-1}$  and  $U = 2.2 - 2.4 \text{ eV}$  being the activation energy of dislocation glide depending on the level of doping. While the relation given by equation (12) is not based on diffusion controlled creep as assumed by RR, its form makes it directly adaptable to the RR model. In the RR model the individual creep strain components at time  $t$  inside the creep zone of a sharp crack subjected at time  $t = 0$  to a mode I stress intensity factor  $K_I$  is given in its adaptation to the crack tip in silicon as

$$\epsilon_{ij}^c = \left( \frac{K_I^2(1-\nu^2)}{EI_n r} \right)^{n/(n+1)} \left[ (n+1) \frac{\alpha t}{\sigma_0^3} \exp \left( -\frac{U}{kT} \right) \right]^{1/(n+1)} \tilde{\epsilon}_{ij}^c(\theta, n), \quad (13)$$

where  $i$  and  $j$  represent the cylindrical coordinates  $r$  and  $\theta$ ,  $I_n$  is an integration constant which has the magnitude of 5.386 for  $n = 3$  (Hutchinson 1968, 1979) and  $\tilde{\epsilon}_{ij}^c(\theta, n)$  are angle-dependent functions representing the distribution of creep strain rate around the mode I crack with well established forms for all integers  $n$  (Hutchinson, 1979). In equation (13),  $E$  and  $\nu$  are Young's modulus and Poisson's ratio for the solid in its isotropic rendering.

Introduction of the ideal cohesive strength  $\sigma_{ic}$  (Rose *et al.* 1981) for cleavage crack propagation under mode I when  $K_I = K_{Ic}$  and  $\sigma_{\theta\theta}$  at  $r = r_c(0(b))$  reaches  $\sigma_{ic}$  gives the distribution of the effective creep strain  $\epsilon_e^c$  in the creep zone at time  $t$  for the present case of silicon with  $n = 3$ , as

$$\epsilon_e^c = \left[ \left( \frac{K_I \sigma_{ic}}{K_{Ic} E} \right)^2 \frac{2\pi(1-\nu^2)}{I_3} \frac{r_c}{r} \right]^{3/4} \left[ 4\alpha t \left( \frac{E}{\sigma_0} \right)^3 \exp \left( \frac{-U}{kT} \right) \right]^{1/4} \tilde{G}(\theta, 3), \quad (14)$$

with the angle-dependent function

$$\tilde{G}(\theta, 3) = \frac{2\tilde{\epsilon}_{r\theta}^c}{3^{1/2}} \left[ 1 + \left( \frac{\tilde{\epsilon}_{\theta\theta}^c}{\tilde{\epsilon}_{r\theta}^c} \right)^2 \right]^{1/2}. \quad (15)$$

The shape and extent of the creep zone in the RR model, interpreted from here on as the *plastic zone*, is formally defined as the region within which the equivalent plastic strain of equation (14) exceeds the equivalent elastic strain of a mode I crack tip, on the simplifying assumption that the inelastic strains inside the plastic zone have no effect upon the surrounding elastic field. To obtain an exact solution for this shape, defined by the equality of the equivalent inelastic and elastic strains, without such an unrealistic assumption, recourse to finite-element methods is required, as was performed by Bassani and McClintock (1981). Thus, defining the tensile effective elastic strain  $\epsilon_e^e$ , as

$$\epsilon_e^e = \frac{1}{3\mu} \left( \frac{3}{2} s_{ij} s_{ij} \right)^{1/2}, \quad (16)$$

where  $s_{ij}$  represents the elements of the deviatoric stress tensor, and using the same normalization factors as in equation (14), the tensile effective elastic strain around a mode I crack can be given as:

$$\epsilon_e^e = \frac{(1+\nu)}{3} \frac{K_I}{K_{Ic}} \frac{\sigma_{ic}}{E} \left( \frac{r_c}{r} \right)^2 \tilde{H}(\theta), \quad (17)$$

with  $\tilde{H}(\theta)$  containing the angle-dependent functions of the mode I crack tip elastic strain field, given in appendix A, § A.4.

Equating the effective strains  $\epsilon_e^c$  and  $\epsilon_e^e$  and solving for the profile of the plastic zone gives

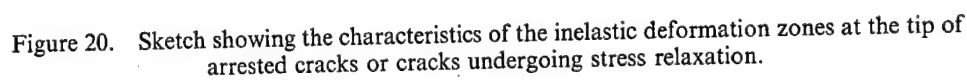
$$\frac{r}{r_c} = \left( \frac{3}{1+\nu} \right)^4 \left( \frac{2\pi(1-\nu^2)}{I_3} \right)^3 \left( \frac{K_I \sigma_{ic}}{K_{Ic} E} \right)^2 \left[ 4\alpha t \left( \frac{E}{\sigma_0} \right)^3 \exp \left( \frac{-U}{kT} \right) \right] \left( \frac{\tilde{G}(\theta, 3)}{\tilde{H}(\theta)} \right)^4. \quad (18)$$

This indicates that, under constant- $K_I$  loading, the plastic zone grows linearly with time, while its shape is determined by the factor  $(\tilde{G}(\theta, 3)/\tilde{H}(\theta))^4$ . The critical angle  $\theta_c$  that maximized  $(\tilde{G}(\theta, 3)/\tilde{H}(\theta))^4$  and defines the principal plane of symmetry

The plastic zone of the RR model then should provide a good representation of the gradients of the dislocation field surrounding the crack tip. In this manner we consider the total shear strain resulting from the emitted crack tip dislocations to be concentrated on the principal plane of shear defined by  $\theta_c$ . The plastic shear strain  $\gamma_{r\theta}$  given by

should then be maximized on this principal plane giving both  $u_\theta$  and  $\partial u_\theta / \partial r = 0$ . The material outside the plastic zone can be approximated to be rigid, along the border OAB of the zone shown in figure 20, in comparison with the much larger plastic strains within the plastic zone. Then, all the inelastic shear displacements within the zone can be considered to accumulate along the border BCO. Integrating the shear displacement increments along this path should then yield a good approximation to the total inelastic crack tip opening displacement. These increments are  $du_r = \gamma_{r\theta}^c(r)r d\theta$  and yield upon integration

where  $2\eta$  is the width of the creep zone at  $r$  (figure 20). If the plastic zone is approximated by an ellipse,  $\eta(r)$  becomes





$$\eta = \frac{R_c}{2} \left[ \frac{r}{R_c} \left( 1 - \frac{r}{R_c} \right) \right]^{1/2}. \quad (21)$$

The inelastic displacement  $u_r(r)$ , at the position  $r$  along the principal shear plane due to the formation of the plastic zone can then be related to the total number  $N(r)$  of dislocations that have traversed beyond  $r$  into the interior, away from the crack tip, by the expression

$$u_r = bN(r), \quad (22)$$

where  $b$  is the Burgers vector of the principal type of dislocation within the plastic zone. On the other hand the shear strain within the plastic zone is determined from the tensile effective plastic strain as

$$\gamma_{r\theta}^c = 2\epsilon_{r\theta}^c = 2\epsilon_e^c \frac{\tilde{\epsilon}_{r\theta}^c(\theta_c, 3)}{\tilde{G}(\theta_c, 3)}. \quad (23)$$

To determine the shear strain within the plastic zone, the expression for the effective tensile plastic strain of equation (14) is combined with the extent of the plastic zone determined from equation (18), by equating  $\theta$  to  $\theta_c = 109^\circ$ , and substituted into equation (23). This yields an expression for the total shear strain within the zone as a function of  $r$  and  $R_c$  in the form of:

$$\gamma_{r\theta}^c = 2 \frac{1+\nu}{3} \frac{K_I}{K_{Ic}} \frac{\sigma_{ic}}{E} \left( \frac{r_c}{R_c} \right)^{1/2} \left( \frac{R_c}{r} \right)^{3/4} \frac{\tilde{H}(\theta_c)}{\tilde{G}(\theta_c, 3)} \tilde{\epsilon}_{r\theta}^c(\theta_c, 3). \quad (24)$$

Within the plastic zone, the inelastic strains are considered to be dominant. To determine the net plastic shear strain  $\gamma_{r\theta}^{cp}$  within the plastic zone, however, the elastic strain  $\gamma_{r\theta}^e(r = R_c)$  at the border must be subtracted, which yields

$$\gamma_{r\theta}^{cp} = 2 \frac{1+\nu}{3} \frac{K_I}{K_{Ic}} \frac{\sigma_{ic}}{E} \left( \frac{r_c}{R_c} \right)^{1/2} \frac{\tilde{H}(\theta_c)}{\tilde{G}(\theta_c, 3)} \tilde{\epsilon}_{r\theta}^c(\theta_c, 3) \left[ \left( \frac{R_c}{r} \right)^{3/4} - 1 \right], \quad (25)$$

where  $\tilde{\epsilon}_{r\theta}^c(\theta_c, 3) = 0.747$  for  $\theta_c = 109^\circ$  (Hutchinson 1968). Then, the total number of dislocations at a distance  $r$  from the crack tip sent into the plastic zone is determined from†

$$N(r) = \frac{u_r(r)}{b} = \frac{2\eta(r)\gamma_{r\theta}^{cp}(r)}{b} = \frac{MR_c}{b} \left[ \frac{r}{R_c} \left( 1 - \frac{r}{R_c} \right) \right]^{1/2} \left[ \left( \frac{R_c}{r} \right)^{3/4} - 1 \right], \quad (26)$$

† We note that as  $r \rightarrow 0$  both  $u_r$  at the crack tip and  $N$  tend towards infinity, owing to the singular nature of the crack tip field in the RR model. Since this singularity is not physical, the value of  $r$  in equations (26) and (29) should be prevented from approaching zero but should instead be cut off at the value of the crack opening displacement, that is at  $r = u_{r\text{tip}}$ . To find this value of  $r$ , equation (26) is solved for  $r$  with  $u_r = r$ . This yields the condition:

$$0 = 1 - 2 \left( \frac{r}{R_c} \right)^{3/4} + \left( \frac{r}{R_c} \right)^{3/2} - \frac{r}{R_c} + 2 \left( \frac{r}{R_c} \right)^{7/4} - \left( 1 + \frac{1}{M^2} \right) \left( \frac{r}{R_c} \right)^{5/2}, \quad (28)$$

from which the effective inelastic crack-tip-opening displacement  $u_{r\text{tip}}$  is obtained, which represents the total number of dislocations emitted from the crack tip and sent into the plastic zone.

where

$$M = 2 \frac{1+\nu}{3} \frac{K_I}{K_{Ic}} \frac{\sigma_{ic}}{E} \left( \frac{r_c}{R_c} \right)^{1/2} \frac{\tilde{H}(\theta_c)}{\tilde{G}(\theta_c, 3)} \tilde{\epsilon}_{r\theta}^c(\theta_c, 3). \quad (27)$$

The negative gradient of equation (26) can be taken as the dislocation density per unit length along the principal shear plane at  $\theta_c$  (the negative sign arises from the convention that the dislocation counting begins at  $R_c$  and increases toward the crack tip). This dislocation density per unit length along  $\theta = \theta_c$  is then given by

$$\frac{-d}{dr} [N(r)] = \frac{M}{4b} \frac{(R_c/r)^{3/4} + (r/R_c)^{1/4} + 2 - r/R_c}{[r/R_c(1 - r/R_c)]^{1/2}}. \quad (29)$$

The results for  $N(r)$  (equation (26)) and  $-(d/dr)N(r)$  (equation (29)) can be compared with values determined from the crack tip stress relaxation experiments. An analysis determining these values is given in § 5.5 below.

### 5.5. Dislocation densities in plastic zones

To determine the dislocation content within the plastic zone expanding around the crack tip during a stress relaxation experiment, dislocation etch pit density information was integrated over the areas of the zone. After sectioning along the (001) median plane and etching, the plastic zone of sample 13 was examined in detail in the scanning electron microscope. Micrographs were taken at grid points superimposed upon the sample, with the etch pit density within each micrograph being determined by individual point counting. Necessarily, more detailed micrographs were required as the crack tip was approached, where finally the density within a few microns of the crack tip was obtained by extrapolation. Along columns of micrographs perpendicular to the crack plane, smooth curves of dislocation etch pit density were fitted to the raw dislocation etch pit density counts. Along the direction perpendicular to the crack plane, the dislocation etch pit density rapidly fell with increasing  $r$ , as expected. The least-squares fit to the data was given by  $\rho = \rho_0(r_0/r)^m$  where  $\rho_0 = 0.736 \times 10^{12} \text{ m}^{-2}$ ,  $r_0 = 5 \times 10^{-5} \text{ m}$  and the exponent  $m = 1.55$  and is shown together with the measured data in figure 21. The curves obtained in this manner were then combined into a single surface utilizing surface interpolation routines which shows also the changes in  $\rho$  in the plastic zone across the thickness of the zone, and is given in figure 22.

The measured dislocation etch pit density from sample 13 was then compared with the results of the model described in § 5.3. First, the dislocation etch pit density was integrated over the entire plastic zone to determine the total number  $N_{\text{pit}}$  of dislocations present in the plastic zone, with the result  $N_{\text{pit}} = 1.45 \times 10^4$ . To calculate  $R_c$  from equation (26),  $N_{\text{pit}}$  is used together with  $r_c = b = 3.83 \text{ \AA}$ , giving  $R_c = 3.23 \times 10^{-4} \text{ m}$ . To obtain this result the following appropriate parameters for silicon were used to evaluate  $M$ , namely  $\nu = 0.215$ ,  $K_{Ic} = 0.89 \text{ MPa m}^{1/2}$ ,  $\sigma_{ic} = 17.7 \text{ GPa}$ ,  $E = 157 \text{ GPa}$ ,  $\tilde{H}(\theta_c) = 2.78$ ,  $\tilde{G}(\theta_c, 3) = 1.02$  and  $\tilde{\epsilon}_{r\theta}^c(\theta_c, 3) = 0.747$ . The experimental conditions specific to sample 13 are listed in table 2. This allows the constitutive equation for silicon, appropriate for these conditions of crack tip stress relaxation to be determined from equation (18). The result was  $\alpha/\sigma_0^3 = 1.60 \text{ MPa}^{-3} \text{ s}^{-1}$ , corresponding to a steady-state creep dislocation density of  $5.86 \times 10^8 \text{ m m}^{-3}$ . These values are several orders of magnitude below the values reported by Alexander and Haasen (1968) of  $\alpha/\sigma_0^3 = 1.34 \times 10^3 \text{ MPa}^{-3} \text{ s}^{-1}$  and a

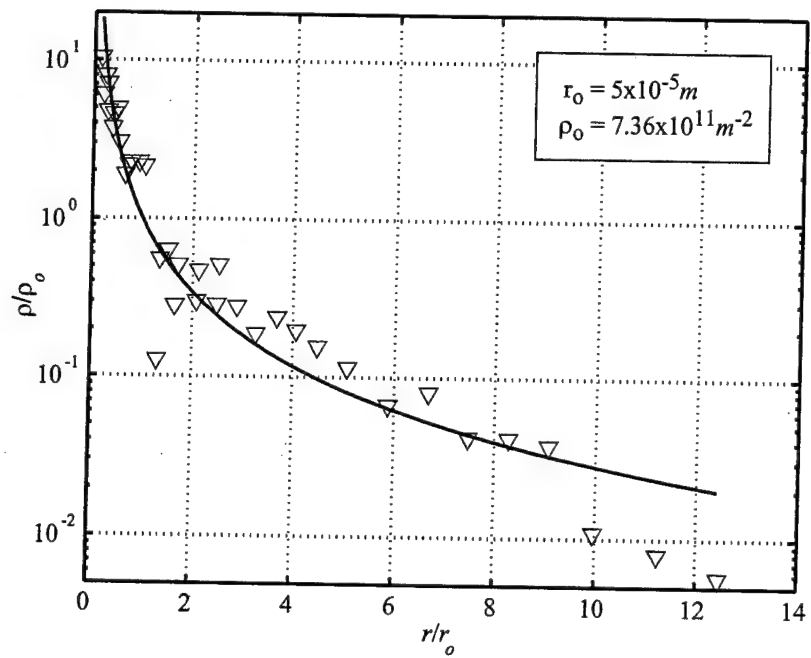


Figure 21. Etch pit density distribution along the spine ( $\theta = \theta_c$ ) of the inelastic deformation zone of sample 13.

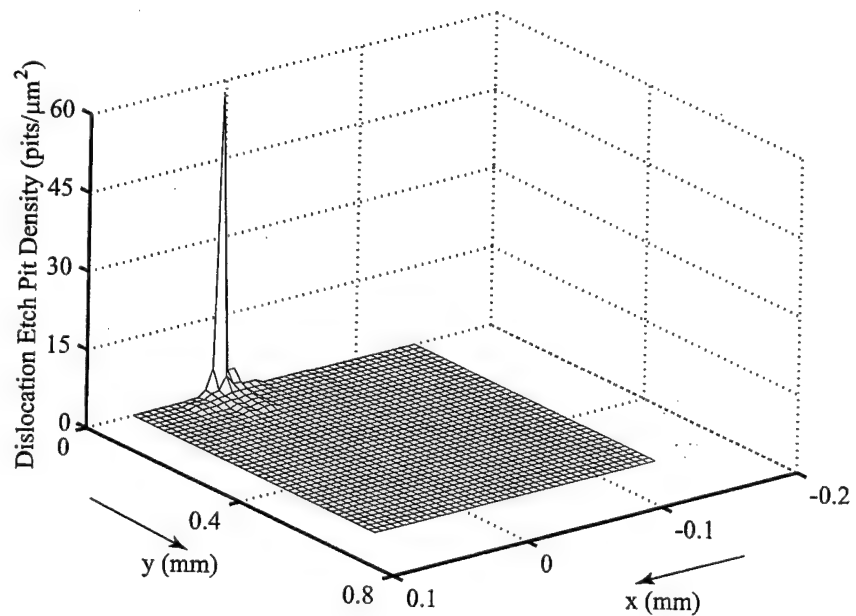


Figure 22. Dislocation (pit) density distribution inside the inelastic deformation zone showing the dislocation gradients, both along the spine of the zone and across the zone.

dislocation density of  $4.9 \times 10^{11} \text{ m}^{-2}$  for conditions of steady-state creep in silicon samples in the same temperature range. This discrepancy, which was encountered earlier by Argon *et al.* (1996) in connection with a model for the brittle-to-ductile transition of fracture in silicon is not surprising. The crack tip plastic zones here, and in all the fracture experiments of previous investigators were undergoing a dynamic process of growth, starting with an initial condition of no dislocation density. Thus, there is no reason to expect that the behaviour had reached a condition of steady state during these stages of crack tip stress relaxation.

The crack-tip-opening displacement  $u_{\text{tip}}$  can now be evaluated both by means of equation (26) or (28) and by the total number  $N_{\text{tip}}$  of dislocations emitted by the crack tip and sent into the plastic zone. Using the above parameters to evaluate  $M = 5.72 \times 10^{-4}$ , and equation (28), results in a value of  $r = u_{\text{tip}} = 8.14 \times 10^{-7} \text{ m}$ . On the other hand, taking  $N(r = u_{\text{tip}}) = 1.45 \times 10^4$  as obtained from integration of dislocation density in the plastic zone from the micrographs results in  $u_{\text{tip}} = 5.55 \times 10^{-6} \text{ m}$ . Considering the nature of the extrapolations needed as the crack tip is approached to obtain  $N_{\text{tip}}$  from the micrographs, the correspondence is pleasing. These results indicate that the crack tip opening  $u_{\text{tip}}$ , which is the displacement resulting from one lobe of the crack tip plastic zone and hence is half the total tip opening displacement, should scale with equation (28); this can be well approximated by

$$0 = 1 - \left(1 + \frac{1}{M^2}\right) \left(\frac{r}{R_c}\right)^{5/2} \quad (30)$$

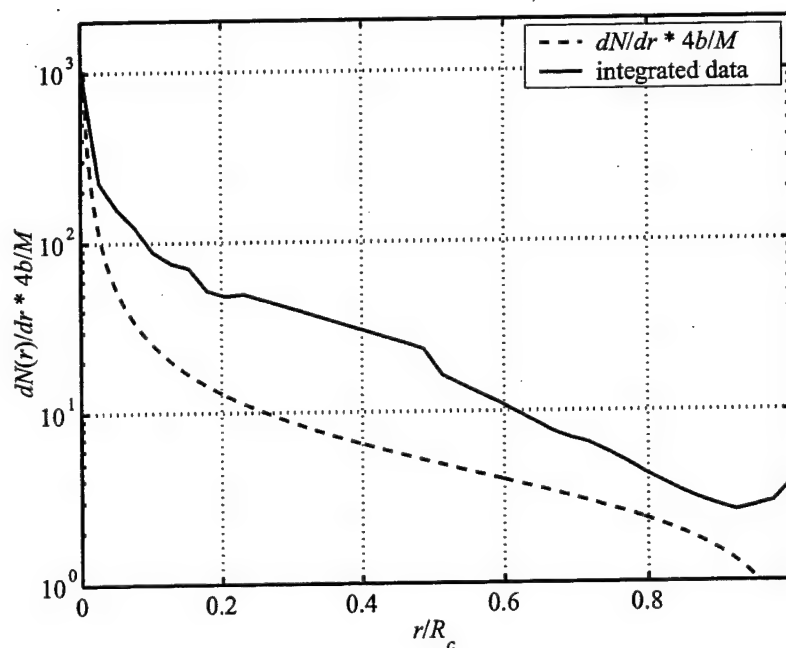


Figure 23. Dislocation etch pit density per unit length along the spine of the plastic zone, comparing the measured dislocation (pit) densities shown in figure 22 with densities assessed from the model of § 5.4.

for small  $M$ , which is indeed the case for these experimental conditions. This more approximate approach predicts that  $u_{\text{tip}} = 8.24 \times 10^{-7}$  m.

The distribution of dislocations within the plastic zone should follow the behaviour determined from equation (29). This was verified by integrating the dislocation etch pit density surface first across the width of the plastic zone, such that the shear of the entire zone is associated with the principal shear plane, and then differentiating this quantity with respect to  $r$ . This yielded a dislocation density per unit length along the principal plane of shear that could be directly compared with equation (29). Both the integrated dislocation density (multiplied by  $4b/M$  to obtain consistent units) and equation (29) are plotted in figure 23. This indicates that the RR development captures the growth characteristics of the crack tip plastic zones quite well for the stress relaxation experiments and those of the more sparsely populated arrest zones, even though dealing with the singular nature of the RR field leads to some imprecision.

### § 6. DISCUSSION

In most of the previous investigations the brittle-to-ductile fracture transition in silicon single crystals (St John, 1975, Brede and Haasen 1988, Hirsch *et al.* 1989, George and Michot 1993) has been studied in a static mode in which at a given temperature the crack driving forces were increased at a constant rate through an applied  $\dot{K}_I$  until either cleavage fracture occurred at a relatively temperature-independent low  $K_{Ic}$  or large scale plastic behaviour occurred without fracture. In this scenario near the brittle-to-ductile transition the crack tip is subjected to a competition between increasing driving force for cleavage and crack tip stress relaxation arising from the sluggish recession of the dislocations emitted from the crack tip. Higher loading rates, that is, higher  $\dot{K}_I$  result in higher  $T_{BD}$  in a systematic manner. The phenomenon in this scenario has been well described and good models of it exist (Brede 1993; Argon *et al.* 1996). While some mechanistic details related to the sites of initiation of the plastic events have been clarified (Hirsch *et al.* 1989, George and Michot 1993), many specific questions related to the selection of slip systems, stages of progress in the development of crack tip shielding and validity of other competing models based on defect mediated melting, and the like (Khantha *et al.* 1994a, 1994b, Khantha and Vitek 1997) could not be readily addressed (Hirsch and Roberts 1996b). Questions related to selection of active slip systems in the crack tip zone have already emerged in the study of George and Michot (1993) which could not be readily dealt with by them.

To satisfy the needs for increased clarity related to the basic mechanisms of the brittle-to-ductile transition a different experimental scenario was introduced by Brede *et al.* (1991) and Hsia and Argon (1994) in which cleavage cracks are propagated up a temperature gradient at given different velocities until they are arrested by thermally initiated processes. In this experiment a mode I crack tip field samples different material 'elements' for certain durations of time at increasingly higher temperatures until the residence time of the crack tip stress field at a material 'element' becomes of the order of the time needed for a fully developed crack tip shielding process to evolve to arrest the crack. Here the arrest process starts from an initial dislocation-free state and goes through well defined stages involving crack tip emission of dislocation embryos which then expand and multiply in an un restrained manner governed only by their mobility in the characteristic overstressed crack tip field. The time required for the full shielding process to evolve decreases

exponentially with increasing temperature, requiring higher temperatures to arrest cleavage cracks with higher velocity. While some early results have been presented in the above-mentioned studies, the scenario had not been developed satisfactorily in these. In the present study of this same scenario we have observed the developments of the arrest process more fully and in greater detail to permit reaching some basic conclusions.

Because of the extreme sensitivity of the growth of brittle cleavage cracks to perturbations of many types the actual experimental arrangement in the present study required the use of more stable DCB samples rather than samples with constant crack tip driving force (constant- $K$  geometry). In this somewhat less ideal arrangement the crack advances in a jerky manner in steps as depicted in figure 8 for a given pin displacement rate, where increasing rates produce progressively shorter residence times of the stepwise advancing crack to material 'elements' of increasing temperatures. Since the arrest of the crack in this dislocation mobility-governed transition phenomenon involves the evolution of a shielding process, the apparently less ideal arrangement has actually proved to be more suitable in the study of the brittle-to-ductile transition. Thus, our experiments have resulted in a number of important findings related to the brittle-to-ductile transition as a rate process. We enumerate these below.

First, through the number of generally successful arrest experiments the expected increase in  $T_{BD}$  with increasing pin displacement rate associated with systematic decreases in the periods of crack jumps was observed and gave an overall activation energy of 1.82 eV for the arrest process. This value of the activation energy is at the very low end of a range of activation energies reported in the literature from a value of 1.8 eV (Kulkarni and Williams 1976) to most of the reported values in the range of 2.2 eV (Imai and Sumino 1983) for dislocation glide in boron-doped silicon.

In the Q configuration involving the propagation of cleavage cracks in the  $\langle 110 \rangle$  direction on the  $\{110\}$  cleavage planes a high degree of slip plane symmetry permits the probing of the arrest process by two alternative sets of symmetrically positioned slip planes in each of which different slip directions can be active. In the first of these a set of oblique planes possesses the highest peak resolved shear stresses but also suffer from a substantial energy barrier to nucleation of dislocations in all their slip directions because of a concomitant need to produce an elementary surface step during the formation of the dislocation embryo which, as shown by Xu *et al.* (1997), increases the saddle point energy quite substantially. In the second set a pair of vertical slip planes making an angle of  $35.2^\circ$  with the crack front have considerably lower peak resolved shear stresses than the oblique planes but have a distinct advantage in possessing the lowest energy barriers to nucleation of dislocation embryos from cleavage ledges since, in at least one system involving also the largest resolved shear stress, there is no concomitant geometrical necessity to produce an elementary free surface as part of the saddle-point configuration.

The detailed etch pit studies of the fracture surfaces of the neighbourhood of the arrested cracks and the BB X-ray topographic images of the subsurface dislocation patterns have demonstrated conclusively that the crack tip plasticity in the arrest phenomenon is exclusively the result of slip activity on the pair of vertical planes that enjoy the significantly lower energy barrier to dislocation emission from the crack tip cleavage ledges. The  $5\text{ }\mu\text{m}$  average spacing along the crack front of active sources indicated by the etch pit studies is in very good agreement with the spacing of the cleavage ledges observable in the Nomarski interference contrast microscopy (figure

9) of cleavage surface features in the flanks prior to the arrest process. The very few instances of activity on the oblique planes could be related directly to the more advantageous emission conditions on these planes near the free surfaces of the specimens, at the side grooves, as indicated by the analysis by Xu *et al.* (1997). These findings reinforce the earlier observations of George and Michot (1993) that in nearly all instances in their experiments, slip activity was not on the systems with the highest resolved shear stress but apparently on the systems that had the lowest energy barriers to dislocation emission from the crack tip. Moreover, A. George (1996, private communication) has noted that a fracture transition can sometimes be entirely overridden with unusually smooth cleavage surfaces.

In the final arrest process when the emitted dislocations (albeit of only one type) fill a plastic shielding zone by a complex process of topological convolutions made possible by multiplicities of double cross slip steps there is a need to deal with the kinematics and the kinetics of the arrest process by more homogenized plasticity models than the more stylized models used in the past (Hirsch *et al.* 1989, Brede, 1993, Hirsch and Roberts, 1996a). We have introduced such a model using the crack tip stress relaxation RR formalism for sharp creep cracks. In an earlier publication (Argon *et al.* 1996) we had demonstrated that this model represents quite well the brittle-to-ductile transition and the dependence of  $T_{BD}$  on  $\dot{K}_I$ . In this study we have demonstrated that it is also fully capable of giving quite good results for the dislocation density gradients in the arrest zones and the key crack tip opening displacements that relate well to the experimental observations.

Finally, we compare our results with the predictions of the defect-mediated melting model of brittle-to-ductile transitions of Khantha, Pope and Vitek (KPV) (1994a, 1994b, 1997) and find that model entirely in conflict with our observations. In the KPV model, large densities of slip dislocation loops are considered to be in thermal equilibrium, akin to thermal equilibria of point defects made possible by large contributions of configurational entropies to the free energy of the collection of defects. An applied shear stress then is thought to make the nucleation of *new loops* (actually always approximated by KPV as two-dimensional dipoles) easier owing to an assumed significant reduction in the elastic properties of the solid containing the assumed high densities of slip loops. Apart from the difficulties of initiating such thermal equilibrium concentrations of loops by processes of homogeneous nucleation in perfect crystals, and having significantly long mean lives to affect the elastic properties, the KPV model would predict activity on all slip systems somewhat in proportion to the level of the resolved shear stresses on these slip systems. This is not what our experiments show. We have demonstrated conclusively that in an initially dislocation-free material the selection of active slip systems is governed by the conditions of emission of dislocations *from the crack tip* where the cleavage surface ledges act as potent sites of heterogeneity for such nucleation. Thus, we find no supporting evidence for the homogeneous nucleation of loops from regions *near but not connected to the crack tip* as considered in the KPV model. While our means of visualization of dislocation patterns were far removed from resolving the assumed large thermal equilibrium concentration of dynamically forming (and collapsing) shear loops postulated in the KPV model, we have found neither any supporting evidence for such populations nor feel any need to invoke them in the brittle-to-ductile transition phenomena that we have reported. Thus, our emphasis is that in silicon (and possibly in all solids with sluggish dislocation mobility) while the brittle-to-ductile transition is ultimately governed by dislocation mobility in the

evolution of the crack tip shielding process, the active dislocations are heterogeneously nucleated at the crack tip from cleavage ledges and are not results of homogeneous nucleation in the interiors from highly stressed regions in the crack tip field, and on all stressed slip systems as viewed by KPV. This is in substantial agreement with the earlier observations of Hirsch *et al.* (1989) and those of George and Michot (1993).

#### ACKNOWLEDGEMENTS

This research has been supported by the Office of Naval Research first through the Applied Mechanics Division and more lately through the Materials Science Division. For their support and continued interest in the research we are grateful to Dr Roshdy Barsoum and Dr George Yoder. We also acknowledge the donation of large boules of highly pedigreed silicon single crystals from MEMC Electronics Materials Inc. for which we are grateful to Dr Harold Korb. Finally, we gratefully acknowledge the key aid of Dr Gabrielle Long and Dr David Black of NIST in helping us to perform the BB X-ray topographic imaging studies of subsurface dislocation patterns at the Brookhaven National Laboratory on the NIST beam line.

#### APPENDIX A

##### § A.1. THE STRESS INTENSITY FINITE-FIELD CORRECTION FACTOR $f(a, w, \lambda)$ OF THE DOUBLE-CANTILEVER-BEAM SPECIMEN (KANNINEN 1973)

The finite-field correction factor  $f(a, w, \lambda)$  for the stress intensity factor  $K_I$  of the DCB specimen configuration of length  $w$ , introduced in connection with equation (1) is given by

$$\begin{aligned}
 f(a, w, \lambda) = & \left( \lambda a \frac{\sinh(\lambda c)^2 + \sin(\lambda c)^2}{\sinh(\lambda c)^2 - \sin(\lambda c)^2} \right. \\
 & + \frac{\sinh(\lambda c) \cosh(\lambda c) - \sin(\lambda c) \cos(\lambda c)}{\sinh(\lambda c)^2 - \sin(\lambda c)^2} \Bigg) \\
 & \times \left( 2(\lambda a)^3 + 6(\lambda a)^2 \frac{\sinh(\lambda c) \cosh(\lambda c) + \sin(\lambda c) \cos(\lambda c)}{\sinh(\lambda c)^2 - \sin(\lambda c)^2} \right. \\
 & + 6\lambda a \frac{\sinh(\lambda c)^2 + \sin(\lambda c)^2}{\sinh(\lambda c)^2 - \sin(\lambda c)^2} \\
 & \left. + 3 \frac{\sinh(\lambda c) \cosh(\lambda c) - \sin(\lambda c) \cos(\lambda c)}{\sinh(\lambda c)^2 - \sin(\lambda c)^2} \right)^{-1}, \quad (A1)
 \end{aligned}$$

with

$$\lambda = \frac{6^{1/4}}{h}, \quad (A2)$$

where  $a$  is the crack length,  $c = w - a$  is the remaining uncracked length and  $h$  is the height of the cantilever arm.



When the DCB specimen contains side grooves reducing the thickness from  $B$  to  $B_n = (B - 2d)$ , there are additional alterations in the finite-field correction factor. This altered factor has been discussed also by Kanninen (1973) but will not be presented here.

§ A.2. FACTOR CORRECTING FOR THE FINITE 'FOUNDATION' STIFFNESS OF THE ARMS IN THE DOUBLE-CANTILEVER-BEAM SPECIMEN (KANNINEN 1973)

The factor  $1/\psi(a, c, \lambda)$  that modifies equation (4) and accounts for the finite stiffness of the foundation of the arms of the DCB specimen is

$$\frac{1}{\psi} = \left( 1 + \frac{3}{\lambda a} \frac{\sinh(\lambda c) \cosh(\lambda c) + \sin(\lambda c) \cos(\lambda c)}{\sinh(\lambda c)^2 - \sin(\lambda c)^2} + \frac{3}{(\lambda a)^2} \frac{\sinh(\lambda c)^2 + \sin(\lambda c)^2}{\sinh(\lambda c)^2 - \sin(\lambda c)^2} + \frac{3}{2} \frac{1}{(\lambda a)^3} \frac{\sinh(\lambda c) \cosh(\lambda c) - \sin(\lambda c) \cos(\lambda c)}{\sinh(\lambda c)^2 - \sin(\lambda c)^2} \right), \quad (\text{A } 3)$$

with  $\lambda$  being as defined by equation (A 2), and where  $c = w - a$  is the remaining uncracked length.

§ A.3. RESOLVED SHEAR STRESS DISTRIBUTIONS AROUND THE CRACK TIP ON THE POTENTIAL SLIP PLANES IN THE Q CRACK CONFIGURATION

In the anisotropic elastic crack tip model of Hoenig (1982) the distribution of stress on specific slip systems is obtained from the solution of a characteristic quadratic equation involving the elastic constants for a condition that  $\text{Im}(\mu_\alpha) > 0$  for  $\alpha = 1, 2$ . For the Q crack tip configuration used in the present experiments this equation is given by:

$$0 = \left[ \frac{1}{2}(s_{11} + s_{12}) + s_{44} \right] x^4 + (3s_{11} - s_{12} - 2s_{44})x^2 + \frac{1}{2}(s_{11} + s_{12}) + s_{44}, \quad (\text{A } 4)$$

with the result that  $\mu_1 = 0.7603 + 0.7079i$  and  $\mu_2 = 0.7063 + 0.7079i$ . The angle-dependent terms  $f_{ij}$ , for the three in-plane components of the crack tip stress field are given by the following expressions:

$$f_{11} = \frac{\mu_2 \mu_1^2}{(\mu_2 - \mu_1)(\cos \theta + \mu_1 \sin \theta)^{1/2}} - \frac{\mu_1 \mu_2^2}{(\mu_2 - \mu_1)(\cos \theta + \mu_2 \sin \theta)}, \quad (\text{A } 5a)$$

$$f_{22} = \frac{\mu_2}{(\mu_2 - \mu_1)(\cos \theta + \mu_1 \sin \theta)^{1/2}} - \frac{\mu_1}{(\mu_2 - \mu_1)(\cos \theta + \mu_2 \sin \theta)}, \quad (\text{A } 5b)$$

$$f_{12} = \frac{\mu_1 \mu_2}{(\mu_2 - \mu_1)(\cos \theta + \mu_1 \sin \theta)^{1/2}} - \frac{\mu_1 \mu_2}{(\mu_2 - \mu_1)(\cos \theta + \mu_2 \sin \theta)^{1/2}}. \quad (\text{A } 5c)$$

Through equation (8) in the text these angle-dependent terms define the in-plane crack tip stresses. For the case of a plane-strain crack tip field, considered here, where the out-of-plane, plane-strain stress  $\sigma_{33}$  also plays a key role, this stress is given by

$$\sigma_{33} = \frac{-s_{12}}{s_{11}} (\sigma_{11} + \sigma_{22}). \quad (\text{A } 6)$$

Then the full plane-strain stress field can be resolved on to the possible  $\alpha$ ,  $\beta$ ,  $\gamma$  and  $\delta$  slip systems yielding equations of the form

$$\sigma_{nm} = \frac{K_1}{(2\pi\rho)^{1/2}} \operatorname{Re} [g_{nm}(\varphi, \psi, \mu_1, \mu_2)], \quad (\text{A } 7)$$

where  $n$  is the slip plane normal,  $m$  is the slip direction parallel to the appropriate Burgers vector,  $g_{nm}$  are the new angle-dependent terms of the resolved shear stress on the slip plane where  $\rho$  and  $\varphi$  are in the slip planes and are analogues to  $r$  and  $\theta$  and, finally,  $\psi$  is the angle between the slip plane and the plane normal to the crack front as seen in figures 3 (a) and (b).

#### § A.4. ANGLE-DEPENDENT FACTOR $\tilde{H}(\theta)$ FOR THE DISTRIBUTION OF EFFECTIVE STRAIN AROUND A MODE I CRACK IN AN ELASTIC SOLID

The factor  $\tilde{H}(\theta)$  introduced in connection with equation (17) can be readily obtained from the well known angle-dependent factors for the mode I elastic strain field and is,

$$\begin{aligned} [\tilde{H}(\theta)]^2 = & \left(8\nu^2 - 16\nu + \frac{19}{2}\right) \left[\cos\left(\frac{\theta}{2}\right)\right]^2 + \left(4\nu^2 - 8\nu + \frac{5}{2}\right) \cos\left(\frac{\theta}{2}\right) \cos\left(\frac{3\theta}{2}\right) \\ & + \frac{3}{2} \left[\cos\left(\frac{3\theta}{2}\right)\right]^2 + 3 \left[\sin\left(\frac{\theta}{2}\right)\right]^2 + 6 \sin\left(\frac{\theta}{2}\right) \sin\left(\frac{3\theta}{2}\right) \\ & + 3 \left[\sin\left(\frac{3\theta}{2}\right)\right]^2. \end{aligned} \quad (\text{A } 8)$$

#### REFERENCES

- ALEXANDER, H., 1986, *Dislocations in Solids*, Vol. 7, edited by F. R. N. Nabarro (Amsterdam: North Holland), p. 113.
- ALEXANDER, H., and HAASEN, P., 1968, *Solid St. Phys.*, **22**, 27.
- ARGON, A. S., XU, G., and ORTIZ, M., 1996, *Cleavage Fracture, George R. Irwin Symposium*, edited by K. S. Chan (Warrendale, Pennsylvania: Metallurgical Society of AIME), p. 125.
- BASSANI, J. L., and MCCLINTOCK, F. A., 1981, *Int. J. Struct.*, **17**, 681.
- BENDER, J. L., and VANHELLEMONT, J., 1994, *Handbook on Semi-Conductors*, Vol. 3, edited by S. Mahajan (Amsterdam: Elsevier), p. 1637.
- BREDE, M., 1993, *Acta metal. mater.*, **41**, 211.
- BREDE, M., and HAASEN, P., 1988, *Acta metal.*, **36**, 2003.
- BREDE, M., HSIA, K. J., and ARGON, A. S., 1991, *J. appl. Phys.*, **70**, 758.
- BULATOV, V. V., YIP, S., and ARGON, A. S., 1995, *Phil. Mag.*, **72**, 453.
- BURNS, S. J., and WEBB, W. W., 1970a, *J. appl. Phys.*, **41**, 2078; 1970b, *ibid.*, **41**, 2086.
- CAI, W., BULATOV, V. V., JUSTO, J. F., ARGON, A. S., and YIP, S., 2000, *Phys. Rev. Lett.*, **84**, 3346.
- GALLY, B. J., 1999, ScD Thesis, Massachusetts Institute of Technology, Cambridge, Massachusetts.
- GEORGE, A., and MICHOT, G., 1993, *Mater. Sci. Engng*, **A164**, 118.
- GILMAN, J. J., KNUDSEN, C., and WALSH, W. P., 1958, *J. appl. Phys.*, **29**, 601.
- HAHN, G. T., AVERBACH, B. L., OWEN, W. S., and COHEN, M., 1959, *Fracture*, edited by B. L. Averbach, D. K. Felbeck, G. T. Hahn and D. A. Thomas (Cambridge, Massachusetts: MIT Press), p. 91.
- HIRSCH, P. B., and ROBERTS, S. G., 1996a, *Cleavage Fracture, George R. Irwin Symposium*, edited by K. S. Chan (Warrendale, Pennsylvania: Metallurgical Society of AIME), p. 137; 1996b, *Acta mater.*, **44**, 2361.

- HIRSCH, P. B., ROBERTS, S. G., and SAMUELS, J., 1989, *Proc. R. Soc. A*, **421**, 25.
- HOENIG, A., 1982, *Engng. Fracture Mech.*, **16**, 363.
- HSIA, K.-J., and ARGON, A. S., 1994, *Mater. Sci. Engng.*, **A176**, 111.
- HUTCHINSON, J. W., 1968, *J. Mech. Phys. Solids*, **16**, 13; 1979, *Non Linear Fracture Mechanics* (Copenhagen: Technical University of Denmark).
- IMAI, M., and SUMINO, K., 1983, *Phil. Mag.*, **47**, 599.
- KANNINEN, M. F., 1973, *Int. J. Fracture*, **9**, 83.
- KANNINEN, M. F., and POPELAR, C. H., 1985, *Advanced Fracture Mechanics* (Oxford: Clarendon).
- KHANTHA, M., POPE, D. P., and VITEK, V., 1994a, *Phys. Rev. Lett.*, **73**, 684; 1994b, *Scripta metal. mater.*, **31**, 1349; 1997, *Acta mater.*, **45**, 4687.
- KHANTHA, M., and VITEK, V., 1997, *Acta mater.*, **45**, 4675.
- KULKARNI, S. B., and WILLIAMS, W. S., 1976, *J. appl. Phys.*, **47**, 4318.
- LANG, A. R., 1973, *Crystal Growth: An Introduction*, edited by P. Hartman, (New York: American Elsevier), p. 444.
- MICHOT, G., 1988, *Cryst. Properties Preparation*, **17-18**, 55.
- NEWKIRK, J. B., 1959, *Trans. Metal. Soc. AIME*, **215**, 483.
- QIAO, Y., and ARGON, A. S., 2001 (to be published).
- RIEDEL, H., and RICE, J. R., 1980, *Proceedings of the 12th National Symposium on Fracture Mechanics*, ASTM Special Technical Publications 700, edited by P. C. Paris (Philadelphia: Pennsylvania: American Society for Testing and Materials), p. 112.
- ROSE, J. H., FERRANTE, J., and SMITH, J. R., 1981, *Phys. Rev. Lett.*, **47**, 675.
- SECCO D ARAGONA, F., 1972, *J. electrochem Soc.*, **119**, 948.
- SIMONS, G., and WANG, H., 1971, *Single Crystals Elastic Constants and Calculated Aggregate Properties*, second edition (Cambridge, Massachusetts: MIT Press).
- ST JOHN, C., 1975, *Phil. Mag.*, **32**, 1193.
- TAN, T. Y., and TICE, W. K., 1976, *Phil. Mag.*, **34**, 615.
- TEMPELHOFF, K., SPIEGELBERG, F., and GLEICHMANN, R., 1977, *Semiconductor Silicon*, 1977, edited by H. R. Huff and E. Sirtl (Pennington, New Jersey: Electrochemical Society), p. 585.
- XU, G., ARGON, A. S., and ORTIZ, M., 1997, *Phil. Mag. B*, **75**, 341.
- ZHOU, S. J., and THOMSON, R., 1991, *J. Mater. Res.*, **6**, 639.

**CLEAVAGE CRACK PROPAGATION RESISTANCE OF GRAIN  
BOUNDARIES IN POLYCRYSTALLINE Fe-2%Si ALLOY:  
EXPERIMENTS AND MODELING**

by Y. Qiao and A. S. Argon<sup>1</sup>

Massachusetts Institute of Technology, Cambridge, MA 02139

**ABSTRACT**

Experiments were carried out on the modes of advance of cleavage cracks through a field of randomly oriented grains at -20C in the pure cleavage range (lower shelf) in very large grain size Fe-2%Si alloy permitting detailed observations of the chronology of percolation of the cleavage crack front across a field of grains. Utilizing previously developed model-based information on the peak resistance to fracture of high angle grain boundaries, producing a given tilt and twist misorientation across them, and detailed measurements of orientations of individual grains in the samples, it was possible to

---

1. Author for correspondence; argon@mit.edu

develop percolation maps of cleavage through the field of grains that paralleled well the experimental observations. On the basis of these experiments and modeling a simple expression is proposed for the effect of grain boundaries on the overall cleavage fracture resistance of low-carbon steel in the lower shelf region.

Additional experiments carried out on medium grain size decarburized 1010 steel with unusually low brittle-to-ductile transition temperature gave very similar results on the mode of percolation of cleavage cracks through grains even though in this case the cleavage propagation was under upper shelf conditions.

Key words: Cleavage in polycrystals; percolation of cleavage through grains; cleavage resistance in the lower shelf

## **1.0 INTRODUCTION**

High angle grain boundaries in steel offer an important resistance to the propagation of cleavage cracks that affects the fracture toughness beneficially, particularly in the brittle-to-ductile transition region. While there has been much emphasis on grain size effects on

the plastic resistance (Hall, 1951; Petch, 1953) and the beneficial effects of grain size reduction on raising the brittle strength are well known (Petch, 1954), the specific role of grain boundaries in affecting cleavage fracture resistance has not been clarified. Based on observations in hydrogen charged Fe-3%Si alloy, Gell and Smith (1966) noted that the resistance of grain boundaries to the transmission of cleavage cracks across them is governed more importantly by the twist misorientation than the tilt misorientation across the boundary. They attributed this to a difficulty in initiating new cleavage cracks in the neighboring grains that would indeed be more strongly influenced by the twist misorientation. Crocker, et al (1996) studied specific forms of break-through across boundaries and classified them into four types related to the observed features of fracture along boundaries. In a quite detailed modeling study Anderson, et al. (1994) considered the mode of propagation of cleavage cracks across hexagonal grains and demonstrated that the cumulative probability of overall fracture in a "weakest link" context of triggering brittle response in structures is directly influenced by the impediments that grain boundaries have on cleavage crack propagation. To our knowledge the only detailed model of the role of grain boundaries on impeding the percolation of cleavage cracks across a field of randomly misoriented grains in steel is that of McClintock (1997). In this he stated a number of criteria of overcoming individual grain boundaries by a quasi-statically advancing cleavage front and calculated the specific work of fracture due

to plastic shear on grain boundaries bridging primary cleavage facets of adjoining cracked grains. There have been no corresponding experimental studies of these phenomena.

In a recent study on the modes of cleavage crack transmission across specific bicrystal grain boundaries in a special Fe-3%Si alloy Argon and Qiao (2002) and Qiao and Argon (2002a) have measured the specific break-through resistances of 17 different high-angle boundaries with random combinations of tilt and twist misorientations and associated these measurements with measurements of fractographic features of these break-through process. The resulting geometrically-based boundary resistance model provided an excellent fit to the measured break-through resistance.

In the present study we have extended the above bicrystal experiments to the growth of cleavage cracks through a field of very coarse grains in a Fe-2%Si alloy and followed the percolation of the cleavage process from grain to grain in considerable detail. These findings have then been incorporated in a model that quite successfully paralleled the experimental observations. On the basis of these findings we have stated a simple relationship for the overall contribution of grain boundaries to cleavage crack-growth-

resistance in the lower shelf region. The experiments and the model are in agreement with many but not all of the predictions of McClintock's (1997) model referred to above.

Finally, to probe the application of our findings to low carbon steels we have carried out experiments on medium grain size decarburized 1010 commercial steel. While this material, in view of its unusually low plastic resistance, had a very low brittle-to-ductile transition temperature, most of the geometrical features of percolation of cleavage fracture through grains were very similar to the observations in the Fe-2%Si coarse grained material, even though in this case such cleavage percolation was representative of conditions at the upper shelf.

In what follows we present our new findings.



## 2.0 EXPERIMENTAL DETAILS

### 2.1 Materials

For the present investigation of the forms of brittle crack propagation across a field of grains in polycrystals, two complementary materials were selected. One was a very coarse-grained Fe-2%Si alloy to complement the previous investigation of the fracture resistance of individual grain boundaries (Argon and Qiao, 2002; Qiao and Argon, 2002a). The other was a fine-grained decarburized 1010 steel. The Fe-2%Si alloy was provided in square pieces cut from hot rolled plates manufactured by Armco Metals of Middlefield, Ohio, with a thickness of approximately 26mm, and lateral dimensions of about 30 by 30cm. The material came from a batch used in an investigation on hot working of metals by Brown, et al. (1989)<sup>1</sup>. In the as received material, there were small carbides of a size below 5 microns. To avoid undesirable interactions of such carbides with brittle crack propagation in the matrix, the material was annealed and decarburized according to a stringent schedule (Birks, 1969; Thelning, 1984) that had been used also in the earlier studies of Argon and Qiao (2002) and Qiao and Argon (2002a). The decarburization schedule consisted of first breaking-down the carbides by a prolonged period of 60 hours

---

1. We are grateful to Professor Anand for making this material available to us.

of soaking the alloy at 1400C in a pure nitrogen environment followed, without interruption, by a holding time of 2.5 hours at 1200C in a hydrogen environment, and ending up with a slow furnace cool to prevent entrapment of and embrittlement with hydrogen. After the decarburization process, no carbides could be observed at fracture surfaces by SEM. The Vickers hardness of this material after the decarburization was 226 Kg/mm<sup>2</sup>. As already stated, the grain size of this alloy was quite coarse and in the range from 3mm to 10mm with a few grains being as large as 30-50mm. Based on the visual examination of low temperature fracture surfaces of individual grains, which will be described in detail in Section 3.1.2 below, the orientation of grains appeared reasonably random. The chemical composition of the Fe-2%Si is given in Table I.

To determine the relevance of the findings on the Fe-2%Si alloy to structural steels, a 1010 steel was chosen as the second material for study. The 1010 steel was provided in the form of rolled plates furnished by Oliver Steel Plate, Inc. of Twinsburg, Ohio. The as received material was in slabs of 26mm thickness and with lateral dimensions of 30 by 60cm, with an original carbon content of about 0.1%. To render this low carbon steel single phase, without a complicating pearlite component, it was subjected to a similar annealing and decarburization process described above for the Fe-2%Si alloy. After the decarburization, the carbon content was reduced to less than 0.05% with all of it being in solution. No car-

bides or a pearlite component could be detected. The grain size of the decarburized 1010 steel was in the range from 20 to 50 microns. Its Vickers hardness at room temperature was 179 Kg/mm<sup>2</sup>.

## 2.2 Specimen preparation

Compact fracture toughness tests (ASTM standard E399) were performed on the decarburized Fe-2%Si alloy. Standard fracture specimens were machined from the material, having dimensions of width  $w = 63.5\text{mm}$ , thickness  $b = 20.3\text{mm}$ , height  $h = 1.2w = 76.2\text{mm}$  and initial crack length,  $a_0$ , in the range of about 39mm. All samples were pre-fatigued to produce well characterized sharp initial pre-cracks.

The decarburized 1010 steel specimens were machined into double-edge cracked plate (DECP) shapes, of width  $w = 19.1\text{mm}$ , thickness  $b = 4.0\text{mm}$ , and initial crack length  $a_0 = 2.5\text{mm}$ . The edge cracks were electrical discharge machined (EDM) in the mid plane of the gauge area by using a 0.1mm copper EDM wire. The machined specimens were annealed for 2 hours at 600C.

## 2.3 Testing procedures

The fracture tests on the compact fracture toughness specimens of Fe-2%Si and DECP specimens of the decarburized 1010 steel were carried out on a Type 5508 Instron machine with a Type 319-007 environmental chamber. The specimens were tested under various temperatures ranging from  $-30^{\circ}\text{C}$  to as high as  $350^{\circ}\text{C}$ . For the high-temperature experiments, the environmental chamber was filled with dry nitrogen gas to prevent oxidization of the fracture surfaces. During the experiments, loads and load-point-displacements were measured and recorded continuously through the machine load cell and the LVDT of the Instron machine. For the compact fracture toughness tests of Fe-2%Si alloy, the temperature range covered entire set of phenomena of a pure-cleavage to mixed-cleavage transition behavior around  $0^{\circ}\text{C}$ , to the conventional brittle-to-ductile transition temperature at around  $250^{\circ}\text{C}$  and up to  $350^{\circ}\text{C}$ .

For the fracture tests on the DECP specimens of decarburized 1010 steel, to reach the lowest possible temperature, a cryogenically rated solenoid valve controlled by an Omega JK12 controller was installed in the piping system of liquid nitrogen to control the low temperature nitrogen gas flow into the chamber responding to the feedback signals from the thermocouple directly attached to the specimen surface. For these lowest temperature tests the commercial temperature controlling system of the chamber was deactivated.

Temperature uniformity in the DECP specimens was reached typically within 15 minutes. However, as already stated above, due to the very low carbon content in the decarburized 1010 steel and the absence of other hardening agents, even at the lower limit of  $-150^{\circ}\text{C}$  of this special environmental chamber the fracture behavior of the material remained to be above its brittle-to-ductile transition temperature

## **2.4 Methods of fracture surface characterization**

To study the forms of interaction between propagating cleavage cracks and grain boundaries, fracture surfaces across the field of fractured grains of three of the Fe-2%Si specimens were characterized in detail. For this purpose a special device was produced to measure the tilt and twist orientation of cleavage fracture surfaces of each individual grain with respect to the lateral specimen surface and the median geometrical plane of the desired crack propagation. The device is shown in Fig.1. The stage of a stereo microscope was replaced by a double-angle vise having a base capable of rotating  $360^{\circ}$  about a vertical axis (x) and able to incline from horizontal by  $45^{\circ}$  up or down about an axis (y), with attached goniometers permitting the rotation angles to be measured to within  $\pm 0.5^{\circ}$ . A parallel light source was fixed on the frame of the stereo microscope as shown in the figure. The system was first calibrated by means of a mirror placed in such a position as to

reflect the light from the light source into the microscope tube along its optic axis. Then the mirror was replaced by the fractured specimen to be characterized. By rotating the vise along the x- and y- axes, the position of the specimen was adjusted so that cleavage facets of each individual grain reflected the light into the microscope. In this way the tilt and twist angles for each grain in the fracture field relative to the external specimen axis could be measured and recorded. The relative tilt and twist angles between individual grains across their common grain boundaries could then be readily calculated from this information.

Through viewing the cleavage surfaces of each grain of the fractured coarse-grained Fe-2%Si alloy, the break-through patterns and river markings could be determined to establish in each case the grain boundary which was penetrated-through first by the propagating cleavage crack. The results were reported as fracture propagation maps to be presented below.

### 3.0 EXPERIMENTAL RESULTS

#### 3.1 Temperature dependence of plastic resistances

Since the key to the brittle-to-ductile transition behavior of metals and alloys, particularly the two iron based materials of Fe-2%Si and the decarburized 1010 steel, is governed primarily by the temperature dependence of their plastic resistance, this information was established first. Figure 2 shows the results for these two materials. The information on the Fe-2%Si alloy was obtained by re-scaling the corresponding information of the Fe-3%Si alloy reported by Qiao and Argon (2002a). The re-scaling was accomplished on the basis of the ratio of the Vickers hardnesses of these two alloys at room temperature. The information on the decarburized 1010 steel was developed through direct determination of the stress-strain behavior of this material in tension experiments carried out at different temperatures, in the same environmental chamber discussed above.

Examination of Fig.2 shows immediately that the expected brittle-to-ductile transition temperature of the two materials will be radically different, based primarily on the temperature dependence of their plastic resistance, as we will amplify further in Section 5.3. The horizontal dotted line related to the curve for the Fe-2%Si alloy together with the large

scatter at low temperatures results from the widespread twinning in the single crystals of the Fe-3%Si alloy tested in a multiple slip orientation that was reported in the previous study. From that study it is also known that the temperature dependent yield stress curve and the corresponding fracture stress curve come together around 680MPa and -60C, indicating that under these conditions yielding and fracture are synonymous. From this we estimate the brittle strength of the Fe-3%Si alloy to be 680MPa and assume that this magnitude should also be close to the brittle strength of the very coarse grained Fe-2%Si alloy of interest to us here. Noting that the average grain size of the Fe-2%Si alloy samples was around 4mm and that of the 1010 steel was around 50 microns, and that the brittle strength should scale inversely with the square root of the grains size, we estimate the brittle strength of the decarburized 1010 steel to be well above 1.0GPa.

Parenthetically, we note that after decarburization, with its very low carbon content it is improper to refer to the decarburized 1010 steel as a steel. It should best be referred to as commercial purity iron. Nevertheless, because of its original designation we will continue to refer to it as decarburized 1010 steel.

### **3.2 Compact fracture experiments on the Fe-2%Si alloy**



Figure 3 shows the dependence on temperature of the measured  $K_{IC}$  fracture toughness of the Fe-2%Si alloy. The figure shows clearly two kinds of fracture work transition, one at around 0C and the other at around 250C. The first, and the one involving the small change in fracture work at 0C was identified to be the pure-cleavage to mixed-cleavage (PC/MC) transition reported by Qiao and Argon (2002a) in their experimental study of fracture resistance of individual bicrystals in Fe-3%Si alloy. In that study it was found that below the transition temperature when a cleavage crack breaks through a grain boundary into a neighboring grain, the break-through occurs at roughly evenly spaced "gates" and forms a tiered cleavage surface in the adjoining grain, resulting in a set of quasi-regularly spaced cleavage strips resembling a staircase with the descent angle of the staircase being governed primarily by the twist misorientation of cleavage planes across the boundary. In the transit of the cleavage crack across the grain boundary the peak cracking resistance is governed by the rate of increase of: a) primarily the additional cleavage surface production in the adjoining grain; and b) secondarily, the increase in plastic shearing work at the grain boundary along the cleavage steps. Above the PC/MC transition, the geometrical features of the transit of the cleavage crack appear nearly identical to those below the fracture transition, but additional plastic work is involved in sigmoidal plastic bending of ligaments between the cleavage strips in the adjoining grain before the ligaments are eventually severed by cleavage, with the additional plastic bending of the ligaments accounting for the

increment in fracture work, over and above, that in the pure cleavage range below the fracture transition. The changed appearance of these is shown in Fig.3.

Figure 4 shows a SEM micrograph of the fracture surface below the PC/MC transition in the present studies with two grain boundaries that have been traversed, while Fig.5 shows a representative area of the fracture surface above the PC/MC transition where in addition to the cleavage surfaces of the tiered fracture in grains, noted in the bicrystal study now manifesting themselves as well delineated river markings, also a coarse form of undercutting of adjoining cleavage processes near grain boundaries is visible which is associated with plastic bending of a coarser set of ligaments. The appearance of the fracture surfaces remain substantially unchanged from that shown in Fig.5 between the PC/MC transition temperature and the traditional BD transition around 250C. Figure 6 shows a prominent example of fracture of a remaining coarse ligament between two substantially offset cleavage strips in a grain where the mutual undercutting of the cleavage processes was followed by considerable sigmoidal plastic bending before eventually a complex cleavage-like fracture process severed the ligament. Another source of considerable additional fracture work, over and above the average fracture work of cracks traversing grain boundaries, is that which is involved when a small fraction of "recalcitrant" grain boundaries eventually give way with considerable complex ductile shearing, after the main fracture front across

grains has gone around them and left them behind. An example of the break-down of such a recalcitrant grain boundary is shown in Fig.7.

Figure 3 shows considerable scatter in the measured  $K_{IC}$  results in the plateau region between the two fracture transitions. This is a direct result of the very coarse grain size in the alloy, making variations between different compact fracture samples large. These variations are less a result of variation of average grain size, but are rather due to the very small number of grains across the critical fracture front where the crack started growing unstably. Thus, between different fracture samples there are large variations in the number of grains across the thickness along the fracture front and their respective twist and tilt misorientations across the front in the direction of overall crack growth. These discrete events and how the main crack percolates through the field of grains is discussed in more detail below in Sections 4.2-4.4.

Finally, Fig.8 shows a region of the fracture surface immediately above the BD transition temperature with a mixture of ductile dimple type separation and continued cleavage type separation. In fact this feature of a strong persistence of cleavage fracture among ductile dimple type fracture remained up to 350C, well above the BD transition, and reflected the

strong tendency to cleavage of grains in this upper shelf behavior even after considerable plastic flow in this strongly solid solution strengthened alloy.

### 3.3 Fracture experiments on the decarburized 1010 steel

The temperature dependence of the fracture toughness tests on the decarburized 1010 steel is given in Fig.9. Because of the relatively very low plastic resistance of this material the fracture resistance as determined from the DECP samples is given by the *plane stress J*-integral value,  $J_{IC}$ , according to well established procedure (Kumar, et al. 1981). Clearly, in the temperature range between -150C and 150C the material is well above its conventional brittle-to-ductile transition temperature indicated by the micrograph of Fig.10 of the fracture surface at -100C, showing an area of ductile dimple type separation among cracked grains. On the whole, however, as Fig.9 indicates, the fracture surface appearance is nearly completely of cleavage type and remains so up to -50C. This is more clearly demonstrated by the fractographs of Figs.11a-11c showing representative fracture surfaces at -125C, -70C, and -40C. This upper shelf cleavage response is indicative of the intrinsically brittle nature of Fe where a terminal cleavage mode of separation can still occur after substantial plastic work, and signals a possibility of a troubling tendency to terminal brittle behavior in large structures.

The *plane stress* fracture toughness values  $J_{IC}$  referred in Fig.9 in the entire temperature range of -150C to 150C are very large, primarily because of the very low plastic resistance of the material devoid of any significant hardening agent and the quite elevated brittle strength estimated to be above 1.0GPa resulting from the moderately small grain size. This has made the DECP sample configuration with the grain dimensions used in this study, more in the nature of a stubby tension specimen, rather than a fracture toughness specimen. Nevertheless, the behavior represented in Fig.9 is that of a very tough, albeit quite soft material in the near-cryogenic temperature range. We discuss this behavior further in Section 5.3 in comparison with the behavior of the Fe-2%Si alloy.

## **4.0 MODELS FOR PERCOLATION OF A CLEAVAGE FRONT THROUGH GRAINS**

### **4.1 Topological features**

A subject of primary interest in the present study was the topology of the forms of percolation of a cleavage fracture front through a field of grains and the overall fracture resis-

tance that arises from this process. For this purpose, a number of Fe-2%Si compact fracture mechanics samples were prepared and were fractured in a manner of ASTM standard E339. While the very coarse-grained nature of this material resulted in considerable scatter in the determination of fracture toughness as we indicated in Section 3.2, this feature was particularly convenient for the detailed study of the percolation of the cleavage front among grains. Such compact fracture experiments were performed at  $-30^{\circ}\text{C}$ ,  $0^{\circ}\text{C}$  and  $21^{\circ}\text{C}$ . Here we will follow only the features of the percolation of the crack front in the experiment carried out in the pure cleavage realm of  $-30^{\circ}\text{C}$ . During the experiment the crack opening load and the crack opening displacement were recorded. As in other such experiments, it was noted that the crack advanced in a jerky manner, involving, on the average, 3 jumps before full separation of the entire specimen occurred. While plastic dissipation at the arrest fronts was slight, through inspection of the field of cleaved grains after the experiment was over, and from the increased compliance of the compact fracture specimen after each jerky advance it was relatively easy to identify the fronts of crack arrest.

The actual mode of advance of the cleavage front among grains was readily possible by studying the patterns of cleavage river markings inside grains. While this process could not identify the position of the crack front at given times it did identify the actual percola-

tion features of the local crack advance direction from grain to grain. Several detailed features of this advance proved to be interesting and amenable to some detailed modeling as we present in Section 4.3 below.

On the basis of the earlier bicrystal study where it was established that the primary resistance to crack advance is the resistance of boundaries to the passage of cleavage cracks across them, it was assumed in the present study also that once a cleavage crack penetrated into a grain it would traverse through it nearly instantaneously in comparison to the time spent in overcoming the grain boundaries. In a jerky advance step the crack front traverses across a significant number of grains in very close succession, making inertial effects likely to be important in this process. Nevertheless, in our considerations we ignore these and treat the crack advance as quasi-static. In this idealization at any stage the further advance of the crack will depend on the local distribution of the momentary crack tip stress intensity  $K_I$ . As a further step in the idealization we note that because of the random misorientation of cracked grains immediately behind the crack front the cracked cleavage planes will be misoriented in relation to the average plane of cracking making the "driving forces" at the crack front to be of mixed mode. In our consideration, however, we also ignore this mixed mode nature of advance and consider only the distribution of the local crack tip mode I stress intensity,  $K_I$ , as if the cracked portion of material immediately

behind the crack front was flat and in the average plane of the advancing crack. Clearly, these simplifications compromise the accuracy of the model that we present in Section 4.3 with the consequences becoming observable in comparison between model results and actual observations. Finally, the advance of the crack front at any particular grain boundary along the front will depend both on the driving forces and the fracture resistance of the boundary. Noting these provisos there are still a number of important observations possible on the topology of the crack advance. These we enumerate below.

We consider a generic square-shaped grain ABCD in the path of the crack front as shown in the cases depicted in Fig.12, where the shaded region represents the cracked regions immediately behind the crack front. In the case of Fig.12a the crack front encounters and exposes a grain that will be subjected to a significant concentration of local  $K_I$ , it then enters the grain from the exposed boundaries AB, BC, and CD simultaneously, or in quick succession. In the case of Fig.12b the crack front encounters a particularly weak grain boundary BC and penetrates through it. While the stress intensity along boundaries BA, AD and DC will be significantly lower because of the re-entrant nature of the initial penetration, the front may still penetrate these boundaries and fan-out from there toward the front and the sides of the grain if the strength of these boundaries are lower than the adjoining boundaries OB and CP along the crack front. When the generic grain occupies a



corner position along the crack front as shown in Figs.12c-12e, the corner will again be subjected to a significant excess of the driving force. In this case several possibilities were found to occur. If boundary AB is tougher than the average, the crack will, as depicted by Fig.12c, penetrate the grain through the boundary BC first and shear boundary AB later which would be subjected to a significant mode III driving force. In most cases, however, if the toughness of boundaries AB and BC are close together the crack front can penetrate the grain through these boundaries in quick succession as depicted in Fig.12d. Other more complex penetrations were also observed occasionally. Whenever the generic grain is penetrated from more than one side more complex river markings are produced in the grain, making a unique determination of sequences of penetration difficult. While all these modes of cracking of grains were observed, the dominant process was the entry of the main crack into a particular grain across only one boundary as we discuss in Section 4.2 below.

In some instances, as already mentioned above, a particular grain boundary may be too tough to be penetrated by the main crack front. Then the front will surround the grain and the "recalcitrant" grain boundary, and leave it behind to be subjected to high levels of combined mode II and mode III, resulting in eventual overcoming of the boundary by a combination of shear deformation and fracture. Our estimates indicate that the contribu-

tion to the overall work of fracture of such tough grain boundaries are significant, and that roughly a fraction of 10%-15% of grain boundary line length exposed by the penetrating crack front is of this type.

#### **4.2 A detailed history of percolation of a cleavage front through a field of grains**

We now consider in some detail the percolation of a specific cleavage front through a field of very coarse grains in a standard compact sample fractured at  $-30^{\circ}\text{C}$ . Figure 13 shows a

macrograph of the fracture surface in this sample (DC01) of Fe-2%Si alloy. River mark-

ings in some grains are discernible in the figure but were very clearly observable in all

cases under moderate magnification. In this particular sample 78 individual grains were

identified between the initial crack tip of the compact fracture sample, along the left bor-

der, and a final region close to the other border of the sample. Some grains in the upper

and lower right side of the field were not identified as well as some grains at the far right

edge. In these regions the crack had been growing already unstably where further details

were not of interest. The individual tilt and twist angles of the principal cleavage plane of

each grain relative to the external borders of the sample were measured with the special

modified stereo microscope illustrated in Fig.1. These angles in degrees are listed in Table

II for all the 78 grains that were tagged. Figure 14 depicts how the orientational relations

of these tilt and twist angles relative to the normal of the median plane to the crack and the crack growth direction were obtained.

Figure 15 shows a cleavage front percolation map of the crack penetrations into each grain in this sample. The left border of the figure is the initial macro crack tip cut into the compact fracture sample. The solid arrows, based on a detailed study of the river markings fanning-out from grain boundaries, indicate the direction from which the individual grain was penetrated. While this penetration was in many instances from only one direction, there was a number of grains that showed multiplicities of river markings indicating simultaneous, or nearly simultaneous, penetration of the grain from more than one direction. The arrow map shows the spatially complex form of the percolation process. Two specific fronts A-A and B-B have been identified by heavy zig-zag lines. These are two fronts of arrest of the jerkily advancing crack, as best as they could be related to the externally monitored crack opening force/displacement information. The final propagation of the crack front beyond the B-B line was in one unstable step. As explained in more detail in the crack front advance model in Section 4.3 it was of interest to glean some insight into the further advance of the crack front from lines A-A and B-B. For this purpose the local mode I crack driving force,  $K_I$ , was calculated along the jagged arrested crack front using Rice's (1985) variational method according to the relation

$$K(z) = K^0[z; a(z)] + \frac{1}{2\pi} \int \frac{K^0[z'; a(z)] \cdot [a(z') - a(z)]}{(z' - z)^2} dz' \quad (1)$$

where  $a(z)$  is the crack length at location  $z$  along the direction parallel to the sample thickness and roughly parallel to the arrested crack front,  $K^0[z; a(z)]$  is the local mode I stress intensity factor at location  $z$  in relation to a virtual reference straight crack-front-segment at  $a(z)$  under the same remote load. In the evaluation of the integral the principal value was taken, and the upper and lower integration limits were taken as 0 and  $h$ , respectively, where  $h$  is the specimen thickness. The result of such an evaluation is shown in Figs. 16a and 16b for the crack fronts AA and BB respectively. The cuspy contours indicate the distribution of the local  $K_I(z)/K_0$  normalized with the overall stress intensity based on the increased specimen compliance. It is seen that the local driving forces for further crack advance are highest at the exposed corners while re-entrant corners are protected, as can be expected. The actual local choice for further penetration of the crack front depends also on the fracture resistance of the individual grain boundaries along the front. Nevertheless, there is a satisfactory correspondence between the level of the driving force and the direction of the further crack advance. The dotted stepped contour across each grain boundary represents the actual local energy release rate (or work of fracture) for a virtual extension

of the crack across the specific grain boundaries determinable from the character of the grain boundary.

A number of statistical observations related to the percolation map of Fig.15 are of interest. Many of the projected grain boundary lines are kinky and some of them have substantial curvature indicating that the grain boundary energy was far from isotropic. Not counting the edges of grains that were free surfaces, the 78 grains possessed 397 edges indicating that the average number of edges of a typical grain was 5.09 rather than 6.0. The frequency distribution of numbers of edges of grains is given in Fig.17. The arrow map of Fig.15 indicates that of the 78 grains 67 were penetrated only through one grain boundary while 11 were penetrated from 2 grain boundaries. This indicates that only 89 grain boundary penetrations governed the form of percolation of the cleavage front across the grains in the particular field. Since each of the 397 boundaries are shared by two grains only a fraction of 0.45 of the boundaries had played a role in the percolation map and the remaining fraction of 0.55 of boundaries separate already cracked grains and must be sheared by a mixture of modes II and III involving a combination of plastic shear and shear fracture. Clearly, of the relatively small number of grains that take part in the percolation process fully 8% of grain edges in the field represented free borders. This makes the statistical information not representative of a large fracture surface in a small-grained

polycrystalline sample. Nevertheless, this information will be useful in reaching some overall conclusions which we will develop in Section 5.

#### **4.3 Modeling the percolation of cleavage fracture fronts through a field of grains**

A special program was developed to model the percolation of a cleavage front in polycrystalline material. The principal assumptions of the model were outlined in Section 4.1 above. The specific grain structure used in the model was that of the compact fracture specimen DC01 of the Fe-2%Si alloy fractured under -30C and examined in detail in Section 4.2 above. The size and shape of each grain was taken from the macrograph of Fig.13 and the graphical depiction of it in Fig.15. The required misorientation angles of the most appropriate cleavage planes of each grain were those listed in Table II.

The initial straight crack front is that given by the left border of the grain field map of Fig.15. The plane of the pre-crack was considered to be in the median plane of the compact specimen. At the beginning of each propagation step, the effective local crack driving force  $K_i$  and the local fracture resistance  $G_{IC}^{(i)}$  of each individual grain boundary  $i$  ( $i = 1, 2, \dots$ ) at the crack front were calculated. The effective crack driving force  $K_i$  was taken to be the line average of the local stress intensity factor  $K(z)$  along the part of the crack front at

the grain boundary of interest. The first-order variation method developed by Rice (1985) was used to calculate  $K(z)$ , according to the expression of Eqn.(1) given in Section 4.2 above. In the numerical integration along the whole crack front, the Romberg algorithm was used.

The local fracture resistance  $G_{ICB}$  of an individual grain boundary used in the model was calculated according to a relationship developed for bicrystal grain boundaries in a previous study for a Fe-3%Si alloy (Qiao and Argon, 2002a) given by:

$$\frac{G_{ICGB}}{G_{IC}} = \frac{1}{(\cos \psi)^2} (\sin \varphi + \cos \varphi) + C \cdot \frac{\sin \varphi \cos \varphi}{\cos \psi} \quad (2)$$

where  $G_{IC}$  is the average work of cleavage fracture inside individual grains and  $C$  is a material constant combining some geometrical features of the topography of the cleavage surface of a grain interior with the shear resistance of the boundary, leading to an estimated value of 0.25 according to a best fit to experimental measurements. The angles  $\psi$  and  $\varphi$  are tilt and twist angles of the adjoining grains across the shared grain boundary and the orientation of the cleavage surface in the grain to be penetrated by the crack front,

respectively. These angles are related to the external angles  $\varphi_0$  and  $\psi_0$  reported in Table

II by expressions:

$$\tan \psi = \frac{l_1 \cot \varphi_0 + l_2 \cot \psi_0 + l_3}{n_1 \cot \varphi_0 + n_2 \cot \psi_0 + n_3} \quad (3a)$$

$$\tan \varphi = \frac{m_1 \cot \varphi_0 + m_2 \cot \psi_0 + m_3}{n_1 \cot \varphi_0 + n_2 \cot \psi_0 + n_3} \quad (3b)$$

where

$$l_1 = \cos \psi_1 \cos \alpha - \cos \varphi_1 \sin \psi_1 \sin \alpha \quad (4a)$$

$$l_2 = -\cos \psi_1 \sin \alpha - \cos \varphi_1 \sin \psi_1 \cos \alpha \quad (4b)$$

$$l_3 = \sin \varphi_1 \sin \psi_1 \quad (4c)$$

$$m_1 = \sin \psi_1 \cos \alpha + \cos \varphi_1 \cos \psi_1 \sin \alpha \quad (4d)$$

$$m_2 = -\sin \psi_1 \sin \alpha + \cos \varphi_1 \cos \psi_1 \cos \alpha \quad (4e)$$

$$m_3 = -\sin \varphi_1 \sin \psi_1 \quad (4f)$$

$$n_1 = \sin \varphi_1 \sin \alpha, n_2 = \sin \varphi_1 \cos \alpha, n_3 = \cos \varphi_1 \quad (4g)$$

with  $\alpha$  being the angle between the grain boundary line on the fracture plane and the z-

axis, and  $\varphi_1$  and  $\psi_1$  being the twist and tilt angles of the cracked grain immediately

behind the crack front.



The ratio of  $K_i/K_{IC}^{(i)}$  (where  $K_{IC}^{(i)} = \sqrt{\frac{EG_{IC}^{(i)}}{(1-\nu^2)}}$ ) of each grain boundary along the crack front was considered and the grain boundary with the largest value of the ratio was taken as the one to be penetrated through first by the propagating crack. A factor  $Q$  was determined which makes this largest value unity, and was then used to determine the overall applied stress intensity factor  $K_I$  on the global sample to advance the crack front through the grain. The propagation of the cleavage crack inside the grain was assumed to be instantaneous, advancing the crack front in the grain of interest. After the grain under consideration was cracked, a new crack front was formed by replacing locally the penetrated grain boundary by the boundaries of the same grain that were not at the initial crack front. Then, the  $K_i$ 's and  $K_{IC}^{(i)}$ 's along the new crack front were calculated and the similar procedure was repeated until all the grains in the specimen were cracked. This procedure established the form of percolation of the crack front through the collection of grains under the provisos of ignoring possible modes II and III as stated above. Based on this procedure, a fracture map was produced and is indicated by the dotted arrows in Fig.18 for each grain. When compared with the experimental arrow map of Fig.15 it is clear that for the first several columns of grains, the model results matched quite well the experimental results. About 70% of the arrows were predicted correctly. However, with continued propagation of the crack, accumulating errors and the increasing complexity of the crack front shape made the model results increasingly less accurate relative to the experimental observa-

tions. In the last several columns of grains, only less than 10% of arrows were predicted correctly. This eventual lack of agreement is attributed primarily to the fact that the local crack driving force at grain boundaries is in reality of mixed mode and not merely of the mode I type, and secondarily to the fact that in this terminal sweep of the cleavage front quasi-static conditions will no longer prevail.

#### **4.4 Model of total work of cleavage through a field of grains**

In Section 4.3 we considered only a model of the percolation of the cleavage process through the field of grains to parallel the observed percolation arrow map of Fig.15. In this section we develop a model to account for the entire work of cleavage fracture in the pure-cleavage (PC) domain at very low temperature where additional plastic dissipation is minimal, but shear fractures along bridging grain boundaries become important. We then project this model to the range of mixed-cleavage (MC) above the pure-cleavage to mixed-cleavage (PC/MC) fracture transition.

We base our model on the basic observations described in Section 4.2 which indicated that in the majority of cases (86% of the time) the cleavage front enters a specific grain from only one neighboring grain. Figure 19a shows a basic set of processes necessary to

account for the overall work of cleavage where we idealize outlines of individual grains as square shaped. The arrows show a scheme of spreading of the cleavage front and the boundaries from which the arrows emanate. The spreading requires a special scenario of penetration of a cleavage front across a boundary separating two grains with a combination of tilt and twist misorientation of the cleavage planes across the boundary plane. This specific scenario and the associated resistance of the boundary to the penetration of the cleavage front across it was discussed in detail by us earlier (Qiao and Argon, 2002a).

We identify three separate and distinct contributions to the overall cleavage work per unit area of projected median macro crack plane that we view as the extension of the plane of the cleavage crack depicted in Fig.19a. The first contribution is the cleavage work across the faces of the grains 1-6 in the figure where each cleavage plane ( $j$ ) has a specific tilt,  $\psi_0^j$ , and twist  $\phi_0^j$  misorientation angle with respect to the median macro crack plane. These angles are listed in Table II for the specific case of grains shown in Fig.15, that we will study. The second contribution is the fracture work across the primary boundaries of percolation of the cleavage front, i.e. those from which the arrows emanate in Fig.19a. This work of break-through of the primary boundaries was discussed in detail in a

previous study referred to earlier (Qiao and Argon, 2002a). The third contribution is the subsequent work of separation by a combination of some plastic shear and shear fracture along the boundaries between adjacent grains that have already been cleaved apart, such as the boundaries between grains 1-2, 5-6, and 2-4 depicted in Fig.19a. Of these the boundary between 2-4 might be a tougher than average recalcitrant boundary that gives way after it is fully surrounded by cleaved grains. For ease of accounting we depict these three contributions for a generic square grain in Fig.19b, where the three contributions to the cleavage fracture work are associated with the corresponding numbers.

The fracture work across grain faces is taken as

$$W_1 = \frac{G_{IC}}{\cos \psi_0^j \cos \phi_0^j} (C_s D^2) \quad (5)$$

where  $G_{IC}$  is the specific cleavage work of fracture in a reference grain with cleavage plane exactly parallel to the median macro-cleavage plane, and the angles  $\psi_0^j$  of tilt and  $\phi_0^j$  of twist of the specific grain ( $j$ ) are given relative to the reference axes of Fig.14, with  $C_s D^2$  being the projected area of the cleavage plane ( $j$ ) of the grain facet on the median plane. In Eqn.(5)  $D$  is taken as the length of the grain boundary in the reference

square grain, and  $C_s$  is a constant determined by grain shape, which is unity for square grains and  $\frac{2}{\sqrt{3}}$  for hexagonal grains.

The work of fracture associated with the break-through of a grain boundary is taken as

$$W_2 = G_{IC} \left[ \frac{1}{(\cos \psi)^2} (\sin \phi + \cos \phi) + C \cdot \frac{\sin \phi \cos \phi}{\cos \psi} \right] \cdot D \Delta x_c \quad (6)$$

where the angles  $\psi_i$  and  $\phi_i$  are the tilt and twist misorientation angles of the cleavage planes across the boundary ( $i$ ) as considered in Eqs.(3a) and (3b), the dimensionless constant  $C$  made up of details of shear displacement along the boundary, *cleavage-like* shear fracture resistance of the boundary, microstructural features of the cleavage river markings inside grains and some related coefficients, all defined in the previous study of break-through-resistance of bicrystal boundaries (Qiao and Argon, 2002a). It is taken as 0.25 on the basis of a single principal fit between experimental measurements and the model of that study, in the range of pure cleavage behavior. The distance  $\Delta x_c$ , as depicted in Fig.19b, is the critical average distance of penetration of a reference cleavage front across a grain boundary where the boundary break-through resistance reaches its peak value. This model-sensitive distance is considered to scale with the grain size  $D$  for

small grain sizes but is expected to be constant for very large grains. It will be assigned a specific magnitude in our model as we discuss below.

Finally, the work of separation of the boundaries left behind by the penetrating cleavage front is taken as:

$$W_3 = Dk^*\delta_c\Delta h \quad (7)$$

where  $\delta_c$  is a critical "preparatory" opening displacement of cleavage planes at the grain boundary plane as depicted in Fig.20b where the boundary separation acquires a "cleavage-like" shear fracture along the average distance  $\Delta h$  between the cleavage planes of the already cleaved adjoining grains, and  $k^*$  is the "cleavage-like" shear fracture resistance of the boundary. The boundary length to be shared by the grains is taken as  $D$  rather than  $2D$ , since each lateral grain boundary of a grain to be sheared is shared by two adjoining grains. Clearly, this process of boundary separation involves a mixture of modes II and III of the "cleavage-like" shear fracture and must also depend on the angle of inclination of the boundary with the median macro crack plane. The micrograph of Fig.21 shows the appearance of such a boundary separated by a combination of shear (the major portion of clearly shown shear markings) and a complex fracture process (identified with the arrow). McClintock (1997) has developed a more detailed model of

this bridging shear fracture based on earlier slip line field analysis (McClintock and Clerico, 1980) which results in very similar observations but using a considerably different scenario of separation involving only plastic "shearing off". None of these details which can be expected to be quite model-sensitive and variable from boundary to boundary will be developed further. Rather, as had been done in the previous study of cracking across bicrystal boundaries, referred to above, we introduce a dimensionless parameter  $B$  that normalizes this work of separation with the principal specific cleavage work  $G_{IC}$  as

$$B = \frac{k^* \delta_c \xi}{G_{IC}} \quad (8)$$

where

$$\xi = \frac{\Delta h}{D} \quad (9)$$

is the ratio of the average vertical separation  $\Delta h$  between the cleavage planes of the adjacent grains to the mean (square) grain size. This latter ratio can be expected to depend on the angles of misorientation between the cleavage planes of the adjoining grains. Moreover, as depicted more realistically in Fig.19a, the distance  $\Delta h$  locally should depend on the distance  $x$  of penetration of the cleavage front across the two adjoining grains and the separation should have a mixed mode character of II and III of fracture as noted above, since none of this detail is realistically amenable to analysis for

every boundary, as must be clear, the choice of a single average fitting parameter  $B$  becomes very attractive. Thus, combining these three contributions into a single specific cleavage work,  $G_{ICPC}$ , of the *polycrystal* median fracture plane, in units of the basic work of cleavage,  $G_{IC}$ , of a reference grain of no misorientation gives

$$\frac{G_{ICPC}}{G_{IC}} = \left\langle \frac{C_s}{\cos \psi_0^j \cos \phi_0^j} \right\rangle + \left\langle \frac{\Delta x_c}{D} \left[ \frac{1}{(\cos \psi)^2} (\sin \phi + \cos \phi) + C \cdot \frac{\sin \phi \cos \phi}{\cos \psi} \right] \right\rangle + B \quad (10)$$

where the brackets across the first and second terms on the RHS of Eqn.(10) indicate an orientation average of all possible cases of sampling of grains of random orientation. Rather than develop this expression as given, we consider a model of the above ratio for each grain in the specific case of the polycrystal field considered in Fig.15 and obtain the cumulative work of fracture for the quasi-statically advancing cleavage front according to the modeled percolation map of Fig.18. The result of this model, following along the same set of steps developed in Section 4.3 for the determination of the percolation arrow map of Fig.18, is shown in Fig.22. In the model, the critical penetration depth  $\Delta x_c$  for break-through of a grain boundary was taken as  $10\mu\text{m}$  for the very coarse-grained material modeled here. Since in the present case the average grain sizes were in the range of  $4\text{mm}$  the ratio  $\Delta x_c/D$  becomes roughly  $0.0025$ , making the contribution of the second term in Eqn.(10) negligible for such large grain size material. As stated above, for very



fine grain material, we assume that  $\Delta x_c$  should become proportional to the grain size, where the second term in the RHS of Eqn.(10) will make a non-negligible contribution. It was found that if  $B$  is in the range from 2.0 to 3.0, the model results produce a very good fit to the experimentally observed fracture toughness.

Parenthetically, we note that the choice of the magnitude of the constant  $B$  as about 2.5, and taking  $\delta_c \approx \Delta x_c = 10\mu\text{m}$ ,  $\Delta h/D \approx 0.5$  and  $G_{IC} = 230\text{J/m}^2$ , derived from the average fracture toughness of  $7.3\text{MPa}\sqrt{\text{m}}$ , measured in a thermal crack-arrest experiment in single crystals of Fe-3%Si alloy (Qiao and Argon, 2002b), would give for the “cleavage-like” shear resistance  $k^*$  a value of about 115MPa. This value of  $k^*$  is in the range of the plastic shear resistance of the alloy under consideration and indicates that the shear fracture process along the bridging grain boundaries could have a substantial plastic shear character, as shown in Fig.21 and very similar to what was considered by McClintock and Clerico (1980).

## 5. DISCUSSION

## 5.1 Contribution of grain boundaries to the cleavage resistance

Based on the detailed considerations of the percolation of cleavage fracture across a field of grains in the coarse-grained Fe-2%Si alloy discussed in Section 4.2 and the models of the percolation map and work of fracture developed in Sections 4.3 and 4.4, it becomes possible to state a general expression for the contribution of grain boundaries to the overall work of fracture of a polycrystal in the extreme lower shelf region of fracture, labelled by us as pure cleavage (PC) fracture. The expression we propose is a generalization of Eqn.(10), benefiting from the numerical model of Section 4.4. For this purpose we re-state Eqn.(10) in its final form below as:

$$\frac{G_{ICPC}}{G_{IC}} = \left\langle \frac{C_s}{\cos \psi_0^j \cos \varphi_0^j} \right\rangle + \alpha \beta \left( \frac{\Delta x_c}{D} \right) \left\langle \frac{1}{(\cos \psi)^2} (\sin \varphi + \cos \varphi) + C \cdot \frac{\sin \varphi \cos \varphi}{\cos \psi} \right\rangle + B \quad (11)$$

In Eqn.(11) in the first term on the RHS  $C_s = 2/\sqrt{3}$  is a factor correcting for hexagonal-shaped grain intersections over the square-shaped grain facets considered in the preliminary rough model; the orientation average of the projection product in brackets is readily evaluated as 1.26. In the second term  $\alpha = \sqrt{3}$  is the ratio of the average grain diameter to the grain edge length of a hexagonal grain and the factor  $\beta = 1.14$  accounts

for the fact that in 14% of cases in the simulation a cleavage crack enters a grain through two faces nearly simultaneously; the orientation average of the term in brackets can be taken as 1.61, as the average value of this factor determined in a previous study of cleavage cracking resistance of bicrystal boundaries (Qiao and Argon, 2002a). The ratio  $\Delta x_c/D$  in this term remains somewhat elusive since the effective penetration distance  $\Delta x_c$  across a boundary where the peak resistance is encountered can only be conjectured.

We have arbitrarily considered this dimension to be around  $10\mu\text{m}$  for very large grains with  $D \gg \Delta x_c$ . As stated above, however, we consider the ratio  $\Delta x_c/D$  to remain a constant for  $D \leq 10\mu\text{m}$ . In any event we note that the second term is the only one with a grain size dependence, which becomes negligible for very large grain sizes and becomes grain size independent for medium to small grain size material. Finally, as discussed in Section 4.4 above, we have chosen the magnitude of  $B$  as 3.0 based on the model of the rate of increase of cleavage fracture work across a field of coarse grains as given in Fig.21. This gives the final form of the cleavage resistance of the polycrystals as:

$$\frac{G_{\text{ICPC}}}{G_{\text{IC}}} = 1.45 + 3.03(\Delta x_c/D) + 3.0 \quad (12a)$$

$$= 4.45 + 3.03(\Delta x_c/D) \quad (12b)$$

We have written Eqn.(12a) deliberately in an expanded form to indicate that the contribution to the overall cleavage work of the cleavage of individual grain interiors is

substantial and represents roughly one third of the total work of fracture, as should be clear from Fig.21. The second term on the RHS of Eqns.(11) and (12a) makes a negligible contribution to the total work of fracture for the large grain material that we have considered specifically even though it is this term that governs the selection of the sites for cleavage break-through across grain boundaries. However, because of the tiered nature of the cleavage break-through across grain boundaries described in detail in the earlier bicrystal study (Qiao and Argon, 2002a) where the majority of break-throughs had been noted to follow a regular mode of penetration, only a relatively small overall change of fracture area results as the cleavage front crosses a typical grain boundary. The somewhat more substantial contribution (roughly two thirds) to the overall work of fracture results from the process of *cleavage-like* shear separation along grain boundaries (Fig.21) between primary cleavage cracking facets in adjoining grains, as had already been concluded by McClintock (1997).

Finally, we return to the exploration of a grain size dependence of the cleavage fracture work. While no important grain size dependence is evident in our model beyond the weak and unimportant grain size dependence represented in the second term of the RHS of Eqns.(11) and (12a, b), we have examined the specific effect experimentally. This dependence was probed through fracture toughness determinations at -20C in the pure

cleavage range in 8 coarse-grained samples, in which the average grain size varied between 1.5mm and 6.0mm. The result is given in Fig.23. It shows very substantial scatter among the measurements, with no discernable grain size dependence which is consistent with our model in which the only grain size dependent contribution might conceivably arise for grain sizes in the range of 50-100 microns but should be negligible in the coarse grain size range of 1-10mm, and disappear for very small grain size material if the ratio  $\Delta x_c/D$  reaches a constant value asymptotically, as was assumed might be the case.

## **5.2 General Observations**

The role of grain boundaries and grain size effects in the fracture resistance of polycrystalline metals, particularly steel, has been well appreciated for many decades and has been modeled by Hall (1951) and Petch (1953) among others. Similarly, the effect of grain size on fracture and the beneficial consequence of grain refinement in increasing the brittle strength of steels is also well known (Petch, 1954). Furthermore, the triggering effects of fracturing grain boundary carbides in initiating brittle behavior in fracture transitions have also been studied to some extent (McMahon and Cohen, 1965; Ritchie, et al., 1973; Lin et al., 1986; Petch, 1986), as we had already noted in Section 1.0. Outside

of these general considerations of grain size effects and phenomena related to triggering of brittle behavior in fracture transitions, specific considerations of the influence of grain boundaries on the cleavage cracking resistance have been few. Of these studies the most noteworthy have been those of Gell and Smith (1966), Anderson et al. (1994) and McClintock (1997). In the work of Anderson et al. (1994), the mode of cleavage fracture across hexagonal grains was considered in some detail to develop realistic cumulative probability distributions of fracture resistance in the context of "weakest link" models of such behavior. Gell and Smith (1966) have made one of the earliest observations on the cracking resistance of individual grain boundaries with known tilt and twist components, in hydrogen charged polycrystalline Fe-3%Si alloy and demonstrated that the major contribution to the cracking resistance of a grain boundary comes from its twist misorientation across the boundary rather than the tilt misorientation. This basic observation, also conjectured by McClintock (1997), was demonstrated directly by us in our earlier bicrystal study (Qiao and Argon, 2002a). The most detailed study of the cleavage cracking resistance of polycrystals, with which we will compare our findings is that of McClintock (1997), who has modeled the form of percolation of a cleavage cracking front across an array of randomly misoriented cubic grains. In his study McClintock makes a series of assumptions that have actually been observed, in part, in the present experimental study. These included the following: that a) grains crack by a

cleavage crack entering them from a neighboring grain rather than by the applied stress on the grain, b) a tilt misorientation across a boundary is far less of an obstacle for penetration across a boundary than a twist misorientation; c) normal expectations apply that cracking in re-entrant channels formed by cleaved adjacent grains do not readily extend while exposed corners on crack fronts are favored for cleavage propagation, and d) certain difficult-to-shear boundaries connecting facets of already cleaved grains (recalcitrant grain boundaries) effectively hold back the propagating cleavage front. While some conclusions of the McClintock model such as an excessive tendency of cracking fronts to advance parallel to the front by laterally propagating cleavage "kinks" along the front, was not found in our observations, many other features were quite similar. The single major departure, however, between the predictions of McClintock and our model has been that the fracture toughness in his model exhibits a square-root type of grain size dependence (linear grain size dependence of work of fracture) while no such grain size dependence resulted from our model. This difference results primarily from considering that the cleavage work of fracture of grain interiors is negligible in comparison with the plastic bridging shear work along boundaries connecting primary cleavage facets, and that the latter process is indeed a plastic shearing-off process. In our model the cleavage work of grain interiors makes up fully one third of the overall fracture work and the bridging shear processes are viewed more as a *cleavage-like* shear fracture

in which the traction drops abruptly to zero after a preparatory constant shear displacement emanating from the cleavage facets as depicted partly in Fig.21 rather than a continuous linear drop characteristic of a pure plastic shearing-off process. Nevertheless, since there are significant uncertainties in both our model and that of McClintock the exact nature of grain size dependence of the cleavage resistance remains unanswered. In any event it is clear that in the very large grain size limit there is no observable dependence which is in support of our model.

### **5.3 The decarburized 1010 steel**

The experimental excursion into the behavior of the 1010 steel was made for the purpose of demonstrating that the findings on the Fe-2%Si alloy could be used in applications to low carbon steels. We note that our findings on the role of grain boundaries on the cleavage fracture resistance of the Fe-2%Si alloy are primarily of a geometrical nature exhibited by the strongly solid solution strengthened single phase bcc material. Thus, the potential applicability of these findings to low carbon steel is appealing. In our experiments with the decarburized 1010 steel where a potentially complicating pearlite component was removed a full demonstration of a parallel behavior to the Fe-2%Si alloy was not quite possible because of the very much reduced level of plastic resistance of the



former shown in Fig.2 that resulted in all fracture measurements on the 1010 steel to be effectively on the upper shelf, even at the lowest test temperature of -150C. This was evident from the large distortions of the DECP specimens at fracture and relegates the fracture work measurements of  $J_{IC}$  to being of plane stress type. Nevertheless, much can be concluded from the cleavage fracture surface features shown in Figs.11a-11c, albeit all being in the nature of terminal cleavage occurring after very substantial amounts of expanded plastic work in the ligament between the two edge cracks. The fracture surface of Fig.11a at -125C shows a field of cleaved grain facets of a distinctly brittle appearance with only weakly delineated river markings which we would have expected to be quite similar to those observable in the pure cleavage realm at the lower shelf below the ductile-to-brittle (DB) transition temperature, which we expect now to be well in the cryogenic temperature range near liquid nitrogen temperature on the basis of the shift of the plastic resistances and the estimate of the brittle strength of the 1010 steel. The fracture appearance in Fig.11b at -70C, now well above the DB transition, shows still a field of cleaved grains, but with well delineated cleavage river markings giving clear evidence of accompanying plastic distortions resulting from the bridging deformations between grains.

The most profound observation derivable from the comparison of the behavior of the Fe-2%Si alloy and the decarburized 1010 steel is the dramatic reduction in the conventional ductile to brittle transition temperature by about 400C, from 250C (for the Fe-2%Si) to -150C (for the decarburized 1010 steel) when all hardening agents are removed from the Fe. We note that this effect is far larger than what might be expected from inspection of Fig.2 and the shift of the temperature dependent plastic resistance curves. This further accentuation of the difference between the DB transitions results from the fact that the  $J_{IC}$  measurements for the 1010 steel are of a plane stress type in a DECP specimen of quite inadequate size and shape while the results for the Fe-2%Si alloy were derived from *bona-fide* plane strain test configurations.

## 6. CONCLUSIONS

In the lower shelf in Fe-2%Si and in low carbon steels cleavage cracks percolate through grains by selectively going through the most exposed grain boundaries with the lowest penetration resistance and subjected to the largest local crack driving forces. While these grain boundaries govern the overall mode of cleavage crack percolation they contribute little to the overall fracture resistance.

The overall fracture resistance is derived roughly in one part by the cleavage resistance of individual misoriented cleavage facets in grains and in two parts by the work of fracture along nearly vertical boundaries bridging the primary cleavage facets of adjoining grains by a combination of plastic shear and a "cleavage-like" shear separation.

Both experiments and modeling of crack percolation mechanisms suggest that the overall cleavage fracture resistance due to the tessellation of the cleavage fracture process by the grain boundaries is largely grain size independent, but increases the fracture resistance in comparison with a flat untessellated cleavage process by a factor of close to 3.0.

Experiments carried out on decarburized 1010 steel indicate that, when present, the percolation of cleavage across grains in the upper shelf region is very similar to that in the lower shelf, which has important implications in the triggering of brittle behavior in structures undergoing initial ductile forms of fracture.

## ACKNOWLEDGEMENT

This research has been supported by the National Science Foundation under grant DMR-9906613. We are also grateful to Professor L. Anand for providing the coarse grained Fe-2%Si alloy plates and to Professor F. A. McClintock for useful discussions.

## REFERENCES

Anderson, T. L., Stienstra, D., and Dodds, R. H., (1994), A thermodynamical framework for addressing fracture in the ductile-brittle transition region, in *Fracture Mechanics: Twenty-fourth Volume*, ASTM-STP 1207, edited by Landes, J. D., et al, ASTM: Philadelphia, p.186.

Argon, A. S. and Qiao, Y., (2002), Cleavage cracking resistance of high angle grain boundaries in Fe-3%Si alloy, *Phil. Mag.*, in the press.

Birks, N., (1969), *Decarburization*, the Iron and Steel Inst., London.

Brown, S. B., Kim, K. H., and Anand, K., (1989), An internal variable constitutive model for hot working of metals, *Internat. J. Plasticity*, **5**, 95.

Gell, M. and Smith, E., (1967), The propagation of cracks through grain boundaries in polycrystalline 3%Silicon-iron, *Acta Metall.*, **15**, 253.

Hall, E. O., (1951), The deformation and ageing of mild steel: III - Discussion of results, *Proc. Phys. Soc.*, **B64**, 747.

Kumar, V., German, M. D. and Shih, C. F., (1981), An engineering approach for elastic-plastic fracture analysis, *EPRI Report NP-1931*, Palo Alto, CA: Electric Power Research Institute.

Lin, T., Evans, A. G., and Ritchie, R. O., (1986), A statistical model of brittle fracture by transgranular cleavage, *J. Mech. Phys. Solids*, **34**, 477.

McMahon, C. J. and Cohen, M., (1965), Initiation of cleavage in polycrystalline iron, *Acta Metall.*, **13**, 591.

McClintock, F. A., (1997), A three-dimensional model for polycrystalline cleavage and problems in cleavage after extended plastic flow or cracking, in *George Irwin Symposium on Cleavage Fracture*, edited by Chan, K. S., TMS, Warrendale, PA, p.81.

McClintock, F. A. and Clerico, M., (1980), The transverse shearing of singly-grooved specimens, *J. Mech. Phys. Solids*, **28**, 1.

Petch, N. J., (1953), The cleavage strength of polycrystals, *J. Iron Steel Inst.*, **174**, 25.

Petch, N. J., (1954), The fracture of metals, in *Progress in Metal Physics*, edited by Chalmers, B. and King, R., Pergamon Press: London, vol.5, p.1.

Petch, N. J., (1986), The influence of grain boundary carbide and grain size on the cleavage strength and impact transition temperature of steel, *Acta Metall.*, **34**, 1387.

Qiao, Y. and Argon, A. S., (2002a), Cleavage cracking resistance of high angle grain boundaries in Fe-3%Si alloy, *Mech. Mater.*, in the press.

Qiao, Y. and Argon, A. S., (2002b), Brittle to ductile transition of cleavage fracture by thermal crack arrest in Fe-3%Si single crystals, to be submitted for publication.

Rice, J. R., (1985), First-order variation in elastic fields due to variation in location of a planar crack front, *J. Appl. Mechanics*, **52**, 571.

Ritchie, R. O., Knott, J. F. and Rice, J. R., (1973), On the relationship between critical tensile stress and particle toughness in mild steel, *J. Mech. Phys. Solids*, **21**, 395.

Thelning, K.-E., (1984), *Steel and its Heat Treatment*, Butterworth: London.

## FIGURE CAPTIONS

Fig.1 Sketch of the modified stereo microscope for determination of inclination of cleavage planes in individual grains relative to sample reference surfaces.

Fig.2 Temperature dependence of tensile yield stresses in Fe-2%Si alloy (as scaled from data on Fe-3%Si single crystals) and decarburized 1010 steel.

Fig.3 Temperature dependence of the fracture toughness,  $K_{IC}$ , and fracture appearance in coarse grained Fe-2%Si alloy.

Fig.4 SEM micrograph of fracture surface of Fe-2%Si below the PC/MC transition at -20C.

Fig.5 SEM micrograph of fracture surface of Fe-2%Si above the PC/MC transition at 20C.

Fig.6 SEM micrograph of a complex bridging fracture between two parallel cleavage facets inside a grain in Fe-2%Si alloy at -20C.

Fig.7 SEM micrograph of a complex fracture along a recalcitrant grain boundary in Fe-2%Si alloy at -20C.

Fig.8 SEM micrograph of fracture surface immediately above the conventional brittle-to-ductile transition at around 250C in Fe-2%Si alloy, showing areas of clear ductile dimple fracture and cleavage fracture.

Fig.9 Temperature dependence of  $J_{IC}$  plane stress fracture toughness in DECP specimens of decarburized 1010 steel showing the persistence of terminal cleavage fracture above the brittle-to-ductile transition in the upper shelf region.

Fig.10 Fracture surface of decarburized 1010 steel at -100C, well above its brittle-to-ductile transition temperature, showing a mixture of cleavage and ductile dimple fracture.

Fig.11 A sequence of SEM micrographs of fracture surfaces in decarburized 1010 steel: a) at -125C; b) at -70C; and c) at -40C.

Fig.12 Various modes of entry of a cleavage front into individual grains: a) penetration into an exposed grain; b) penetration into a grain through a particularly weak boundary; c) and d) cracks entering into grains with an exposed corner.

Fig.13 Macrograph of a fracture surface of a compact fracture specimen of very coarse grained Fe-2%Si alloy. The vertical thickness dimension is 26mm.

Fig.14 Orientation relationship of cleavage facets in individual grains, relative to external specimen axes.

Fig.15 The cleavage fracture percolation map through the grains of the sample shown in Fig.13, showing also two crack arrest fronts A-A and B-B.

Fig.16 The calculated distribution of local stress intensity factors  $K_I$  along the fracture fronts A-A and B-B.

Fig.17 Histogram showing the distribution of numbers of grain edges in the fracture field of Fig.15, not counting grain edges bounded by free surfaces.

Fig.18 Computed cleavage fracture percolation map using information on grain boundary resistance determined from Qiao and Argon (2002a).

Fig.19 a) A schematic view of the types of boundaries overcome by the cleavage front. Boundaries with emanating arrows are those that govern the form of penetration of the



fracture front from grain to grain. Boundaries between 1-2, 5-6, and 2-4, in various measure, require extensive fracture work to bridge primary cleavage facets; b) simplified field in a generic square grain: (1) cleavage work inside grain; (2) work of fracture for going through the principal boundary controlling the percolation process; (3) boundaries requiring large amount of bridging fracture work by plastic shear and cleavage-like separation.

Fig.20 Stages of bridging fracture work: a) initial outline of grain boundary bridging primary cleavage facets; b) preparatory plastic crack tip displacement triggering subsequent "cleavage-like" separation.

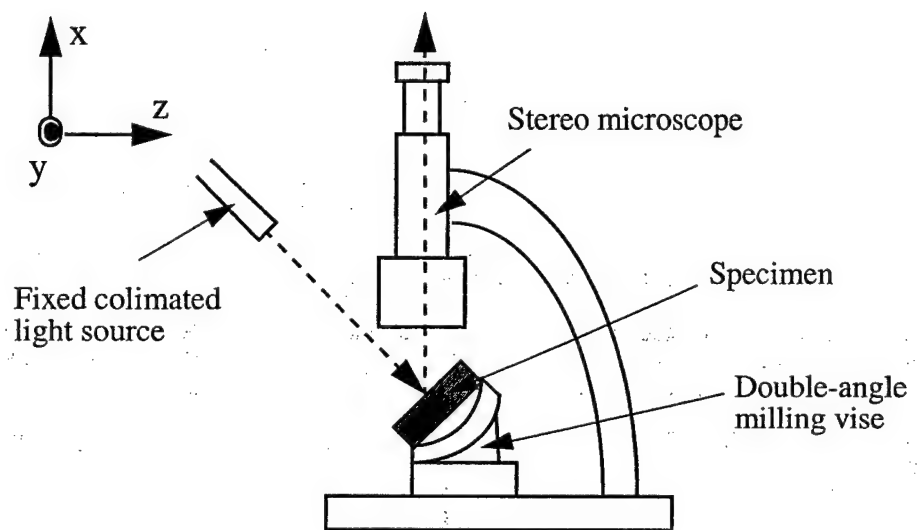
Fig.21 SEM micrograph of the surface of separation by shear in a typical boundary connecting two cleaved facets in adjacent grains. Most of the surface shows signs of plastic shearing. Portion identified by an arrow shows a fracture type separation.

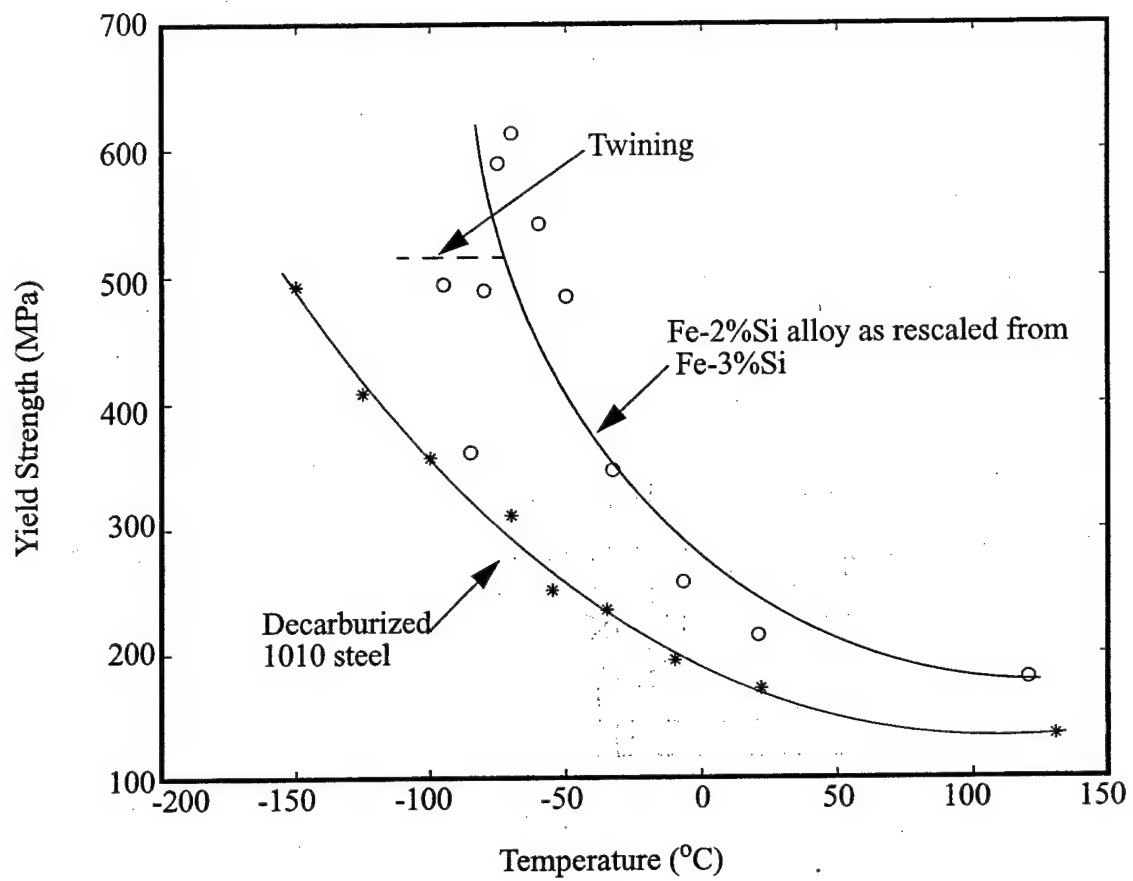
Fig.22 Result of computer simulation of overall fracture work for an advancing crack front through the family of grains shown in Fig.15. Stars indicate accumulated fracture work due to cleavage of grain interiors, open circles indicate cumulative fracture work contributed by the severance of the bridging grain boundaries.

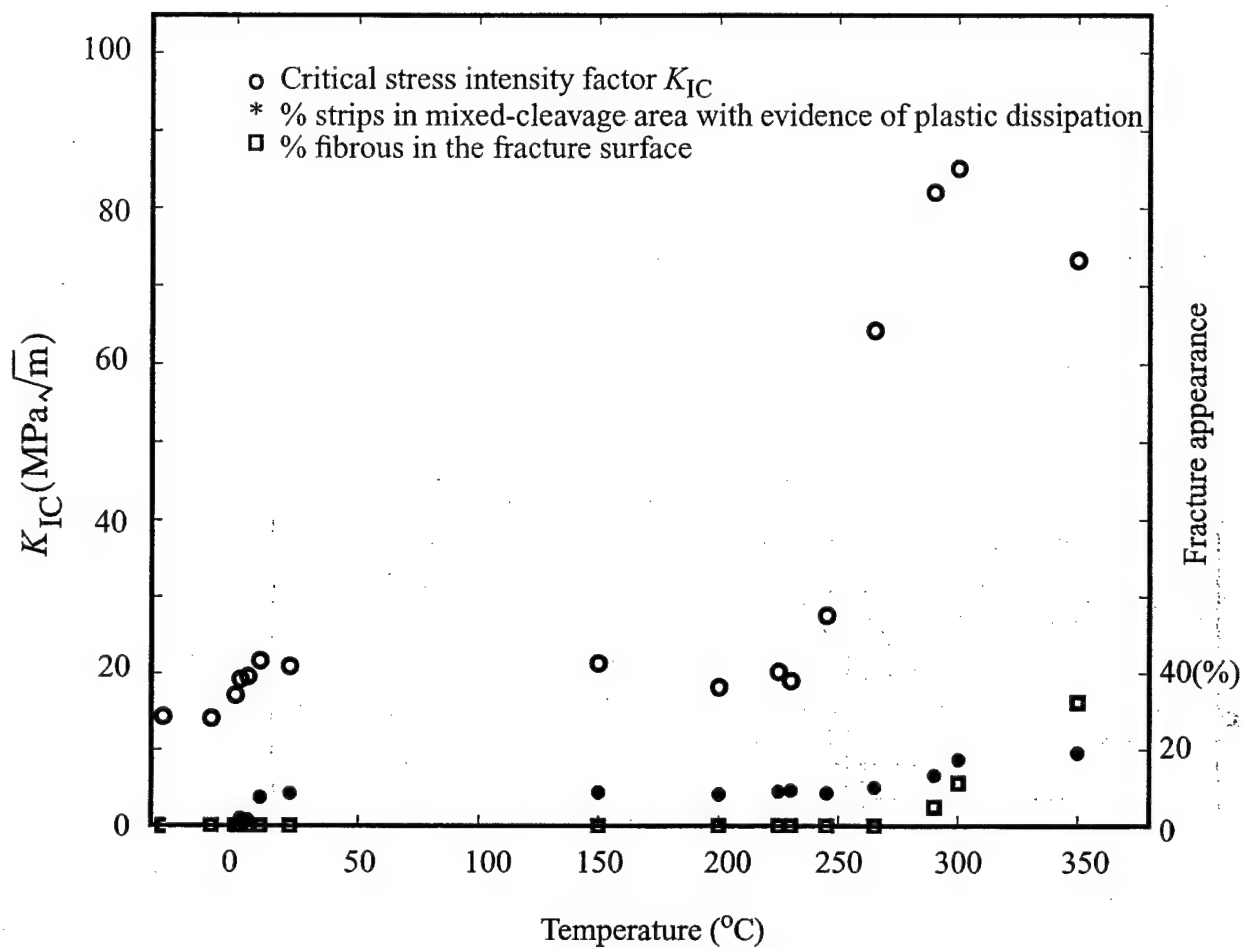
Fig.23 Grain size dependence of critical stress intensity of fracture at -20C in Fe-2%Si alloy.

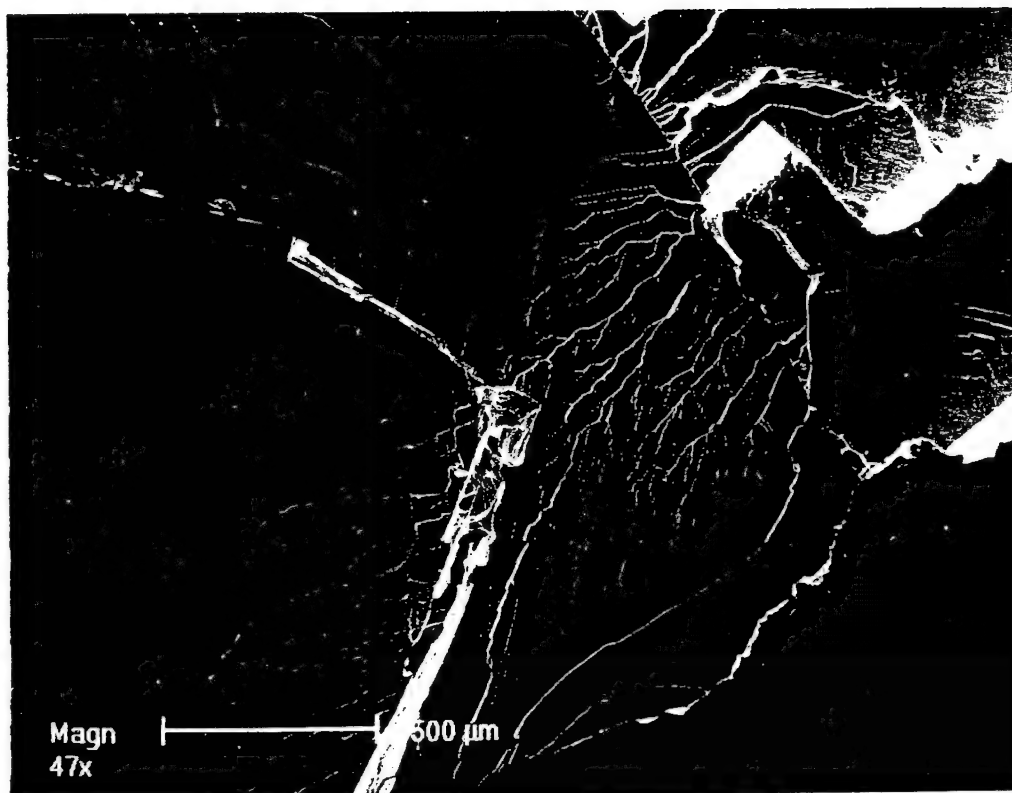
## TABLES

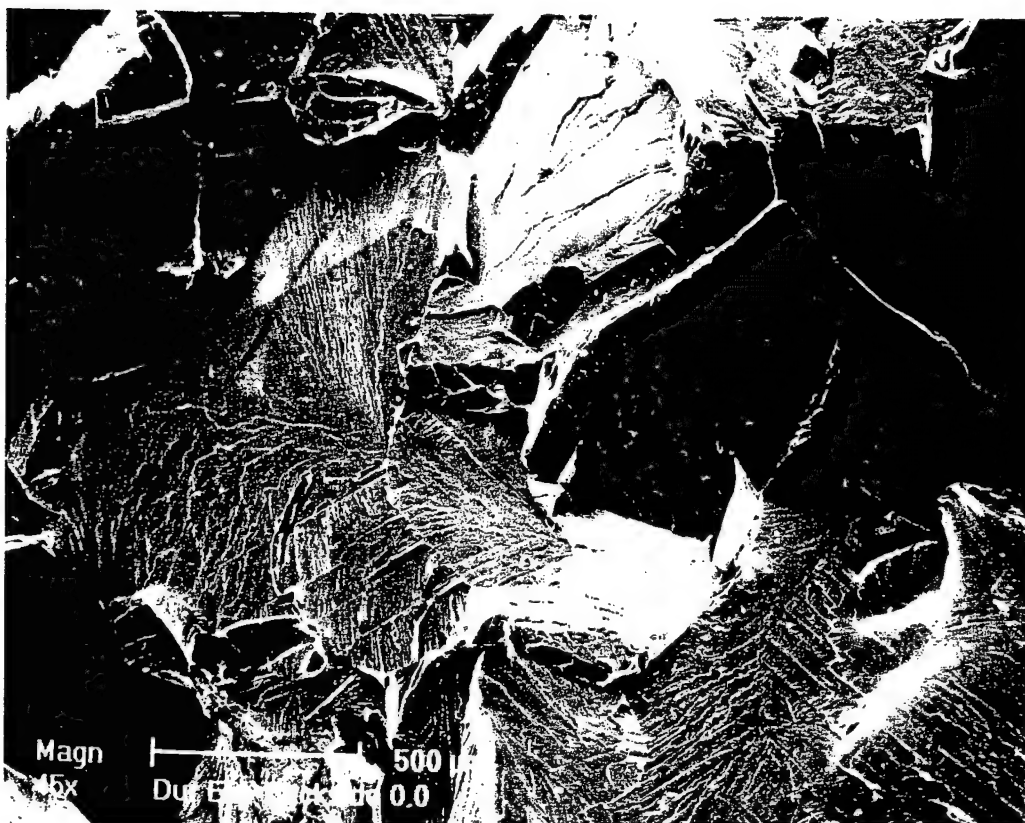
1. Chemical composition of the Fe-2%Si alloy.
2. The tilt and twist misorientations of principal cleavage facets of 78 individual grains in the compact fracture sample of Fig.15 referred to external axes.





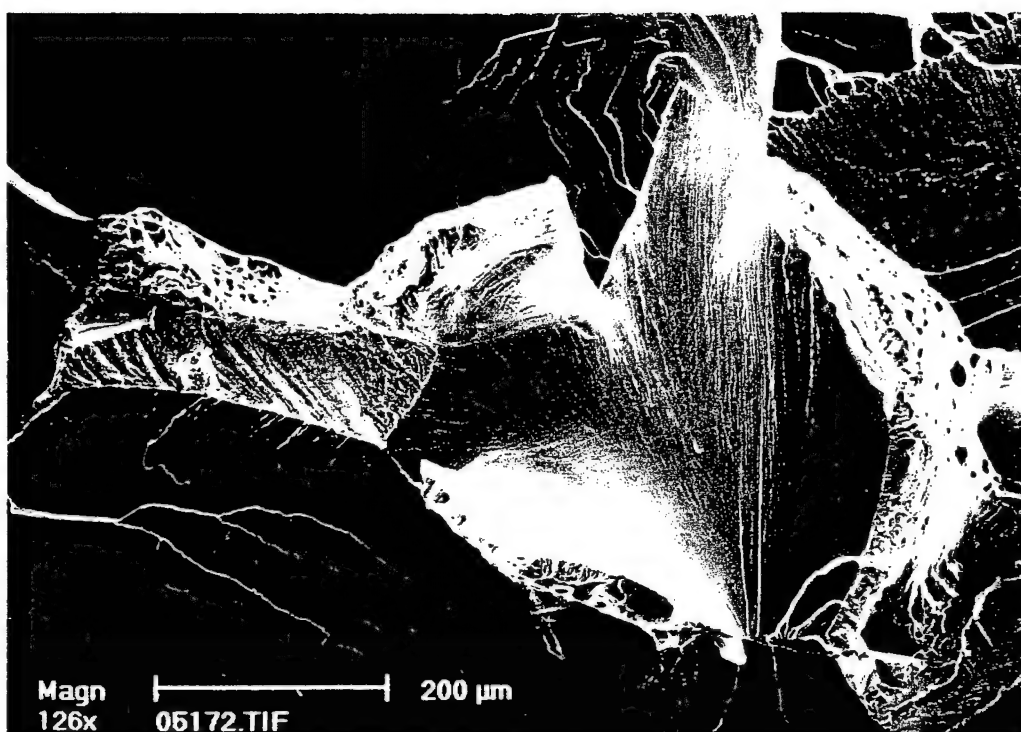


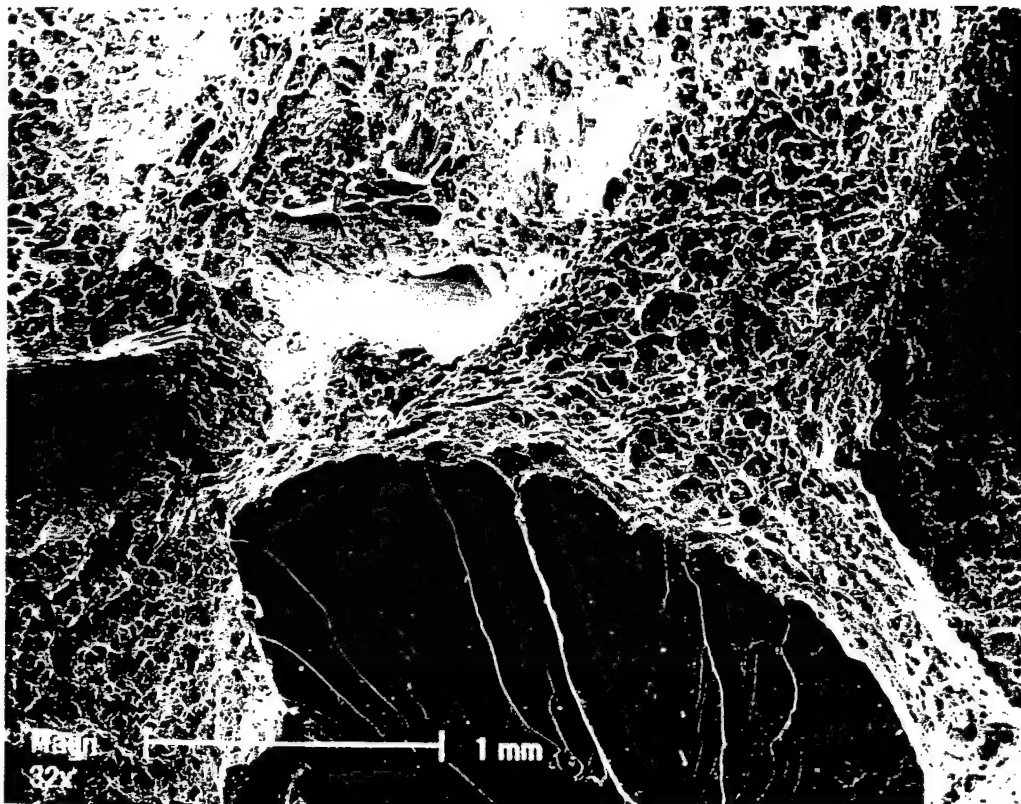


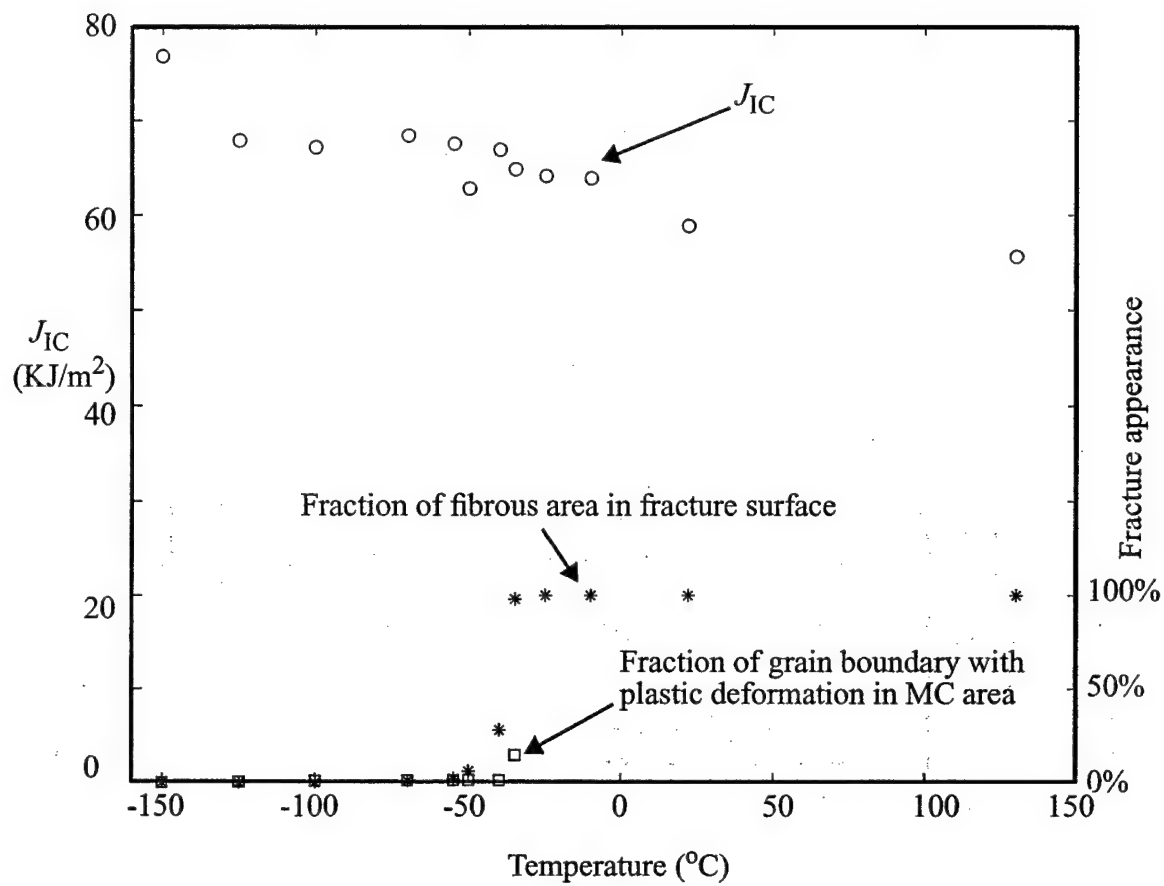


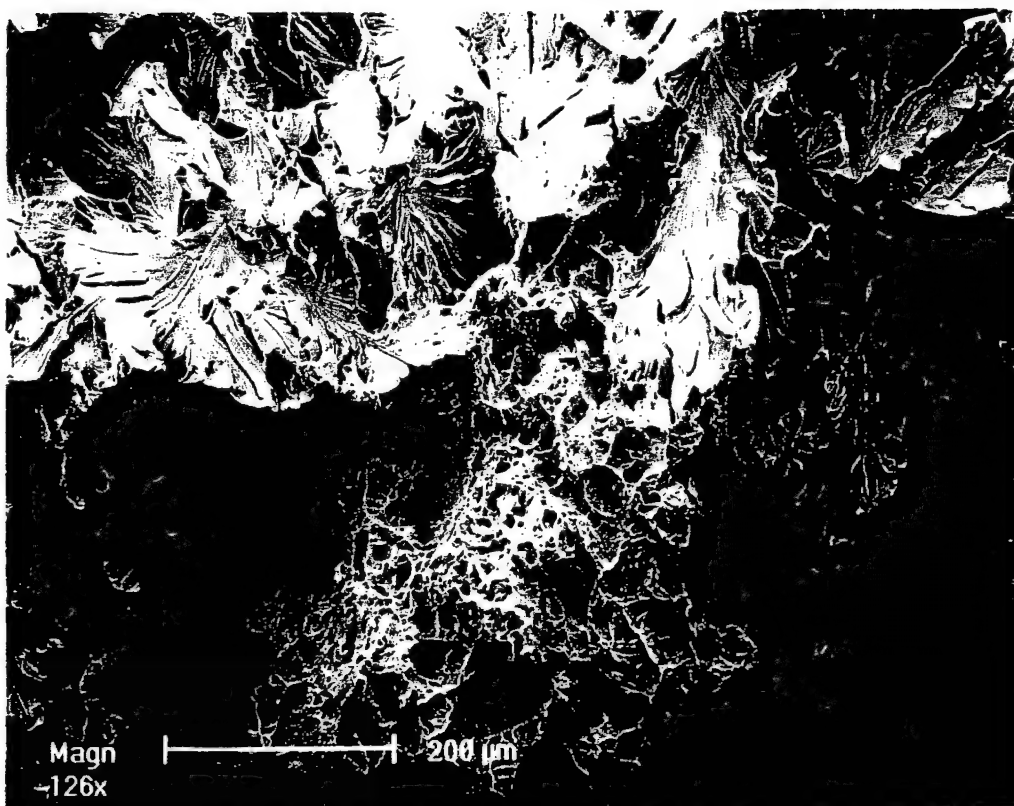






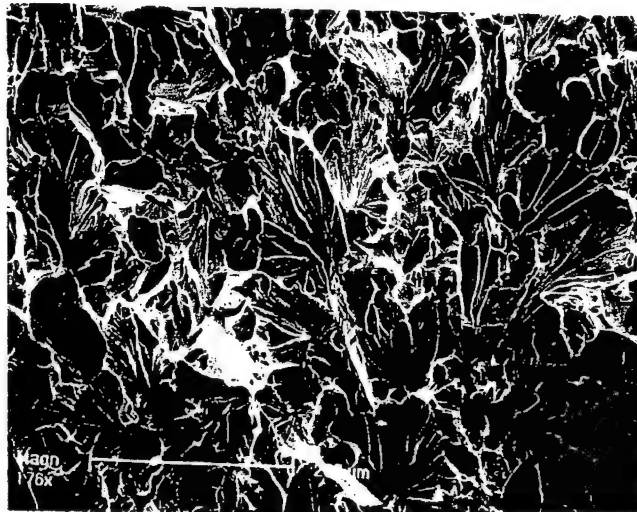




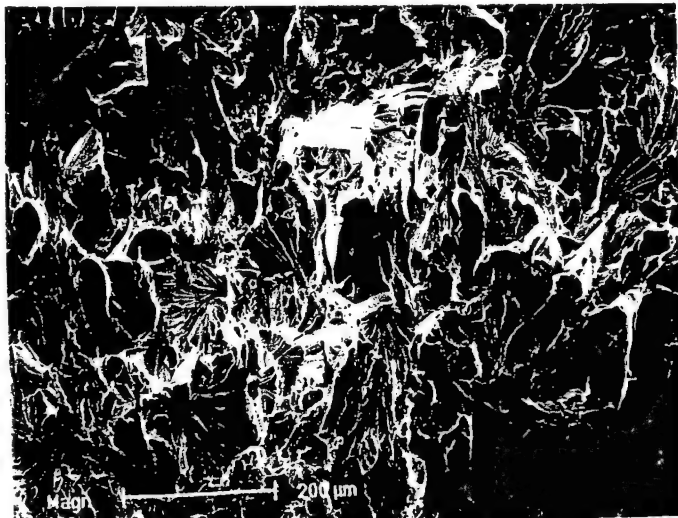




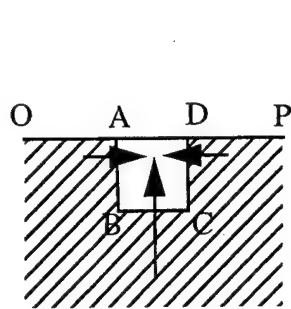
(a)



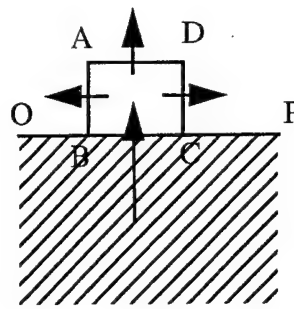
(b)



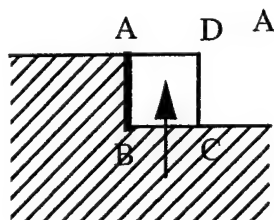
(c)



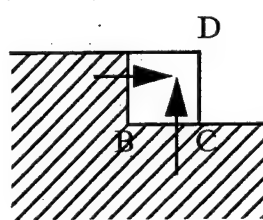
(a)



(b)

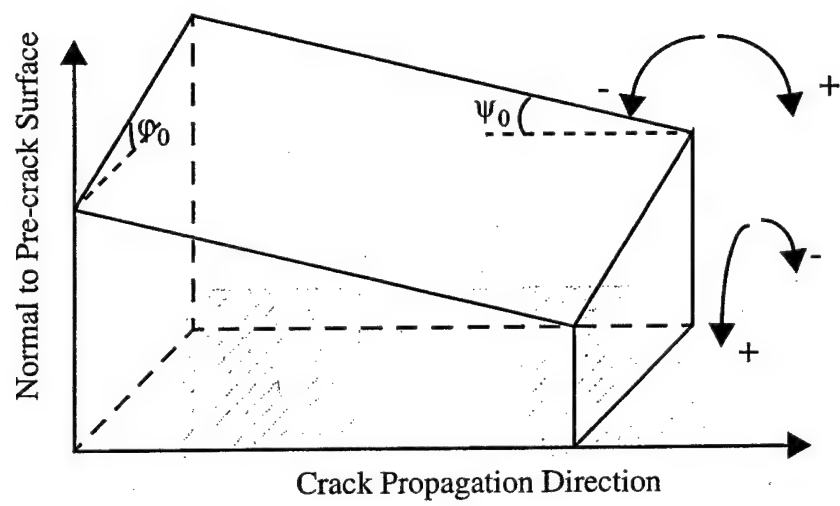


(c)

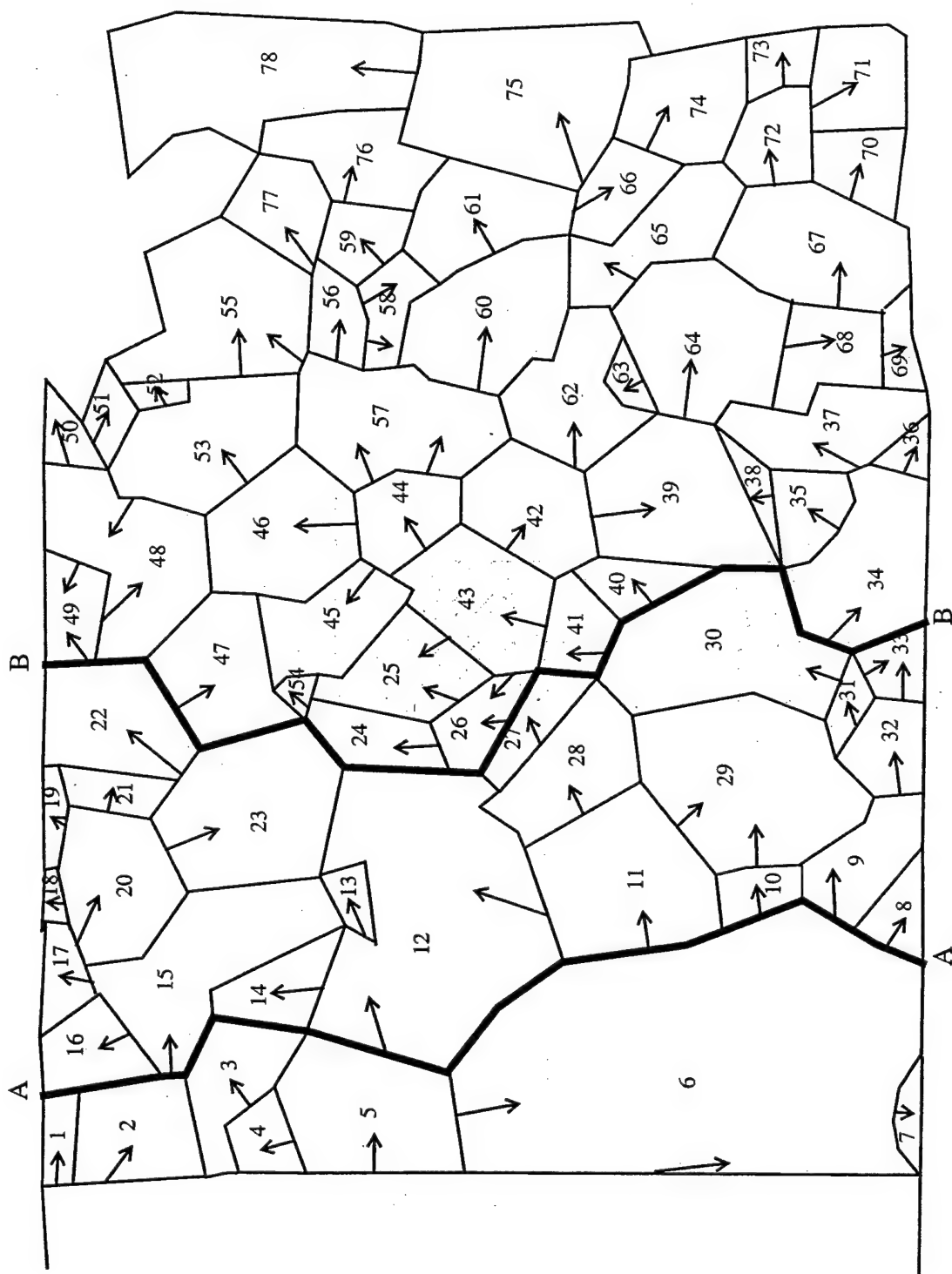


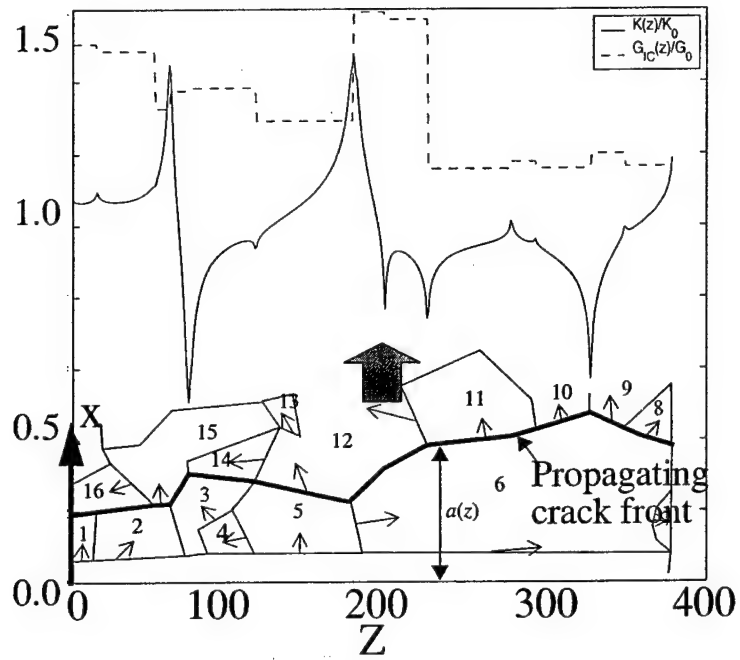
(d)



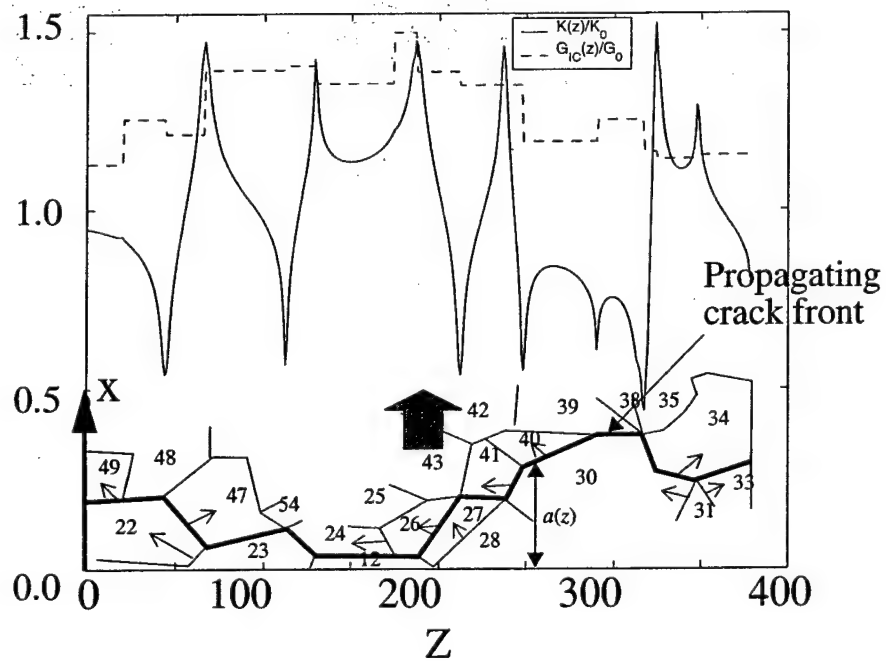




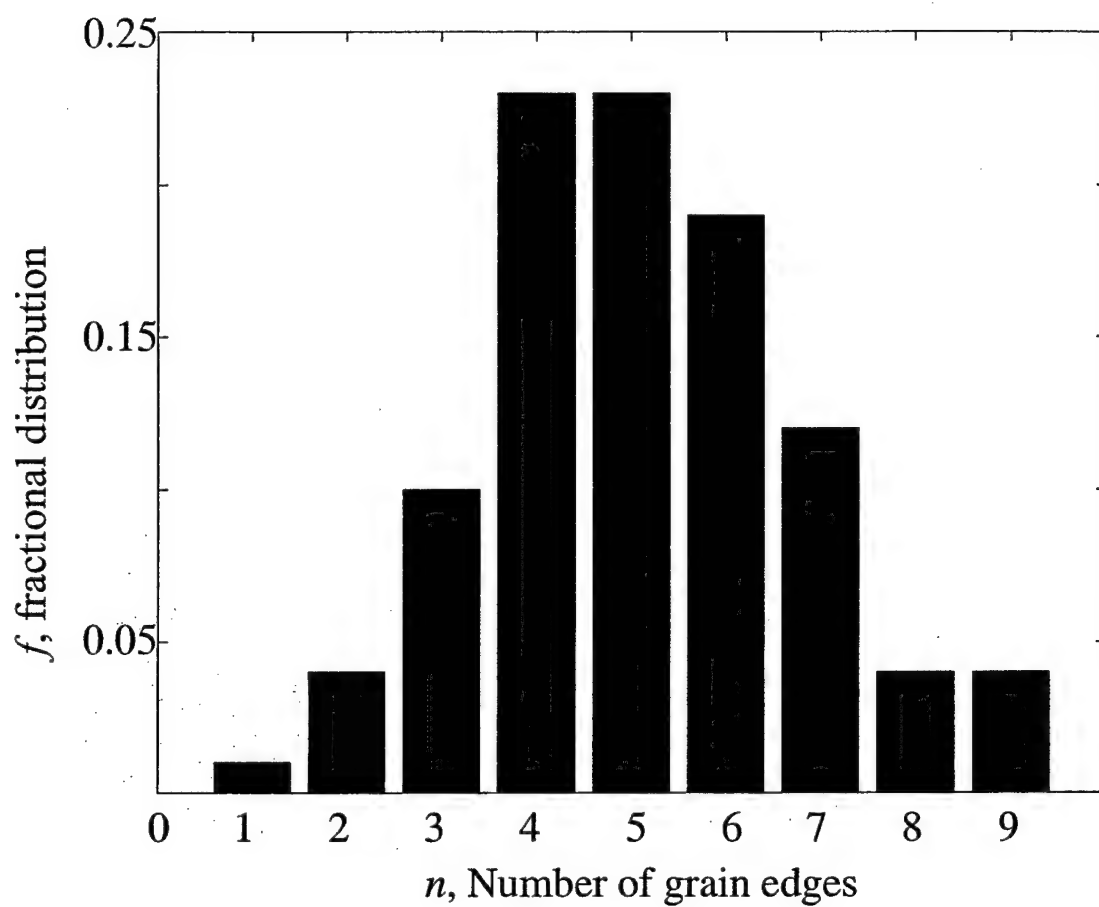


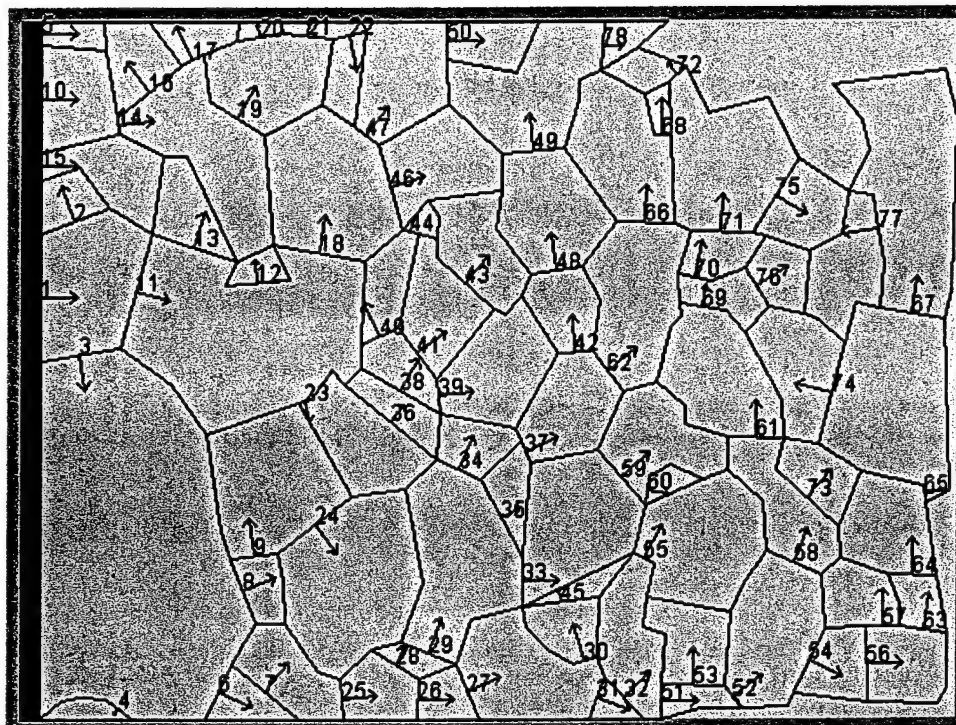


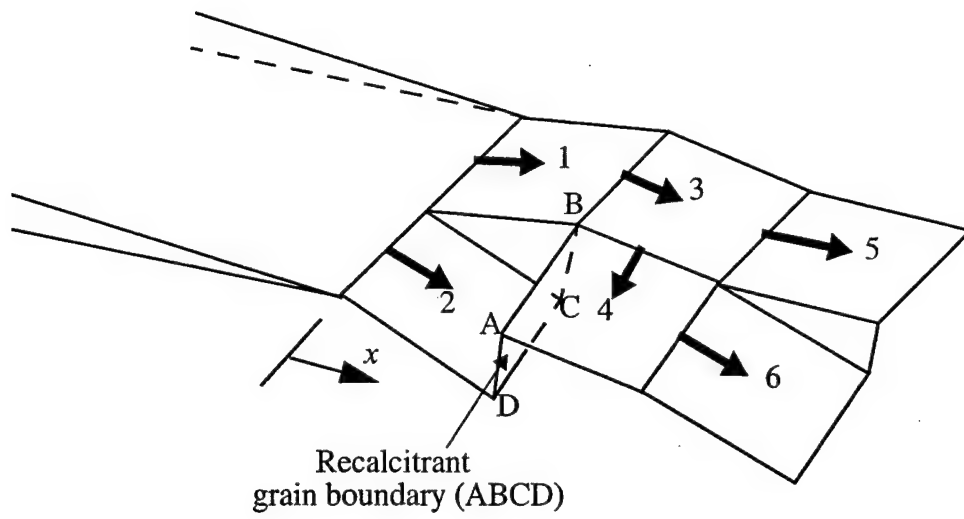
(a) Crack front A-A



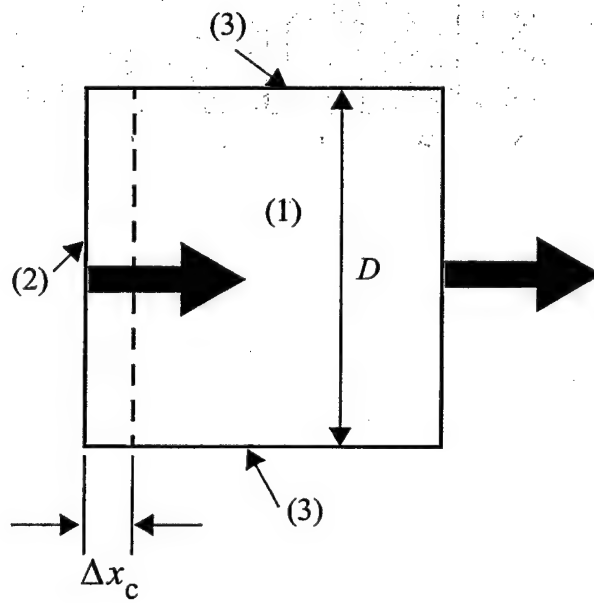
(b) Crack front B-B



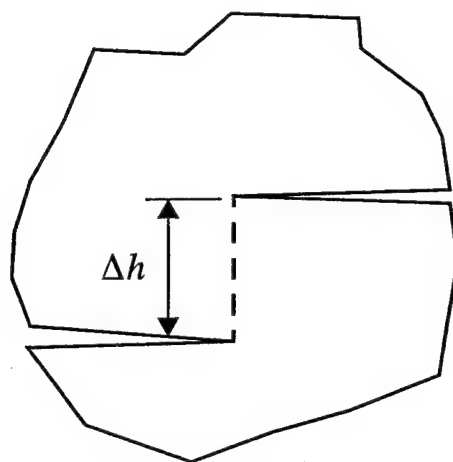




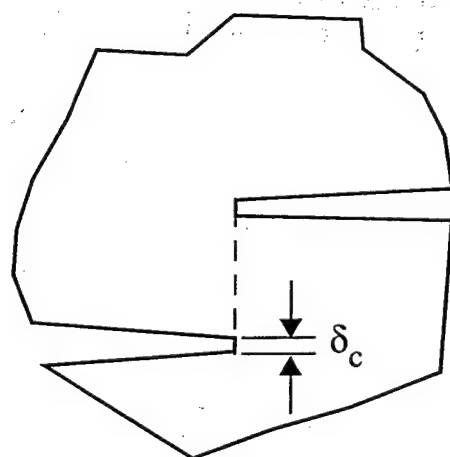
(a)



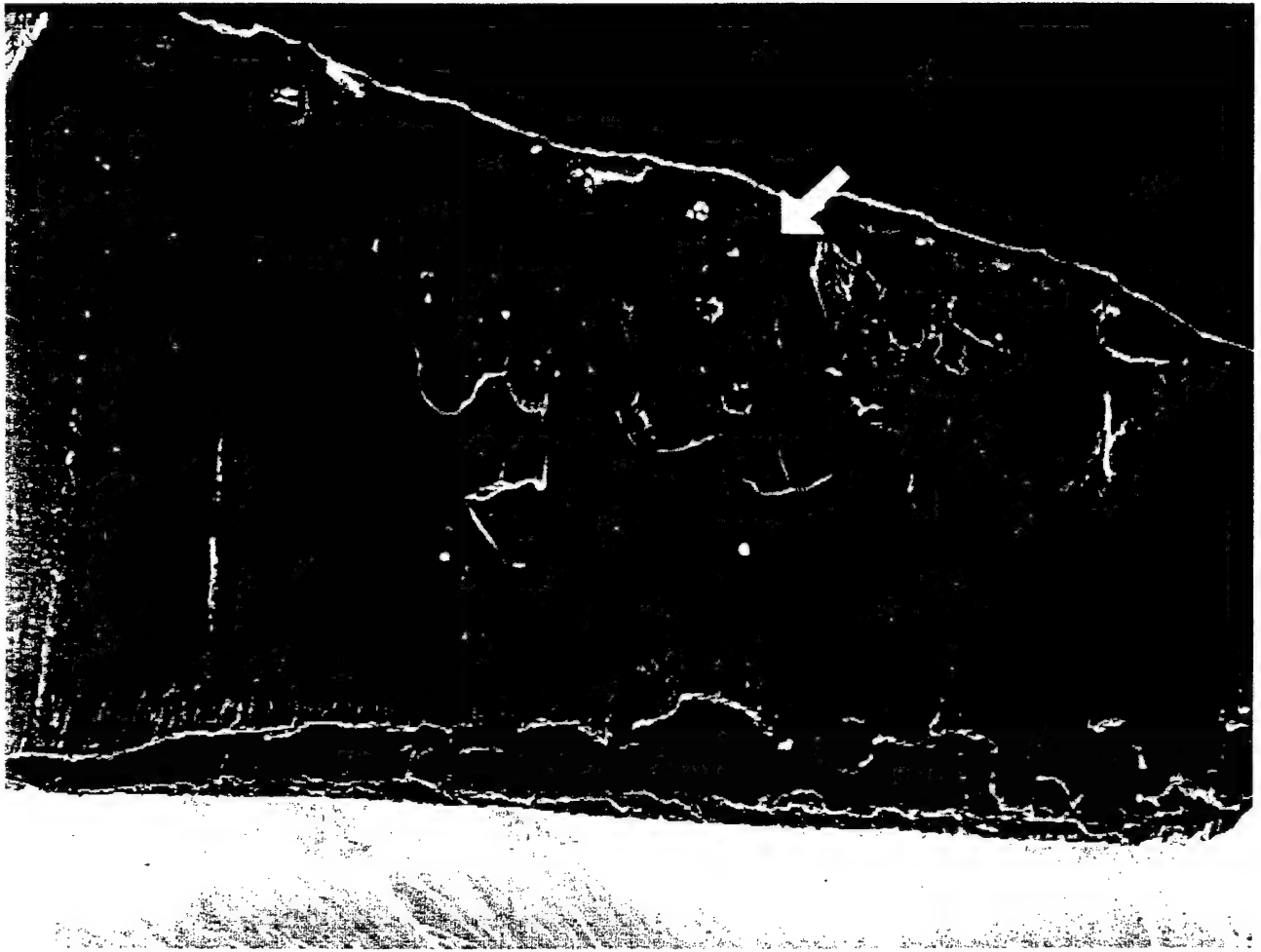
(b)

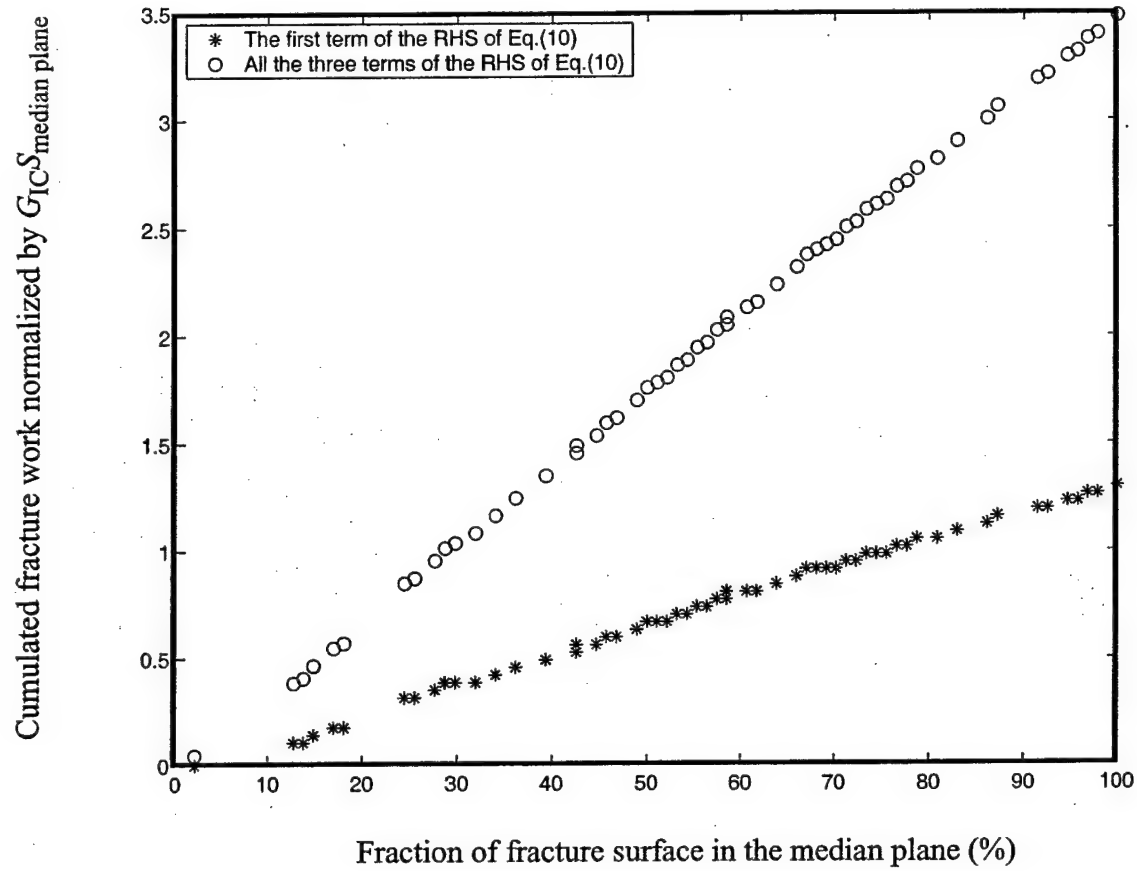


(a)

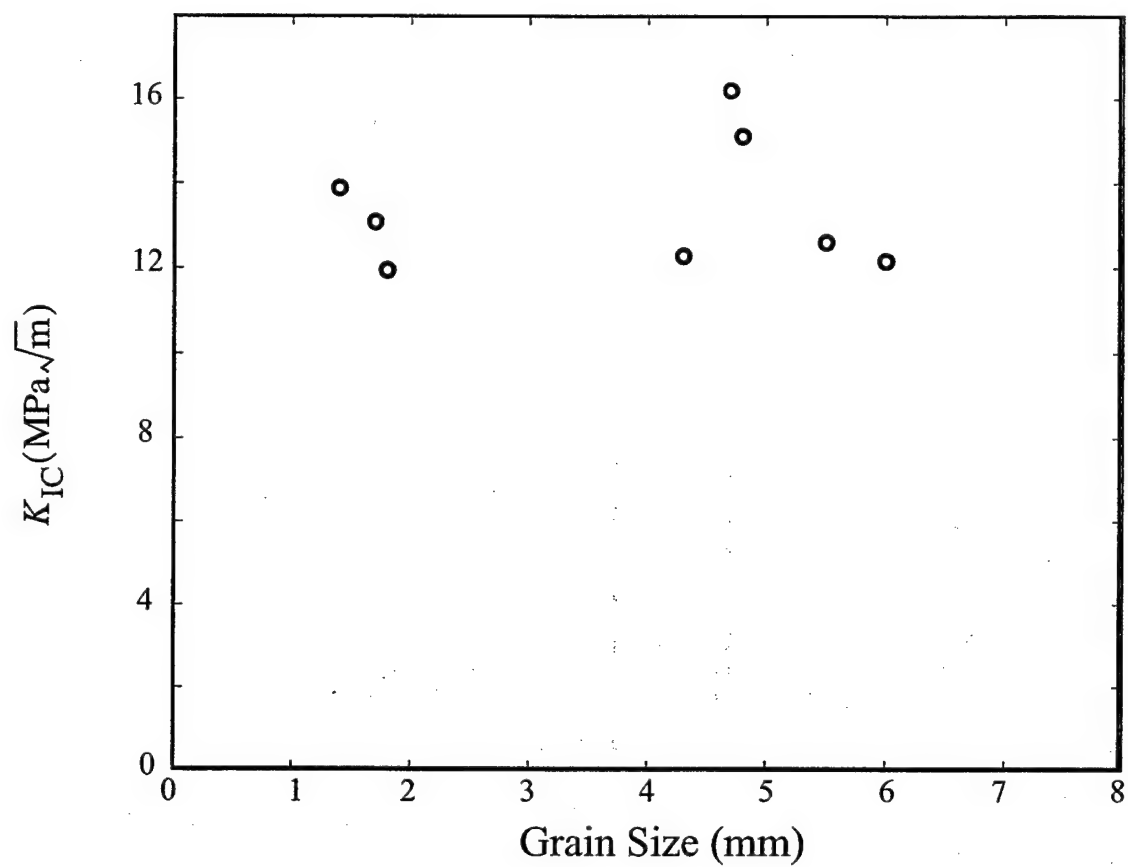


(b)









## Critical configurations for dislocation nucleation from crack tips

By G. XU†, A. S. ARGON‡

Massachusetts Institute of Technology, Cambridge, Massachusetts 02139, USA

and M. ORTIZ

California Institute of Technology, Pasadena, California 91125, USA

[Received 25 January 1996 and accepted in revised form 16 June 1996]

### ABSTRACT

In the present paper, we analyse several activation configurations of embryonic dislocations nucleated from the tip of a cleavage crack. The activation configurations include nucleation on inclined planes, on oblique planes and on cleavage ledges and are treated within the classical framework of Peierls. A variational boundary integral method with an interplanar tension-shear potential developed earlier is used to solve for the saddle-point configurations of embryonic dislocation loops and their associated energies. Based on the assumption that the brittle-to-ductile transition in cleavage fracture is a nucleation-controlled process (as is expected to be the case in bcc transition metals such as  $\alpha$ -Fe) the results of the calculations are used to estimate the brittle-to-ductile transition temperatures. It is concluded that only dislocation nucleation on cleavage ledges furnishes realistic values of the transition temperature. The homogeneous nucleation of dislocations on either inclined or oblique planes requires transition temperatures well above the melting point. This implies that nucleation of dislocations from a crack tip in intrinsically brittle crystals is only possible at local crack front heterogeneities such as cleavage ledges, and that the homogeneous nucleation of dislocations from a straight crack front is not possible. This conclusion is supported by the experimental observation that dislocation nucleation from a crack tip is a rare event which occurs preferentially at heterogeneities.

### § 1. INTRODUCTION

The abrupt transition in the fracture behaviour of some materials from ductile to brittle (or brittle to ductile) with small changes in temperatures remains a key concern in many structural applications. This phenomenon has been viewed from two different perspectives. In applications where the ductility of a material is relied upon, the transition is viewed as the sudden onset of brittleness. The complex phenomena associated with a ductile-to-brittle (D-B) transition in polycrystalline steels, involving as a key step the deformation-induced production of propagating cleavage microcracks, have been studied experimentally in detail (Hahn, Averbach, Owen and Cohen 1959) and have been modelled theoretically to some degree (Stroh 1954, 1955, 1957, Lin, Evans and Ritchie 1986, 1987).

---

†Present address: TerraTek, Inc., 420 Wakara Way, Salt Lake City, Utah 84108, USA.

‡Author for correspondence.

By contrast, in the brittle-to-ductile (B-D) transition a competition is believed to take place between cleavage fracture and plastic shielding, with eventual blunting of the propagating cleavage crack either by dislocation emission from the crack tip or by background plastic relaxation. The crack arrest and eventual blunting mechanism depends upon temperature, loading rate and the ability of the vicinity of the crack tip to undergo plastic deformation. This B-D transition has been explained either in the static framework of a stationary crack (St John 1975, Brede and Haasen 1988, Hirsch, Roberts, Samuels and Warner 1989a, Hirsch, Samuels and Roberts 1989b, George and Michot 1993), or in the dynamical framework of the arrest of a propagating cleavage crack with increasing temperature and decreasing loading rate (Gilman, Knudsen and Walsh 1958, Brede, Hsia and Argon 1991, Hsia and Argon 1994).

Models of the B-D transition just described (Kelly, Tyson and Cottrell 1967, Rice and Thomson 1974) have led to the notion of intrinsically ductile materials (most fcc metals, some hcp metals and bcc tantalum), which do not cleave and do not undergo a fracture transition. The remaining solids, including most bcc transition metals, are intrinsically brittle, that is cleavable, and are therefore susceptible to a B-D transition. The fundamental supposition is that, while background plastic relaxations can suppress the transition temperature, the ultimate arbiter of the transition is the ability, or the lack of it, of the crack tip to emit dislocations that can shield the crack and trigger widespread plastic deformation before the crack can propagate by cleavage.

The accumulating experimental evidence on Si (St John 1975, Brede and Haasen 1988, Hirsch *et al.* 1989a, b, George and Michot 1993) and the insight provided by the most recent modelling studies (Schöck and Püschl 1991, Rice and Beltz 1994, Xu, Argon and Ortiz 1995a) suggest that the activation configuration of a dislocation embryo is in the form of a double kink. This observation permits the identification of two distinct types of B-D transition. In the bcc transition metals where barriers to kink mobility are low, the B-D transition is likely to be governed directly by the formation of dislocation embryos at the crack tip, resulting in a nucleation-controlled transition. By contrast, in semiconductors and compounds the observational evidence suggests (Yonenaga, Onose and Sumino 1987, Maeda and Yamashita 1989, Sumino 1989, Yonenaga *et al.* 1989, Yonenaga and Sumino 1989), and modelling verifies (Bulatov, Yip and Argon 1995), that kink mobility is hindered by substantial energy barriers, rendering the B-D transition controlled by dislocation mobility away from the crack tip.

Ultimately, a full understanding of the nucleation-controlled or the mobility-controlled B-D transitions must come from atomistic models of the formation and outward propagation of the dislocation embryo at the crack tip. Before such modelling can be meaningfully attempted, much progress can be made by recourse to hybrid continuum-atomistic approaches (Schöck and Püschl 1991, Rice, Beltz and Sun 1992, Rice and Beltz 1994, Xu *et al.* 1995a) based on the use of a Peierls interplanar potential (Peierls 1940, Nabarro 1947, Foreman, Jaswon and Wood 1951). In a recent development of this technique by Xu *et al.* (1995a), an additional surface production resistance was introduced into the interplanar potential, and the appropriate saddle-point configurations of the dislocation embryo were determined by recourse to a variational boundary integral method advanced by Xu and Ortiz (1993). Xu *et al.* (1995a) concluded that the energetics of dislocation embryo formation on inclined slip planes containing the crack tip, against an additional surface

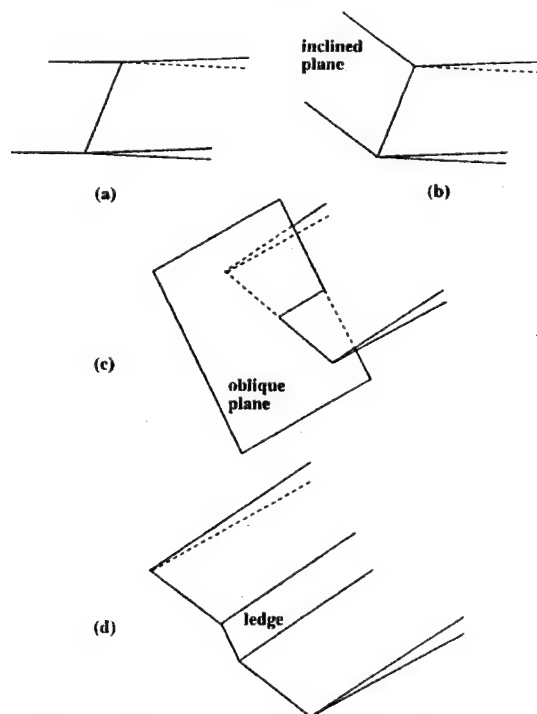
production resistance, is quite unfavourable and does not explain the known B-D transition temperatures. On this basis, it was conjectured that nucleation may be more favourable on oblique slip planes or, as numerous experimental observations have suggested, may occur heterogeneously at the crack front (Chiao and Clarke 1989, Samuels and Roberts 1989, George and Michot 1993). These dislocation nucleation mechanisms are investigated in this communication.

In § 2 we begin by describing the three alternative mechanisms to be appraised, namely nucleation on inclined planes, on oblique planes and on cleavage ledges on the crack front. Following a brief description in § 3 of the fundamental methodology employed in calculations, the three nucleation mechanisms are analysed in turn in § 4. In particular, the B-D transition temperature is estimated from the calculated activation energies. We find that only nucleation on cleavage ledges leads to realistic estimates of the transition temperature. In § 5 we endeavour to put our findings in general perspective.

## § 2. DISLOCATION NUCLEATION MODES

Several alternative modes of dislocation nucleation from crack tips have been contemplated in the past. The modes differ mainly in the relative geometry of the slip plane, the crack surface and the crack front. The configurations considered include nucleation of dislocations on the extension of the crack surface (fig. 1 (a)), nucleation on an inclined plane containing the crack front (fig. 1 (b)), nucleation on an oblique plane (fig. 1 (c)) and nucleation on a cleavage ledge (fig. 1 (d)).

Fig. 1



Alternative modes of dislocation nucleation from a crack tip.

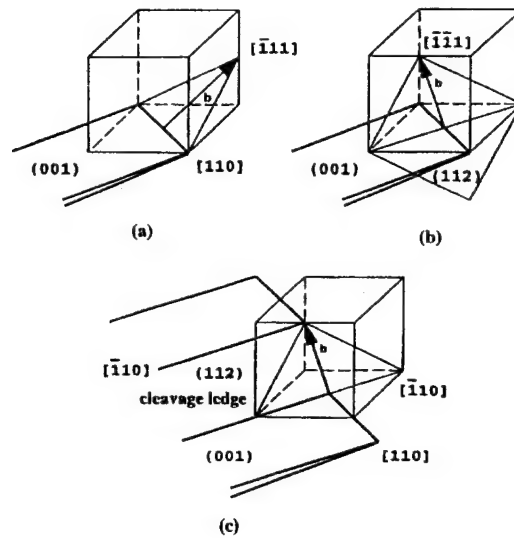
Using the Peierls model of interplanar slip, Rice (1992) and Rice *et al.* (1992) analysed the athermal nucleation of straight dislocations on the extension of the crack surface under pure mode II and mixed mode loading (fig. 1(a)). From this pioneering analysis, Rice *et al.* concluded that nucleation occurs when the crack tip energy release rate attains the unstable stacking energy of the slip plane, at which point half a dislocation core has been formed at the crack tip. Rice and Beltz (1994) have performed a three-dimensional perturbation analysis of dislocation nucleation on the extension of the crack surface which gives the saddle-point configurations and their dependence on the applied energy release rate. Rice and Beltz (1994) also compared their analysis with an earlier approximate calculation of Schöck and Püschl (1991). Xu *et al.* (1995a) have applied a variational boundary integral method to the same problem. In the Xu *et al.* (1995a) approach, the tension-shear potential is modified so as to account for surface production resistance. The results of these calculations indicate that, with the incorporation of surface production, homogeneous nucleation of dislocations on inclined planes is unlikely. This observation notwithstanding, in the interest of completeness we revisit this mode of nucleation in §4.2 for a particular configuration pertaining to  $\alpha$ -Fe.

Experimental observations (Burns and Webb 1970a, b), and the consideration of peak stress levels at the crack tip (Argon 1987), point to dislocation nucleation on oblique planes, such as shown in fig. 1(c), as a likely dislocation nucleation mechanism. This mechanism has the additional advantage of involving nearly no free surface production. Moreover, as observed by Burns and Webb (1970a, b) and pointed out by Argon (1987), the nucleated dislocation can extend self-similarly as a loop attached to the crack tip, which results in steadily increasing shielding. These favourable features notwithstanding, approximate analyses carried out by Argon (1987) and A. S. Argon and D. Deng (1987, unpublished research available on request) suggest that this mode of nucleation also fails to furnish realistic values of the transition temperature. This conclusion is reinforced by the more accurate analysis of §4.3.

The nucleation modes just described are examples of homogeneous nucleation, inasmuch as all points along the crack front are accorded an equal probability of being a nucleation site. However, numerous experiments (Chiao and Clarke 1989, Samuels and Roberts 1989, George and Michot 1993) have shown that actual dislocation nucleation events are rare and occur only at special sites along the crack front, namely at heterogeneities. Extensive documentation of these special sites by George and Michot (1993) has shown them to be mostly cleavage ledges. These ledges form frequently in response to local deviations of the crack driving force away from the crack plane. In cases in which the local stress intensity factor on the cleavage ledge has a substantial  $K_{III}$  component, a dislocation of screw type can be nucleated at the ledge without surface production. Moreover, a usually present substantial  $K_I$  component acting across the plane of the ledge should further promote this mode of nucleation. The analysis presented in §4.4 reveals that, of all the modes considered, dislocation nucleation on ledges is the most energetically favourable and that which leads to the most realistic estimates of the B-D transition temperature. For definiteness, we restrict our attention to  $\alpha$ -Fe and the geometries displayed in fig. 2.

The preferred growth direction of a  $\{100\}$  cleavage crack in  $\alpha$ -Fe can be ascertained by computing the dependence of the energy release rate on the crack front direction within the framework of anisotropic linear elasticity. For pure mode I

Fig. 2



Alternative modes of dislocation nucleation from crack tips in  $\alpha$ -Fe: (a) inclined plane; (b) oblique plane; (c) cleavage ledge.

loading, the analysis consigned to the Appendix reveals that the energy release rate is minimum for a crack front in the  $\langle 110 \rangle$  direction, which is therefore taken to define the most likely crack front direction. Figure 2 displays the crystallography of the nucleation modes: a  $\frac{1}{2}[\bar{1}11]$  dislocation nucleating in an inclined  $(1\bar{1}2)$  plane in fig. 2(a), a  $\frac{1}{2}[\bar{1}\bar{1}1]$  dislocation nucleating in an oblique  $(112)$  plane in fig. 2(b) and a  $\frac{1}{2}[\bar{1}\bar{1}1]$  dislocation nucleating in a cleavage ledge on the  $(112)$  plane in fig. 2(c). In our estimation, these cases represent the most likely configurations for each nucleation mode.

### § 3. METHOD OF ANALYSIS

The analysis builds on the recent developments of Xu *et al.* (1995a), who have extended the scope of the variational boundary integral method of Xu and Ortiz (1993) to encompass problems of dislocation nucleation from atomically sharp cracks. In this model, a slip plane connected to the crack is viewed as an extension of the crack surfaces with a nonlinear interlayer potential acting across it. Thus the crack and the slip plane on which the dislocation nucleates are jointly regarded as a three-dimensional crack system embedded in the linear elastic solid. The interlayer potential acting across the slip plane is modelled by combining the universal binding energy relation of Rose, Ferrante and Smith (1981) with a skewed shear resistance profile (Foreman *et al.* 1951). The interplanar displacements and the crack-opening displacements are represented by a continuous distribution of curved dislocations. This approach introduces no artificial discontinuity between the elastic crack opening and inelastic interplanar slip and separation. The technique has been described in complete detail by Xu and Ortiz (1993) and Xu *et al.* (1995a). In this section, we

briefly outline those aspects of the method which are pertinent to the treatment of the special activation configurations described in §2.

We consider a semi-infinite cleavage crack and a slip plane intersecting the crack front. The crack-slip plane system is loaded remotely by a  $K$  field. The crystallographic slip plane is chosen to be the most advantageous for slip. As the driving force increases, an embryonic dislocation forms progressively until it reaches an unstable equilibrium configuration. The load corresponding to this unstable configuration is defined as the critical driving force for nucleation. The embryonic dislocation profile is characterized as a distribution of interplanar inelastic displacements, defined by Rice (1992) as

$$\delta = A - A^e, \quad (1)$$

where  $A$  and  $A^e$  denote the total and elastic interplanar displacements respectively. The opening displacement  $\mathbf{u}$  of the crack surface, including the inelastic displacements along the slip plane, can be written as

$$\mathbf{u} = \bar{\mathbf{u}} + \delta, \quad (2)$$

where  $\bar{\mathbf{u}}$  represents the standard  $K$  displacement field for a reference semi-infinite crack. The term  $\bar{\mathbf{u}}$  matches the behaviour of the crack-opening displacements far away from the tip. Consequently, the additional term  $\delta$  modifying  $\bar{\mathbf{u}}$ , which is the primary unknown in the analysis, is expected to decay rapidly to zero with distance away from the crack tip. In this manner,  $\delta$  can be restricted to a finite domain  $\hat{S}_c \cup \hat{S}_s$ , where  $\hat{S}_c$  lies on the crack surface and  $\hat{S}_s$  on the slip plane, connected to the crack front.

Following the procedure introduced by Xu *et al.* (1995a) and Xu and Ortiz (1993), the potential energy of the whole system can be written in the form

$$\Pi[\bar{\mathbf{u}} + \delta] = W[\bar{\mathbf{u}} + \delta] + V[\delta] = W_1[\bar{\mathbf{u}}] + W_1[\delta] + W_2[\bar{\mathbf{u}}, \delta] + V[\delta], \quad (3)$$

where we identify  $W_1[\bar{\mathbf{u}}]$  as the elastic strain energy of the system, free of inelastic modifications,  $W_1[\delta] + V[\delta]$  as the self-energy of the system of inelastic modifications consisting of the distributed dislocations and the interplanar interaction energy on the slip plane, and  $W_2[\bar{\mathbf{u}}, \delta]$  is the interaction energy of the initial unmodified system with the second system of modifications. Of these energies those of relevance in the variational approach are those that depend on the unknown inelastic modification  $\delta$ . They have the forms given below. The self-energy of the inelastic modification is given as

$$\begin{aligned} W_1[\delta] = & \frac{\mu}{4\pi} \int_{\hat{S}_c + \hat{S}_s} \int_{\hat{S}_c + \hat{S}_s} \frac{[\mathbf{e}_i \cdot (\mathbf{n} \times \nabla \delta_j)_2][\mathbf{e}_j \cdot (\mathbf{n} \times \nabla \delta_i)_1]}{R} dS_1 dS_2 \\ & - \frac{\mu}{8\pi} \int_{\hat{S}_c + \hat{S}_s} \int_{\hat{S}_c + \hat{S}_s} \frac{[\mathbf{e}_i \cdot (\mathbf{n} \times \nabla \delta_i)_1][\mathbf{e}_j \cdot (\mathbf{n} \times \nabla \delta_j)_2]}{R} dS_1 dS_2 \\ & + \frac{\mu}{8\pi(1-\nu)} \int_{\hat{S}_c + \hat{S}_s} \int_{\hat{S}_c + \hat{S}_s} [\mathbf{e}_i \times (\mathbf{n} \times \nabla \delta_i)_1] \cdot \mathbf{T} \cdot [\mathbf{e}_j \times (\mathbf{n} \times \nabla \delta_j)_2] dS_1 dS_2, \end{aligned} \quad (4)$$

where  $(\cdot)_1$  and  $(\cdot)_2$  denote two different points on the domain  $\hat{S}_c \cup \hat{S}_s$ ,  $R$  is the distance between these two points,  $\mathbf{e}_i, i = 1, 2, 3$ , are Cartesian basis vectors,  $\mathbf{n}$  is the normal vector to the crack surface or the slip plane and  $\mathbf{T}$  is a tensor with components

$$T_{ij} = \frac{\partial^2 R}{\partial x_i \partial x_j}. \quad (5)$$

The interaction energy between the elastic crack field and the inelastic modifications is

$$W_2[\bar{u}, \delta] = K_I Q_I[\delta] + K_{II} Q_{II}[\delta] + K_{III} Q_{III}[\delta], \quad (6)$$

where

$$Q_I[\delta] = \int_{\hat{s}_c + \hat{s}_s} \mathbf{n} \cdot \boldsymbol{\sigma}_I \cdot \boldsymbol{\delta} dS, \quad (7a)$$

$$Q_{II}[\delta] = \int_{\hat{s}_c + \hat{s}_s} \mathbf{n} \cdot \boldsymbol{\sigma}_{II} \cdot \boldsymbol{\delta} dS, \quad (7b)$$

$$Q_{III}[\delta] = \int_{\hat{s}_c + \hat{s}_s} \mathbf{n} \cdot \boldsymbol{\sigma}_{III} \cdot \boldsymbol{\delta} dS, \quad (7c)$$

and  $\boldsymbol{\sigma}_I$ ,  $\boldsymbol{\sigma}_{II}$  and  $\boldsymbol{\sigma}_{III}$  are stresses of the standard  $K$  fields in modes I, II and III respectively, for unit stress intensity factor. The integration is partly extended over the real crack surface since the front of the reference semi-infinite crack is actually located some distance away from the physical crack front. This treatment permits the use of a non-singular Dugdale-Barenblatt crack as a reference crack to improve systematically the quality of the numerical solution (Xu and Ortiz 1993). Finally, the potential energy of the interplanar inelastic deformation on the slip plane is

$$V[\delta] = \int_{\hat{s}_s} \Phi[\delta] dS, \quad (8)$$

where  $\Phi[\delta]$  is an interplanar potential defined per unit area of the slip plane. It is possible to model the general potential  $\Phi[\delta]$  with shear displacements allowed in all directions on the slip plane. However, atomistic simulations have shown that displacements and the attendant shear resistance take place predominantly in the direction of the dominant Burgers vector (Yamaguchi, Vitek and Pope 1981, Sun *et al.* 1991, Juan and Kaxiras 1996). Therefore we adopt the constrained displacement hypothesis of Rice (1992) and Sun *et al.* (1994), whereby the interplanar shear displacement  $\Delta_r$  is constrained to be aligned with the Burgers vector direction. The shear separation resistance  $\tau$  and tension separation resistance  $\sigma$  follow from the inelastic shear displacements  $\delta_r$  and tensile separation displacement  $\delta_\theta$  through the relations (Beltz and Rice 1991, Xu *et al.* 1995a)

$$\delta_r = \Delta_r - \frac{h}{\mu} \tau(\Delta_r, \Delta_\theta), \quad (9a)$$

$$\delta_\theta = \Delta_\theta - \frac{h}{c} \sigma(\Delta_r, \Delta_\theta), \quad (9b)$$

and

$$\tau(\Delta_r, \Delta_\theta) = A(\Delta_\theta) \left[ \sin\left(\frac{2\pi\Delta_r}{b}\right) + \frac{\beta-1}{2} \sin\left(\frac{4\pi\Delta_r}{b}\right) \right], \quad (10a)$$

$$\sigma(\Delta_r, \Delta_\theta) = \left[ B(\Delta_r) \left( \frac{\Delta_\theta}{L} \right) - C(\Delta_r) \right] \exp\left(-\frac{\Delta_\theta}{L}\right), \quad (10b)$$

with



$$A(\Delta_\theta) = \frac{\pi\gamma_{us}^{(u)}}{b} \left[ 1 + \frac{1}{q} \frac{q-p}{1-p} \frac{\Delta_\theta}{L} \right] \exp\left(-\frac{\Delta_\theta}{L}\right), \quad (11a)$$

$$B(\Delta_r) = \frac{2\gamma_s}{L} \left\{ 1 - \frac{q-p}{1-p} \left[ \sin^2\left(\frac{\pi\Delta_r}{b}\right) + \frac{\beta-1}{4} \sin^2\left(\frac{2\pi\Delta_r}{b}\right) \right] \right\}, \quad (11b)$$

$$C(\Delta_r) = \frac{2\gamma_s}{L} \frac{p(1-q)}{1-p} \left[ \sin^2\left(\frac{\pi\Delta_r}{b}\right) + \frac{\beta-1}{4} \sin^2\left(\frac{2\pi\Delta_r}{b}\right) \right], \quad (11c)$$

$$q = \frac{\gamma_{us}^{(u)}}{2\gamma_s}, \quad (12a)$$

$$p = \frac{\Delta_\theta^*}{L}, \quad (12b)$$

where:

$\mu$  is the shear modulus,

$c$  is the uniaxial strain elastic modulus,

$b$  is the magnitude of Burgers vector,

$h$  is the interatomic layer spacing,

$L$  is the interplanar tensile displacement at  $\sigma = \sigma_{\max}$ ,

$\gamma_{us}^{(u)}$  is the unrelaxed unstable stacking energy,

$\gamma_s$  is the surface energy,

$\Delta_r$  is the total interplanar shear displacement,

$\Delta_\theta$  is the total interplanar normal displacement, and

$\Delta_\theta^*$  is the relaxed interplanar tensile displacement at  $\sigma = 0$  in the saddle-point configuration and

$\beta$  is the skewness parameter in the interplanar shear resistance.

A traction-displacement relation including the effect of surface production on an inclined slip plane at the crack tip has been proposed by Xu *et al.* (1995a). The material constants for  $\alpha$ -Fe used in calculations are taken from table 1 of Xu *et al.* (1995a) and are reproduced here for convenience in table 1.

The unknown displacements  $\delta$  follow by rendering the potential energy  $\Pi[\bar{\mathbf{u}} + \delta]$  stationary. This is achieved by discretizing the integral equation with six noded elements distributed on the crack surface. The nonlinear equations are solved by a Newton-Raphson iteration. The saddle-point configurations are activated by introducing a small perturbation into the system at the bifurcation point, based on the solution of a first-order eigenvalue problem if necessary. Solutions are obtained by

Table 1. Material properties for  $\alpha$ -Fe.

Slip system	$T$ (K)	$\mu$ ( $10^5$ MPa)	$c$	$\gamma_{us}^{(u)}$ (J m $^{-2}$ )	$2\gamma_s$ (J m $^{-2}$ )	$\beta$	$p$	$q$	$L/b$
$\frac{1}{2}[111](1\bar{1}0)$	4.2	0.756	3.125	0.517	3.33	2.25	0.217	0.155	0.187
$\frac{1}{2}[\bar{1}\bar{1}1](112)$	4.2	0.756	3.125	0.581	3.80	1.74	0.210	0.153	0.215

recourse to interplanar displacement control achieved through the introduction of Lagrange multipliers.

#### § 4. DISLOCATION NUCLEATION ANALYSIS

##### 4.1. Three modes of nucleation

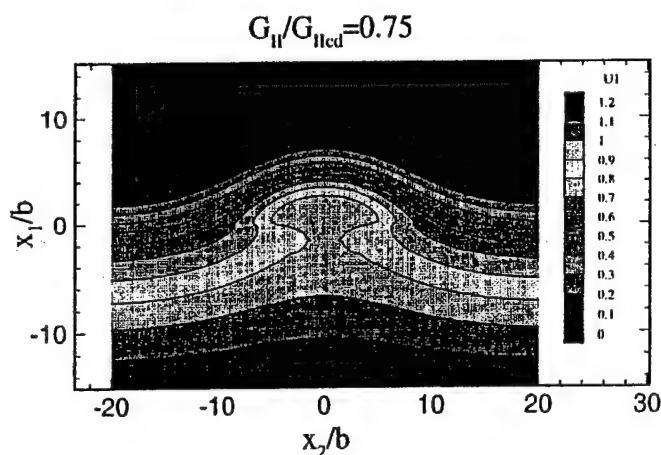
In this section we analyse the nucleation of dislocations from a cleavage crack in  $\alpha$ -Fe as processes typical of bcc metals in which kink mobility is high. We consider the three competing mechanisms discussed in § 2, namely nucleation on an inclined plane, on an oblique plane, and on a cleavage ledge. The principal objective of the calculations is the determination of the saddle-point configurations and the dependence of the corresponding activation energies on the crack driving force. These results are subsequently used to estimate the B-D transition temperatures for each geometry. The geometry furnishing the most realistic value of the B-D transition temperature may be reasonably identified with the preferred nucleation configuration in  $\alpha$ -Fe.

##### 4.2. Nucleation of dislocations on the inclined plane

The previous analysis of Xu *et al.* (1995a) showed that nucleation of dislocations on the inclined planes is quite unlikely for most crystals. Nevertheless, for comparison with the other modes of nucleation, we shall re-examine the nucleation of dislocations on the inclined plane (112) in  $\alpha$ -Fe as depicted in fig. 2(a).

We begin by solving the saddle-point configuration of a dislocation under a pure mode II type of loading. The crack surface on the (001) plane probes the (112) slip plane with the crack front being parallel to the [110] direction. Two representative saddle-point configurations of the dislocation embryo under normalized loading levels  $G_{II}/G_{IIcd}$  of 0.75 and 0.50 are illustrated in fig. 3 and fig. 4 respectively. The dependence of the activation energy on the crack front driving force from a series of such solutions is plotted in fig. 5.

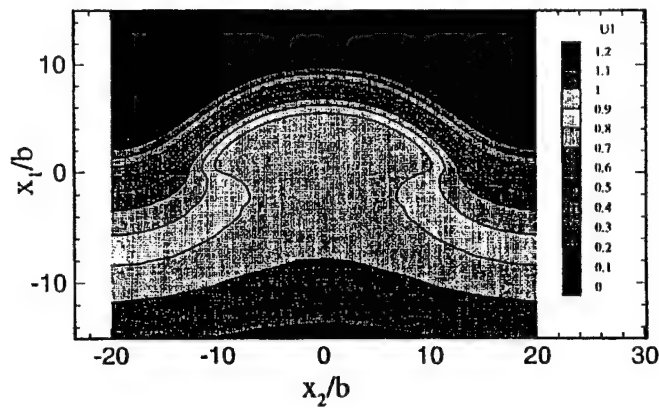
Fig. 3



The saddle-point configuration at  $G_{II}/G_{IIcd} = 0.75$  under mode II loading.

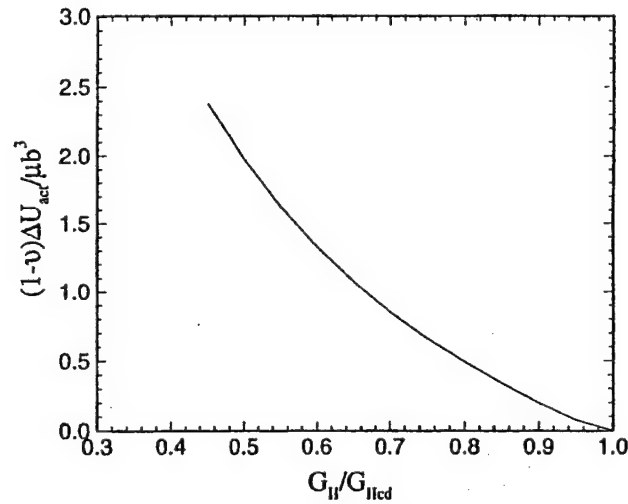
Fig. 4

$$G_{II}/G_{IIcd}=0.50$$



The saddle-point configuration at  $G_{II}/G_{IIcd} = 0.50$  under mode II loading.

Fig. 5



The activation energy for dislocation emission under pure mode II loading.

To obtain remote mode I loading, we assume that the nucleation process is essentially equivalent to the mode II crack case under a loading equal to the effective stress intensity factors on the inclined plane, which are,

$$K_I^{\text{eff}} = K_I \cos^3 \left( \frac{\theta}{2} \right), \quad (13a)$$

$$K_{II}^{\text{eff}} = K_I \cos^2 \left( \frac{\theta}{2} \right) \sin \left( \frac{\theta}{2} \right). \quad (13b)$$

More precisely, these stress intensity factors are those at the tip of a small crack emanating from the crack tip in the direction of the slip plane (Cotterell and Rice 1980). The critical mode I loading for nucleation of a straight dislocation in two dimensions on the inclined plane can then be estimated from the analysis of Rice using eqn. (13*b*) and is given by

$$\frac{G_{\text{Icd}}}{G_{\text{Ic}}} = \frac{8}{(1 + \cos \theta) \sin^2 \theta} \frac{\gamma_{\text{us}}}{2\gamma_{\text{s}}}. \quad (14)$$

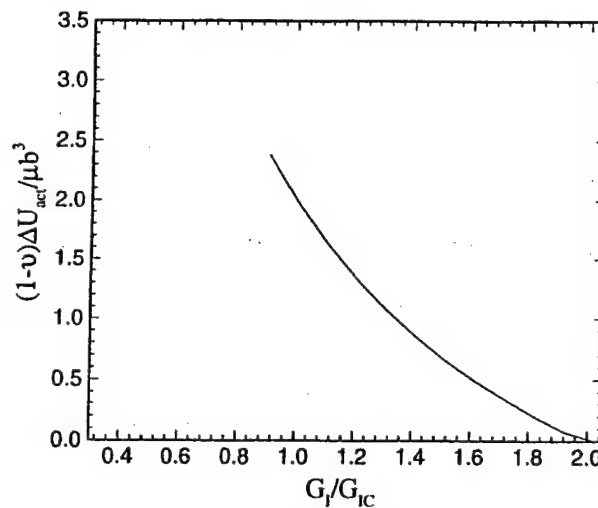
However, this estimate which considers neither tension softening nor surface production resistance underestimates the energetics of the configuration for most transition metals and intermetallics (Xu *et al.* 1995a) because, while the tension softening does make nucleation somewhat easier, the surface production resistance makes it comparatively much more difficult. The dependence of the activation energy of the actual three-dimensional saddle-point configuration analysis on the remote mode I loading is shown in fig. 6, as rescaled from fig. 5 through eqn. (13*b*).

#### 4.3. Nucleation of dislocations on the oblique plane

As remarked in § 2, dislocation nucleation on oblique planes has been put forth as a likely mode of nucleation. However, the capability required for the analysis of this mechanism had been heretofore unavailable. Approximate analyses based on the consideration of perfect dislocations and the introduction of a core cut-off radius have led to estimates of the B-D transition temperatures several orders of magnitude higher than what is experimentally observed, prompting suggestions that nucleation should involve fractional dislocations (Argon 1987).

In this section, we provide a direct analysis of the formation of dislocation embryos on oblique planes in  $\alpha$ -Fe. A comparison of resolved shear stresses on all

Fig. 6



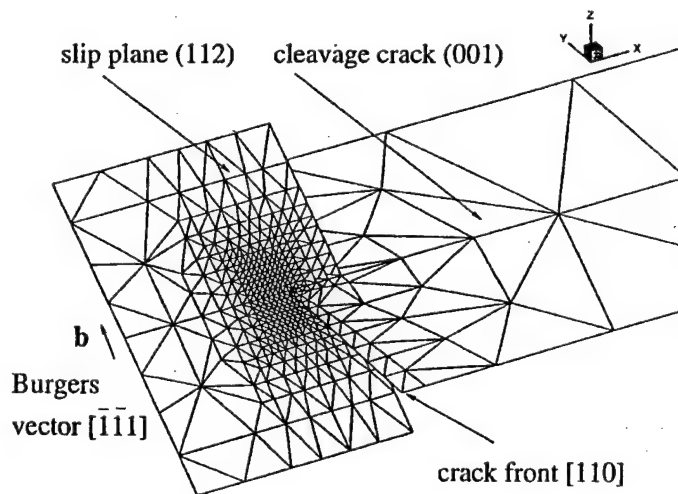
Dependence of the activation energy for dislocation nucleation on the inclined {112} planes on the remote mode I loading.

potentially active slip systems points to the configuration in fig. 2(b) as the most favourable for nucleation. In calculations, we artificially constrain the cleavage plane from propagating to enable the computation of the critical driving force for dislocation nucleation. If the resulting athermal critical driving force is less than  $G_{Ic}$  for cleavage, the crystal is intrinsically ductile. Contrariwise, if the critical driving force is greater than that for cleavage, the crystal is cleavable or intrinsically brittle. However, on the verge of crack propagation by cleavage, a dislocation can still be nucleated through thermal activation. The calculation of the activation energy for such thermally assisted dislocation nucleation is therefore of primary interest.

Figure 7 shows the geometry of the problem and the mesh used in the analysis. A close-up view of a typical saddle-point configuration of an embryonic dislocation loop emanating from the crack tip is shown in fig. 8 for the geometry of fig. 2(b). The calculated dependence of the activation energy on the crack driving force near the athermal threshold is shown in fig. 9. The critical driving force at the athermal threshold and the attendant activation energies are so high that they render the nucleation mechanism highly improbable. The calculation was discontinued at  $G_I/G_{Ic} = 1.6$  when the improbability of the mechanism had become amply clear. The activation energy at  $G_I/G_{Ic} = 1.0$  can be estimated by extrapolation, which provides an adequate basis for reaching a firm negative conclusion *vis-à-vis* the likelihood of the mechanism. One factor which contributes to rendering the mechanism ineffective is the fact that the resolved shear stress decays away from the crack tip in all directions, making the area-averaged shear stress smaller than that on the inclined plane.

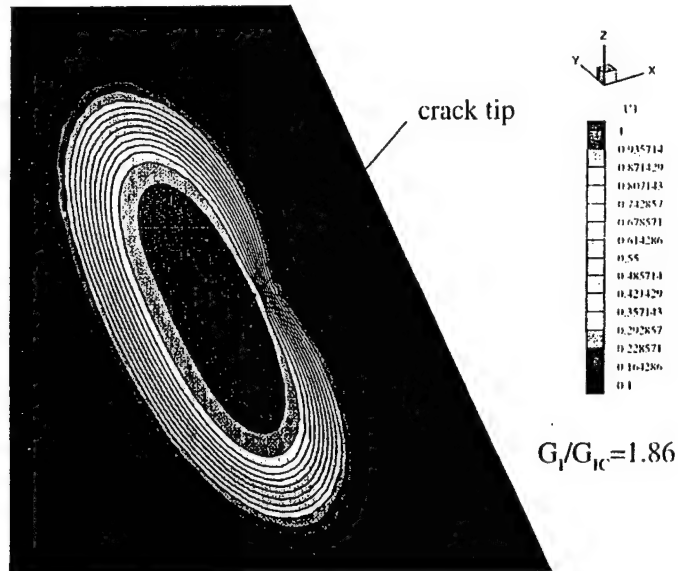
It should be noted that in the above analysis the inelastic displacements across the slip plane were treated as total displacements for computational convenience. This tends to underestimate slightly the activation energy as will be demonstrated subsequently. Moreover, we have only considered two-sided activation configura-

Fig. 7



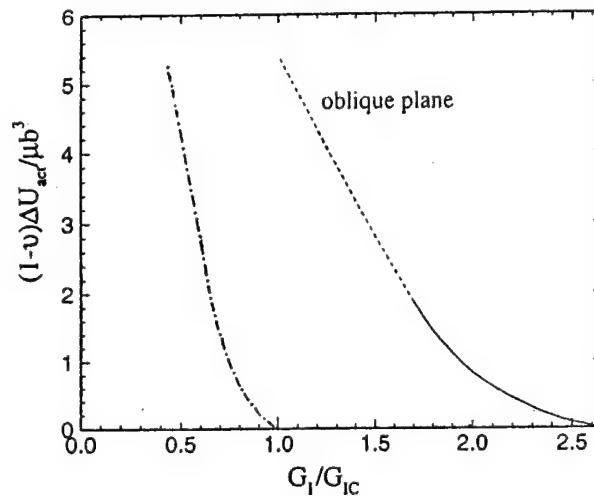
Mesh used in the analysis of dislocation nucleation on an oblique plane in  $\alpha$ -Fe for the geometry shown in fig. 2(b).

Fig. 8



The saddle-point configuration of a dislocation embryo emitted from the crack tip on an oblique plane in the interior.

Fig. 9



Activation energy for dislocation nucleation on an oblique plane in the interior (---, —) and near a free surface (— · —).

tions in our analysis. One-sided configurations, in which dislocation embryos expand primarily on one side of the oblique plane, might conceivably require lower activation energies. However, in view of the results just described, it seems unlikely that this reduction in the activation energy should be sufficient to justify a detailed analysis of one-sided configurations.

The above analysis establishes convincingly that nucleation of dislocations on oblique planes in the interior of the cracked solid is most unlikely. A very different conclusion can be reached, however, for this mechanism where the crack front reaches a free surface where no plane strain stress is present, and the resolved shear stresses on the oblique planes become much higher. An estimate of this enhanced nucleation probability on the oblique plane near the surface is easily obtained by rescaling the driving forces in fig. 9, in proportion to the resolved shear stresses on the oblique slip planes near the free surface against those in the interior as (for the geometry of fig. 2(b))

$$\frac{G_{\text{Is}}}{G_{\text{Ii}}} = \left( \frac{3 - 4\nu}{3} \right)^2, \quad (15)$$

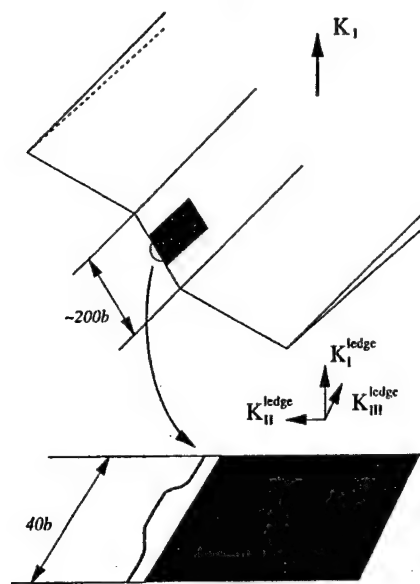
where  $G_{\text{Is}}$  and  $G_{\text{Ii}}$  are respective energy release rates required for initiation of a dislocation near the free surface and in the interior. The result for  $\alpha$ -Fe with  $\nu = 0.291$  is shown as the chain curve in fig. 9, which now suggests almost spontaneous embryo formation near the free surface. This, however, is not true, since in this case at least a partial surface ledge must be produced, which will make the nucleation more difficult, but presumably still much easier than in the interior. An abundance of such nucleation events has been observed by George and Michot (1993).

#### 4.4. Nucleation of dislocations on a cleavage ledge

Cleavage surfaces in metallic crystals invariably contain ledges parallel to the direction of crack propagation. These are likely to form when the principal tension driving the crack deviates slightly on a local scale, requiring the crack to make small adjustments along its front. This microroughness of the cleavage surface depends also on the crystallography of the cleavage planes and crack propagation direction as well as on temperature. The height of the observed ledges can range from several atomic spacings to microns. Numerous observations (Chiao and Clarke 1989, Hirsch *et al.* 1989a, b, George and Michot 1993) have revealed that dislocation nucleation at a crack front is a relatively rare phenomenon associated with crack front heterogeneities. This strongly suggests that ledges are likely sites for heterogeneous nucleation of dislocations (Zhou and Thomson 1991). In what follows we analyse this mechanism as it is likely to operate in  $\alpha$ -Fe.

Consider a cleavage crack propagating under mode I loading. The crack contains ledges of a width of roughly a hundred atomic spacings distributed along its front, as depicted later in fig. 11. The presence of a considerable local mode III stress intensity factor acting on the ledge is expected to promote nucleation. Moreover, the direction of the Burgers vector of the dislocation embryo, which is parallel to the local crack front on the ledge, requires no fresh surface production. In view of the mesh size requirements to resolve adequately the dislocation embryo, a direct simulation of the complete system does not appear possible at present. This difficulty can be side-stepped by the approximate two-scale approach sketched in fig. 10. The distribution of stress intensity factors along the front of the crack, including the ledge, is first calculated by recourse to a linear elastic analysis. The small stretch of ledge on which the dislocation embryo nucleates is then idealized as a semi-infinite crack subjected to the local stress intensity factors determined in the first analysis. Because of the vastly disparate scales of the ledge and the activation configuration, the results

Fig. 10

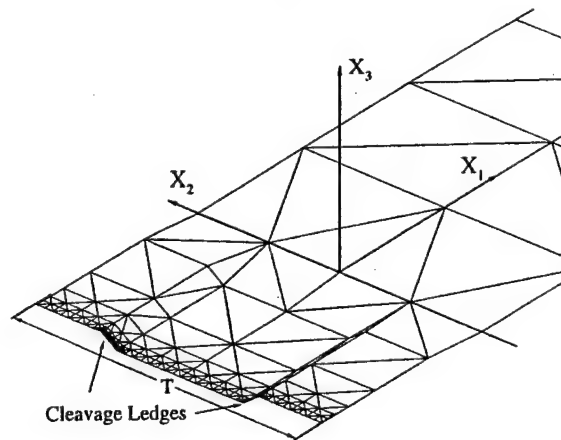


Dislocation nucleation on a cleavage ledge.

obtained in the manner just outlined should be ostensibly identical with those obtained from a direct simulation.

The distribution of stress intensity factors on the crack front can be readily calculated by the boundary element method of Xu and Ortiz (1993). The mesh used in the analysis is shown in fig. 11. As is evident from the figure, two symmetric ledges are included in the mesh. This permits the enforcement of periodic boundary

Fig. 11



Mesh used in the computation of the stress intensity factors along a crack front containing cleavage ledges.



conditions, which greatly facilitates the calculations (Xu and Ortiz 1993). For small width-to-separation ratios, the interaction between the ledges may be expected to be negligible. The calculated stress intensity factors are shown in fig. 12. On the ledge, the dominant stress intensity factors are  $K_I^{\text{ledge}} \approx 0.81K_I$  and  $K_{III}^{\text{ledge}} \approx 0.35K_I$ . On the verge of brittle fracture, it therefore follows that  $K_{III}^{\text{ledge}} \approx 0.35K_{Ic}$ . For mode III loading, Rice (1992) has determined the athermal critical condition for nucleation of a screw dislocation to be

$$G_{IIIcd} = \gamma_{us} = \frac{1}{2\mu} K_{IIIcd}^2. \quad (16)$$

Using the relation

$$G_{Ic} = 2\gamma_s = \frac{1-\nu}{2\mu} K_{Ic}^2, \quad (17)$$

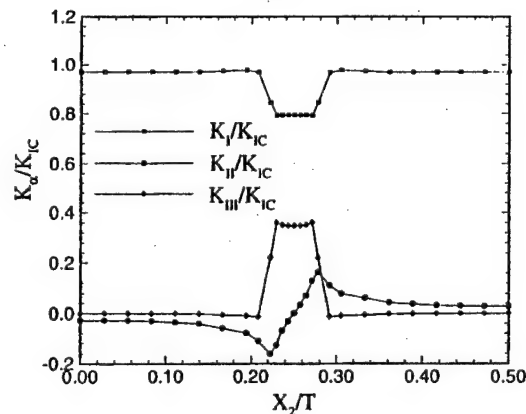
we obtain

$$K_{IIIcd} = \left( \frac{(1-\nu)\gamma_{us}}{2\gamma_s} \right)^{1/2} K_{Ic} = 0.357K_{Ic} > 0.350K_{Ic}. \quad (18)$$

This calculation suggests that screw dislocations cannot be nucleated spontaneously below the critical condition for cleavage, which is consistent with the expectation that  $\alpha$ -Fe single crystals be intrinsically brittle. However, the small difference between the numerical factors is most likely to be below the accuracy of the calculation, which viciates the argument to a considerable extent. Indeed, consideration of tension softening, the effect of anisotropy and uncertainties in the material parameters can all change eqn. (18) to some degree. The calculation does nevertheless provide a first indication that screw dislocation nucleation from a ledge may indeed be much easier than nucleation on inclined and oblique planes.

Next we consider a semi-infinite crack under simple mode III loading. Tension softening has been shown to be of little consequence up to values of  $K_I$  of the order of  $0.9K_{Ic}$  (Xu *et al.* 1995a) and can therefore be safely neglected. Figures 13 and 14 show two saddle-point configurations of the embryonic screw dislocations for nor-

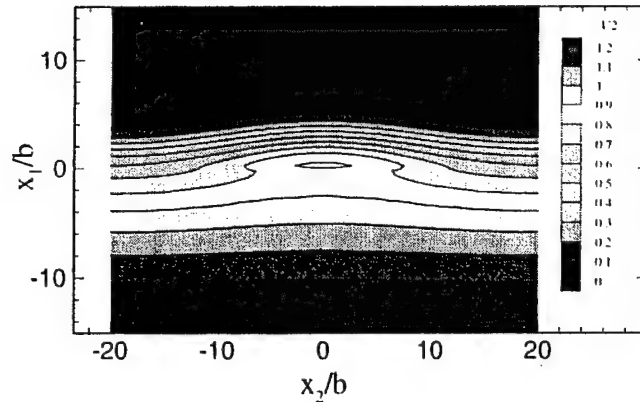
Fig. 12



Distribution of stress intensity factors on a cleavage ledge.

Fig. 13

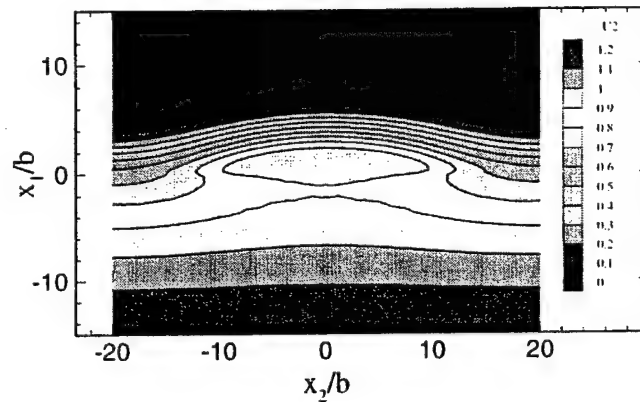
$$G_{III}/G_{IIIcd}=0.75$$



The saddle-point configuration for nucleation of a screw dislocation from a cleavage ledge,  
 $G_{III}/G_{IIIcd} = 0.75$ .

Fig. 14

$$G_{III}/G_{IIIcd}=0.50$$



The saddle-point configuration for nucleation of a screw dislocation from a cleavage ledge,  
 $G_{III}/G_{IIIcd} = 0.50$ .

malized load levels  $G_{III}/G_{IIIcd} = 0.75$  and  $0.50$ . Interestingly, these saddle-point configurations are flatter than those of edge dislocations, shown in figs. 3 and 4, as befits the lower line energies of screw dislocations. As the screw dislocation bows out, it tends to form double kinks with short edge components. By way of contrast, the screw double kinks of the edge dislocation embryo tend to be longer and the edge segment shorter (figs. 3 and 4). Computationally, this requires a larger periodic domain in the case of the screw embryo, which inevitably increases the size of the problem. The dependence of the activation energy on the crack driving force is

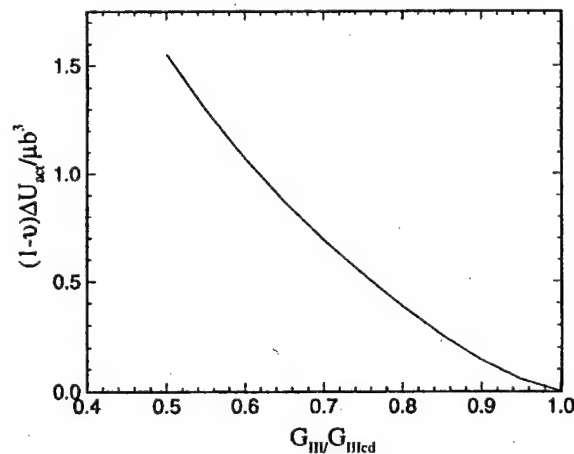
shown in fig. 15. The low values of the activation energy relative to those computed for nucleation on inclined and oblique planes is particularly noteworthy.

Finally, we endeavour to ascertain the magnitude of the errors incurred as a result of the various simplifications adopted in the calculations. In order to estimate the effect of tension softening, we consider the simple two-dimensional problem of a semi-infinite crack subjected to mixed mode I and III. We take the ratio  $K_{III}/K_I$  to be  $0.35/0.81 = 0.43$ , which is the case of interest in the ledge problem. We also wish to estimate the effect of identifying the interlayer inelastic displacements with the total displacements, that is of setting  $\Delta = \delta$ , a simplification which has been adopted for computational convenience. Physically, this corresponds to taking the interplanar distance  $h$  across the slip plane to be zero. In the ledge problem, we have additionally set the parameter  $p = 0$  for want of a better estimate. Figure 16 shows the effect on the activation energy of variations in these parameters. As is evident from the figure, the  $h = 0$  approximation accounts for modest errors of the order of 15% at most, over much of the range of  $G_I/G_{Ic}$ . The effect of tension softening in the range  $0 \leq K_I \leq 0.43K_{III}$  is indeed seen to be negligible. The lowest curve for the activation energy has been calculated for  $p = 0.217$  as a reasonable estimate. It shows that non-zero values of  $p$  can reduce the activation energy significantly, which indicates the need for more reliable estimates of this parameter. The effect of the periodicity of the computational model on the activation energy was found by Xu *et al.* (1995a) to decay rapidly with increasing size of the period.

#### 4.5. Estimates of the brittle-to-ductile transition temperature

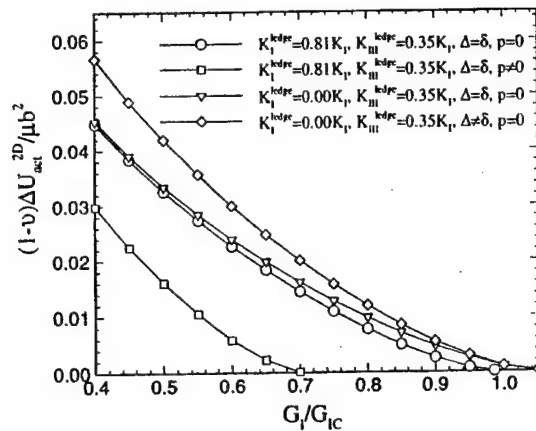
As noted in the foregoing, the B-D transition in bcc transition metals, and particularly in  $\alpha$ -Fe, is most likely probably controlled solely by dislocation nucleation. Therefore, the preceding results can be used to estimate the B-D transition temperatures attendant to the three nucleation modes considered, namely nucleation on inclined planes, on oblique planes, or on cleavage ledges. No precise experimental

Fig. 15



The activation energy for dislocation emission in simple mode III loading, at the cleavage ledge.

Fig. 16



Parametric sensitivity of the activation energy for dislocation emission on cleavage ledges.

measurements of the transition temperature of single-crystal  $\alpha$ -Fe are available. The transition temperature for polycrystalline low-C steel is about 250 K, as determined from Charpy impact experiments (McClintock and Argon 1966). In the absence of more direct measurements, we shall suppose the transition temperature for pure  $\alpha$ -Fe to be in the range 250–300 K. A B–D transition scenario achievable experimentally was proposed by Argon (1987) and consists of the arrest of a cleavage crack propagating against a temperature gradient.

The evaluation of the B–D transition temperature from the activation energy can be effected as suggested by Xu *et al.* (1995a), who give the relation

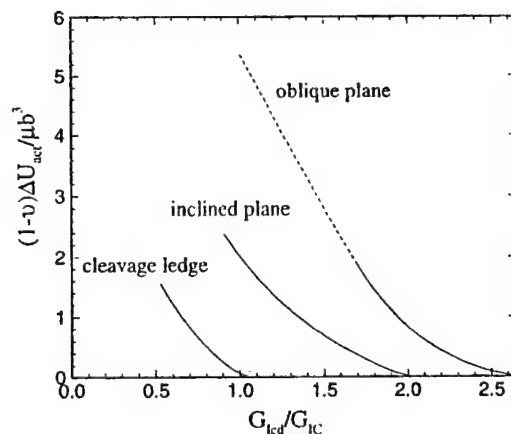
$$T_{BD} = \left( \frac{\ln(c/v)}{\alpha} + \eta \frac{T_0}{T_m} \right)^{-1} T_0. \quad (19)$$

Here  $T_0 \equiv \mu b^3 / k(1-\nu) \approx 1.2 \times 10^5$  K; the melting temperature  $T_m = 1809$  K for  $\alpha$ -Fe;  $\alpha = (1-\nu) \Delta U_{act} / \mu b^3$  is the normalized activation energy;  $c$  is the speed of sound;  $v \approx 1 \text{ cm s}^{-1}$  is a typical crack propagation velocity, giving  $\ln(c/v) \approx 10$ ;  $\eta \approx 0.5$  is a coefficient describing the temperature dependence of the shear modulus which, to a first approximation, is presumed of the form

$$\mu = \mu_0 \left( 1 - \eta \frac{T}{T_m} \right). \quad (20)$$

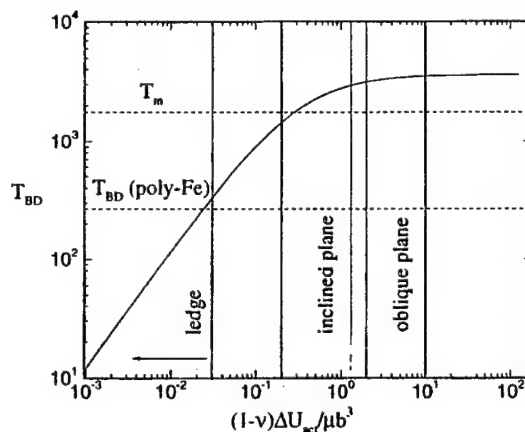
The dependence of the activation energy for nucleation of dislocation embryos on the energy release rate  $G_I$  is shown in fig. 17 for each of the three modes of nucleation considered in the foregoing. The activation energy at the critical driving force for cleavage, that is, at  $G_I / G_{IC} = 1$ , determines the transition temperature through eqn. (19). This relation is plotted in fig. 18, together with the activation energies for nucleation on inclined planes, oblique planes and ledges. Also shown in the figure is the value of the transition temperature for polycrystalline Fe. It is evident from this comparison that only nucleation on cleavage ledges results in transition temperatures which approach the expected value for  $\alpha$ -Fe. The remaining two mechan-

Fig. 17



The activation energies for dislocation nucleation at a crack tip in  $\alpha$ -Fe, for three different modes of nucleation.

Fig. 18



The estimated B-D transition temperatures in  $\alpha$ -Fe.

isms grossly overestimate the transition temperature. These results strongly suggest that dislocation nucleation from a crack tip in  $\alpha$ -Fe is an inhomogeneous process. The dislocation loops which eventually shield the crack are emitted from ledges distributed along the crack front.

### § 5. DISCUSSION

We have viewed the transition in fracture behaviour from ductile to brittle or, more fundamentally, from brittle to ductile as a manifestation of crack-tip-initiated plasticity counteracting the tendency for brittle behaviour by cleavage cracking. In this regard, we have distinguished two different behaviours: that in which the transi-

tion is controlled by nucleation of dislocation embryos from the crack tip, which is characteristic of bcc transition metals, and that in which the transition is controlled by the mobility of dislocations away from the crack tip, which is typical of semiconductors and compounds. The distinguishing characteristic between these two behaviours is the mobility of kinks on dislocations. Experiments indicate that in bcc transition metals (at anything but the lowest temperatures) there is little resistance to the motion of kinks along dislocation lines. By contrast, in semiconductors such as Si and other compounds for which good information on dislocation mobility exists (Yonenaga *et al.* 1987, 1989, Yonenaga and Sumino 1989) it is known that the stress dependence of the dislocation velocity is nearly linear, implying that a process of kink drift controls dislocation motion. Computer simulations (Bulatov *et al.* 1995) confirm that kink motion along dislocations is indeed hindered by very substantial energy barriers in Si. These observations suggest that the B-D transition is nucleation controlled in bcc transition metals and mobility controlled in semiconductors and semiconducting compounds.

An additional mechanism which can influence fracture behaviour is crack-tip shielding by general 'background' plasticity. A particularly elegant and compelling analysis of this mechanism was advanced by Freund and Hutchinson (1985). Based on the known rate dependence characteristics of steels, which exhibit a marked stress upturn at high strain rates, Freund and Hutchinson (1985) demonstrated that brittle fracture can take place at high crack propagation velocities. This results in progressively diminishing inelastic response but that the transition is smooth and spread out, and far from being abrupt. The importance of background plasticity effects has been demonstrated experimentally by Hirsch *et al.* (1989a), who have shown that the sharp B-D transition in dislocation-free Si becomes diffuse, and moves to somewhat lower temperatures, when the crystals are initially dislocated by a pre-deformation step. The effect of background plasticity can therefore be regarded as one of modulating the B-D transition, with the ultimate controlling mechanism residing in crack-tip-initiated processes.

It is observed that intrinsically brittle materials such as crack-free Fe (Allen 1959) and W (Argon and Maloof 1966a) single crystals can often be plastically deformed at cryogenic temperatures with low plastic resistance when they are in pure form but fracture in a brittle manner when they are less pure and exhibit a high plastic resistance. This observation has been used as an argument in support of the background plasticity model of the fracture transition. This is partly correct. An intrinsically brittle solid only demonstrates its brittle characteristics when a crack is present. In well prepared Fe and W crystals, cracks do not exist initially and need to be produced by plastic deformation, most prominently by the intersection of deformation twins (Argon and Maloof 1966b). This requires a relatively high stress to nucleate the twins. In pure metallic crystals, the plastic yield stress is usually below the critical stress required for twinning, and brittle microcracks are not produced until the flow stress is raised by strain hardening to a sufficient level for twinning.

In the present paper we have reported on the key process of dislocation nucleation from crack tips in bcc transition metals, and particularly in  $\alpha$ -Fe, where nucleation is expected to be the controlling process. We have noted that, as is now well established (Schöck and Püschl 1991, Rice *et al.* 1992, Rice and Beltz 1994, Xu *et al.* 1995a), at the saddle point the critical activation configuration of the nucleated dislocation consists only of partially completed core matter. Consequently, we have termed these configurations dislocation embryos.

We note that a cursory examination of the shapes of the dislocation embryos shown in figs. 3 and 4, for the case of the inclined plane, and to a lesser extent, those in figs. 13 and 14, for the substantially screw-type embryos on cleavage ledges might give the counter-intuitive appearance of closed loops that are in the process of formation. This is an illusion since the level contours shown in these figures pertain to the total displacements at the crack tip where only the bulged portions of these, in the region of  $x_1/b > 0$ , could be associated with the inelastic displacements of the embryo. A reference line passed through  $x_1/b = 0$  (the initial geometrical crack front) shows clearly that the embryo approximates to somewhat less than a half-ellipse but results in the partial penetration of the crack tip displacements into the embryo, giving an overall mushroom-type appearance.

The present study, as was our original work, as well as that of Rice *et al.* (1992), is based on the Peierls concept of describing the fundamental inelastic response by an interplanar tension-shear potential. The analysis of the shapes of the embryos and the dependence of the activation energies for their formation on the applied energy release rates were performed self-consistently, utilizing quantities such as  $\mu$ ,  $\gamma_{us}$  and  $\gamma_s$  that had been determined by the best available atomistic approaches (Sun, Beltz and Rice 1993) and were presented also by us earlier (Xu *et al.* 1995a). Thus, while published information of these quantities based on experimental measurements may have a considerable latitude in certainty, our results should have greater accuracy in the relative placement of the modes of response that we have simulated. Clearly, however, on an absolute basis, such as in the determination of the transition temperatures of fig. 18, the results should be viewed with more caution. Nevertheless, the energetics of the embryos that we have analysed indicate that the very large uncertainties in the transition temperatures of previous considerations (discussed by Xu *et al.* (1995a)) have now been eliminated.

In our present study we have examined three plausible modes of nucleation: on inclined planes containing the crack front, on oblique planes intersecting the crack front, in the interior and near a free surface and, finally, on cleavage ledges along the crack front. Our analysis has confirmed our earlier finding (Xu *et al.* 1995a) that nucleation on inclined planes in  $\alpha$ -Fe entails energy barriers that are too high to be overcome, at impending crack advance, at temperatures below the melting point. Contrary to expectations, our analysis has also established that dislocation nucleation on oblique planes in  $\alpha$ -Fe requires even higher energies in the interior of the solid, which translates into transition temperatures well above the melting point. Since in this mode of nucleation no significant free surface is produced, the finding is surprising but can be explained by noting that, while the peak shear stress near the crack tip is higher on the oblique planes than on inclined planes, the area-averaged shear stress is significantly lower in the former case, owing to the rapid decay of stresses in all directions away from the tip. A rather different conclusion was reached, however, for oblique planes near a free surface where no plane-strain stress exists and shear stresses on oblique planes are much higher. Here, were it not for a need of some surface ledge production, emission of dislocations should be nearly spontaneous. Such preponderance of dislocation emission where the crack reaches free surfaces has been observed by George and Michot (1993).

Both the inclined plane modes and the oblique plane modes are instances of homogeneous nucleation, inasmuch as every segment of the crack front constitutes an equally likely nucleation site. However, numerous experiments (Chiao and Clarke 1989, Samuels and Roberts 1989, George and Michot 1993) have demonstrated that

nucleation is a rare event and occurs only at particular sites along the crack front. These sites are nearly always associated with cleavage ledges. A preliminary analysis of heterogeneous nucleation at ledges had been carried out by Zhou and Thomson (1991), who found the mechanism to be quite favourable.

We have analysed dislocation nucleation on cleavage ledges in  $\alpha$ -Fe, where we have taken the crack front to coincide with the  $\langle 110 \rangle$  direction and the ledges to be on  $\{112\}$  planes. This mode is favoured in two important ways. Firstly, the embryo is of a predominantly screw type and, hence, has a low line energy; it involves no surface production. Indeed, our results show that the energetics of this mode in  $\alpha$ -Fe are so favourable that it borders on being a spontaneous process. The B-D transition temperatures that are estimated for this mode are well within the expected range for low-C steel, that is around 250–300 K. This mode of initiation of dislocation activity also furnishes a ready explanation for the observation of Michot (1988) and George and Michot (1993) that such activity often occurs on planes with low resolved shear stress.

Analyses based on Peierls potentials represent the best minimum-commitment approach to an atomistic analysis. Consequently, we view our results as less than a final answer. These limitations notwithstanding, it can be safely argued that the previously existing gap between experiment and theory pointed out by Argon (1987) has been substantially closed at present. Our finding that the key event is a process of heterogeneous nucleation is well in keeping with most other nucleation-controlled phenomena in nature (see Martin and Doherty (1976) for a discussion). Further refinements of the model can be derived from the direct atomistic simulation of the crack-tip processes. These, which have proven unwieldy in the past, can now be more readily attempted using our activation configurations as a first guess of the initial position of the crack-tip atoms. One outstanding problem that remains to be addressed concerns the mobility-controlled fracture transition. A perceptive model of Brede (1993) should be amenable to a more rigorous analysis by our variational boundary integral method. In particular, it should be possible to account for rate effects within the present theory by introducing a rate and temperature-dependent resistance law for dislocation motion.

In closing, we note that the ability of dislocation nucleation at the crack tip to account for the exceedingly sharp transitions observed in some materials has been questioned by Khanta, Pope and Vitek (1994a,b), who have advocated a critical phenomena approach akin to statistical mechanical theories of defect-mediated melting. However, the preponderance of the observational evidence appears to support the crack-tip dislocation nucleation mechanism. Indeed, the detailed and meticulous direct X-ray imaging experiments of George and Michot (1993) of the stages of evolution of the crack tip plastic response, starting from nucleation at crack tip heterogeneities and followed by the very rapid spread and multiplication of dislocation length from such sources, is a convincing direct demonstration of the vast number of degrees of freedom available to dislocations for populating the highly stressed crack tip zone. We know of no present experimental evidence for the large thermal equilibrium concentrations of stiffness-attenuating dislocation dipoles that are predicted by the model of Khanta *et al.* (1994a,b).

#### ACKNOWLEDGEMENTS

This research was supported by the Office of Naval Research (ONR) under Contract No. N00014-92-J-4022, with an additional supplement for the present



simulation for which we are grateful to Dr R. Barsoum of that agency. M.O. gratefully acknowledges support from the ONR under Contract No. N00014-90-J1758. We acknowledge fruitful discussions with Professor J. R. Rice and Professor E. Kaxiras of Harvard University and Dr R. Thomson of the National Institute of Standards and Technology. Moreover, we acknowledge support from the Army Research Office under a Supplementary Equipment Grant No. P-33768-MA-RIP for purchases of computer equipment used in this work. The computations were carried out in the facilities of the Mechanics of Materials group at Massachusetts Institute of Technology, and those of the Solid Mechanics group at Brown University.

## APPENDIX

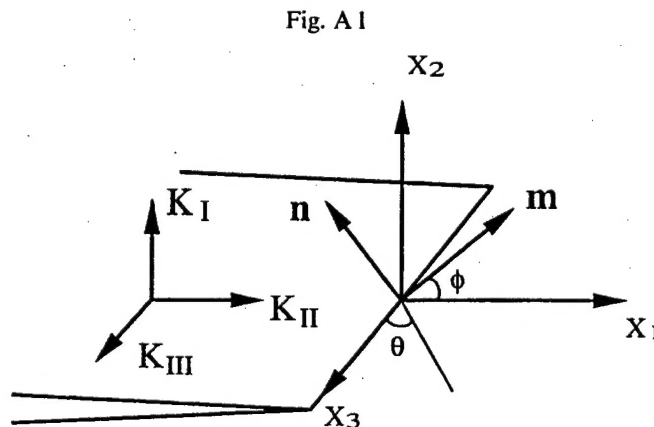
### ASYMPTOTIC SOLUTIONS OF THE CRACK TIP IN THE ANISOTROPIC SOLID

Cracks and dislocations in anisotropic solids were investigated by Stroh (1958) in the manner most useful to our present study. A comprehensive review of the theory of dislocations in anisotropic solids has recently been given by Lothe (1992). The asymptotic solutions of the semi-infinite crack in anisotropic solids used here are obtained by taking the limit of the solution of a slit crack given by Barnett and Asaro (1972), who modelled the slit crack as the superposition of three sets of straight dislocations. The variational boundary integral method developed by Xu and Ortiz (1993) and Xu *et al.* (1995b) is an extension of this approach to three dimensions.

With reference to fig. A 1, the three stress intensity factors  $K_i$  ( $i = 1, 2, 3$ ) are defined as

$$\sigma_{i2}|_{x_1 \rightarrow 0, x_2=0} = \frac{K_i}{(2\pi x)^{1/2}} + \text{non-singular terms.} \quad (\text{A } 1)$$

The opening displacements  $u_i$  are given by



A semi-infinite crack in an anisotropic solid.

$$u_i = 4B_{ij}^{-1}K_j\left(\frac{-x_1}{2\pi}\right)^{1/2}, \quad (\text{A } 2)$$

and the energy release rate  $G$  for crack extension is

$$G = \frac{1}{2}K_i B_{ij}^{-1} K_j. \quad (\text{A } 3)$$

Here  $\mathbf{B}$  is a positive-definite symmetric second-rank tensor that depends only on the direction of the crack front. For isotropic solids,  $\mathbf{B}$  takes the diagonal form

$$B_{11} = B_{22} = \frac{\mu}{1-\nu}, \quad B_{33} = \mu. \quad (\text{A } 4)$$

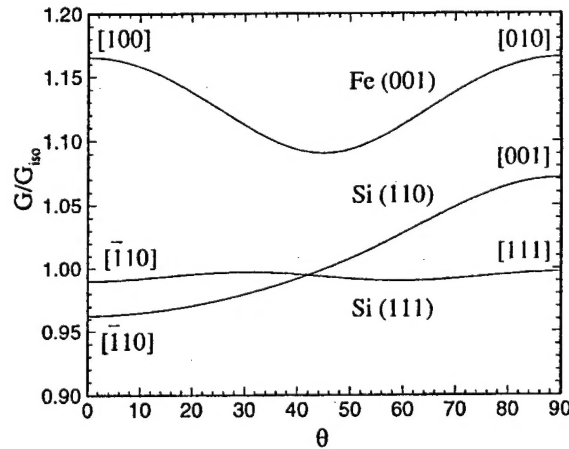
For anisotropic solids,  $\mathbf{B}$  is given by the integral

$$\mathbf{B} = -\frac{1}{2\pi} \int_0^{2\pi} [(\mathbf{mn})(\mathbf{nn})^{-1}(\mathbf{nm}) - (\mathbf{nm})] d\phi, \quad (\text{A } 5)$$

where  $\mathbf{m}$  and  $\mathbf{n}$  are mutually orthogonal unit vectors normal to the crack front; the matrix  $(\mathbf{mn})$  is, in components,  $(\mathbf{mn})_{jk} = m_j c_{ijkl} n_l$ , and  $c_{ijkl}$  are elastic constants of the solid.

For  $\alpha$ -Fe,  $c_{11} = 2.431 \times 10^5$  MPa,  $c_{12} = 1.381 \times 10^5$  MPa and  $c_{44} = 1.219 \times 10^5$  MPa. The resulting dependence of the energy release rate on crack front orientation is plotted in fig. A 2, where  $G_{\text{iso}}$  is the energy release rate computed from average elastic constants. Similar results are shown for Si on (111) and (110) planes, in which case  $c_{11} = 1.677 \times 10^5$  MPa,  $c_{12} = 0.650 \times 10^5$  MPa and  $c_{44} = 0.804 \times 10^5$  MPa. It follows from this calculation that the preferred crack front orientation for cleavage fracture on the (001) plane in  $\alpha$ -Fe is parallel to the [110] direction. Likewise, the directions [110] and [111] are preferred for cleavage on (110) and (111) planes respectively in Si.

Fig. A 2



The variation in energy release rate with crack front orientation in Fe and Si.

## REFERENCES

- ALLEN, N. P., 1959, *Fracture*, edited by B. L. Averbach, D. K. Felbeck, G. T. Hahn and D. A. Thomas (Cambridge, Massachusetts: MIT Press), p. 123.
- ARGON, A. S., 1987, *Acta metall.*, **35**, 185.
- ARGON, A. S., and MALOOF, S. R., 1966a, *Acta metall.*, **14**, 1449; 1966b, *Ibid.*, **14**, 1463.
- BARNETT, D. M., and ASARO, R. J., 1972, *J. Mech. Phys. Solids*, **20**, 253.
- BELTZ, G. E., and RICE, J. R., 1991, *Modeling the Deformation of Crystalline Solids: Physical Theory, Application and Experimental Comparisons*, edited by T. C. Lowe, A. D. Rollett, P. S. Follansbee and G. S. Daehn (Warrendale, Pennsylvania: Metallurgical Society of AIME), p. 457.
- BREDE, M., 1993, *Acta metall. mater.*, **41**, 211.
- BREDE, M., and HAASEN, P., 1988, *Acta metall.*, **36**, 2003.
- BREDE, M., HSIA, K. J., and ARGON, A. S., 1991, *J. appl. Phys.*, **70**, 758.
- BULATOV, V. V., YIP, S., and ARGON, A. S., 1995, *Phil. Mag. B*, **72**, 452.
- BURNS, S. J., and WEBB, W. W., 1970a, *J. appl. Phys.*, **41**, 2078; 1970b, *J. appl. Phys.*, **41**, 2086.
- CHIAO, Y.-H., and CLARKE, D. R., 1989 *Acta metall.*, **47**, 203.
- COTTERELL, B., and RICE, J. R., 1980, *Int. J. Fract.*, **16**, 155.
- FOREMAN, A. J., JASWON, M. A., and WOOD, J. K., 1951, *Proc. phys. Soc. A*, **64**, 156.
- FREUND, L. B., and HUTCHINSON, J. W., 1985, *J. Mech. Phys. Solids*, **33**, 169.
- GEORGE, A., and MICHOT, G., 1993, *Mater. Sci. Engng*, **A164**, 118.
- GILMAN, J. J., KNUDSEN, C., and WALSH, W. P., 1958, *J. appl. Phys.*, **29**, 600.
- HAHN, G. T., AVERBACH, B. L., OWEN, W. S., and COHEN, M., 1959, *Fracture*, edited by B. L. Averbach, D. K. Felbeck, G. T. Hahn and D. A. Thomas (Cambridge, Massachusetts: MIT Press), p. 91.
- HIRSCH, P. B., ROBERTS, S. G., SAMUELS, J. and WARNER, P. D., 1989a, *Advances in Fracture Research*, Vol. 1, edited by K. Salama, K. Ravi-Chandar, D. M. R. Taplin and P. Rama Rao (Oxford: Pergamon), p. 139.
- HIRSCH, P. B., SAMUELS, J., and ROBERTS, S. G., 1989b, *Proc. R. Soc. A*, **421**, 25.
- HSIA, K. J., and ARGON, A. S., 1994, *Mater. Sci. Engng. A*, **176**, 111.
- JUAN, Y., and KAXIRAS, E., 1996 *Phil. Mag. A*, **74**, 1367.
- KELLY, A., TYSON, W. R., and COTTRELL, A. H., 1967, *Phil. Mag.*, **15**, 567.
- KHANTA, M. POPE, D. P., and VITEK, V., 1994a, *Phys. Rev. Lett.*, **73**, 684; 1994b, *Scripta metall. mater.*, **31**, 1349.
- LIN, T., EVANS, A. G., and RITCHIE, R. O., 1986, *J. Mech. Phys. Solids*, **34**, 477; 1987, *Metall. Trans. A*, **18**, 641.
- LOTHE, J., 1992, *Elastic Strain Fields and Dislocation Mobility*, edited by V. L. Indenbom and J. Lothe (Amsterdam: Elsevier), p. 269.
- MCCLINTOCK, F. A., and ARGON, A. S., 1966, *Mechanical Behavior of Materials* (Reading, Massachusetts: Addison-Wesley), chapter 17.
- MAEDA, K., and YAMASHITA, Y., 1989, *Structure and Properties of Dislocations in Semiconductors*, edited by S. G. Roberts, D. B. Holt and P. R. Wilshaw (Bristol: Institute of Physics), p. 269.
- MARTIN, J. W., and DOHERTY, R. D., 1976, *Stability of Microstructure in Metallic Systems* (Cambridge University Press).
- MICHOT, G., 1988, *Crystal Properties and Preparation*, Vols. 17 and 18 (Aedermannsdorf, Switzerland: Trans Tech Publ.), p. 55.
- NABARRO, F. R. N., 1947, *Proc. phys. Soc. A*, **59**, 256.
- PEIERLS, R. E., 1940, *Proc. phys. Soc. A*, **52**, 34.
- RICE, J. R., 1992, *J. Mech. Phys. Solids*, **40**, 235.
- RICE, J. R., and BELTZ, G. E., 1994, *J. Mech. Phys. Solids*, **42**, 333.
- RICE, J. R., BELTZ, G. E., and SUN, T., 1992, *Topics in Fracture and Fatigue*, edited by A. S. Argon (Berlin: Springer), p. 1.
- RICE, J. R., and THOMSON, R., 1974, *Phil. Mag.*, **29**, 73.
- ROSE, J. H., FERRANTE, J., and SMITH, J. R., 1981, *Phys. Rev. Lett.*, **47**, 675.
- SAMUELS, J., and ROBERTS, S. G., 1989, *Proc. R. Soc. A*, **421**, 1.
- SCHÖCK, G., and PÜSCHL, W., 1991, *Phil. Mag. A*, **64**, 931.
- ST JOHN, C., 1975, *Phil. Mag.*, **32**, 1193.

- STROHL, A. N., 1954, *Proc. R. Soc. A*, **223**, 404; 1955, *Ibid.*, **232**, 548; 1957, *Adv. Phys.*, **6**, 418; 1958, *Phil. Mag.*, **3**, 625.
- SUMINO, K., 1989, *Structure and Properties of Dislocations in Semiconductors*, edited by S. G. Roberts, D. B. Holt and P. R. Wilshaw (Bristol: Institute of Physics), p. 245.
- SUN, Y., BELTZ, G. E., and RICE, J. R., 1993, *Mater. Sci. Engng.*, **A170**, 67.
- SUN, Y., RICE, J. R., and TRUSKINOVSKY, L., 1991, *High Temperature Ordered Intermetallic Alloys IV*, Materials Research Society Symposium Proceedings, Vol. 213, edited by L. A. Johnson, D. T. Pope, and J. O. Stiegler (Pittsburgh, PA: Materials Research Society), p. 243.
- XU, G., and ORTIZ, M., 1993, *Int. J. Numer. Methods Engng.*, **36**, 3675.
- XU, G., ARGON, A. S., and ORTIZ, M., 1995a, *Phil. Mag. B*, **72**, 415.
- XU, G., ARGON, A. S., ORTIZ, M., and BOWER, A. F., 1995b, *Computational Mechanics '95, Theory and Applications*, Vol. 2, edited by S. N. Atluri, G. Yagawa, and T. A. Cruse (Berlin: Springer), p. 2874.
- YAMAGUCHI, M., VITEK, V., and POPE, D., 1981, *Phil. Mag. A*, **43**, 1027.
- YONENAGA, I., ONOSE, U., and SUMINO, K., 1987, *J. Mater. Res.*, **2**, 252.
- YONENAGA, I., and SUMINO, K., 1989, *J. Mater. Res.*, **4**, 355.
- YONENAGA, I., SUMINO, K., IZAWA, G., WATANABE, H., and MATSUI, J., 1989, *J. Mater. Res.*, **4**, 361.
- ZHOU, S. J., and THOMSON, R., 1991, *J. Mater. Res.*, **6**, 639.